Automated detection of ventricular tachycardia locations using a combined physics and deep learning approach

Monaci, Sofia

Awarding institution:
King's College London

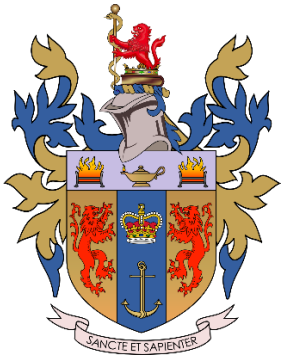

School of Biomedical Engineering & Imaging Sciences

King's College London

Automated detection of ventricular tachycardia locations using a combined physics and deep learning approach

Sofia Monaci

This dissertation is submitted for the degree of

Doctor of Philosophy

Supervisors:

Dr Martin J. Bishop

Dr Andrew P. King

24 August 2022

A Mamma, Babbo e Flavia, senza di voi questo lungo viaggio non sarebbe stato possibile…

ABSTRACT

Ventricular tachycardia (VT) is a serious cardiac arrhythmia, and an important cause of sudden cardiac death (SCD) and morbidity. Therefore, the management of the tachycardia is of importance to prevent degeneration into fibrillation, SCD and improve quality of life. Implantable cardiac electronic devices are the first-line therapy for most VT patients at high risk. However, the most effective, curative option against incessant VT is considered ablation therapy. The success of an ablation procedure is heavily dependent on the accurate localisation of the sites responsible for the initiation and maintenance of the tachycardia (e.g. focal ectopy, isthmus, exit/entrance). The identification of these optimal ablation targets is carried-out via either invasive and time-consuming electrophysiological (EP) mapping strategies (e.g. pace-mapping) or non-invasive modalities, which all rely on the surface electrocardiogram (ECG). Difficulties in inducing the arrhythmia in haemodynamically unstable patients and/or with limited conventional treatment options might challenge the acquisition of the ECG, and affect correct identification of ablation targets. In addition, recurrence of the VT may occur if the clinical episode has not been properly targeted. These limitations of current ablation mapping strategies warrant the development of more specifically targeted solutions to increase ablation success rate and terminate VT in the long-term.

With this research, we aim to improve ablation planning and identification of VT ablation targets by utilising the information stored as electrograms (EGM) in implanted devices, that the majority of VT ablation patients have *in-situ*. By doing so, we could target the clinical episodes, as well as reduce the need for VT induction, ultimately improving safety, speed and accuracy of ablation. We intend to achieve this by using computational models to simulate implanted device EGMs and investigate their utility in in-silico pace-mapping. In addition, we will use computational simulations to generate a vast library of ECGs and EGMs of different VT episodes, which will be useful in conjunction with deep learning approaches to automate the localisation of VT critical sites. Finally, we aim to evaluate our in-silico platforms within clinical settings.

Our research was successful in showing the utility and power of simulated, multi-vector EGM recordings for the identification of critical VT sites in both in-silico pace-mapping and automated algorithms. We reported results comparable to using the ECGs. In addition, we were able to evaluate our platforms in clinical settings, when

using clinical VT ECGs. Despite the lack of EGM recordings of the clinical VT episodes, given the extensive computational analyses carried-out throughout this Thesis, we believe that the performance of our platforms would return promising results when using real VT EGMs, thus underscoring the importance of this proof-of-concept research to improve VT management and ablation planning.

ACKNOWLEDGMENTS

This journey has been incredible, and I am both proud and astonished of what we have accomplished. I would like to emphasize the "we" as it has been one of the toughest and challenging projects I have ever set out to complete, both professionally and personally, in a quite unique moment of history, and I could have never completed this PhD without the support and help of my supervisors, my family and friends, and many academics and colleagues spread all over the world.

I would like to express my deepest gratitude to my first supervisor, Dr Martin Bishop. His constant support and patience helped me channel frustration into perseverance, use failures to build success and never lose my enthusiasm and love for research. His knowledge and guidance helped visualise and construct ideas into concrete and useful pieces of work and grow from an engineering student to a well-rounded researcher. I would like to deeply thank my second supervisor, Dr Andrew King, for his useful remarks, immense knowledge, and support. He opened the door to the fascinating world of AI, helped me tackle many of the challenges associated with its application in medicine, and broaden my critical thinking skills.

I would also like to thank Prof Gernot Plank and all his research group at the Medical University of Graz, especially Dr Karli Gillette, and Prof Aldo Rinaldi, Prof Mark O'Neill, Dr Ronak Rajani, Dr John Whitaker, Dr Rahul Mukherjee and Mark Elliott for their clinical expertise.

I would like to thank all my friends and colleagues at King's College London for their help in this journey, for making covid a bit more bearable, for the countless lunches and after-work pints. A special thanks to Esther, Marina, Shuang, Cristobal, Stefano, Damiano, Fernando and Hugh.

Outside of work, I would like to thank my long-term friends, Melissa, Chloe, Jade, Tobias, Toby, Harry, Ari, Ahmed, Richard and Marianne for always believing in me, for giving me the strength to keep going when everything seemed lost, for listening and helping me see things under a different light.

Finally, I would like to thank my parents, my sister, my grandma and my aunt. My biggest dream since I was 12 was to study and live in London, pursue all my passions and goals, and become the person I am today. This thesis would have not been possible without them.

PUBLICATIONS

- Monaci S, Strocchi M, Rodero C, Gillette K, Whitaker J, Rajani R, et al. In-silico pace-mapping using a detailed whole torso model and implanted electronic device electrograms for more efficient ablation planning. Comput Biol Med. 2020;125:104005.
- Monaci S, Gillette K, Puyol-Antón E, Rajani R, Plank G, King A, et al. Automated Localization of Focal Ventricular Tachycardia From Simulated Implanted Device Electrograms: A Combined Physics–AI Approach. Front Physiol. 2021;12:943.
- Qian S, Monaci S, Mendonca-Costa C, Campos F, Gemmell P, et al. Optimization of defibrillation thresholds in right-sided ICD generator placement using a cohort of whole-torso models. *Submitted to JACC: Clinical Electrophysiology. 2022.*
- Monaci S, Qian S, Gillette K, Puyol-Antón E, Elliott M, et al. Non-invasive Localisation of Post-Infarct Ventricular Tachycardia Exit sites to Guide Ablation Planning: A Computational-AI Platform Utilising the 12-lead Electrocardiogram and Intracardiac Electrograms from Implanted Devices. Europace. 2022. 00, 1-9.

CONTENTS

LIST OF FIGURES

LIST OF TABLES

NOMENCLATURE

Ca^{2+}: Calcium

C_m: Membrane Capacitance

Na^{+}: Sodium

2D: Two-Dimensional

AHA: American Heart Association

AI: Artificial Intelligence

ANN: Artificial Neural Network

APD: Action Potential Duration

AVN: Atrio-ventricular Node

BSP: Body Surface Potential

BZ: Border Zone

CA: Catheter Ablation

CARP: Cardiac Arrhythmia Research Package

CC: Correlation Coefficient

CI: Coupling Interval

CIED: Cardiac Implantable Electronic Devices

CL: Cycle Length

CMR: Cardiac Magnetic Resonance Imaging

CNN: Convolutional Neural Network

CRT-D: Cardiac Resynchronisation Therapy Devices

cSBRT: Cardiac Stereotactic Body Radiotherapy

CV: Conduction Velocity

CVD: Cardiovascular Disease

D: Diffusion Tensor

DL: Deep Learning

DT: Decision Tree

$\mathrm{E_{ion}}$: Equilibrium Potential

EAM: Electro-anatomical Mapping

ECGi: Electrocardiogram Imaging

ECV: Extracellular Content Volume

F: Faraday Constant

FC: Fully-Connected

FDM: Finite Difference Method

FEM: Finite Element Method

FVM: Finite Volume Method

$\mathrm{g_{ion}}$: Membrane conductance

$\mathrm{g_{Na}}$: Sodium conductance

GNB: Gaussian Naive Bayes

HH: Hodgkin and Huxley

$\mathrm{I_{stim}}$: Extracellular Stimulus Current

$\mathrm{I_a}$: Axial Current

$\mathrm{I_{bCa}}$: Background Calcium Current

$\mathrm{I_{bK}}$: Background Potassium Current

$\mathrm{I_{CaL}}$: L-type Calcium Current

$\mathrm{I_{foot}}$: Foot Current

$\mathrm{I_{ion}}$: Ionic Current

$\mathrm{I_K}$: Potassium Current

$\mathrm{I_{K1}}$: Inward Rectifying Potassium Current

$\mathrm{I_{Ks}}$: Slow Delayed Rectifier Current

$\mathrm{I_{leak}}$: Leak Current

$\mathrm{I_m}$: Transmembrane Current

$\mathrm{I_{Na}}$: Sodium Current

I_{NaCa}: Sodium-Calcium Exchanger Current

I_{NaK}: Sodium-Potassium Pump Current

I_{pCA}: Plateau Calcium Current

I_{pK}: Plateau Potassium Current

I_{to}: Transient Outward Current

ICD: Implantable Cardioverter Defibrillator

IVC: Inferior Vena Cava

J_e: Extracellular Current Density

J_i: Intracellular Current Density

K^+: Potassium

K_r: Rapid Delayed Rectifier Potassium

LA: Left Atrium

LAD: Left Anterior Descending Artery

LAT: Local Activation Time

LBBB: Left Bundle Branch Block

LCX: Left Circumflex Artery

LF: Lead Field

LGE: Late Gadolinium Enhancement

LMCA: Left Main Coronary Artery

LSTM: Long-Short Term Memory

MAD: Mean Absolute Deviation

MI: Myocardial Infarction

ML: Machine Learning

NCX: Sodium Calcium Exchanger

SR: Sinus Rhythm

PES: Programmed Electrical Stimulation

PM: Pace Map

PS: Purkinje System

PVC: Premature Ventricular Contraction

R_a: Cable Resistance

RA: Right Atrium

RBBB: Right Bundle Branch Block

RCA: Right Coronary Artery

RE: Reaction-Eikonal

RF: Random Forest

RNN: Recurrent Neural Network

ROC: Receiver Operating Characteristic Curve

RV: Right Ventricle

RyR: Ryanodine Receptor

SAN: Sino-atrial Node

SERCA: Sarco-endoplasmic Calcium ATPase

SNR: Signal-to-Noise Ratio

SoO: Site of Origin

S-PM: Reference-less Correlation Spatial Gradient Pace Map

SVC: Superior Vena Cava

SVM: Support Vector Machine

T: Temperature

TAVI: Trans-catheter Aortic Valve Implantation

TT: Ten Tusscher

UVC: Universal Ventricular Coordinate

v: Local Conduction Velocity

V_m: Transmembrane Potential

VF: Ventricular Fibrillation

σ: Conductivity

σ_e: Extracellular Conductivity

σ_i: Intracellular Conductivity

σ_m^*: Harmonic Conductivity

φ_e: Extracellular Potential

σ_i: Intracellular Potential

1

INTRODUCTION

“The beginning is perhaps more difficult than anything else,

but keep heart, it will turn out all right”

Vincent Van Gogh

1.1 MOTIVATION

Cardiovascular diseases (CVD) are the leading cause of death globally, accounting for ~17.9 million deaths per year worldwide[1]. There are many underlying causes of CVDs, but increased life expectancy and escalating behavioural risk factors (unhealthy diet, physical inactivity, tobacco and alcohol consumption) have contributed significantly to a steep increase of CVDs in recent years. Sudden cardiac death (SCD) accounts for 25% of all cardiovascular deaths(1). Aside from mortality, management of CVD and prevention of SCD imposes a huge financial and social burden on health services and societies, warranting more specifically targeted and better therapies.

The leading cause of SCD is attributed to cardiac arrhythmias, and in particular to the degeneration of ventricular tachycardia (VT) into fibrillation (VF). Arrhythmias are characterised by a disruption of the cardiac electrical activity, which causes uncoordinated and unsynchronised contractions of the chambers of the heart, and can compromise blood circulation and pumping. The electrical disorganisation in the ventricles may become lethal if the heart rate increases drastically and becomes completely chaotic, impairing the heart's mechanical pumping function. Thus, VT management plays a central role in preventing VF and SCD, and improving morbidity.

The management of VT episodes often starts with implanting cardiac electronic devices that detect potential arrhythmic activity, and apply appropriate electrotherapy to terminate it. However, alternative therapies are needed in the presence of recurrent VT episodes that cause frequent device shocks, and increase morbidity and mortality rates. In this setting, ablation therapy has been proposed as a more effective, long-term option to device therapy. Ablation consists of delivering energy into the myocardial tissue in order to cause permanent lesions, thus preventing the propagation of the VT. A successful termination of the VT relies however on the correct identification of the sites critical to the

[1] https://www.who.int/news-room/fact-sheets/detail/cardiovascular-diseases-(cvds)

initiation and maintenance of the arrhythmia. The localisation of these substrates remains a significant clinical challenge, demonstrated by approximate ~ 50% recurrence rate within a year of VT ablation(2).

Numerous techniques exist for the identification of VT optimal ablation targets. They mostly rely on acquiring and/or reconstructing electrophysiological (EP) measurements of the heart's electrical activity during the tachycardia from either intracardiac catheters or body surface measurements. In the last decades, technological growth and the necessity of improving VT therapies(3) have driven the field of EP, helping increase the robustness and efficacy of these mapping procedures. There has been an important shift from point-to-point registration of cardiac electrical activity, to multimodal, state-of-the-art approaches(4) that combine mapping and imaging to generate near-real time electroanatomic (EAM) maps of a patient's heart. The integration of both structural and functional information allows a more accurate characterisation of the clinical VT(5), especially in the presence of structural heart disease, as well as simplifying data acquisition and manipulation. On one hand, EAM mapping strategies have revolutionised our mechanistic understanding of arrhythmias, as well as clinical procedures. On the other, however, they are still associated with several risks and limitations, which challenge the mapping of non-sustained and/or hemodynamically poorly tolerated VTs, and the management of non-inducible episodes. Non-invasive reconstruction of cardiac activity from body surface measurements has been demonstrated useful in guiding pre-procedure planning of VT ablations in those difficult and delicate scenarios. However, there are concerns relating to its precision and accuracy compared to invasive modalities.

At this stage, it is important to mention one invasive EP mapping strategy that plays an important role in this Thesis: pace-mapping. This technique represents a valid bridge between more invasive EP strategies and non-invasive methods to accurately describe VT dynamics and substrates in haemodynamically unstable patients. Briefly, pace-mapping consists of electrically stimulating the ventricular myocardium from different locations to identify the site(s) that more closely reproduces the morphology of the clinical VT episode during sinus rhythm.

All non-invasive and invasive strategies, particularly pace-mapping, rely on the surface 12-lead electrocardiogram (ECG) to describe VT dynamics and help identify optimal ablation targets. Since its origin, this simple, widely available, non-invasive tool has been an integral part of the initial evaluation of a patient suspected of having cardiac-related problems(6,7). Over time, the use of the ECG has expanded significantly to the interpretation of complex arrhythmias(8–11), myocardial infarction(12), other ECG abnormalities(13), and has become essential to localise VT main drivers and guide ablation. The recording of the ECG during the clinical and/or EP-induced VT is however one of the major challenges that limits current EP mapping strategies, and thus successful VT termination. Moreover, recurrence of the tachycardia post-procedure is favoured if there is a mismatch in morphology between EP-induced and clinical episodes.

In recent studies(14,15), alternative recordings of the heart rhythm in the form of electrograms (EGMs) stored in cardiac implantable electronic devices have been proposed to help characterise the clinical VT, and overcome the issues presented with the ECG. However, there is a need to explore further the potential and utility of implanted device EGMs in the context of VT characterisation and ablation planning, which could also benefit device programming, shock/pacing delivery, and a wide range of other VT-related diagnostic, therapeutic, prognostic processes. Leveraging and analysing further the role of EGMs in VT management and ablation planning represents the fundamental motivation behind this Thesis, which will be investigated with computational modelling.

Over the last century, experimental investigations have helped elucidating many cardiac physiological and pathological mechanisms, but it is due to the advent of computational and mathematical models(16–20) that our understanding of cardiac arrhythmias, and VT, has reached a new level of depth, allowing improvements in risk stratification strategies(21,22), therapy guidance, ablation planning(23–25), and in the growth of personalised medicine(26–32), paving the way towards the “digital twin” vision(33).

In contrast to experimental studies, computational simulations and models allow to reproduce tissue and organ mechanisms at a much faster pace, and are not limited by laboratory bench costs or the sets of parameters that can be observed and analysed. Thus, modelling allows the analysis and exploration of a wider range of scenarios, which will be useful in this Thesis to carry-out EGM-based VT investigations. Computational modelling also overcomes the ethical constraints associated with invasive clinical research, carried-out on patients, as well as simplifying data collection, storage and manipulation. Additionally, computational simulations allow higher resolution, three-dimensional (3D) spatio-temporal representation of the electrical signal, and VT dynamics, that could not be feasible with invasive EP mapping.

Despite the numerous benefits of modelling, proving reliability and clinical translation of computationally simulated scenarios is extremely challenging, and relies, in turn, on the availability of experimental and clinical datasets. Because of the intrinsic physical and mathematical assumptions modelling is built upon, and the complexity and variability of human anatomy, physiology and pathophysiology, there are different ways of gathering evidence that can be used to show the trustworthiness and validity of a model for clinical use(34). These are: 1) *verification*, related to the validity of assumptions governing the model equation as well as the fidelity of the model parameter values; 2) *calibration*, tuning, fitting, optimising the model to match as closely as possible experimental/clinical data; 3) *validation*, testing the model on independent, real-world data that was not used in the construction of the model itself(35). Hence, according to the intended use of a computational framework, there are different ways of ensuring fidelity of simulated results, and we will attempt such validation in this Thesis.

In the last ten years, there has been an exponential growth of other mathematical and statistical computer-based tools used in medicine, falling under artificial intelligence (AI), enabled by the increase in big labelled datasets, computing power and cloud storage(36). From the automation of surgical interventions(37,38), to the rapid detection of diseases from images(39,40) and/or signals(41,42), to long-term predictions(43), the integration of human and AI has started to have an

impact for clinicians, healthy systems and patients. In the context of arrhythmias and EP, a branch of AI, referred to as machine learning (ML), has been used and extensively investigated to interpret pulse irregularities and arrhythmia classification from ECGs(44,45). There has also been an increasing interest in ML applied to intracardiac mapping, implantable devices and EP procedures(46,47).

Recently, the automation of ECG interpretation for the identification of VT ablation targets has attracted the attention of a large portion of academic and clinical research(48–51). However, we believe that this task would significantly benefit from more advanced, non-linear feature extraction methods, such as deep learning (DL). DL is a type of ML with increased complexity and abstraction, that allows more advanced predictive investigations, but typically relies on the availability of bigger training datasets. At the moment, the difficulty in getting access to big data, in interpreting and explaining the results of DL architectures, and in building trust among clinicians, are limiting the progress of the field in automating VT localisation. We hypothesise that the continuous recording of cardiac implanted devices, generating a large amount of data under different conditions, could favour the use of DL approaches to improve VT management. However, at the moment there is a need to test this hypothesis, and to further understand how best to use EGM recordings for such a purpose. The integration of computational models with AI could help face and solve some of these questions, and help extend VT investigations beyond the ECG, to implanted device EGMs.

1.2 THESIS GOAL

The goal of this Thesis is to develop safer and more targeted strategies to aid VT ablation by using EGM recordings stored in cardiac implantable devices. We hope to show how preliminary VT ablation planning could benefit from non-invasive modalities using computational modelling and AI/DL tools that target the actual, clinical information, as well as reduce the need for VT induction and more time-consuming, invasive procedures. By guiding and improving ablation planning with the use of computational models, DL tools and EGM recordings, VT recurrence, and therefore morbidity and

mortality caused by the tachycardia, could be reduced, benefitting patients, physicians and health services.

Our main goal will be addressed in four steps. Firstly, we will show how EP computational models can be used to generate an accurate, non-invasive in-silico pace-mapping platform to investigate VT dynamics and VT ablation target delineation from implanted device EGMs. Secondly, we will use computational simulations to provide bigger training and testing datasets for DL architectures to automate the detection of VT critical sites from ECGs and EGMs (for two different types of tachycardia). Lastly, we will evaluate our computer-based tools and pipelines in clinical settings.

1.3 THESIS OUTLINE

We will now describe the overall structure of this Thesis. The Thesis begins in **Chapter 2** with background information on cardiac anatomy and physiology, illustrating the structure and function of the healthy heart. Particular emphasis is then given to cardiac electrophysiology, and to abnormalities in the normal electrical stimulation of the heart leading to VT. This is followed by a detailed description of VT mechanisms and management, laying the foundation and motivation of this Thesis.

In **Chapter 3**, we describe in detail the mathematical formulations that allow the construction of cardiac computational models which aim to reproduce the electrical activity of the heart under normal and arrhythmic scenarios. We illustrate well-established methods, as well as more novel approaches to model cardiac electrical behaviour, and how these simulations can be performed on 3D patient-specific models generated from imaging datasets. Moreover, we describe the fields of AI, ML and in particular specific DL architectures and tools, which will be used throughout this Thesis to automate VT detection.

Chapter 4 reviews previous work in the field of VT target ablation detection, both in terms of clinical approaches and computer-based algorithms. To begin with, a historical perspective of ECG-based conventional pace-mapping is presented, followed by alternative approaches that detect other critical

VT sites, and the feasibility of utilising implanted device EGMs for similar purposes. Then, the Chapter dives into the description of a variety of existing algorithms aimed at localising VT from ECGs, helping understand how computational modelling and AI can bring benefits to clinical EP procedures.

In **Chapter 5**, we utilise the tools presented in previous Chapters to create an in-silico pace-mapping platform that can be used to provide safe, non-invasive and efficient guidance of ablation planning. The platform is used to investigate how simulated implanted device EGMs can be used in addition to ECGs to detect VT ablation targets, and what the benefits of computational modelling are in this context.

Chapter 6 presents a very fast and efficient computational environment for the generation of datasets that can be used to train and test DL architectures for the automated localisation of focal VT. The work presented here builds upon all previous Chapters, and it also aims to illustrate different modelling aspects that can influence the performance of the AI architectures.

In **Chapter 7**, another computational-AI platform is presented, aiming at extending the localisation of VT critical sites to more complex VT episodes, and addressing the limitations of previous Chapters. Here, different computational scenarios are investigated to be able to show applicability of the pipeline in clinical settings. The Chapter concludes with a first evaluation of our work on clinical data.

Additional evaluation of our platforms follows in **Chapter 8**, where we present the main challenges of translating our tools into clinical settings. Three different clinical datasets are used to evaluate both in-silico pace-mapping and automated VT localisation, and highlight the necessary steps to allow the progress of the field.

Finally, the Thesis concludes with **Chapter 9**, bringing together the work done in each of the preceding Chapters, and summarising the main findings. We will also highlight possible extensions and future directions, and how the work presented in this Thesis could be of importance for the clinical, modelling and AI communities in the context of cardiac arrhythmias.

2

CLINICAL BACKGROUND

In this Chapter, we touch upon the main concepts of cardiac anatomy & physiology, cardiac electrophysiology and cardiac arrhythmias, building the clinical foundation of this Thesis. In Section 2.1, we provide an introduction to the structural and functional aspects of a normal, healthy heart. In Section 2.2, we dive into the electrical excitation of the heart, responsible for synchronous contraction of the organ and efficient blood circulation. In Section 2.3, we move on to describe abnormalities in the cardiac electrical conduction system, leading to arrhythmias, and specifically to ventricular tachycardia. Section 2.4 is dedicated to describing the main diagnostic tools used to manage VT, such as the electrocardiogram, imaging modalities and mapping strategies, whereas Section 2.5 describes the main therapeutic options (implantable devices and ablation procedures). The Chapter ends with Section 2.6, a brief summary of the importance of VT management in the context of the work we carry-out in the following Chapters.

2.1 Cardiac Anatomy & Physiology

The heart is responsible for the continuous circulation of blood in the body, supplying oxygen and vital nutrients to other tissues and organs. The position and gross anatomy of the heart is depicted in **Figure 2.1**. The heart is located within the thoracic cavity, medially between the lungs, and it is protected by a membrane known as the *pericardium*. The heart consists of four chambers, the right (RA) and left atria (LA), and the right (RV) and left (LV) ventricles (**Figure 2.2**). The wall separating the left and right chambers is referred to as the *septum*. Deoxygenated blood from the peripheral regions of the body enters the RA from the superior (SVC) and inferior vena cava (IVC), it is pumped into the RV and then propelled to the lungs – where it gets oxygenated - through the pulmonary artery. This blood flow between the heart and lungs is known as *pulmonary circulation*. Oxygenated blood returns to the LA through pulmonary veins, and it then reaches the LV, which pumps out the blood to the rest of the body via the aorta. This circulation is known as *systemic*. Nutrients and oxygen are supplied to the heart itself via the coronary system, which wraps around the outside of the heart.

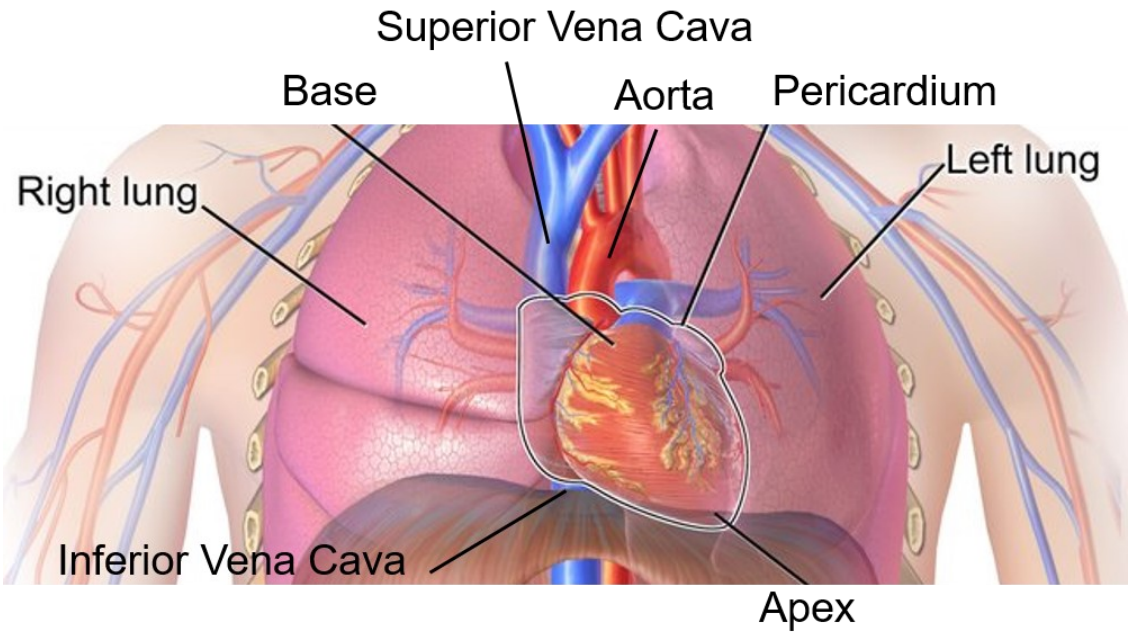

Figure 2.1. *Position of the heart in the chest. Frontal plane showing major thoracic organs, veins and arteries. Adapted from* [2]

[2] https://steemit.com/medicine/@shamabaig/location-of-the-heart-in-the-chest-cavity

There are two main coronary arteries that supply blood to the left and right side of the heart: the left main (LMCA) and the right (RCA) coronary arteries, respectively. The former branches out into the left anterior descending artery (LAD) and the left circumflex artery (LCX), whereas the RCA divides into smaller branches.

The wall of the heart is comprised of three layers: the *epicardium* – outer layer -, the *myocardium* – middle, muscular layer - and the *endocardium* – inner layer (**Figure 2.2**).

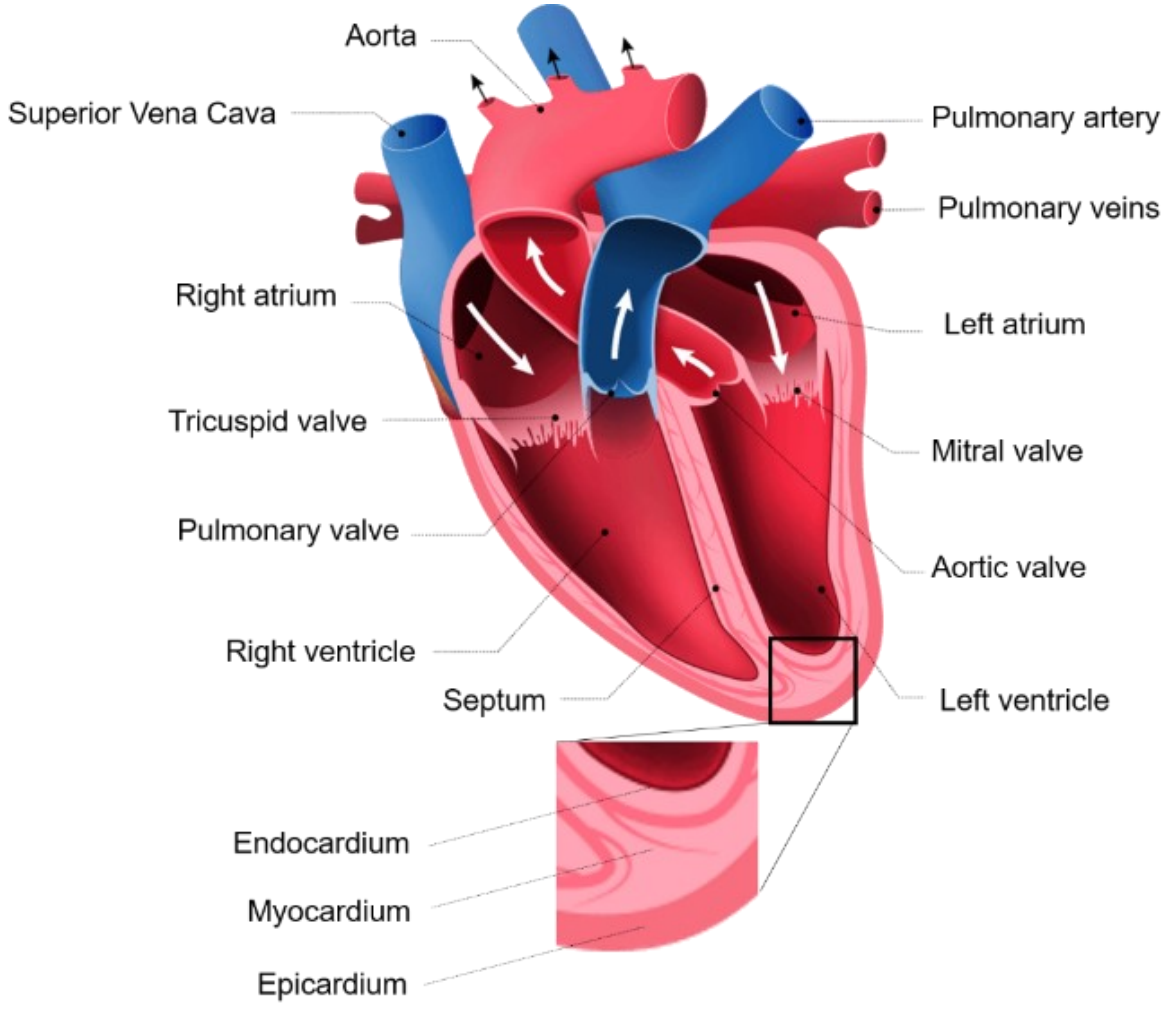

Figure 2.2. Cardiac chambers and wall layers. Longitudinal cross-section section of the heart showing the important structural features and composition of the wall. Adapted from [3].

[3] https://www.hiclipart.com/free-transparent-background-png-clipart-dhtjq

The myocardium is composed of inter-connected sheets of tissue, where contractile cardiac cells, or *cardiomyocytes*, - bundled together by collagen - lie longitudinally and form cardiac fibres. Each fibre consists of chains of *myofibrils* (rod-like units), made of repeating sections of *sarcomeres*. Each sarcomere is composed of long proteins that organise into thick and thin filaments, called *myofilaments*, which, by sliding past each other, allow the cardiac muscle to contract and relax. The *sarcoplasmic reticulum* envelopes each myofibril, and is transversed by structures called *T-tubules*, extensions of the *sarcolemma* (cell membrane of the cardiomyocytes), which are an important determinant of cardiac cell function, as we will see **below.** Cardiomyocytes are electrically excitable and are the smallest muscular subunits driving the contraction of the heart, hence allowing pumping of the blood at a bigger scale.

2.2 CARDIAC ELECTROPHYSIOLOGY

In this section, we will briefly describe cardiac electrophysiology at a macroscopic and microscopic level to understand how the electrical wave propagates in a healthy heart, and how this is driven by changes in electrical charge within cardiac fibres.

2.2.1 Cardiac Electrical Conduction

Regular and continuous contraction of the heart is made possible by cyclic excitation of the heart, which is driven by specialised cardiomyocytes, known as *pacemaker cells*, primarily situated in the *sinoatrial node* (SAN) in the RA. These cells are capable of triggering spontaneous changes in electrical charge - referred to as *action potentials* (AP) - across the cell membrane, which then spread to the rest of the heart and are able to excite the contractile cardiomyocytes in both atrial and ventricular chambers. In brief, as illustrated in **Figure 2.3A,** the electrical impulse travels rapidly from the SAN through both RA and LA, initiating atrial contraction, and it is collected in the *atrioventricular node* (AVN), located at the base of the RV. After slowing down at the AVN to allow blood to be pumped to the ventricles, the electrical impulse travels rapidly through a specialised bundle of conducting fibres,

the *Bundle of His*, which divides into two major *right* and *left bundle branches*, allowing the excitation to reach the endocardium of both RV and LV. Ventricular contraction is then triggered by the impulse just described exciting a complex network of fibres located in the endocardial layer of the *apex* (bottom part) of the heart, known as the *Purkinje system* (PS). Finally, the electrical impulse travels upwards and outwards, and the excitation cycle repeats.

Under normal circumstances, the rhythm at which the heart excites – known as *sinus rhythm* (SR) - is between $60\ beats\ per\ minute\ (bpm)$ at rest and $180 - 200\ bpm$ during peak exercise, resulting in highly coordinated and synchronised contractions of atrial and ventricular chambers.

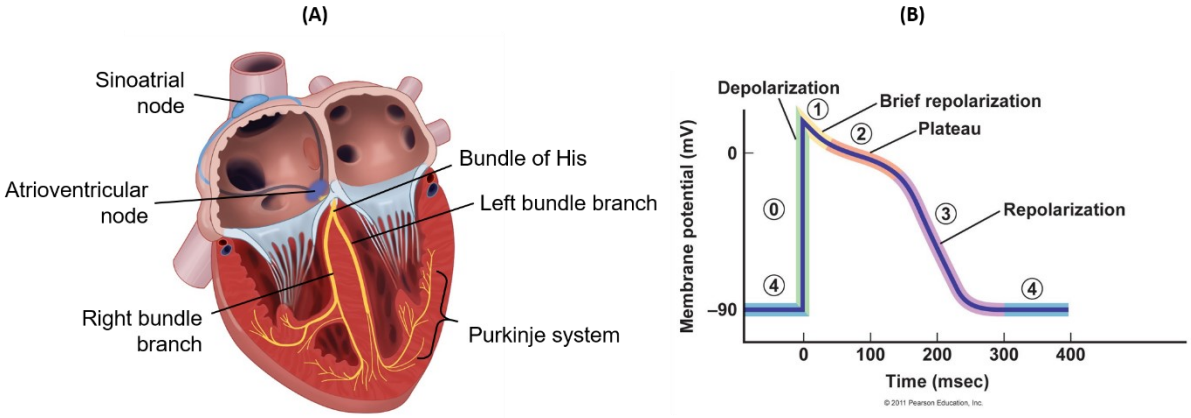

Figure 2.3. *Cardiac electrical conduction system and action potential. (A): Illustration of the primary locations responsible for the conduction of the excitation wave in the heart. Adapted from [4]. (B) Morphology and features of a ventricular cardiomyocytes action potential. Adapted from [5].*

2.2.2 Cardiac Action Potential

At a macroscopic level, cardiac contractions are hence driven by the electrical conduction system just described. At a cellular level, the propagation of the electrical excitation wave is made possible by APs, changes in *transmembrane potential* (V_m) over time t - following flow of ions in and out of the cells – travelling from cell to cell through *gap junctions*– regulated pores that allow electrical coupling between cardiomyocytes. These APs drive the release of calcium (Ca^{2+}) in the fibres, which is then

[4] http://droualb.faculty.mjc.edu/Course%20Materials/Physiology%20101/Chapter%20Notes/Fall%202011/Chapter_13%20Fall%202011.htm/
[5] https://anatomytool.org/content/leiden-drawing-cardiac-conduction-system-no-labels

responsible for their coordinated contraction. The two main forces driving ions across the cell membrane are chemical (ions moving down their concentration gradient) and electrical (ions moving away their like charges). The AP in a typical ventricular human cell (**Figure 2.3B**) can be described as being governed by relative changes in current (flow of ions) and conductance (how easy current flows through a media) of three main ions: sodium (Na^+), potassium (K^+) and Ca^{2+}, as illustrated in **Figure 2.4**. Each of them is responsible for a different stage of the cardiac AP, occurring in a series of five phases. It is worthwhile mentioning that APs in pacemaker cells differ from the APs in contractile cardiomyocytes; for the purpose of this Thesis, we will only acknowledge this difference, and move on to describe the AP in contractile cardiomyocytes. During *phase 4*, the cell membrane is kept at rest at a negative V_m of $-90\ mV$ due to a constant outward leak of K^+through inward rectifying channels, and closure of Na^+ and Ca^{2+} channels. The impulse from neighbouring cells opens voltage-gated Na^+ channels, causing sodium ions to flow into the cell and raising the transmembrane potential. When V_m approaches a threshold potential ($-70\ mV$), a self-sustaining Na^+ inward current rapidly depolarises V_m above $0\ mV$ (*phase 0*). Meanwhile, when V_m is greater than $-40\ mV$, L-type ("long-opening") Ca^{2+} channels open, causing a small but steady influx of Ca^{2+} down its concentration gradient. After the fast depolarisation phase, also called AP *upstroke,* Na^+ channels close and an initial repolarisation phase (*phase 1*) occurs, where some K^+ channels open briefly leading to an outward flow of K^+ that lowers V_m to approximately $0\ mV$. This is followed by a V_m plateau (*phase 2*) just below $0\ mV$, where the constant inward flow of $Ca^{2+}$is electrically balanced out by the outward movement of K^+ through the slow-delayed rectifier current I_{Ks} (leaking down its concentration gradient). It is important to mention that the small but constant flow of calcium into the cell during this phase plays a significant role in the excitation-contraction coupling process described **below**. This balance of ions is then interrupted during the repolarisation phase (*phase 3*), where Ca^{2+} channels close, and the Ks and rapid delayed rectifier potassium Kr channels cause a large exit of positive charge from the cell, restoring the membrane resting potential to a negative value of $-90\ mV$ (*phase 4*). The normal transmembrane ionic concentration gradients are restored by the Na^+-

Ca^{2+}exchanger and $Ca^{2+} - ATPase$, which return sodium and calcium ions to the extracellular environment, and by the $Na^{+} - \mathrm{K}^{+}\ ATPase$ returning potassium ions to the intracellular space. From *phase 0* to early *phase 4*, the cell cannot be stimulated again; this period is called *effective refractory period* and is fundamental to allow the heart to adequately fill with blood and ejection to occur before the whole excitation cycle begins again.

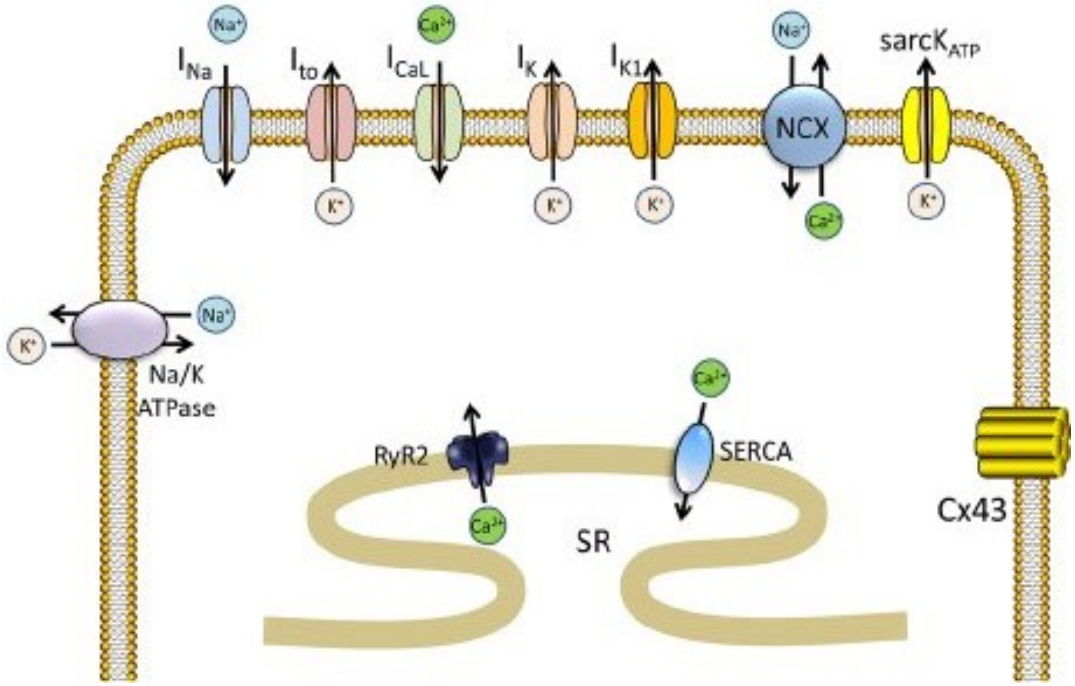

Figure 2.4. *Ionic channels responsible for AP and excitation-contraction coupling. The major channels found on the transmembrane of a cardiac myocyte are the sodium-potassium pump ($N_a/K\ \ ATPase$), $N_a, Ca_L, K, K_1\ and\ I_{to}$, which are responsible for the flow of corresponding ions, and changes in electrical charge as described above. Moreover, other important channels like Sodium-Calcium exchanger (NCX), ryanodine receptor 2 (RyR2) and the sarcoendoplasmic reticulum Ca_{2+} ATPase (SERCA) are responsible for the excitation-contraction coupling. $sarcK_{ATP}$ stands for sarcoplasmic potassium pump, and $Cx43$ for connexion 43, but are not particularly of interest for this Thesis. Adapted from* (52).

2.2.3 Excitation-Contraction Coupling

The process whereby an electrical AP leads to contraction of cardiac muscle cells is referred to as the excitation-contraction coupling, and calcium is the crucial mediator coupling electrical excitation to physical contraction. During *phase 2*, the inward flow of Ca^{2+} is insufficient to trigger contraction of myofibrils. However, as previously described, the sarcolemma contains invaginations, the T-tubules,

that bring L-type Ca^{2+} channels in close contact with specialised Ca^{2+} release receptors on the sarcoplasmic reticulum, called ryanodine receptors (RyR). When calcium ions enter the cell, these receptors change conformation, inducing a larger release of calcium which triggers the contraction of the myofilaments. Whereas the specifics of the contractile cycle are beyond the scope of this Thesis, it is important to mention that the excitation-contraction coupling is achieved through the action of contractile proteins, enabling the conversion of the chemical signal into mechanical energy. The end of the contraction is followed by release of calcium ions back to the sarcoplasmic reticulum and the extracellular volume via the sarco-endoplasmic calcium ATPase (SERCA) pump and sodium calcium exchanger (NCX) respectively.

2.3 CARDIAC ARRHYTHMIAS

Under certain circumstances, the normal electrical excitation of the heart may be compromised and become disorganised, which may affect cardiac contraction and blood circulation. Abnormalities of the heart's rhythm are known as *cardiac arrhythmias,* and can arise in both atria and ventricles. Whereas atrial arrhythmias are not directly life-threating, electrical disorganisation in the ventricles can be lethal, as these chambers exert greater impact on both pulmonary and system circulations.

The most dangerous ventricular arrhythmia is VF, where the heartrate can reach up to $300\ bpm$, causing the ventricles to quiver rather than contract, and impairing blood ejection. VF is often preceded by VT, where the ventricular chambers can still contract in a coordinated fashion, but the heartrate exceeds $100\ bpm$ for three or more consecutive beats. Although VT is not directly lethal, its management is of extreme importance to avoid degeneration into VF, and SCD.

2.3.1 Ventricular Tachycardia

The mechanisms and causes of VT are extremely complex, and for simplicity we will define this arrhythmia according to its duration, morphology and main driver. VT can be either *sustained* (lasting

more than $30s$) or *not-sustained* (less than $30s$), it can present the same morphology beat to beat (*monomorphic* VT) or be irregular (*polymorphic* VT).

Sustained, monomorphic VT can originate in the presence or absence of structural heart disease. In structurally normal hearts, the most common form of VT is *focal*(53), where electrical activation spreads in all directions from a point source in the ventricles. The main causes of focal VTs are: *triggered activity*, abnormal impulse generation in response to a previous stimulus(54); *abnormal automaticity*, shifts of the origin of cardiac excitation from the SAN to elsewhere in the heart; or *micro-reentry*, break-down of the excitation wave in small circulating waves(55). In the presence of structural heart disease, the primary mechanism underlying VT is *macro-reentry*(56,57), where the activation wavefront travels in a circular pattern due to a functional or anatomical obstacle. Thus, a re-entrant mechanism is self-sustaining cardiac rhythm abnormality where the AP propagates in a similar manner to a closed-loop circuit(54). For re-entry to occur, certain criteria must be met, that are related to the presence of a unidirectional block within a conducting pathway, critical timing and relationship between the wavelength of the wave and refractoriness of the tissue(58). As it can be seen in **Figure 2.5**, when the cardiac impulse meets an obstacle, the presence of a functional and/or structural unidirectional block will force the electrical wave to propagate through a specific 'arc' and will self-sustain if it finds excitable tissue ahead after a cycle. Therefore, the anatomical circuit must be longer than the wavelength of the electrical wave, so that there is a gap between the head and tail of the circulating wave. As a consequence, timing and the wavelength of the cardiac impulse are critical for re-entry to occur. The wavelength is defined as the product between the conduction velocity of the wave and the functional refractory period of the tissue. This implies that conditions shortening the refractory period or depressing conduction will result in shorter wavelengths, increasing the likelihood of VT initiation and maintenance(59). Functional and/or structural substrates supporting the arrhythmia are usually located within damaged (*scarred*) tissue, which is the reason why this type of arrhythmia is referred to as *scar-related* VT. Healed *myocardial infarction* (MI) is the most frequent clinical setting for the development of scar-related, monomorphic, sustained VTs(60). MI occurs due

to an occlusion of a coronary vessel (due to plaque rupture) which causes prolonged reduction (if not cessation) of blood flow to a region of the heart (ischemia). This results in the inflammation and necrosis (death) of cardiac myocytes, and formation of an infarct scar. Over time, the infarcted myocytes are replaced by collagenous tissue (fibrosis), which are not excitable and cannot conduct electrical wave.

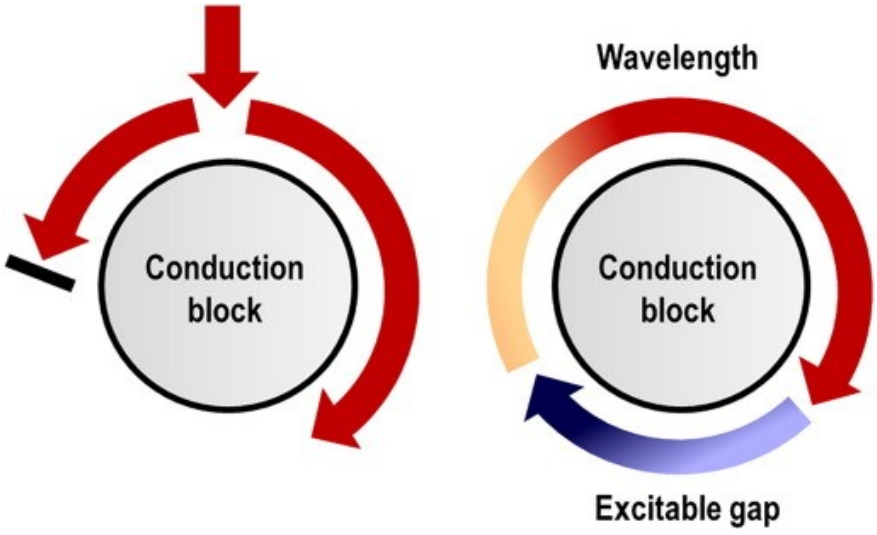

Figure 2.5. *Illustration of re-entrant circuit*(61)*. When the electrical impulse encounters a central obstacle, unidirectional block (black line in the left figure) must occur in one of the pathways, creating a circular movement. For re-entry to occur, the head of the wave (red) must meet an excitable gap (blue). In other words, the anatomical length of the circuit must equal or exceed the re-entrant wavelength*

These may be interspersed with tracts of surviving myocardium, which are referred to as border zone (BZ) regions. The extent of myocardial scarring depends on the severity and duration of ischemia, and scars can be located anywhere in the heart, and anywhere across the myocardium (they can be epicardial, endocardial or even span transmurally). Size, shape and locations of an infarct can result in different wave propagation patterns, affecting the normal excitation of the heart, and giving rise to VT. However, as described in (62), the primary routes of post-infarct VT re-entrant circuits can be summarised and simplified as shown in **Figure 2.6**. In general, the non-conducting, fibrotic regions (shown in black) force the electrical wave to propagate through channels, known as diastolic isthmuses(62). Along an isthmus, two regions of importance are usually identified: the exit and the

entrance. In a single-loop circuit, the electrical propagation occurs around a single area of inexcitability (**Figure 2.6A**). In higher-loop circuits, the electrical wave bifurcates at the isthmus exit, then the resulting wavefronts travel around the regions of inexcitability, and finally re-join at the entrance. The most common VT re-entrant pattern is the double-loop circuit (**Figure 2.6B**), also referred to as *figure-of-eight* VT, characterised by two areas of inexcitability and a single isthmus. The "origin" of the VT, which is the point of earliest diastolic activation, is defined as the *exit site*, and it is located at the isthmus exit.

In the remainder of this Chapter, we will portray the main diagnostic and therapeutic options utilised for the clinical management of these post-infarct, re-entrant VT episodes, with a secondary focus on focal VTs as well.

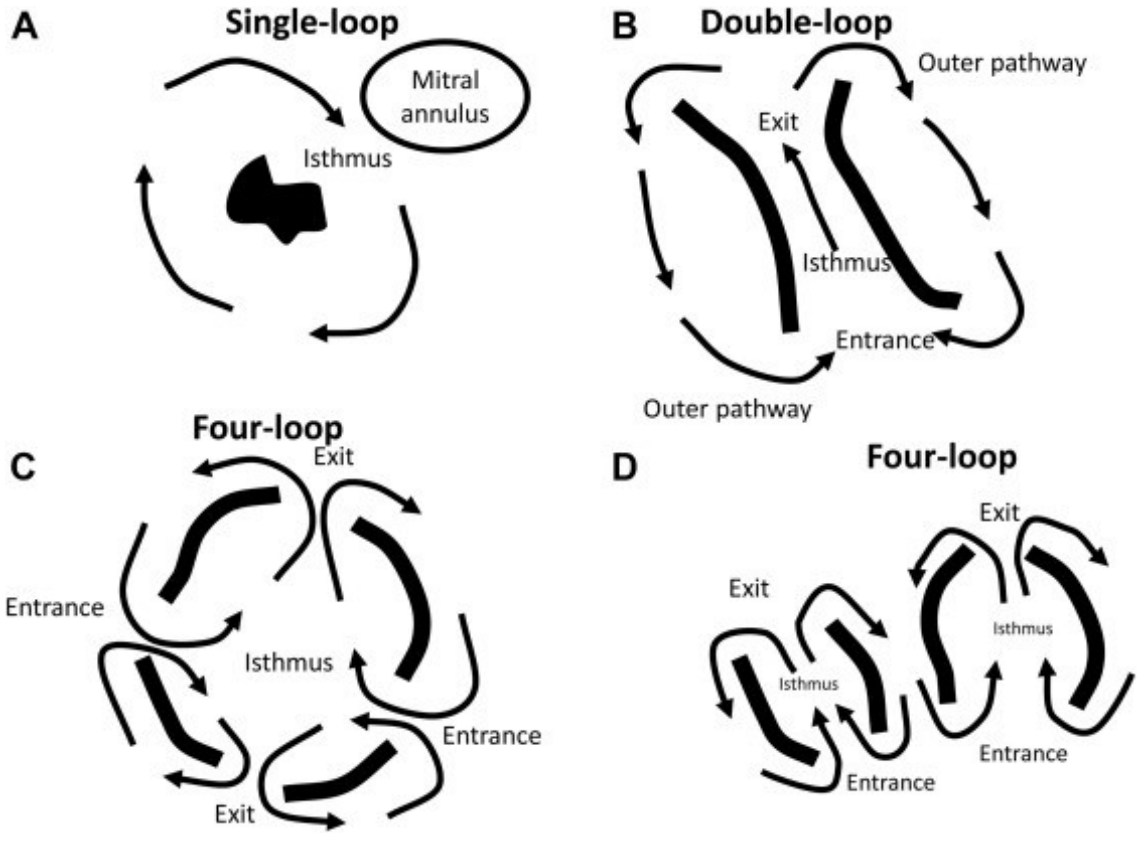

Figure 2.6. *Patterns of VT macro-reentry*(62)*. The electrical wave always propagates around regions of non-conducting tissue (in black) but can follow different pathways according to the structure and number of these areas and presence of isthmus(es).*

2.4 VT DIAGNOSIS

The initial assessment of a patient suspected of having a cardiac arrhythmia begins with an assessment of their clinical history and a physical examination. Although young and healthy patients may be asymptomatic, the most common signs of an electrical disturbance are palpitations (thumping sensation in the chest), syncope (fainting) and/or pre-syncope. Different physical tests can then be performed to gain more information about the presence of associated structural heart disease. However, the primary tool of choice for initial classification, characterisation and management of VT is the 12-lead ECG(8), an inexpensive, non-invasive, risk-free test that describes cardiac electrical activity from body surface measurements. ECG investigations are usually followed by screening the patient with non-invasive imaging modalities, such as computed tomography (CT) and cardiac magnetic resonance imaging (CMR) - with or without additional extracellular content volume (ECV) measurements - that allow a more thorough assessment of the possible anatomical substrate underlying the tachycardia. After all these non-invasive tests are carried-out, if VT and/or a structural heart disease cannot be ruled out, more expensive, time-consuming and invasive studies are requested to guide and plan VT treatment, which usually involve describing and localising the tachycardia through EP mapping. The diagnosis and management of VT can therefore be described as depending upon three tools, the surface ECG, non-invasive cardiac imaging, and EP mapping, which will be further described in the following subsections.

2.4.1 The Surface Electrocardiogram

The cardiac electrical activity described in **2.2 Cardiac Electrophysiology** can be detected from the surface of the body as a waveform, resulting from the generation of an electrical field that spreads from cardiac cells through the body to the outer layer of the skin. These surface potentials, known as body surface potentials (BSP), are detected in clinical practice through the placement of 9 electrodes on the arms, legs and chest of a patient, which are then processed to return the 12-lead ECG. An ECG is therefore an attenuated composite recording of the electrical activity of the heart. In other words,

an ECG is the sum of the potential differences that occur as the heart is depolarised and repolarised. The physics behind the ECG is explained in more details in **3.1.2 Physics of Electrocardiography**, however the key concepts behind ECG electrodes, bipolar and unipolar leads will now be briefly described. The standard placement of the ECG electrodes is illustrated in **Figure 2.7A**, and consists of three limb electrodes (RA, LA and LL) and six precordial electrodes (V1 – V6). The potentials measured at these electrodes are then used to create the ECG leads (vectors describing how the electrical wave propagates in the heart). The limb electrodes are used in pairs to create bipolar leads $I - III$, as seen in **Table 2.1**, and to define a practical 'reference' potential, known as the *Wilson Central Terminal* (WCT). The latter is the average of the limb potentials ($\frac{(RA+LA+LL)}{3}$), and it is used for the creation of six unipolar precordial leads. The final three ECG lead (aVR, aVL, aVF), known as *augmented* unipolar leads, are generated by measuring the potential between each limb electrode and a variation of the WCT, where the measurement electrode in question is omitted from the calculation. This allows to obtain signals that are 50% larger than when using the full WTC formulation. In summary, an ECG electrode is a conductive pad placed onto the skin to record electrical activity, whereas an ECG lead is a vector describing how the electrical wave propagates in the heart (in other words, a graphical representation of the heart's electrical activity). Unipolar leads are constructed from an electrode and a reference, and bipolar leads from the difference of two electrodes. During SR, a typical ECG tracing is made up of the following features (**Figure 2.7B**), which are related to specific points of the cardiac cycle: *P wave*, *QRS complex*, *ST segment*, *T wave*, *U wave, PR interval, QT interval*.

P wave describes atrial depolarisation (electrical wave spreading from SAN to AVN), which is followed by atrial contraction. **PR segment** represents the conduction of the electrical signal from the AVN to the *Bundle of His*, and branches, which is followed by ventricular excitation (**QRS complex**), leading to ventricular contraction shortly after. The **ST segment** can be related to the plateau phase of a ventricular AP, as it represents the period in which both ventricles are depolarised. Ventricular repolarisation then causes the **T wave**, which sometimes can be followed by the **U wave** (repolarisation of papillary muscle or PS). The **PR interval** refers to the period of time between the

onset of atrial depolarisation (P wave) and ventricular depolarisation (QRS complex). The **QT interval** is equal to the duration of an average ventricular AP.

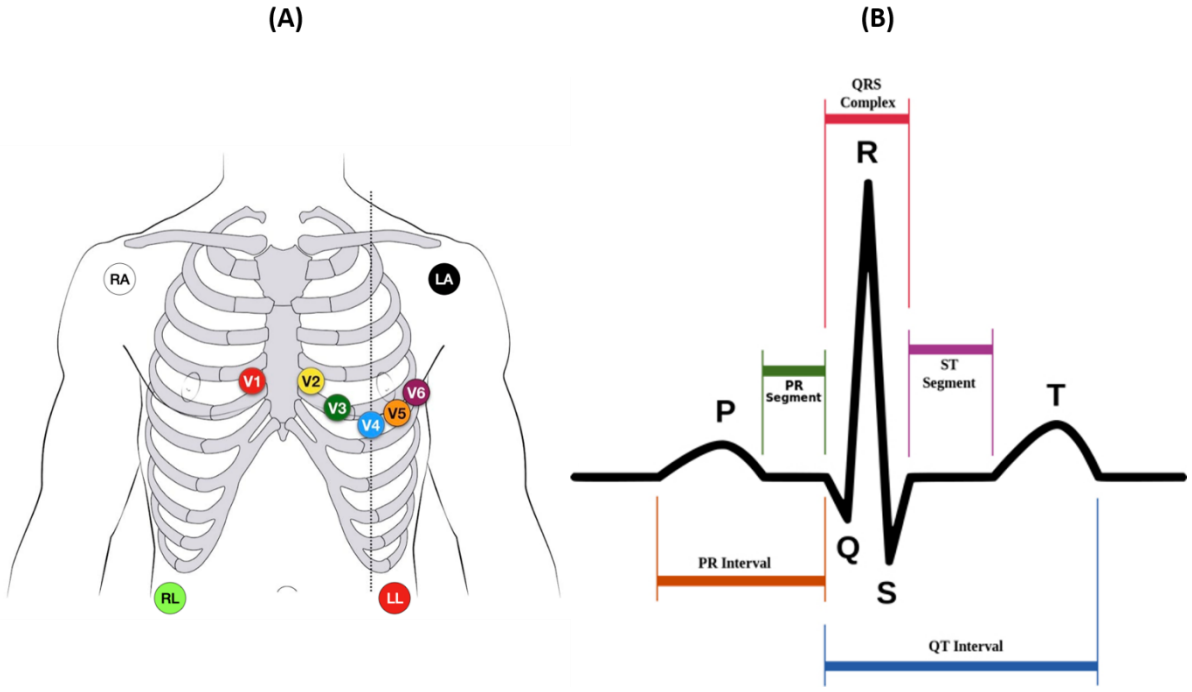

***Figure 2.7**. Placement of ECG electrodes and waveform features. (A): RA and LA leads are placed on the right and left shoulders respectively, with LL as close as possible to the left leg. The ground – RL – is usually positioned on the right leg. V1 and V2 are placed in the 4th intercostal space, on the right and left side of the sternum respectively, with V4 on the left mid-clavicular line of the 5th intercostal space. V3 is placed midway between V2 and V4. V5 and V6 can be found on the same level of V4 (5th intercostal space), on the anterior axillary and mid-axillary line respectively. Courtesy of [6]. (B): Illustration of the different waves, segments and intervals of an ECG (P and T waves, QRS complex, PR and ST segments and PR and QT intervals). Courtesy of [7]*

All these features are extremely important for the diagnosis of cardiac rhythm abnormalities, and in particular for the initial regionalisation of the VT(63). The precordial lead $V1$, as nearly orthogonal to the ventricular septum, can resolve right sided activation (net positive QRS complex) from left sided activation (net negative QRS complex), abnormalities that derive from an electrical block of the right or left bundle branch respectively(8,64). Concordance of polarity between precordial leads can help

[6] https://litfl.com/ecg-lead-positioning/
[7] https://en.wikipedia.org/wiki/QRS_complex

discern basal (positive QRS) from apical (negative QRS) VTs(65), whereas QRS width can resolve septal VTs (narrow QRS) from free-wall VTs (wider QRS)(66). These simple principles are extremely valuable for the localisation of focal VTs in structurally normal hearts. However, the presence of scar can alter wavefront conduction(8), as we have seen in **2.3 Cardiac Arrhythmias**, reducing the accuracy of the ECG in predicting the VT exit site. In this context, imaging and ECVs are important tools for the description of VT substrates in presence of structural heart diseases.

Standard 12-lead Electrocardiograms

$V1 = V1 - \frac{(RA + LA + LL)}{3}$	$V5 = V5 - \frac{(RA + LA + LL)}{3}$	$III = LL - LA$
$V2 = V2 - \frac{(RA + LA + LL)}{3}$	$V6 = V6 - \frac{(RA + LA + LL)}{3}$	$aVR = RA - \frac{LA + LL}{2}$
$V3 = V3 - \frac{(RA + LA + LL)}{3}$	$I = LA - RA$	$aVL = LA - \frac{RA + LL}{2}$
$V4 = V4 - \frac{(RA + LA + LL)}{3}$	$II = LL - RA$	$aVF = LL - \frac{LA + LL}{2}$

Table 2.1. *Standard 12-lead ECG recordings. Left and right columns showing precordial leads (V1-V6) and limb leads (I-III, aVR, aVL and aVF) respectively.*

2.4.2 Non-invasive Cardiac Imaging

Non-invasive cardiac imaging plays an important role in establishing the aetiology of VT, and in describing the anatomical substrate of the arrhythmia. Inexpensive tools such as *echocardiography* (ultrasound waves that help image the moving heart using a probe positioned on the chest or abdomen), and *coronary angiography* (ionising radiations (x-rays) emphasising cardiac blood vessels with the aid of a dye) can return valuable information on wall thinning, coronary obstruction and presence of myocardial scar(5). However, they lack sufficient image resolution for a more detailed scar analysis, for which CMR is considered the gold standard(5). MR imaging is based upon the use of

three different magnetic fields (static, gradient and radiofrequency) to excite and detect hydrogen protons in the body along any plane (chosen by changing the direction of the gradient magnetic field). Given the higher concentration of hydrogen atoms in soft-tissue organs (higher in water and fat), MRI is optimal for returning high quality, high contrast, images of soft tissues (e.g. brain, heart, muscles). Moreover, it can be utilised with different contrast agents and different radiofrequency pulse sequence parameters to image different tissues and organs, or highlight specific properties. For myocardial scar evaluation, CMR is extremely powerful when combined with a contrast agent – *gadolinium* (Gd) – for a technique known as late gadolinium enhancement MRI (LGE-MRI). According to the uptake and washout patterns of this agent in the extracellular space of the myocardium, signal intensity varies, and can help discern healthy myocardium from MI, characterise different scar patterns and inflammation, and quantify extent of the scar through the wall (scar transmurality) and wall thickness. Presence of fibrotic tissue within the myocardium can also be detected in terms of ECVs (extracellular content volume measurements) via a specific MRI mapping technique(67). LGE-MRI and MRI ECVs are therefore exceptional at depicting the structural substrate underlying scar-related VTs and at localising MI. However, it is important to mention the limitations associated with MRI, which challenge its application on a daily basis. Despite constant advances in the field, MRI cannot be performed in patients with metal implants (and metal cardiac implanted devices), respiratory and cardiac motions may compromise image resolution, and accurate scar characterisation via LGE-MRI or ECVs may be too dependent on the operator's expertise and image post-processing techniques.

Another non-invasive imaging modality that can provide high-resolution, 3D images of the heart is CT. CT utilises a detector and a rotating beam of x-rays to return multiple projections of the internal structures of a patient. A grey-scale 3D image is then reconstructed from these projections, where pixel intensities depend on the attenuation of the x-ray beam through the tissue. The higher the attenuation (such as in bones), the brighter the tissue will appear in the CT image. The lower the attenuation (such as in fat and/or air), the darker it will appear. CT is therefore useful at returning

high-resolution, high-contrast images of different tissues and organs. Although the dose of exposure to ionising radiations needs to be as low as reasonably possible, and its use justified, CT is a valid alternative to CMR as it is cheaper and quicker to perform, provides better in-plane and slice resolutions, it is not challenged as heavily by respiratory and cardiac motions, and it is not restricted to a specific group of patients. Recently, ECVs have been measured from CT scans as well, providing important information on cardiac fibrosis distribution and MI without the need for MRI or LGE-MRI.

Overall, MRI and CT are powerful and invaluable tools for VT diagnosis, for heart disease characterisation and for providing a general picture of the patient's cardiac anatomy. Furthermore, as we will see in the following subsection, they have been increasingly used in conjunction with invasive techniques to guide VT treatment procedures.

2.4.3 Cardiac Electrophysiological Mapping

Cardiac mapping refers to the process of identifying, characterising and localising an arrhythmia via EP studies. Although the surface 12-lead ECG and non-invasive imaging modalities represent the first choices for the diagnosis and initial management of VT, a complete and accurate picture of the VT morphology, arrhythmogenesis and sustenance can only be provided via invasive EP mapping techniques, which usually require a catheter to be placed in close proximity to the cardiac wall. Convectional techniques use two-dimensional (2D) fluoroscopic images to guide one, or a combination, of four main strategies(68), which return 3D descriptions of a patient's EP substrate: *entrainment mapping*, *activation mapping*, *substrate mapping* and *pace-mapping*. **Entrainment mapping** is the gold standard for describing re-entrant VTs, especially in the presence of structural heart disease. It consists of pacing (artificially, electrically stimulating) the heart during the tachycardia with timed, premature stimuli to establish points where there is an interaction (referred to as *resetting*(69)) with the re-entrant circuit. The efficacy and outcome of entrainment relies on inducing sustained, hemodynamically well-tolerated VTs. **Activation mapping** consists of returning maps of relative times between electrograms recorded at specific points around the heart (during the

tachycardia) and a reference ECG signal, providing important information on the overall electrical activation of the heart during the VT. This strategy is well established for identifying triggered activity or abnormal automaticity (hence, focal VTs), but it is limited in describing more complex, re-entrant circuits. Moreover, as for entrainment mapping, it requires sustained and tolerated VTs. On the other hand, both **substrate** and **pace-mapping** are carried-out by pacing the heart during SR, reducing the need for mapping during prolonged periods of tachycardia. They are the preferred mapping strategies in presence of poorly tolerated infarct-related VTs. In substrate mapping, the arrhythmogenic substrate of a VT can be characterised by specific EGMs, such as low-voltage, fractionation, long duration, isolated late potentials and split signals(70). In pace-mapping, the QRS morphologies of the paced beats are compared with the QRS complex of the clinical or clinically-induced VT. In doing so, a correlation map can be drawn at the pacing locations, which helps localise the exit site(s) and/or site of origin of a VT, by highlighting the point(s) of highest correlation. The wavefront propagation of a paced beat in close proximity to the exit site (or site of origin) of a VT will have a similar morphology to the wavefront propagation of the re-entrant (or focal) VT itself, leading to high correlation values between the QRS complex of the paced beat and the VT QRS.

In the last decades, the EP mapping modalities just described have been used in conjunction with 3D anatomical systems(71) to ensure better and safer navigation of the catheters, to reduce fluoroscopy exposure, and most importantly to paint a more detailed picture of both anatomical and EP substrate of a patient in real time. These EAM systems represent the present and future of EP studies.

Recently, there has been a significant improvement in the development of non-invasive tools to characterise one's EP substrate. In this context, electrocardiographic imaging (ECGi) has been showing promise at generating non-invasive EA maps from external measurements. ECGi utilises BSPs, acquired from a vest with 250 electrodes placed on a patient's torso, to reconstruct epicardial activation, voltage and repolarisation maps during SR or VT. ECGi is usually paired with other imaging modalities (e.g. CT) to reconstruct anatomical (epicardial) shells of the ventricles. This novel, non-

invasive modality plays a vital role in the management of VT patients unable to undergo more invasive mapping.

2.5 VT TREATMENT

The main therapeutic options utilised to either terminate, cure or reduce tachycardia episodes are: device-based, lesion-forming and/or drug-based. The cornerstone of VF prevention is the implantable cardioverter defibrillator (ICD), which helps restore SR when an arrhythmia is detected by delivering shocks to the RV. Other implanted devices, such as pacemakers and/or cardiac resynchronisation therapy devices (CRT-D), are also the first therapeutic option in the presence of structural heart diseases (which impair mechanical contractions of the heart) to prevent degeneration of VT into VF, and SCD. However, the only curative therapeutic option against VT is considered to be ablation, which changes the VT substrate through lesions delivered to the myocardium that can ultimately terminate and cure the arrhythmia in the long term. Ablation therapies usually involve the delivery via catheters of high energy, tissue heating shocks, referred to as catheter-based ablations (CA)(57). Nevertheless, non-invasive therapies have also been recently introduced, such as cardiac stereotactic body radiotherapy (cSBRT)(72,73), to manage VT patients with conditions that do not allow invasive, catheter-based procedures. In cSBRT, radiations delivered from outside the body denature the myocardial tissue of interest, initiating inflammatory processes that can lead to radiation-induced fibrosis and be beneficial for the termination of the arrhythmia(74). Finally, it is worth mentioning the role and importance of antiarrhythmic drugs in terminating highly symptomatic, acute episodes of VT (and other chronic arrhythmias, such as atrial fibrillation), although they do not represent the first choice of treatment for chronic VT episodes.

Pharmacological management of VT usually involves the administration of beta-blockers, amiodarone, calcium-channel blockers, and/or sotalol(75). In patients with structurally normal hearts, initial trial of beta-blockers or calcium-channel blockers can be used for both acute and long-term suppression of VT, if the latter is haemodynamically stable. Despite the limited efficacy of these drugs, their side-

effect profile is relatively favourable. In presence of structural heart diseases, the cornerstones of medical therapy are beta-blockers and amiodarone, which have been shown to minimise inappropriate shocks when used in conjunction with ICDs. Beta-blockers used as combination therapy have been shown to decrease mortality in patients with VT, heart failure (HF) and reduced ejection fraction (EF), however might be ineffective if used alone, and may lead to hypotension and AV-block. On the other hand, amiodarone is effective at prolonging ventricular refractory period by delaying the potassium outflow in both monomorphic and polymorphic VTs, however it is known to be associated with high incidence of side effects primarily affecting the thyroid, the lungs and the liver(76). Therefore, overall although medical therapy of VT can be more immediate, less expensive, and fairly effective in the short-term, it is not without important contraindications, it is dependant of the type of VT and underlying disease, and on the history profile of the patient.

In the following subsections, we will describe in more detail the field of cardiac implantable electronic devices (CIED) – mainly ICDs and CRT-Ds - and ablative procedures - mainly radiofrequency CA and cSBRT -, which constitute the main therapies we aim to optimise throughout this Thesis.

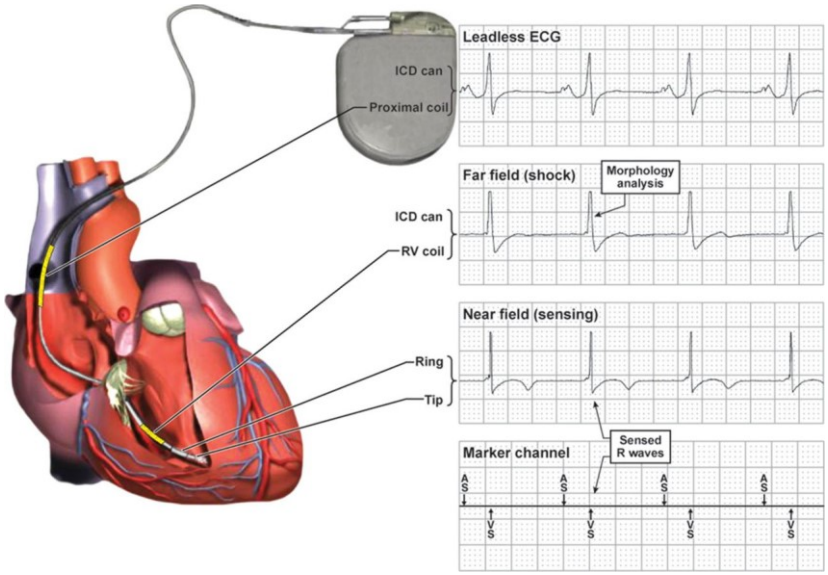

Figure 2.8. *Standard ICD configuration and corresponding EGM fields*(77)*. Longitudinal cross-section of the heart showing apical RV lead, with corresponding sensing, pacing and shock electrodes, and ICA pulse generator. Right-side illustrating standard EGM fields extracted from RV lead sensing electrodes.*

2.5.1 Implantable Devices

The ICD is the treatment of choice for primary and secondary prevention of VT or VF(78). As illustrated in **Figure 2.8**, a standard ICD consists of an active pulse generator (CAN) usually placed in the left pectoral region, and a lead through the RV(77). The RV lead has sensing, pacing and defibrillation capabilities, which are the primary functions of an ICD. The electrodes – non-insulated segments - on the RV lead (RV coil, SVC coil and RV tip and ring) allow constant monitoring of the heart rate through electrogram (EGM) vectors (known as fields) between the different parts, stored in the device CAN. The RV lead usually lies in the RV blood pool, close to the RV free wall (referred to as *apical RV lead*). In some cases, the RV lead can be located close to the septum (*septal RV configuration*). When a rhythm abnormality is detected (which usually requires careful programming of the device in the first place), pacing protocols or high-energy shocks can be delivered to the RV through the RV ring or RV coil respectively. The main EGM fields utilised for monitoring and detecting a tachycardia are far-fields (between the device CAN and the SVC and/or RV coils), and near-fields (between the RV coil and tip and/or RV ring and tip). Although standard ICDs do not have a lead sensing LV activity, recent advances in the field are pushing for the introduction of such a LV lead to improve sensing and pacing capabilities of the device(79).

A CRT-D is a type of pacemaker (device monitoring and pacing the heart at regular intervals) which is also able to defibrillate the heart in the event of an acute arrhythmic event. CRT-Ds share important properties with ICDs; they both have a pulse generator and a RV lead with sensing and pacing electrodes. In addition, CRT-Ds have a lead passing through the coronary sinus, wrapping around the LV epicardium, able to sense and pace the electrical activity of the left chamber(80).

2.5.2 Ablative Procedures

Despite the importance of implanted devices in preventing SCD in VT patients, there are many limitations associated with these devices, including recurrence of the VT, compromised quality of life due to high energy shocks, device infections and/or malfunctions. All these problems warrant the use

of a more curative therapeutic modality to treat the tachycardia: ablation. Conventional lesion-forming therapies involve the delivery of radiofrequency energies (in the range of $350\ to\ 500\ kHz$) via catheters, which heat up, and damage a piece of myocardial tissue responsible for the initiation and/or maintenance of the tachycardia episode. Radiofrequency CA is effective against both focal and re-entrant VT episodes (with or without structural heart disease), with ~ 80% success rate in patients with frequent, symptomatic VT episodes(81). However, its success hinges on the correct description of the clinical VT dynamics, and accurate localisation of the exit site(s) - or focal origin(s) - of the tachycardia(82–84), and on targeting all possible VT morphologies. In this context, the invasive EP mapping strategies described in **2.4.3 Cardiac Electrophysiological Mapping** play a central role in the planning and execution of effective radiofrequency CA.

There has been a lot of advances in the delivery of catheter-based ablation procedures – cryoablation, bipolar catheters, high-intensity focused ultrasound(85) - to overcome the limitations of conventional radiofrequency (which are, for instance, high tissue temperature, collateral damages, gaps in lesion lines). Although such advances represent exciting areas of novelty and research, we will direct our focus towards a non-invasive ablation modality which represents an extremely novel, alternative option to CA when catheter access is not possible: cSBRT. The principles behind cSBRT follow those applied in conventional radiotherapy for the treatment of tumours: radiation is delivered from external sources to target submillimetre targets in the body. However, instead of low-dose radiations delivered over a long period of time, cSBRT utilises higher dose radiations in a single fraction(73). The most challenging aspect of cSBRT is the delineation of the target volume to ablate. Pre-procedure planning cannot be executed via invasive mapping, thus requires the use of non-invasive tools such as ECGi.

2.6 SUMMARY

The basics of cardiac anatomy and physiology are fundamental to understand the structural and functional mechanisms of cardiac rhythm disturbances. Among the arrhythmias, VT represents a huge

burden for the society, given the associated risk of SCD(86). The majority of diagnostic and therapeutic tools utilised to manage VT rely on the localisation of the sources causing, initiating and/or maintaining the arrhythmia, which is dependent on the ability of inducing and recording the VT episode(s). In this context, both diagnosis and treatment (device pacing and/or fibrillation, and ablation therapies) could greatly benefit from computational (in-silico) studies, and AI algorithms, enabling the exploration of different scenarios from the standard clinical procedures. The work of this Thesis builds around these two fields, which will be described in the following Chapters, to optimise guidance and planning of VT therapeutic procedures with computer-based tools.

3

COMPUTATIONAL BACKGROUND

This Chapter dives into the basic principles and formulations of cardiac computational modelling, and different AI architectures, which will enable us to develop the platforms aimed at improving VT ablation planning. Therefore, this Chapter is of importance to understand how patient-specific models can be generated from imaging data, how VT can be simulated, and how different formulations can be used to develop efficient and fast computational environments. Moreover, a deeper understanding of different AI tools is necessary to choose the right architecture(s) and parameters to analyse time series (such as ECGs and EGMs). This Chapter is structured as follows. Section 3.1 describes how cardiac action potentials and electrical conduction can be represented mathematically. Section 3.2 presents the numerical methods utilised to solve those mathematical models, with a particular emphasis on finite element methods. In Section 3.3, a brief overview of image segmentation and mesh generation is given, enabling a deeper understanding of how imaging data can be processed to generate anatomical meshes upon which EP mathematical formulations are numerically computed. Then, Section 3.4 explains the fundamentals of AI, and DL, with a focus on the specific architectures and tools utilised in this Thesis, in particular convolutional neural networks, long-short term memory cells and attention mechanisms. The Chapter concludes with a brief summary (Section 3.5) of the importance of this computational background in the context of this research.

3.1 CARDIAC EP MODELLING

Computational modelling refers to the process of describing a phenomenon via mathematical expressions, which can then be solved numerically using computer programs and algorithms. In other words, modelling allows simulation of complex systems and situations, which would be difficult and impractical to reproduce in real life. Over the course of the last 60 years, computational models in the context of cardiac EP(87,88) have deepened our knowledge of arrhythmias(16,17,89), have helped develop and improve therapies(90), and have contributed to the growth of precision medicine(32,91). In this section, we will focus on describing the fundamentals of cardiac electrophysiological modelling: how cardiac AP and electrical propagation can be represented mathematically.

3.1.1 Mathematical Representation of Cardiac AP in a Cell

Cell as an Electrical Circuit

To mathematically represent a cardiac AP as described in **2.2 Cardiac Electrophysiology**, a cardiomyocyte can be thought of as an electrical circuit (**Figure 3.1**), where the cell membrane can be modelled as a capacitor (C_m), storing electrical charge, and the various ion channels as resistors in parallel, regulating the flow of a total ionic current (I_{ion}) from the intracellular to the extracellular space, and vice versa. Therefore, the change of the membrane potential V_m over time is dependent on I_{ion} and C_m , and can be described mathematically as the following differential equation

$$\frac{dV_m}{dt} = -\frac{I_{ion}}{C_m} \qquad (3.1)$$

Recalling **2.2.2 Cardiac Action Potential**, the movement of ions across the cell membrane depends upon the concentration gradient of that ion in the intra- and extracellular spaces (size quantified using the chemical potential) and upon the presence of an electrical field, or electrical gradient. The transmembrane potential V_m determines the electrical gradient, and an ion's equilibrium (or reverse) potential, defined as E_{ion} in **Equation (3.2)**, known as the *Nerst Equation*, is the voltage necessary to

perfectly oppose the chemical gradient (net movement of an ion down its concentration gradient), permitting the equilibrium of an ion species. As a consequence, I_{ion} of a specific ion can be described in terms of this equilibrium potential, the membrane potential, and the membrane conductance to that ion g_{ion}, as shown in **Equation (3.3)**.**(3.3)(3.3)**

$$E_{ion} = \frac{RT}{zF} log_{10} \frac{[ion]_{out}}{[ion]_{in}} \quad (3.2)$$

$$I_{ion} = g_{ion}(V_m - E_{ion}) \quad (3.3)$$

R is the gas constant, T the temperature, F Faraday constant, z the valency (charge) of the ion and $[ion]_{out}$ and $[ion]_{in}$ are the concentrations of the ion outside and inside the cell, respectively.

Hodgkin and Huxley Model

This representation of a living cell as an electrical circuit (**Figure 3.1**) to describe excitation and conduction was firstly introduced by *Hodgkin* and *Huxley*(92) in 1952 (*HH model*). Their work aimed at describing the EP of a giant nerve fibre, and they devised experiments to represent I_{ion} as closely as possible to real mechanisms. They proposed a representation of I_{ion} in terms of three currents (I_{Na}, I_K and I_{leak}), and described the membrane conductance g_{ion} of an ion as being regulated by different time and voltage-dependent gating variables (according to the properties of the channels and/or pumps taken into consideration for that specific ion), which represent the degree of opening of a certain ion channel. Each gating variable can be modelled as in **Equation (3.4)**, following first-order kinetics, can either be activating or inactivating and are independent of each other for a given ion channel type.

$$\frac{dx}{dt} = \alpha_x(1 - x) - \beta_x x \quad (3.4)$$

x represents a generic gating variable (which could be $m(t)$ or h(t), for instance, for g_{Na}), and α_x and β_x are voltage-dependant, and are called the *transition rate* constants. α_x represents the number of times per second that a closed gate opens, while β_x the number of times per second that an open gate closes. At steady state, $\alpha_x(1 - x) = \beta_x x$, which leads to $x_\infty = \frac{\alpha}{\alpha + \beta}$.

The solution of **Equation (3.4)** for a gate ($x = x_\infty - (x_\infty - x_{start})e^{-t/\tau_x}$) can therefore be written in terms of its steady state value, and a time constant $\tau_x = \frac{1}{\alpha_x + \beta_x}$, describing the rate at which the gate attains its equilibrium value.

Example of g_{Na} is reported below, in **Equation (3.5**).

$$g_{Na} = m(t)^3 h(t) \bar{g}_{Na} \quad (3.5)$$

$\bar{g}_{Na}$ is the maximum conductance, dependant on the specific ionic conductance taken into consideration.

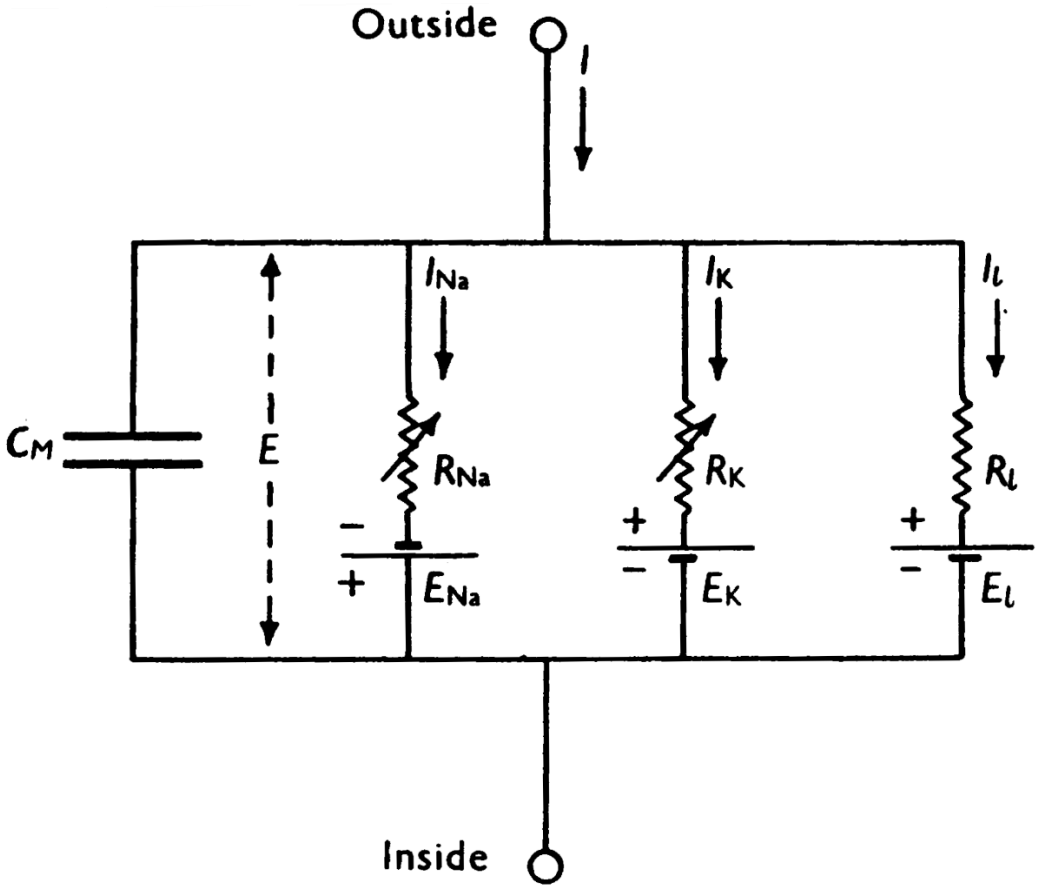

Figure 3.1. *Representation of a cell as an electrical circuit*(92)*. From the HH model, the cell membrane separating intracellular (inside) and extracellular (outside) spaces was represented as a capacitor Cm, in parallel to three different resistances, regulating the passage of sodium, potassium and leak currents (considered the major ions in charge of the cell AP).*

Human Ventricular Cardiac Models

The full formulation of HH model is beyond the scope of this Thesis, as it is not well suited to describe cardiac potentials. However, in 1960 the HH model was adapted by *Noble*(93) to model a Purkinje cell (by changing the representation of I_{ion} to fit the primary mechanisms behind a cardiac AP), giving birth to cardiac electrophysiological modelling as we know it. Since then, I_{ion} has been represented in various ways depending on the types of ion channels and/or pumps, gating mechanisms, and type of cardiomyocyte taken into consideration. In the context of human ventricular cardiac cells, the most utilised and well-established cell model is the *Ten Tusscher (TT) model* – firstly formulated in 2004(94).

Briefly, TT model describes I_{ion} in terms of all major ionic - I_{Na}, I_{CaL} (L-type Ca^{2+} current), I_{to} (transient outward current), I_{Kr}, I_{Ks} and I_{K1} – and exchange currents – such as I_{NaCa} (Na^{+}/Ca^{2+} exchanger current), I_{NaK} (Na^{+}/K^{+} pump current), I_{pCa} and I_{pK} (plateau Ca^{2+} and K^{+} currents respectively), and I_{bCa} and I_{bK} (background Ca^{2+} and K^{+} current respectively), as seen below

$$I_{ion} = I_{Na} + I_{CaL} + I_{to} + I_{Kr} + I_{Ks} + I_{K1} + I_{NaCa} + I_{NaK} + I_{pCa} + I_{pK} + I_{bCa} + I_{bK} \quad (3.6)$$

Model parameters were fit according to experimental data of the time, and each current was expressed similarly to **Equation (3.3)**, **(3.4)** and **(3.5)** (with modifications). Moreover, the model includes a simple calcium dynamic that reproduces realistic calcium transients CaT. Examples of AP, CaT, and major currents generated by the model with parameters corresponding to a human epicardial ventricular cell can be seen in **Figure 3.2**.

The model used in this study was a revision of TT model (referred to as TT2(95)), carried-out in 2006 to attempt the description of electrical instability of human ventricular cells. TT2 model is very similar to the previous implementation, only incorporating newer experimental restitution data and improved description of intracellular calcium dynamics.

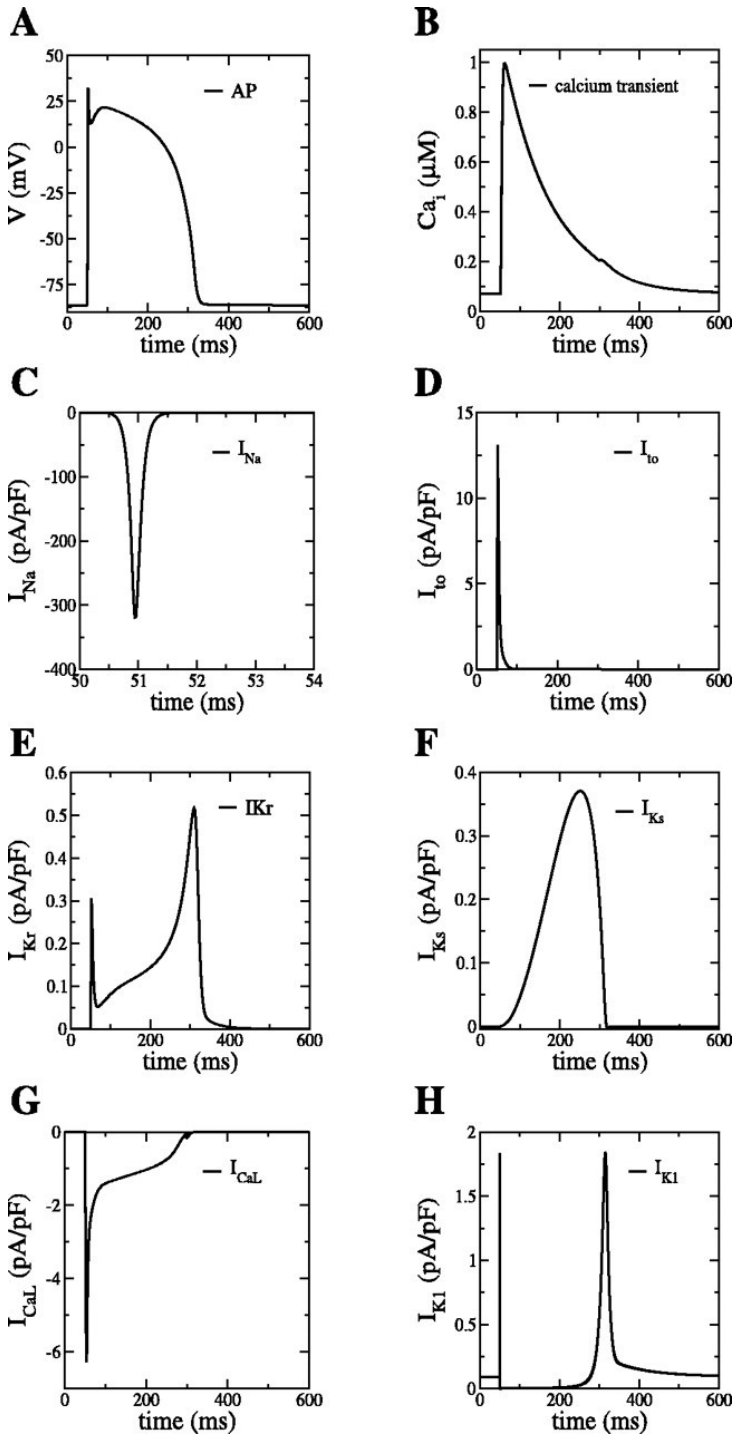

Figure 3.2. Example of TT2 model(94). (A): AP of a human epicardial ventricular cell. (B): corresponding calcium transient (B): (C): fast sodium current. (D): transient outward current. (E): rapid delayed potassium rectifier current. (F): slow delayed potassium rectifier current. (G) L-type calcium current. (H): inward rectifier current.

3.1.2 Mathematical Representation of Cardiac AP Propagation

The Cable Equation

To model the propagation of a cardiac AP from cell to cell, the cardiac fibre can be simplified to a cable (long cylindrical piece of membrane separating intracellular and extracellular domains). In doing so, V_m is not only dependent upon a time variable, but also upon space (x), which increases the complexity of **Equation (3.1)**. The electrical propagation along the cable is driven by a transmembrane current I_m and an axial current I_a. The latter is dependent upon the change of V_m across the cable and its resistance R_a to the flow, as shown below.

$$I_a = -\frac{1}{R_a}\frac{\partial V_m}{\partial x} \tag{3.7}$$

Given that a change in I_a over two points in the cable is equal and opposite to I_m - from Kirchhoff's law of conservation of charge -, as shown in **Equation (3.8)**, and I_m equals to **Equation (3.1)**, electrical propagation in a 1D cable, known as the *cable equation*, can be expressed as in **Equation (3.9)**

$$I_m = -\frac{\partial I_a}{\partial x} = \frac{1}{R_a}\frac{\partial^2 V_m}{\partial x^2} \tag{3.8}$$

$$C_m\frac{\partial V_m}{\partial t} + I_{ion} = \frac{1}{R_a}\frac{\partial^2 V_m}{\partial x^2} \tag{3.9}$$

Bidomain Representation

To accurately model a cardiomyocyte, both intracellular and extracellular domains need to be described, requiring an extension to the cable equation just described, and additional equations. This representation of cardiac electrical propagation in all its complexity is known as the *bidomain model*. In this model, the transmembrane potential V_m is written in terms of both intracellular φ_i and extracellular φ_e potentials,

$$V_m = \varphi_i - \varphi_e \tag{3.10}$$

Each potential is responsible for the generation of an electrical field ($-\nabla\varphi$) which, according to the conductivity of that domain ($\boldsymbol{\sigma}$), influences the amount of electrical current flowing through a unit cross-sectional area (electrical current density J). Each intracellular J_i and extracellular J_e current densities can be written as

$$J_i = -\boldsymbol{\sigma}_i \nabla\varphi_i \tag{3.11}$$

$$J_e = -\boldsymbol{\sigma}_e \nabla\varphi_e \tag{3.12}$$

Within a region of tissue β, the transmembrane current I_m must equal the current leaving the intracellular space, and the current entering the extracellular space. Given the definition of J above, I_m can be therefore written in terms of **Equation (3.11)** and **(3.12)** as follows

$$\beta I_m = -\nabla \cdot J_i = \nabla \cdot J_e \tag{3.13}$$

$$\beta I_m = \nabla \cdot (\boldsymbol{\sigma}_i \nabla\varphi_i) \tag{3.14}$$

$$-\beta I_m = \nabla \cdot (\boldsymbol{\sigma}_e \nabla\varphi_e) \tag{3.15}$$

By substituting I_m with **Equation (3.1)**, as in **Equation (3.9)**, it follows that

$$\beta\left(C_m \frac{\partial V_m}{\partial t} + I_{ion}\right) = \nabla \cdot \boldsymbol{\sigma}_i \nabla\varphi_i \tag{3.16}$$

At any point in space, the transmembrane current is conserved, meaning that **Equation (3.14)** and **(3.15)** lead to

$$\nabla \cdot (\boldsymbol{\sigma}_i \nabla\varphi_i) + \nabla \cdot (\boldsymbol{\sigma}_e \nabla\varphi_e) = 0 \tag{3.17}$$

By substituting the definition of φ_i from **Equation (3.10)**, and introducing intracellular and extracellular stimulus currents $I_{stim,i}$ and $I_{stim,e}$ for completeness, **Equation (3.16)** and **(3.17)** become

$$\beta\left(C_m \frac{\partial V_m}{\partial t} + I_{ion}\right) + I_{stim,i} = \nabla \cdot (\boldsymbol{\sigma}_i \nabla V_m) + \nabla \cdot \boldsymbol{\sigma}_i \nabla\varphi_e \tag{3.18}$$

$$\nabla \cdot (\boldsymbol{\sigma}_i \nabla V_m) + \nabla \cdot ((\boldsymbol{\sigma}_{i+} \boldsymbol{\sigma}_e) \nabla \varphi_e) = I_{stim,i} - I_{stim,e} \quad (3.19)$$

These last two equations, together with **Equation (3.10)**, represent the bidomain model, thoroughly reviewed by *Henriquez*(18) in 1993 in the context of cardiac EP modelling.

Physics of Electrocardiography

As introduced in **2.4.1 The Surface Electrocardiogram**, the ECG is a widely used technique to retrieve information regarding the electrical functioning of the heart in a non-invasive manner. In 1908, Einthoven described the first clinically-relevant ECG setup(96), and invented the "triangle" of limb-leads, which is still used today, in 1912(97). In 1924, Einthoven was awarded the Nobel Prize in physiology and medicine for the invention of the ECG, which has seen further developments since, with the addition of the precordial leads and the concept of *central terminal* by Wilson(98). To understand how to model the ECG (and/or the EGMs) in-silico in the remainder of this Thesis, it is important to describe the physics of the ECG in more details.

Along a cardiac fibre surrounded by extracellular space as described **above**, the depolarisation of the cell due to in-flow of Na^+ makes φ_i positive, and leaves φ_e negative. This generates a current that flows in the direction of propagation within the intracellular space, and in the opposite direction in the extracellular space (as ${\varphi_e}^+ \rightarrow {\varphi_e}^-$ at the wavefront), as shown in **Figure 3.3**. As a result, a current loop forms (**Figure 3.4A**), generating a *dipole source* (**Figure 3.4B**). Mathematically, the volume density of a dipole can be expressed as

$$p = -\sigma_i \frac{\partial V_m}{\partial x} \quad (3.20)$$

σ_i is the intracellular conductivity and $\frac{\partial V_m}{\partial x}$ is the change of intracellular membrane potential along the fibre.

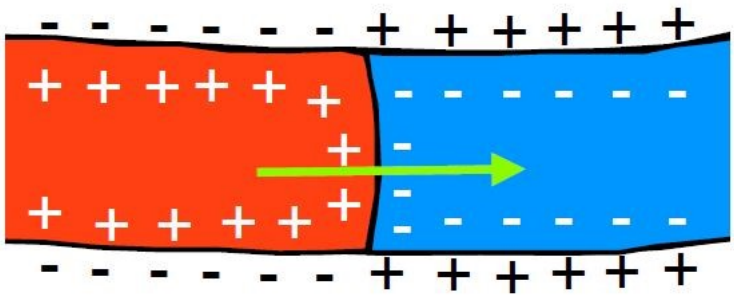

Figure 3.3. *Example of dipole source formation at the wavefront. The direction of electrical propagation (indicated by the green arrow) is where* $\varphi_i{}^- \rightarrow \varphi_i{}^+$ *due to the flow of sodium channel within the intracellular domain. This causes* $\varphi_e{}^+ \rightarrow \varphi_e{}^-$ *in the extracellular domain, effectively setting up a dipole source.*

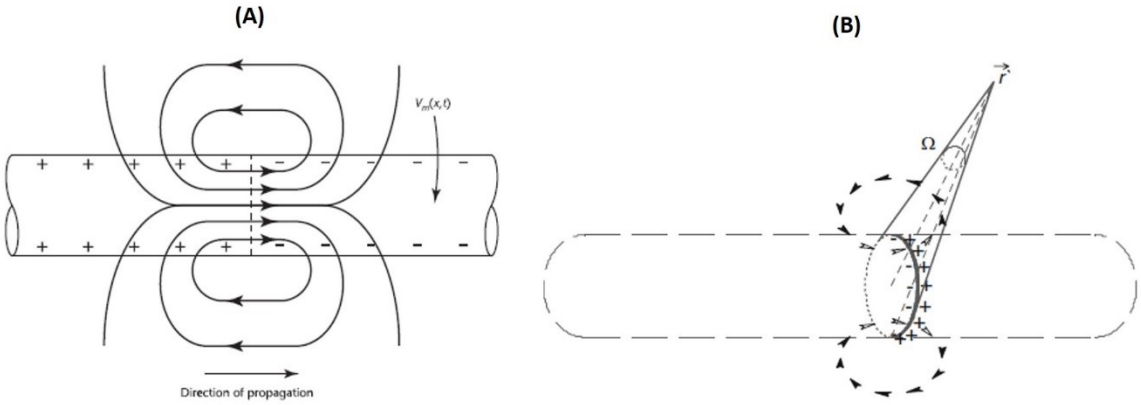

Figure 3.4*. Current loops and dipoles along an idealised cardiac fibre. (A) shows current loop during depolarisation forming at the wavefront. (B) shows the corresponding dipole which can be measured at a distance vector* $\vec{r}$ *in the extracellular space* Ω*.*

The total potential at a distance r in the extracellular space can be evaluated in terms of these dipole sources (with moment $\boldsymbol{p}$) as follows

$$V(\boldsymbol{r}) = \frac{\boldsymbol{p} \cdot \hat{\boldsymbol{r}}}{r^2} \qquad (3.21)$$

As illustrated in **Figure 3.5**, it is clear that the shape of the resulting signal depends on both the distance of the dipole from the electrode and the relative distance between the dipole moment

(direction of propagation) with the lead vector (imaginary line joining the wavefront with a point along the direction of $\boldsymbol{r}$)**.**

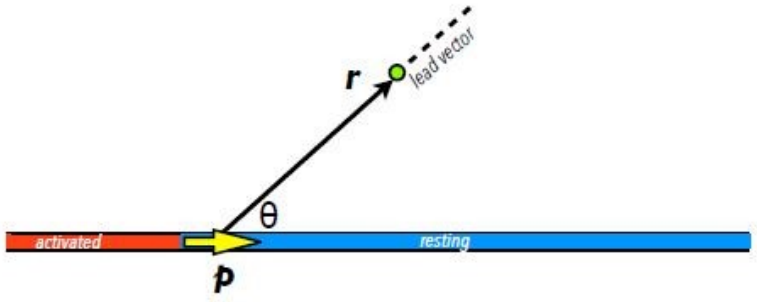

Figure 3.5. *Electric potential at a distance* $\boldsymbol{r}$ *due to a dipole* $\boldsymbol{p}$*.*

These concepts of dipoles and lead vectors are extremely important to understand the origin of the ECG. At any instant in time during activation of the heart, a single resulting dipole can be defined, named the *heart dipole* or *vector* $\mathbf{H}$**.** The magnitude and direction of this vector changes following the cardiac activation wavefront, as shown by the yellow arrow in **Figure 3.6**. The signal, *lead voltage,* of the heart dipole can be found by its projection onto a lead vector. In the 12-lead ECG, the lead vectors are found from 9 electrodes placed on the skin, as briefly introduced in **2.4.1 The Surface Electrocardiogram.**

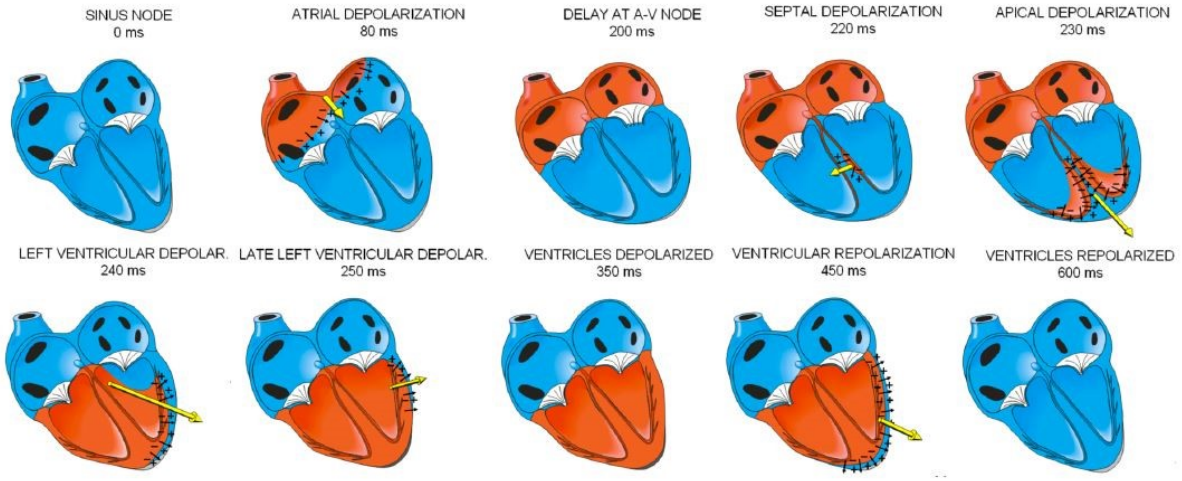

Figure 3.6. *Changes in magnitude and direction of the heart dipole as the heart activates. From top to bottom, from left to right, the magnitude and direction of the heart dipole (yellow) changes as the electrical wavefront (red) activates the heart (blue) at different points in time.*

Monodomain Representation

Under certain circumstances, when φ_e is not of interest, representing the cardiac tissue in all its complexity is not necessary, and the bidomain model can be simplified to a single equation, assuming that both intra- and extracellular domains are anisotropic to the same degree. The conductivity of the system is therefore represented by $\boldsymbol{\sigma} = \boldsymbol{\sigma}_i(\boldsymbol{\sigma_i} + \boldsymbol{\sigma_e})^{-1}\boldsymbol{\sigma_e}$, and **Equation (3.18)** can be simplified to

$$\beta_m \left(C_m \frac{\partial V_m}{\partial t} + I_{ion} \right) + I_{stim} = \nabla \cdot (\boldsymbol{\sigma} \nabla V_m) \qquad \textit{(3.22)}$$

This simplified formulation of the cardiac tissue EP is known as the *monodomain* model, and it is particularly useful when investigating scenarios (e.g., VT mechanisms) that require longer simulations. However, it cannot be utilised to describe the effects of the conducting bath (e.g. blood, membranes etc) surrounding myocardial cells. Other formulations have been proposed to model cardiac EP to either reduce computational time further (e.g. eikonal(99), reaction-eikonal(100)), or derive φ_e within a computationally efficient environment (e.g. pseudo-bidomain(101), lead field(102)).

Pseudo-Bidomain Representation

So far, we have seen that in order to model extracellular potentials (within a torso model, for instance) and compute ECGs and/or implanted device EGMs, one needs to utilise the bidomain representation presented above. However, to reduce computational burden, other methods have been proposed to capture both φ_e and φ_i: the pseudo-bidomain representation, and the lead field (LF) method.

In the pseudo-bidomain formulation presented by (103), an augmented version of the monodomain **Equation (3.22)** is used, where the conductivity tensor $\boldsymbol{\sigma}$ has an harmonic form ($\boldsymbol{\sigma_m^*}$), and can either describe conductivity within the tissue bulk or along the surfaces. In doing so, bath-loading effects upon activation sequences can be accounted for. This augmented approach is then combined with an infrequent solve of the elliptic portion of the bidomain representation (**Equation (3.19))** (only solved at those instances corresponding to specified output granularity), allowing to reproduce the advantages of the bidomain formulation at a cheaper computational cost. In other words, V_m is used

to find φ via the elliptic solve, but φ does not affect the solution of V_m, as opposed to the bidomain formulation.

Lead Field Method

To obtain ECGs and/or EGMs of longer EP simulations (e.g. sustained, monomorphic VT episodes), the pseudo-bidomain formulation is still not ideal. Because of this, (102) introduced the LF method to split such computational problems into two parts: a *hard* part, only solved once, and an *easy* part, run as many times as necessary according to the investigation(s) to perform. In other words, the computations on the extracellular bath are executed only once, and saved at specific points of interest (such as ECG electrodes locations and/or implanted device sensing parts), and then these results can be combined with different solutions of the intracellular domain. In mathematical terms, φ_e on a few locations of interest can be computed utilising a Green's function to represent $\nabla \cdot ((\boldsymbol{\sigma}_{i+}\, \boldsymbol{\sigma}_{\boldsymbol{e}})\, \nabla$ in **Equation (3.19).** Given that an ECG lead for instance is a linear combination of φ_e, a linear combination of Green's functions is utilised for each location of interest, leading to matrices named *lead fields* $Z(\vec{x})$.

These lead fields represent the *hard part* of the method, and are only computed once as

$$\nabla \cdot ((\boldsymbol{\sigma}_{i+}\, \boldsymbol{\sigma}_e)\, \nabla Z(\vec{x}) = \sum_i c_i\, \delta(\vec{x} - \vec{x}_i) \qquad \textit{(3.23)}$$

where $\vec{x}_i$ are the extracellular locations of interest, c_i are the relative contributions of two or more of these locations, and δ is the delta function. The intracellular EP is then solved utilising the monodomain formulation, and extracellular potentials over time $V(t)$ at the locations of interest are computed with an integration over the myocardium as

$$V(t) = \int \nabla Z(\vec{x}) \cdot\, \boldsymbol{\sigma_i}\, \nabla V_m \mathrm{d}\vec{x} \qquad \textit{(3.24)}$$

Reaction-Eikonal Formulation

When only local activation times T of cardiac EP are of interest (instead of V_m over time), the *eikonal* model can be utilised

$$v\sqrt{\nabla T^t \boldsymbol{D} \nabla T} = 1 \qquad (3.25)$$

where v is the local conduction velocity and $\boldsymbol{D}$ the anisotropic tensor accounting for the fibre orientation. As we will see in the following section, T can be computed very efficiently with the *fast-marching algorithm*, which returns sufficiently accurate results at lower spatial resolutions and computational costs as compared to other formulations. The eikonal model is therefore well suited to a clinical workflow as it returns simple, rapid and accurate EP solutions in a matter of seconds(100). Because of the inability of the model to return voltage distributions and/or describe more complex EP effects within a cell, (100) proposed the so-called reaction-eikonal (RE) formulation, which allows to gain at least three orders of magnitude more central processing unit (CPU) time than a standard reaction-diffusion simulation. In the RE, the monodomain formulation is manipulated so that activation sequences derived with the eikonal model drive the propagation of the depolarisation wavefront, ultimately reducing computational time and power as compared to the classic reaction-diffusion model. There exist two variations of the RE model: one which reproduces the repolarisation effects of the electrical wave (known as RE+ with diffusion), and one which ignores them (RE- without diffusion). The latter may result in a distortion of the signature of repolarisation in EGMs and/or ECGs. In RE+, a foot current (I_{foot}) driven by the activation times solved with the eikonal model is added to the diffusion term of the monodomain formulation (right-hand side of **Equation (3.22)**). In RE-, the diffusion term is replaced entirely with (I_{foot}) as shown below,

$$\beta_m \left(C_m \frac{\partial V_m}{\partial t} + I_{ion} \right) = I_{foot} \qquad (3.26)$$

3.2 NUMERICAL METHODS

Cardiac electrical activity (at cellular and tissue levels) has been so far described mathematically through sets of differential equations. Partial differential equations modelling boundary value problems (e.g., space-dependant) can be solved utilising a numerical method of choice among finite difference (FDM), finite volume (FVM) and finite element (FEM) methods. Whereas FDM is the most direct approach to solve differential equations, FEM is the most suitable and accurate to solve problems over irregular, complex domains, such as the heart, and will be of use throughout this research. The fast-marching algorithm will also be briefly described as important to solve eikonal formulations. To numerically integrate differential equations with a given initial value (e.g., time-dependant), other numerical methods, such as Euler and Runge-Kutta, are typically used. Briefly, with the forward Euler, the value of the next estimated solution value $y_n = y_{n-1} + (t_n - t_{n-1})\, f(t_{n-1}, y_{n-1})$. The Euler method can therefore be viewed as approximating an integral to a polynomial of degree 0 over the interval $[t_{n-1}, t_n]$. In other methods (e.g., Runge-Kutta), integrals are approximated by higher-order polynomials.

3.2.1 Finite Element Method

Given the complexity of FEM, we will only describe the general characteristics of the method. In FEM, the domain of choice is represented as a *mesh* of discretised points, or *nodes*, grouped together into finite *elements*. The shape of these elements depends on the specific scenario being modelled, and on the dimensionality of the problem (tetrahedra and triangles are usually used for 3D and 2D simulations respectively). On the other hand, the number of elements in a mesh dictates solution accuracy, computational efficiency, and how well local effects can be reproduced. To be able to solve a differential equation in such a discrete domain, the equation is first simplified into its *weak form*, and then *discretised*. To obtain the weak form, the differential equation is mathematically manipulated into an integral, which is easier to solve. By doing so, the boundary conditions imposed on the problem are also “relaxed”, meaning that the result of the weak form will never be exact, but

will converge to the mathematical solution. The weak form of a differential equation is then discretised by transforming the integral into a linear combination of polynomial functions (referred to as *basis functions*), with weights assigned on each node of an element. These weights are first solved *locally* on each element, and then the local solutions are combined *globally* to establish continuity across neighbouring nodes. This global solution u can then be expressed in matrix form,

$$u = A^{-1}F \qquad (3.27)$$

where A contains the global weights across the domain, and F the global basis functions utilised to solve the problem. This matrix form can then be solved iteratively using a numerical algorithm. Throughout this work, cardiac EP problems have been modelled and solved utilising Cardiac Arrhythmia Research Package (CARP)(104) software, which allows to solve monodomain, bidomain and other formulations utilising FEM. The software also allows to simulate different ionic models, and different EP protocols and scenarios, and output various parameters, variables and maps.

3.2.2 Fast-Marching Algorithm

To solve the eikonal equation with the fast-marching algorithm, the gradient in **Equation (3.25)** is replaced by a first-order approximation (e.g., finite forward difference between consecutive nodes in a grid separated by a spacing h, $\frac{df(x)}{dx} = \frac{f(x+h) - f(x)}{h}$). Then, each node of the discretised domain can be labelled as *far* (not yet visited), *considered* (visited with a value tentatively assigned) or *accepted* (visited with value permanently assigned), and T at any node only depends on its neighbours with smaller values. Initially, all nodes are labelled as far, and $T = \infty$ $(large\ positive)$ on all nodes. The starting point and corresponding T are assigned a value of 0 and labelled as *considered*. Next, in a loop, the node of the *considered* group with the lowest value of T is labelled as *accepted,* and the neighbouring points are either labelled as *considered* if they were in the *far* set, or the corresponding value of T is computed. This is repeated until all nodes have been labelled as *accepted*.

3.3 ANATOMICAL MODELLING

To model cardiac EP numerically, the domain of interest needs to be discretised into a mesh. Whereas initial EP study of ventricular AP and conduction were carried in 1D, 2D or 3D idealised shapes of the ventricles, in recent years advances in medical imaging modalities (e.g. MRI and CT) have led to the generation of more sophisticated ventricular and/or torso meshes(105–107), reproducing the anatomy with high resolution and fidelity, ultimately leading to more patient-specific computational investigations. The generation of these patient-specific meshes is possible by initial segmentation and post-processing of the anatomical structures of interest from the patient's imaging data.

3.3.1 Image Segmentation

Image segmentation refers to the process of extracting a particular structure from the rest of the image with the use of manual, semi-automatic or automatic image processing tools, as it can be seen in **Figure 3.7**. These tools can vary from simple *paint brushing* (manually segmenting the region of interest) and *thresholding* (more automatic segmentation according to different pixel intensities), to *canny edge detection* (automatically highlighting edges of objects) or *region growing* (an iterative approach that segments a structure according to similarities with a seed chosen by the user). Whereas some of these tools will be used in the following Chapters to segment different thoracic and abdominal organs for the construction of torso models, it is important to mention some more advanced methods for the segmentation of cardiac chambers, fundamental to accurately model and investigate cardiac EP.

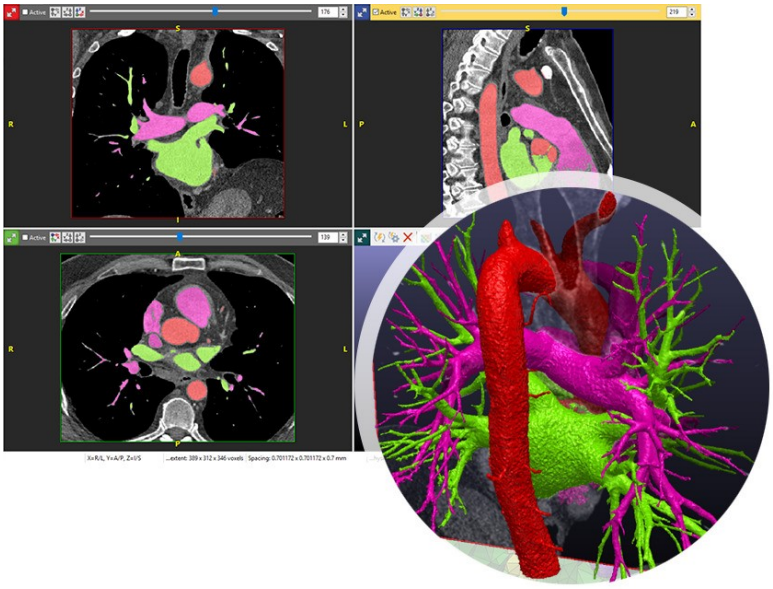

Figure 3.7. *Example of cardiac segmentation from CT imaging data. The three grey boxes in the background show three different segmented structures: the aorta in red, the left atrium in green and the right atrium in purple. The round picture in the front illustrates the 3D surfaces of those anatomical structures. Courtesy of [8].*

In general, segmentation of cardiac chambers, mainly carried-out from MRI or CT image datasets, can be grouped into *edge-based*, *model-fitting* and *ML/DL* approaches. Edge-based methods are mostly semi-automatic, and use a curve (active contour algorithm) in the image domain that evolves and distorts from the initial position to adapt to a specific contour. Model fitting approaches use prior knowledge of the shape and geometry of the object of interest, and are therefore dependant on the segmentation and availability of cardiac atlases. Finally, ML/DL methods involve training an algorithm on labelled data, and are fully automatic. A more detailed description of all these approaches can be found in (108).

3.3.2 Mesh Generation

Once a 3D imaging dataset has been segmented, a mesh for each different structure can be generated. *Mesh generation* is a challenging and complex problem in computer science, and we will only touch the general idea behind it. A mesh can either be *structured* (regular grid of cells) or *unstructured* (an

[8] https://www.synopsys.com/simpleware/software/auto-segmenter-modules.html

irregular network of nodes and cells), which requires a more complex way of storing adjacency and connectivity information between cells.

Cardiac and torso meshes are generally unstructured. Different grid generation approaches exist according to the desired element shape. For instance, triangles and tetrahedra can be created following geometrical criteria (e.g. *Delaunay Triangulation*(109)), *advancing-front methods*(110), or *octree methods*(111). Delaunay Triangulation consists of dividing the space into non-overlapping triangles (in 2D) or tetrahedra (in 3D). In 2D, each triplet of points forms a triangle if it can be circumscribed by a circle that does not include any other point. Similarly, in 3D each pair of four points forms a tetrahedron if it can be circumscribed by a sphere.

Advancing-front methods consist of adding individual elements one at a time to an existing front of previously generated elements. In 2D, this front is represented by nodes on the boundary of the domain, from which triangular elements form until the domain is entirely covered. In 3D, the front is a surface grid constructed on the surface boundaries of the domain, which then "advances" through tetrahedral elements. For more information on this, refer to (112).

The octree method involves recursive subdivision of the domain into cells; it is quite simple to implement, and is favourable for the generation of unstructured cardiac meshes. This method is at the basis of most meshing software utilised for cardiac modelling (and for this research), such as *Tarantula*(26) or *Simpleware*™(Synopsys, Inc., Mountain View, USA).

3.4 Artificial Intelligence

AI refers to the process of mimicking intelligence and actions with the use of machines. In medicine, AI can be found in surgical robots, in smart appliances (e.g. smart-watches), in algorithms for image segmentation, image and/or signal processing and so on.

ML is a subfield of AI which can be described as a set of computer algorithms, based on mathematical and statistical methods, able to extrapolate patterns within a certain input domain, establish relationships and make predictions(113). ML can be categorised into different types, with the most common being *supervised* and *unsupervised* algorithms. S*upervised* ML algorithms try to learn the existing relationship(s) between input features and/or observations and a target of interest(114), so that predictions can be made on a new dataset based on this learnt knowledge. The type of problems solved with supervised algorithms are either *classification* problems – predictions based on discretised classes – or *regression* problems – predictions based on continuous values. *Unsupervised ML* algorithms try to discover certain relationships between the input features, with the aim to reduce dimensionality of the problem, detect outliers, or cluster the input space(114).

In this Thesis, we will mainly utilise a subset of ML algorithms, named *deep learning*. In the following subsection, we will first describe the concept of artificial neural networks (ANN). This will then enable the understanding and description of different DL architectures.

3.4.1 Artificial Neural Networks

ANNs are inspired from biological neural connections present in the brain. The basic unit of a human brain is the *neuron,* illustrated in **Figure 3.8A**. Billions of these neurons exist in the human nervous system, and they are connected via *synapses*, responsible for regulating the passage of information from a cell to another. The actual signal then travels through *dendrites* and *axons* to reach other neurons. As illustrated in **Figure 3.8B**, the unit of an ANN can be thought of as a neuron, where each synapse with other cells is represented mathematically by a *weight* w, that can be learnt and can regulate the arrival of information travelling through the axons x of the connected neurons. These weighted activations are then summed together in the cell body of the neuron, after which a *bias* (error) term b is added, and the output is activated if a certain threshold is reached. This *firing* of information from the cell body of a neuron to its axon is represented mathematically by a so-called *activation function* f.

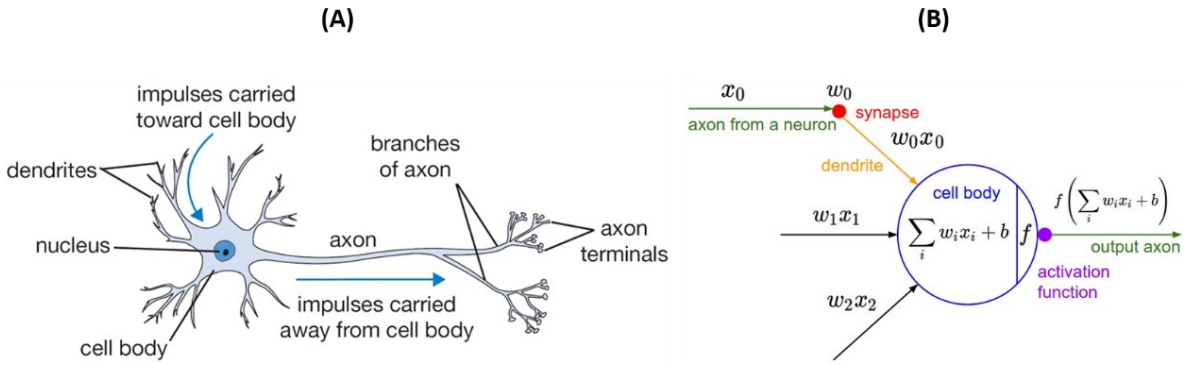

Figure 3.8. *Basic unit of a human brain and an artificial neural network. (A): A human neuron is composed of a cell body, small ramifications called dendrites where the signal arrived from other neurons, and a long branch on the opposite side, called axon, where the impulse is carried away from the cell body. (B): Similarly to a human neuron, the unit of an ANN has a ""cell body" which receives information in terms of weights w from the axons of other neurons, information that is then sent out if the activation function exceeds a certain threshold. Adapted from [9].*

At a higher level, an ANN is made of multiple interconnected layers of neurons, as shown in **Figure 3.9.** Each ANN has an input layer and an output layer, with N hidden layers in-between that determine the depth of the network.

DL architectures are based on these ANNs, and are therefore characterised by "deep" structures; they are usually made of multiple layers able to progressively extract higher-level features from the input domain. After every layer, the input data is decomposed into a more abstract representation, making DL algorithms more complex to fully understand and explain step by step. DL algorithms can still tackle both unsupervised and supervised tasks, but they do not require initial feature extraction.

The main DL architectures used throughout this research are convolutional neural networks (CNNs), long-short term memory cells (LSTMs), and attention mechanisms.

[9] https://cs231n.github.io/convolutional-networks/.

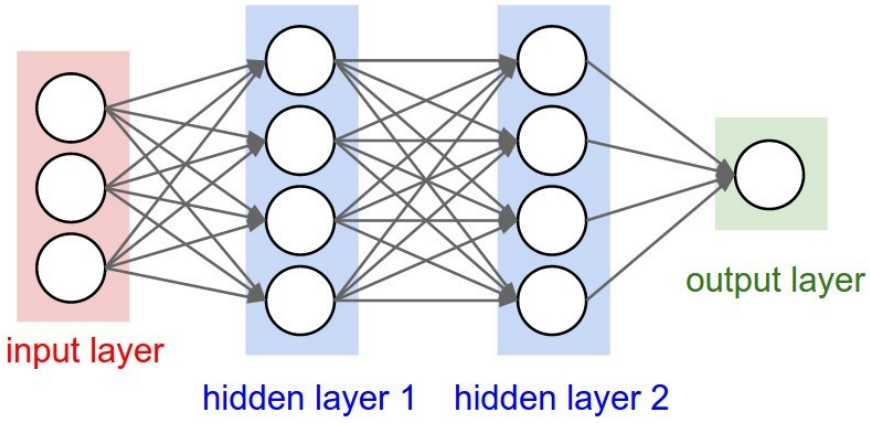

Figure 3.9. *Example of a 3-layer artificial neural network. This ANN is made of two hidden layers (blue), in between an input layer (red), which is not count towards the total number of layers of the network, and an output layer (green) Courtesy of* [8].

Convolutional Neural Networks

CNNs share the same properties and structure with a generic N-layer ANN described above, however they are mainly used to process high-dimensional inputs, such as images. The neurons of each hidden layer are therefore arranged along the dimensions of the input data. CNNs are constructed utilising three main types of hidden layers: *convolutional*, *pooling* and *fully-connected (FC)* layers. An example of a generic CNN architecture is illustrated in **Figure 3.10.**

In each convolutional layer, the input image is "analysed" by neurons through sets of learnable small filters (or kernels), which slide (more precisely, convolve) across the whole spatial domain, and return activation (feature) maps that describe the responses of the kernels at every spatial position. (Each kernel convolves with the input, one at a time, returning an activation map. The maps of N kernels are then stacked in 3D, returning an output volume that is passed to the following layer). By doing so, in each convolutional layer, the neurons are not all connected with the previous layer, but only to a local region of the input. The output feature maps of each convolutional network therefore summarise the learned features of the input.

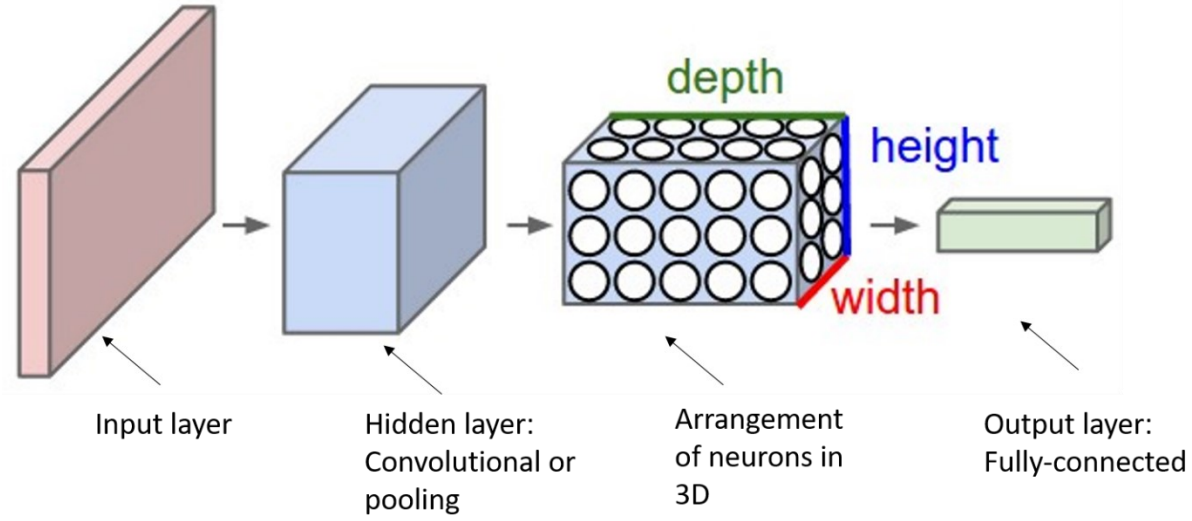

Figure 3.10. *Simplified structure of a CNN. In a CNN, the input is volumetric (red), and it is processed locally by convolutional layers (where neurons are arranged along the three dimension), and the output is flattened by a fully-connected layer to return class or regression scores. Adapted from [8].*

Pooling layers usually alternate with convolutional layers to downsample the feature maps along width and height, helping the network become more invariant to small translations of the input (that could result in different feature maps). There are different types of pooling layers, such as *max pooling*, *average pooling* and *global pooling*. Max pooling consists of reducing the number of features of the feature map so that only the maximum element within the region covered by the filter is selected. A visual example of max pooling can be seen in **Figure 3.11A**. As a result, max pooling is performed when there is an interest in emphasising the most prominent features of the previous feature map. When performing average pooling, the elements covered by the pooling filter are averaged (**Figure 3.11B**). Finally, global pooling reduces a feature map to a single value (i.e. $n_h \; x \; n_w \; x \; n_c \; \rightarrow \; 1 \; x \; 1 \; x \; \; n_c$). Global pooling can be either max or average (**Figure 3.11C**).

FC layers are usually found at the end of a network (as output layers) to transform the output of the previous layers into predictions (either *class scores* or *regression values*).

In conclusion, CNNs are able to extract spatial features and relationships within volumetric datasets, and make predictions accordingly. They are less powerful in analysing and storing temporal relationships, for which recurrent networks and LSTMs are preferred.

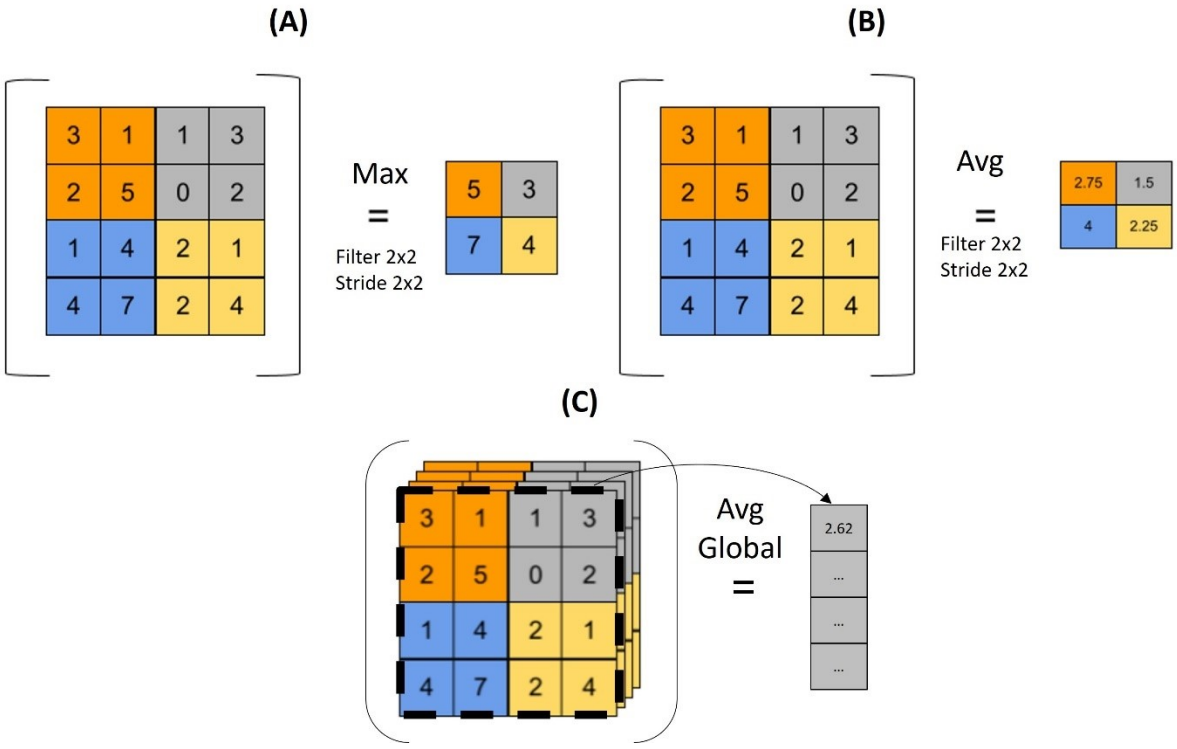

Figure 3.11. *Pooling operations. (A) shows max pooling, utilising a 2x2 filter with 2x2 stride. The regions in the feature map (left) covered by the pooling filer are highlighted in different colours, and the corresponding results after the operation are shown on the right. Similarly, (B) shows average pooling. (C) illustrates average global pooling. Adapted from [10].*

Long-short Term Memory

Instead of being composed of a linear progression of different layers, recurrent neural networks (RNN) can be thought of repetitions of the same neural layer, able to learn to make predictions based on current and past information. RNNs are therefore represented as 2-layer networks with a loop within the hidden layer, as illustrated in **Figure 3.12A**. Although in theory RNNs should be able to remember

[10] https://androidkt.com/explain-pooling-layers-max-pooling-average-pooling-global-average-pooling-and-global-max-pooling/

long-term information, in practice they are only suitable for learning "short-term" dependencies, a problem which is overcome in LSTMs(115).

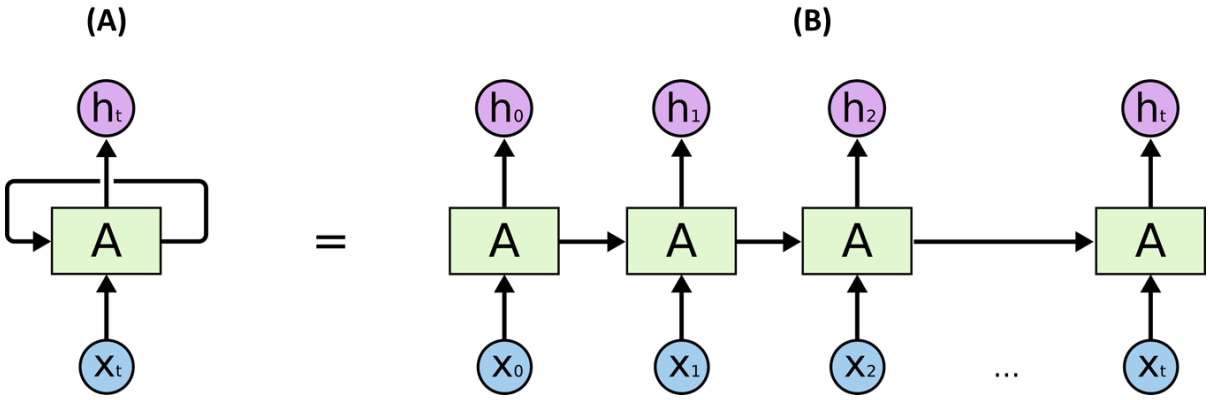

Figure 3.12. *Example of a RNN. (A): The RNN has an input layer (blue), a single hidden layer (green) that loops over itself, and an output layer (purple). (B): The RNN can be thought of a linear chain of the same hidden layer A. Courtesy of* [11].

LSTMs were firstly introduced by *Hochreiter* and *Schmidhuber* in 1997(116). As illustrated in **Figure 3.13**, in a conventional LSTM, the "repeating" hidden layer is made of four interacting layers (instead of one) – given the name of *hidden state* -, which pass information to a *cell state* through three gates. Briefly, in the hidden state, a $sigmoid$ function first decides what information of the input is discarded from the cell state. Then, in the following step, a $sigmoid$ function interacting with a $tanh$ function is responsible for deciding what new information is stored in the cell state. Finally, in the last step the output is filtered (a $sigmoid$ is utilised to decide which part of the cell state to output, and then a $tanh$ to filter it). Different variations of this classical representation of a LSTM exist, but they are beyond the scope of this Thesis. The interested reader is directed to (117–119) for further details on the topic.

[11] https://colah.github.io/posts/2015-08-Understanding-LSTMs

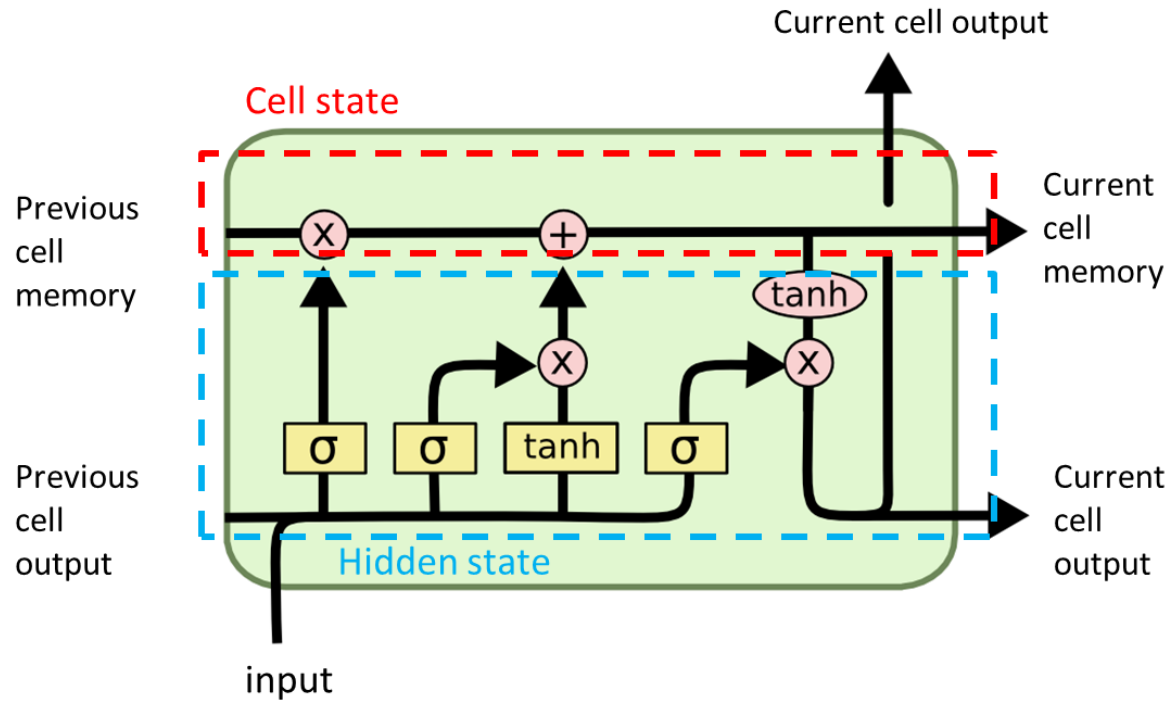

Figure 3.13. *Example of an LSTM cell. Adapted from [9].*

Attention Mechanisms

Similarly to the concept of a neural network mimicking the human nervous system in a simplified manner, an attention mechanism tries to implement the human cognitive process of selectively focusing on relevant information, and discarding other information. Attention mechanisms are usually part of a bigger network, and they are not only utilised to improve detection performance, but also to help interpret the network prediction. Particularly in medicine, being able to interpret the results of a DL architecture is of importance to build trust among the clinicians that might use the network.

One of the reasons why attention mechanisms were introduced by *Bahdanau*(120) in 2015 was to be able to improve the performance of encoder-decoder networks(117) that utilised LSTMs and RNNs to capture and focus on relevant information only. The main drawback of these networks was the rapid decrease in performance as the dimensionality of the input data increased. In the attention mechanism proposed by *Bahdanau,* the output vector was a weighted sum of all hidden states, instead of being a filtered version containing only the most relevant information (as in LSTMs). In general, an

attention mechanism has the structure shown in **Figure 3.14.** Since attention mechanisms were introduced, different versions now exist, which differ in the way the context vector (and therefore the weighted sum) is computed, and how these weights are learnt. The interested reader is referred to (121) for further details.

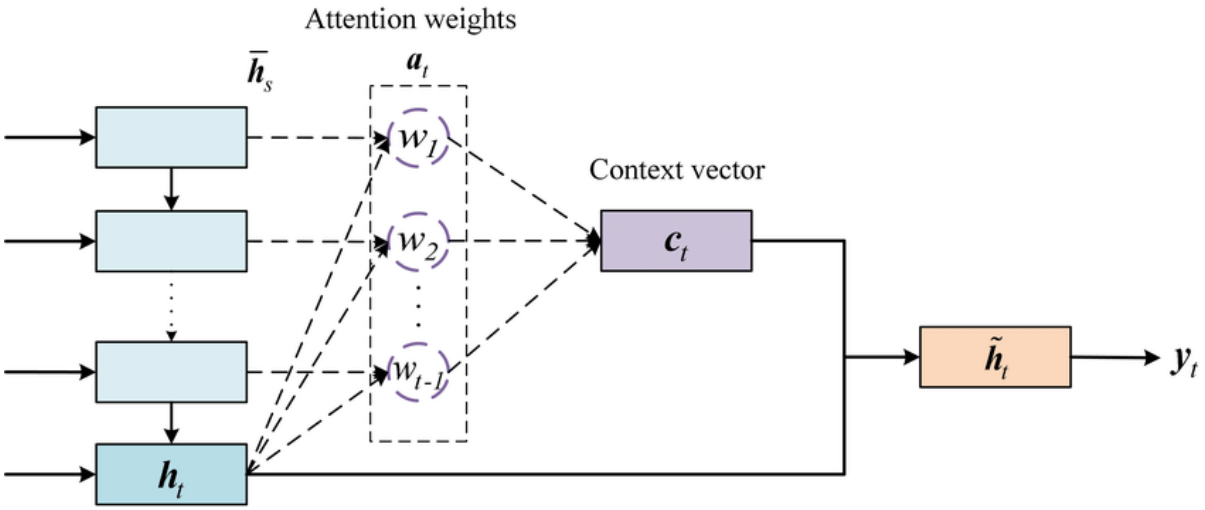

Figure 3.14. *General structure of an attention mechanism*(122)*. The final output y_t for a given target h_t is computed as a weighted sum of all hidden states $\bar{h}_s$, where the attention weight vector (containing the "contributions" of each hidden layer) is learnable.*

3.4.2 Useful Tools

The design of an AI architecture is critical to achieve high performance, and each individual component is chosen according to the type of problem to solve, the input dataset, the output domain, and the prediction task. In addition to this, there are a lot of other tools and algorithms that can be utilised to improve the AI performance, ranging from input data processing and augmentation techniques, to hyper-parameter optimisation, to different types of testing and training algorithms. In the following paragraphs, we will briefly mention the relevant tools and techniques utilised in this Thesis.

Dealing with Limited Amount of Data

Data augmentation. Because of the nature of DL algorithms, characterised by multiple and complex hidden layers and a large number of parameters to learn, the training performance of the network is

highly dependent on the size of the input dataset. The nature of this training dataset also influences the performance of the network when tested on unseen domains. To be able to build robust, trained networks that are able to perform a task under different conditions, the training dataset needs to be sufficiently diverse, and account for different situations that could occur during testing (e.g. rotated and/or zoomed images, noisy signal and so on). In this context, the problem of a limited training dataset can be overcome via data augmentation: the process of synthetically enhancing the training dataset. For instance, when dealing with images, data augmentation can consist of applying different transformation matrices, or different image filters, which help create multiple, slightly different copies of the "same" image. These alterations are interpreted as separate entities by the network, and should help increase its robustness during prediction. When dealing with time series, data augmentation can be performed through, for example, the addition of noise, or the inclusion of different cropped windows of the signal. This said, it is extremely important to remember that the performance of a network is only as good as the training datasets, and therefore data augmentation should be carefully planned and executed.

K-fold cross validation. Another way of dealing with limited data samples is by performing k-fold cross-validation, which is a resampling procedure consisting of splitting the input dataset k times into training and validation, and then computing the performance of the network after training and validating the various sub-samples k times.

Transfer learning. In many cases when there is a limited amount of data to perform a certain task, a network previously trained on a similar dataset can be used as the starting point of the new problem (by re-training part of the "old" network on the new, limited dataset). This transfer of knowledge between two similar domains, one for which there is an abundance of training data, and one for which there is a limited amount, is known as *transfer learning.* It is obvious that for transfer learning to successfully work, there has to be a relationship between the datasets utilised for initial training and re-training, as well as between the tasks to perform. The way transfer learning leverages the

knowledge of one task to perform a second task is typically by utilising the parameters of the first architecture to initialise the training of the second. There are different types of transfer learning according to the relationships between the source and target domains, tasks and implementation. The interested reader is directed to (123) for a survey on this topic.

Class-weighting. When the training dataset is unbalanced (the labels associated with the training inputs are not uniformly distributed across all classes), the training algorithm can be modified to take into account this unequal distribution of classes, so that they are all given equal importance on gradient updates. This prevents the model from predicting the most frequent classes more often. Equal importance of all classes is achieved by weighting them according to the training label distribution. That is, each class weight w_i is found by dividing the total number of training samples $n_{samples}$ by the product between the total number of classes $n_{classes}$and the number of samples for each class $n_{samples_i}$.

$$w_i = \frac{n_{samples}}{n_{classes} * n_{samples_i}} \text{ for } i = 1, \dots n_{classes} \quad \textit{(3.28)}$$

Dealing with Hyper-Parameters

Hyper-parameter optimisation. Within a network, there are a lot of variables, called *hyper-parameters*, that make up its structure and influence its performance. These hyper-parameters include, but are not limited to, the *learning rate* (how fast the learnable weights are updated), the *activation function*(s), the *kernel size* and number (which influences the width of the network), the depth of the network, the amount of regularisation and/or drop-out (randomly discarding information of neurons during training), the number of *batches* (how many sub-datasets the training input is divided into) and number of *epochs* (how many times the network iterates through the training dataset). The *batch size*, not to confuse with the number of batches, is how many training samples there are in each batch. The number of *iterations* refers the number of batches needed to complete one epoch. Tuning all these hyper-parameters is of importance to achieve an optimal network

performance, and avoid *overfitting* and *underfitting*. Briefly, overfitting refers to a model that has learned too much noise, and therefore performs well during training but underperforms during validation/testing (i.e. on data that has not been seen before). Underfitting occurs when the model is not learning properly, thus affecting both training and testing performances. For instance, a low number of epochs can cause the model to underfit as the number of time the weights of the network have been updated is not enough. However, too many epochs can cause the model to overfit as the model learns patterns from the training data that do not generalise well to the testing.

The best way to choose all these hyper-parameters is through optimisation techniques that, given sets of each hyper-parameter of interest, are able to return the combination of values that optimises the training performance of the architecture. There are different existing optimisation methods in the literature, such as *grid search*, *random search*, *Bayesian optimisation*, *gradient-based optimisation*, and we refer the reader to (124) for further details.

Cyclic learning. One important hyper-parameter mentioned above is the learning rate. Normally, it is set to a static value at the beginning of the training, and it is decreased after every n epochs to help convergence of the model. In certain situations, it is useful to prescribe a learning rate which has a *cyclic* nature to increase the chance of reaching a better solution. This process of prescribing a cyclic learning rate(125) is known as *cyclic learning*, and might also be used to train an ensemble of models (i.e. store the model after each cycle) and use the best model on the validation/testing set.

Test-time drop-out. Drop-out is an efficient regularisation technique primarily utilised during training to randomly discard information of neurons within hidden layers(126). In doing so, the network is less prone to *overfitting*. Under certain situations, to model prediction uncertainties for instance, drop-out can be utilised during testing(127), resulting in multiple different predictions of the same dataset.

3.5 SUMMARY

In this Chapter, we introduced and described the computational methods and AI algorithms utilised throughout this Thesis. These will enable us to model focal and post-infarct VTs on meshes generated from patient-specific imaging data, and optimise and automate VT ablation target identification. As it will be seen in the following Chapters, the proposal of new and efficient formulations described in this Chapter (e.g. the RE and LF methods) will allow to generate vast libraries of VT simulations that will be sufficient to train and analyse different AI architectures. CNNs, LSTMs and attention mechanisms will be used to extrapolate spatial and temporal features from extracellular potential signals (e.g. ECGs and/or implanted device EGMs), and establish relationships with sources of activation of corresponding VT episodes. The identification of these sources could improve ablation planning and outcomes. In conclusion, this Chapter has provided a concise but tailored description of cardiac modelling and AI. This will be sufficient to enable the reader to understand the **4 Literature Review**, where a more detailed, cohesive story of the use of clinical, modelling and AI tools in the context of VT will be told.

4

LITERATURE REVIEW

The previous Chapters provided a background for the clinical and computational aspects of this research. In this Chapter, we move our focus to reviewing clinical and computational tools utilised to identify ablation targets for ventricular tachycardia, aiming at improving pre-procedure planning and treatments. To thoroughly understand the remainder of this Thesis, Section 4.1 gives an overview of the evolution of pace-mapping, followed by its limitations (Section 4.2). Then, Section 4.3 describes the advances in both clinical and computational and/or AI algorithms to detect origins of focal and scar-related VTs from ECGs. The limitations associated with these methods are reported in Section 4.4, and finally the Chapter concludes with Section 4.5, a summary of the motivation of this work in relation to the review here presented.

4.1 PACE-MAPPING

In **2.4.3 Cardiac Electrophysiological Mapping,** we briefly introduced the concept of pace-mapping to identify VT substrates in SR, and aid ablation. Now, a more thorough review of the history and utility of pace-mapping will be given, together with a description of novel techniques proposed to improve ablation outcomes.

4.1.1 ECG-based Approaches

Pace-mapping has proven useful for identifying both sites of origin (SoO) and exit sites of focal and scar-related aetiologies when the tachycardia is poorly tolerated (over 70% of cases(128,129)), the ectopy occurs at low frequency(130) and/or the focal arrhythmia is difficult to initiate(131). Compared to entrainment and/or activation mapping, pace-mapping requires a shorter period of sustained VT, hence overcoming the requirement for haemodynamic tolerance of the latter. Moreover, compared to substrate-based approaches, that are also performed in SR but are less precise and effective(70), pace-mapping may target the clinical episode more specifically.

Historically, the birth of pace-mapping(132–134) coincides with the proposal and use of the 12-lead ECG to regionalise sustained, recurrent VTs(64). Although the concept of pace-mapping was firstly introduced in the early 1970s from animal studies(135,136), and the strategy was proposed in 1979 for clinical application(132), the first thorough investigation of this mapping strategy was carried by Josephson et al(134) in 1982, analysing the benefits and pitfalls of pace-mapping in clinical practice. They suggested the utility of pace-mapping in patients with non-inducible or rapid VT who could not undergo intraoperative mapping, but also stressed the impracticability of the procedure at the time (i.e. it was neither easier nor quicker). Since then, pace-mapping has significantly improved and gained more relevance within clinical settings to target recurrent VTs.

Pace-mapping is usually performed by pacing the ventricle(s) at $2\ ms$ pulse width at a cycle length equal to the clinical episode (if available), or at $400\ ms$ (if not)(137). The identification of the

myocardial area to pace relies on clinical indicators such as echocardiography, Q-wave topography, VT morphologies, as well as presence of low voltage areas ($< 1.5\ mV$)(138,139). The exit site and/or SoO is then located by finding the pacing location with the closest QRS complex to the target VT QRS (from 12-lead ECGs). Traditionally, the match between a paced QRS and the VT QRS was established in a binary fashion for each lead (qualitatively), and then the sum of all leads returned a pace-map score, with 12/12 being a perfect match and >=10/12 a good match(128). With the advent of novel EAM mapping systems, more quantitative methods have been proposed to define the degree of match to the clinical arrhythmia(140). In Gerstenfeld et al. (140), the comparison between a paced 12-lead ECG and the target VT ECG was established by two different measures: the mean absolute deviation (MAD), and the correlation coefficient (CC). For MAD computations, the sum of the absolute difference between the paced signal and the VT signal across all leads was divided by the sum of their absolute sums (after each waveform was normalised by removing the mean amplitude). CC was computed in the usual fashion between waveforms of corresponding leads, and then the average CC was computed (to obtain a single value).

Whereas pace-mapping for the identification of focal arrhythmias is quite straightforward, pacing in proximity of re-entrant circuits can lead to different configurations, and needs to be carefully interpreted. This is because of the presence of a diastolic isthmus which returns different QRS morphologies when pacing at the exit or the entrance of such a corridor. De Chillou et al.(141) analysed this transition more thoroughly, and highlighted the value of pace-mapping for the localisation of post-infarct VT critical isthmuses. Traditionally, pace-mapping is utilised to identify VT exit sites, primarily aiding procedures such as linear ablation(142). However, targeting VT isthmuses (for scar de-channelling ablation(143), for instance) would also be beneficial, and (141) showed that the exit of an isthmus could be easily identified by good correlations >= $84\% \pm 7\%$ between paced traces and the VT signal, and entrances of the channel by poor correlations. This finding was of importance to recognise the utility of pace-mapping in identifying the orientation of the isthmus, and to highlight the difference with entrainment mapping, where a match between pacing and the

reference VT is seen all along the isthmus. Moreover, they invalidated the assumption that correlation percentages decrease gradually and homogenously when moving away from the exit site. An example of a pace-map identifying the orientation of a potential isthmus is illustrated in **Figure 4.1**. To generate these maps, before computing CC for each pacing point as described above, the target VT waveforms of each lead were slid along the corresponding lead of each pace QRS until the best match was found (by standard CC). This was repeated for all leads, and then the average CC for that pacing location was computed (and the procedure repeated for all pacing sites). Another example of a pace-map showing CCs at different pacing points (with corresponding QRS complexes) can be seen in **Figure 4.2.**

In general, the performance of conventional pace-mapping in identifying exit sites is quantified against successful ablation sites (post-procedure). The spatial resolution ranges between $11 - 28\,mm$ (mean: $18 \pm 5\,mm$)(144), similar to activation mapping which is more time-consuming, invasive and not practicable for poorly tolerated VTs.

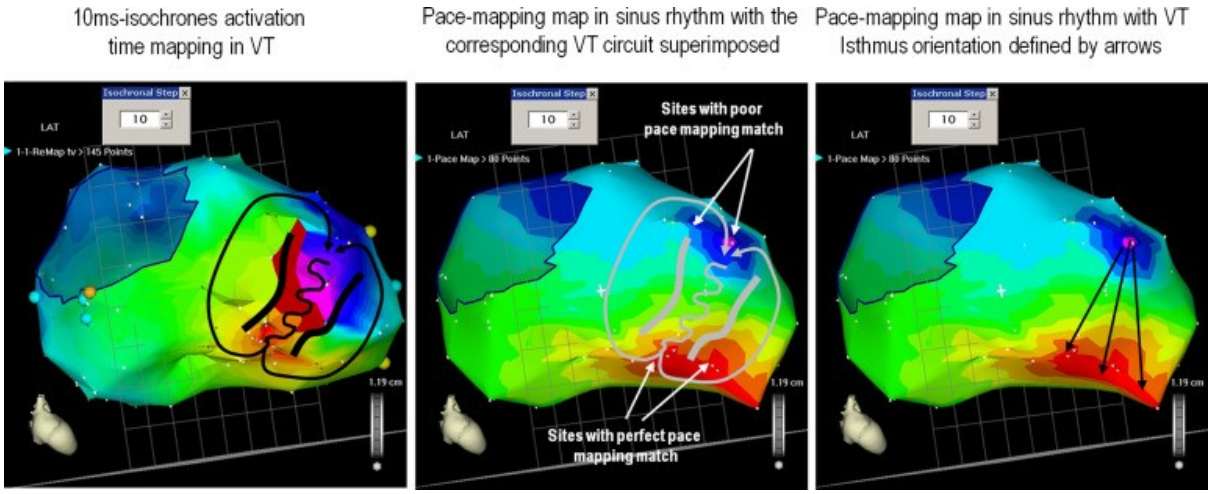

Figure 4.1. *Example of isthmus identification via pace-mapping*(141)*. Activation map of the VT circuit of interest is shown on the left panel. Corresponding correlation pace-map (centre), computed between the traces of different pacing locations and the reference VT signal, highlights regions of high CC in red, identifying possible exit site of the circuit, and sites of poor CCs, relatable to isthmus entrance. Orientation of the VT isthmus is shown on the right panel, going from poor to good correlations.*

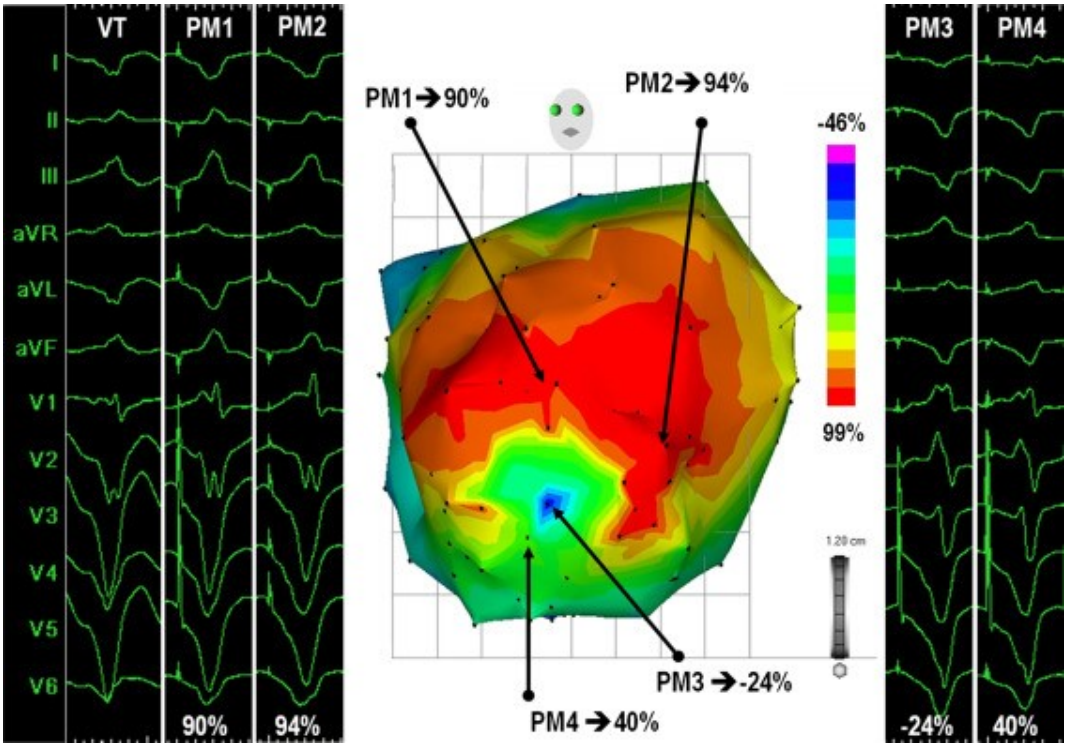

Figure 4.2. *Example of a pace-map utilising de Chillou methodology*(141)*. The reference VT 12-lead ECG QRS is shown on the far left panel. QRSs of four different pacing locations (named PM1, PM2, PM3 and PM4) are shown from left to right, with their positions highlighted in the pace-map (centre). As above, the rainbow colourbar goes from poor CCs (purple/blue) to near-to-perfect (red).*

The abrupt change in QRS morphology between exit and entrance of an isthmus seen in (141) led the same group to propose an alternative, novel pace-mapping method to identify slow conduction channels, named *reference-less gradient pace-mapping*(145). The proposed approach also overcame one of the limitations of conventional pace-mapping: the necessity of a reference VT 12-lead ECG. The new methodology consists of creating correlation maps solely on the ECG data obtained during pace-mapping, by computing CCs for each paced beat against neighbouring paced beat QRS complexes (within a sufficiently small neighbourhood $\|\delta x\| < 20\ mm$), as below

$$C_{PacedQRS(x)}(x + \delta x) = \frac{1}{12}\sum_{lead=1}^{12} correlation(S^{lead}_{PacedQRS}(x), S^{lead}_{PacedQRS}(x + \delta x)) \qquad (4.1)$$

where $C_{PacedQRS(x)}(x + \delta x)$ is the correlation coefficient of a paced beat x against a paced beat at $x + \delta x$, and $S^{lead}_{PacedQRS}$ is the QRS of a lead at location x or $x + \delta x$.

These correlations are then transformed into a spatial gradient map in units of $correlation\ \%/mm$

$$\begin{aligned} G_{PacedQRS/PacedQRS} &= \left|\nabla C_{PacedQRS(x)}(x + \delta x)\right| \\ &\cong \frac{\left|C_{PacedQRS(x)}(x + \delta x) - C_{PacedQRS(x)}(x)\right|}{\|\delta x\|} \\ &= \frac{\left|C_{PacedQRS(x)}(x + \delta x) - 100\%\right|}{\|\delta x\|} \end{aligned} \quad (4.2)$$

where 100% comes from the correlation of a pacing site x with itself. It is important to mention that to create these gradient maps, the original mesh generated from the pacing locations is divided into further sub-triangles (3 for each triplet of points) (**Figure 4.3D**).

The resulting reference-less gradient pace-map $G_{PacedQRS/PacedQRS}$ can be compared to the conventional pace-map (named $C_{PacedQRS/VT}$) in **Figure 4.3**; the reference-less map highlights regions above a certain threshold ($> 3.125\ \%/mm$) where the greatest change in QRS morphology between paced beats is seen, ultimately signifying slow propagation zones (and thus critical VT isthmuses), in contrast to the conventional pace-map, where high CCs relate to VT exit site(s).

4.1.2 EGM-based Approaches

Two studies(14,15) demonstrated the potential of utilising existing EGM recordings from ICDs as the reference signals for conventional pace-mapping, aiming at targeting non-inducible clinical episodes and potentially reducing the need for VT induction. Yoshida et al. (14) were the first to assess the utility of ICD EGMs to differentiate clinical VTs from other morphologies, as well as quantify the spatial resolution of EGM-based pace-mapping in comparison to conventional ECG-based. They considered ICDs from different manufacturers, including Medtronic, Inc. (Minneapolis, Minnesota), Boston Scientific Corporation (Natick, Massachusetts), and St. Jude medical, Inc. (St. Paul, Minnesota). They

considered only two vectors of intracardiac EGMs: a far-field between can and RV coil, and a near-field.

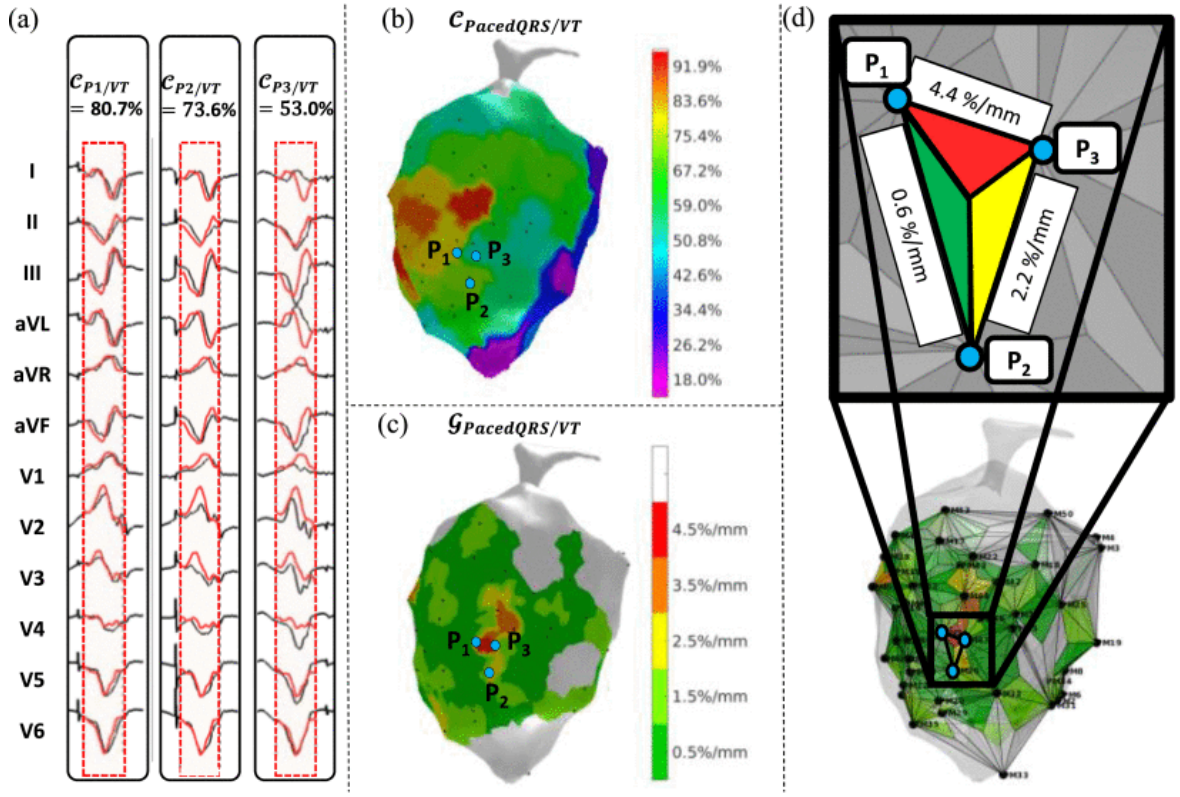

***Figure 4.3**. Example of conventional pace-mapping and reference-less gradient pace-mapping*(145). *(A) Visual comparisons between VT QRSs and three different pacing sites (P1, P2, P3). (B): Conventional correlation map in %, and (C) reference-less gradient pace map in %/mm. (D): Subdivision of the original mesh into a set of three triangles for each triplet of points.*

The correlation between the paced 12-lead ECGs and/or 2-vector EGMs and the targeted VT trace was computed by aligning the QRS complexes, computing correlation coefficients and root mean square difference for each lead, and then averaging the results across all leads to obtain a single value. A cut-off value was established from receiver-operating characteristic curve (ROC) analysis to establish whether a pace-map was targeting the clinical VT or not. In doing so, the group concluded that ICD EGMs may be an accurate surrogate for 12-lead ECGs in differentiating clinical VTs from other episodes, although the spatial resolution of EGM-based pace-maps was more variable and not as good as ECG-based pace-maps.

After this promising study on the utility of intracardiac EGMs to aid ablation planning, the group later showed(15) how 2-vector ICD EGMs can be indeed used to identify VT targets for ablation of non-inducible clinical VTs. They obtained pace-maps between the 2-vector ICD EGMs of the paces and all VT morphologies (documented but non-inducible, and induced), and used the results of those maps to guide ablation. When compared with control (ECG-guided ablation planning), the group saw a lower VT recurrence rate in the ICD-EGM-guided group, showing the feasibility of EGM-based pace-mapping to improve ablation outcomes.

4.1.3 Limitations

One major limitation of current pace-mapping techniques is that they are carried-out either epicardially or endocardially, and there is an ongoing debate to decide which one to perform on a patient-to-patient basis(146,147). A recent study showed the potential of combining endo- and epicardial pace-mapping(148) to determine whether to perform endocardial or epicardial ablation, and identify possible intramural location of a VT isthmus (if a good match is not visible in either endocardial or epicardial maps). However, a more extensive investigation on the matter is required, and there is a need for actual 3D pace-maps.

EGM-based pace-mapping has showed its utility in targeting clinical, non-inducible episodes and aiding ablation planning. However, the lower resolution compared to ECG-based approaches limits its day-to-day applicability. We believe that this limitation stems from the use of only two sensing vectors, and could be overcome by investigating different implanted device configurations and EGM vectors. Given the advances in design and technology of medical devices(79), such a study could really help in reducing VT recurrence rate, and the need for VT induction.

4.2 Targeting Focal VTs

As seen so far, the surface 12-lead ECG is extremely useful(8) in guiding pre-procedure ablation planning, and is at the basis of all conventional and advanced mapping methods. In the following

subsections, we will describe in more details the principal qualitative and quantitative algorithms that have been proposed to identify VT ablation targets from surface ECGs, and some of the modelling and AI studies aimed at automating such ECG-based localisation approaches. We will first expand on targeting focal VT episodes, and we will then move on to the localisation of more complex, scar-related tachycardia.

4.2.1 Clinical Algorithms

Briefly, as seen in previous Chapters, the QRS is representative of ventricular activation, and has been initially utilised to qualitatively regionalise focal, idiopathic VTs(8,64,149). In 1981, Josephson et al.(64) conducted the first study correlating QRS patterns of different idiopathic VTs with their SoOs, determined by catheter and intraoperative mapping. In their study, 22 VTs had a right bundle branch block (RBBB) configuration, and 19 a left bundle branch block (LBBB), and they were able to find characteristic QRS patterns across leads differentiating anterior to posterior and septal origins. The main findings were the presence of a q wave in lead I and/or $V6$ in anterior VT-RBBB and VT-LBBB. In the latter, a superior axis of the q wave indicated a possible origin in the inferior aspect of the anterior septum, whereas an inferior and rightward axis localised the origin in the superior aspect of the anterior septum. Finally, R waves were present in lead I and $V1 - V6$ for VT-RBBB, and in lead I and $V2, V3\ and\ V6$ for VT-LBBB. These guidelines became the gold standard for initial diagnosis of VT. Because of the limitations associated with ECGs to precisely identify VT origins, later in the 1980s other studies(150–153) showed the feasibility of utilising body surface mapping to locate focal VTs. The resolution of BSP maps (BSPM) was firstly investigated in 1990 by SippensGroenewegen et al.(154), which also attempted to create a reference database containing a wide spectrum of electrocardiographic map patterns for different VTs in structurally normal hearts. Briefly, they created QRS integral (QRSI) maps constructed from the 62-lead time integral values (product of the sampling interval with the sum of potentials within a time interval) for a total of 182 endocardial pacing sites (distributed across the RV and LV) among 12 patients. From these maps, SippensGroenewegen et al.

were able to identify 38 different regions in the RV (13) and LV (25) that had characteristic QRS patterns for different pacing sites. This database was used in later studies as a lookup table to match paced QRS integrals with an endocardial segment, however the localisation resolution was limited to the average segment size ($\sim 3.3 \pm 1.4\ cm^2$). Furthermore, the match between a pace-map and any map from the database was purely qualitative and operator dependent.

4.2.2 Computer-based Algorithms

A more continuous localisation of cardiac activation sites was proposed in 2000 by Potse et al.(155). They proposed a computer algorithm that, in simple terms, transformed each QRSI map into a covariance matrix and then expressed the latter in terms of the first three eigenvalues and eigenvectors. These were then treated as Cartesian coordinates in 3D space, transformed to spherical coordinates, and mapped to a specific location in the LV endocardial surface. They reported a localisation resolution between 10.2 and $14.6\ mm$, outperforming all previous studies.

Continuous epicardial activation can also be derived from BSPMs using the inverse solution. For a more detailed description of the inverse problem, we refer the reader to (156–158). The inverse problem is however associated with some important limitations (e.g. impossibility of describing endocardial, intramural and/or septal activity), which has led to the proposal of many other quantitative algorithms(50,159–161), utilising computer-based approaches. For instance, Sapp et al.(50) developed a rapid computational approach that combined a discrete localisation on the basis of template 12-lead ECGs from known pacing LV sites with a continuous localisation using linear regressions on a generic LV model. They also showed how to tailor the latter to patient-specific LV anatomies, improving the overall localisation. They obtained mean localisation errors of $12 \pm 8\ mm$ and $\sim 5\ mm$ for the population-based regression and patient-specific regression respectively. The proposed algorithm was however dependent on EAM maps of the patient, which led the same group to develop a similar workflow utilising CT imaging instead(162). The last two studies were useful not only in the context of focal VTs and premature ventricular contractions (PVC), but also of scar-related

VTs, and will be assessed in more detail the following section. As well as utilising linear regression, Zhou et al.(160) also performed a comparison with other non-linear machine learning methods, such as random-forest (RF) and support-vector (SVM) regressions, reporting higher accuracies compared to linear algorithms(50).

Another study by He et al. (161) looked at classifying and localising PVCs from 12-lead ECGs via four different machine learning methods: SVM, RF, decision tree (DT) and Gaussian naïve Bayes (GNB). However, their localisation was limited to only 11 regions of the ventricles. Briefly, beats were first extracted from the ECG datasets. Then, a SVM binary classifier was developed to discern between PVC and normal beats. Subsequently, different QRS features were extracted from the PVC beats, clustered and labelled to 11 different regions of the ventricles, and finally classification performance of each machine learning method was evaluated.

Lastly, in the context of AI-based focal localisation, we will mention the work of Yang et al.(159), as it will be necessary to understand **Chapter 6**. They were the first to use a DL approach for the automation of PVC localisation, and by using computational EP simulations in the training stage of their algorithm, they were able to explore a wider range of scenarios and improve on the limitations of previous studies. In brief, they utilised ECGs from computationally simulated focal beats around the ventricles to train CNN architectures to output the PVC SoOs. They tested their algorithm on 90 PVC traces across 9 patients and compared the resulting predictions against ablation outcomes. To be able to localise PVCs, they developed two similar 5-layer, 2D, classification CNNs, as shown in **Figure 4.4** (hidden layer – pooling layer – hidden layer – pooling layer – FC layer)**.** One, named *Segment CNN*, aimed at classifying the segment of origin of the PVC (out of 25 segments, 17 in the LV and 8 in the RV), and the other, named *EpiEndo CNN*, performed a binary classification to establish the surface (endocardial or epicardial) of origin. From these probability distributions, they then developed an equation which, by incorporating the centres of gravity CoG_{ij} of the 25 segments (computed on the epicardial and

endocardial surfaces of each segment), was able to output the PVC origin in Cartesian Coordinates, relatable to the ventricular mesh of interest.

$$S = \sum_{i=1}^{N} P_{seg}^{i} \times \left(\sum_{j=1}^{N} P_{epiendo}^{j} \times CoG_{ij} \right) \quad (4.3)$$

The PVC source S is the sum of the product of each segment probability P_{seg}^{i} adjacent (and normalised) to the output segment with the sum of the epicardial and endocardial probabilities $P_{epiendo}^{j}$ multiplied by the centres of gravity of the corresponding segment.

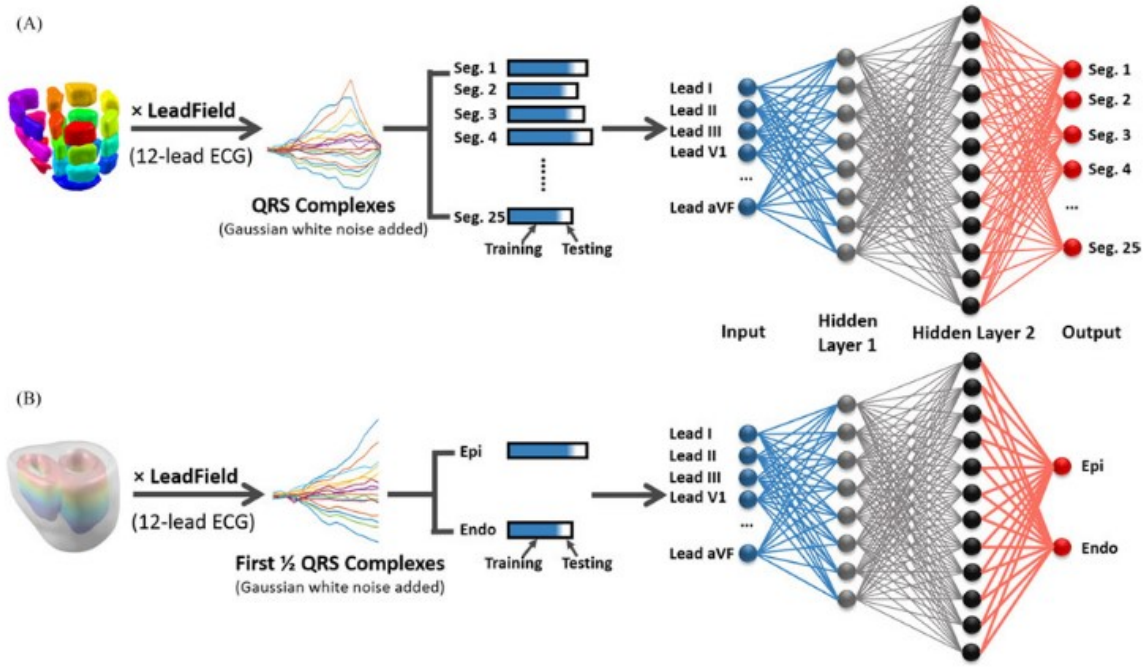

Figure 4.4. *CNN architectures from Yang et al.*(159)*. (A) shows segment CNN, which takes in 16-lead QRS complexes and outputs the segment of origin of 25 segments. B) classifies whether the source of origin is in the endocardial or epicardial surface, from the first half of 16-lead QRS complexes.*

The inputs to both CNN architectures, given their 2D nature, were square matrices made of QRS complexes downsampled to 16 time points from 16-lead ECGs (the standard 12-lead ECGs with additional 4 vector combinations $LL - RA - LA$; $LA - RA - LL$; $RA - LA - LL$; $\frac{(LL + RA + LA)}{3}$). For *EpiEndo* classification, only the first half of the QRS complexes was used. Whereas a more detailed description of Yang's methodology and CNN structure will follow in **6 Automated Focal VT**

Localisation, it is worthwhile mentioning that they achieved a mean localisation of $10.9 \pm 5.5\,mm$ between the predicted PVC origins and ablation targets in the 9 patients, obtaining a very desirable localisation for clinical purposes.

4.3 TARGETING SCAR-RELATED VTS

Whereas a qualitative localisation of focal activation in structurally normal hearts from 12-lead ECGs can, and has been shown to, be fairly accurate, it can be highly challenging in presence of fibrosis and/or infarcts, that largely influence QRS morphologies. This stems from the fact that the diastolic isthmus responsible for the re-entrant activation pattern usually lies within dense scar, which is electrically silent and has no representation on the surface ECG(8). In addition, the circular pattern of the VT episode can create electrical 'holes' that reduce the accuracy of the ECG in predicting VT exit sites. Thus, more advanced and specific methods to target scar-related VTs have been proposed over the years to overcome this issue, aiding ablation planning and attempting to reduce the need for more invasive mapping strategies.

4.3.1 Clinical Algorithms

The first studies aimed at regionalising re-entrant VT exit sites in presence of myocardial infarction from ECGs were by Miller et al.(163) and Kuchar et al.(164) in the late 1980s. The former(163) established relationships between the location of a VT exit site and a combination of four features from 12-lead ECGs after performing endocardial mapping: location of infarction, bundle branch block type configuration, quadrant of QRS axis and precordial R wave progression pattern. Similarly, Kuchar et al. (164) separated QRS configurations resulting from LV endocardial pacing after devising a new mapping grid, so that apical and basal VT sites could be identified according to QRS patterns in leads $V1$ and aVR, anterior and inferior by that in leads II, III and $V6$, and septal and lateral using leads I, aVL and $V1$.

Building on those studies, in 2007 Segal et al.(165) proposed an ECG algorithm that detected endocardial, infarct-related VT exit sites in 9 endocardial regions by correlating VTs with ECG features determined by noncontact mapping. In 2011, Wijnmaalen et al.(166) attempted to develop an algorithm that differentiated LBBB scar-related and non-scar-related VTs according to QRS duration, frontal plane axis, QRS amplitude in $V2$ and QRS-S (interval in lead $V1$ between QRS onset and S-wave). In general, they found that scar-related VTs had longer QRSd ($> 155ms$), longer QRS-S ($> 90ms$) and smaller QRS amplitude in $V2$ ($> 1.55\ mV$) than non-scar-related VTs.

4.3.2 Computer-based Algorithms

One of the first automated ECG-based analyses was proposed by Yokokawa et al.(49) in 2012. After performing LV pace-mapping within scar tissue in 34 post-infarction patients to identify VT exit sites, a SVM algorithm was created and trained on the 12-lead ECG pace-map morphologies to classify the location of a post-infarct VT episode within a 10-segment subdivision of the LV. The algorithm was trained for each pair of 2 different regions to break the problem into several binary classifications, and they obtained an accuracy of 69% for the first top-ranked region, and 88% for the top 2 (the classified region and/or its neighbour). They compared their algorithm with Milller's (163) and Segal's (165), outperforming both methods in terms of testing accuracy. The median spatial resolution of the 10-segment LV model was $15\ cm^2$ (6% of the entire LV endocardial area).

Another segment-based algorithm was developed in 2018 by Andreu et al.(48). QRS amplitudes in the six limb leads and in $V3$ and $V4$ were used to establish the VT exit site location within the 17-segment American Heart Association (AHA) model(167,168). As shown in **Figure 4.5**, the segment of origin was established after a three-step procedure: firstly, the limb lead I, II or III with the highest absolute voltage magnitude was taken into consideration. Then, the adjacent limb lead (aVL, aVF or aVR) with the highest absolute voltage was used to determine the group of 3 segments where the VT may originate. Finally, polarity of leads $V3$ and $V4$ determined apical (both negative), mid (discordant) or basal (both positive) location.

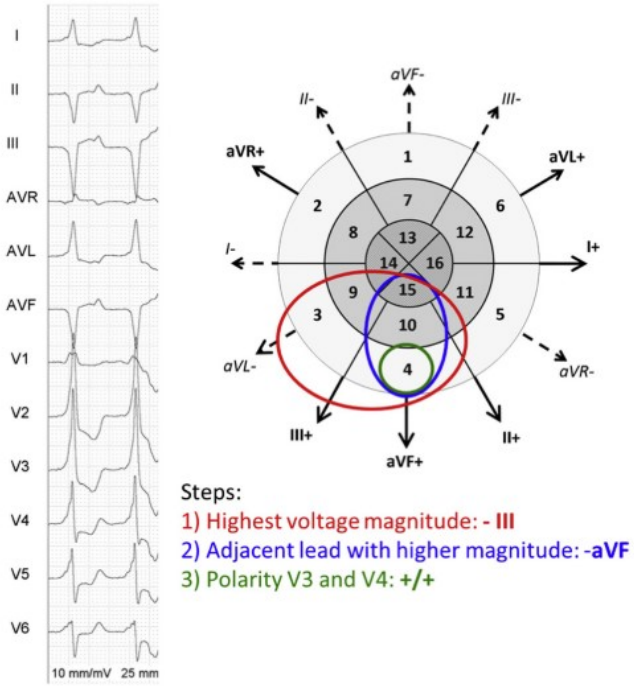

Figure 4.5. *Example of Andreu et al.*(48) *algorithm. Red circle highlights the limb lead with the highest absolute voltage (-III). Between its adjacent leads (aVL- and aVF+), aVF has the higher absolute voltage, and it is taken into consideration to decide the wedge of segments of interest. Finally, the positive polarity of both V3 and V4 signifies a basal location of the VT exit site (green circle).*

The algorithm correctly identified 81.9% of the segments of origin of the VTs, established during EAM mapping. Interestingly, they saw that the size and/or presence of an infarct did not affect the algorithm performance.

The algorithm proposed in 2019 by Zhou et al.(160) to identify focal VT SoOs, was later tested and assessed(169) for the identification of VT exit sites in presence of structural heart disease. The algorithm, as previously mentioned, consists of a three-step procedure. Firstly, QRS integrals of one VT beat (automatically detected) are computed to generate a 12-lead ECG integral pattern that is compared against template integral patterns generated from each of 16 segments of a generic LV endocardial surface. This comparison yields to an initial, approximate localisation of the VT exit site. Then, population-based regression coefficients (estimated by associating a VT exit site with each of 238 triangular elements of a generic LV endocardial surface) are used to improve localisation accuracy within the segment identified during template matching. Finally, patient-specific coefficients

(calculated from 3-lead ECGs and known pace-mapping sites on the patient-specific heart geometry), are used to achieve further precision. This study proved to be effective in localising VT exit sites for 25 VT morphologies, achieving accuracies of $\sim 9mm$ and $\sim 7mm$ for population-based and patient-specific localisation, respectively. In addition to requiring a lot of manual inputs and steps, this algorithm still heavily depends on the acquisition of complete EAM maps at different pacing sites to acquire patient-specific coefficients, and is limited to localising endocardial sites only.

The same group later addressed(51,170) some of the limitations of their study by omitting the first two steps of the algorithm, and only performing patient-specific, EAM-based localisation to detect both VT exit sites and PVC origins in patients with structural heart diseases. They carried-out a retrospective and prospective assessment of the algorithm in a cohort of 42 VT/PVC patients from two different centres. The predicted VT sites were compared with the clinically identified sites during activation and/or pace-mapping, and achieved a mean localization of $6.5 \pm 2.6\ mm$, retrospectively, and $5.9 \pm 2.6\ mm$, prospectively. Although these results are extremely desirable, the algorithm can only be performed during an EAM procedure, and thus might not have many advantages over conventional pace-mapping and/or completely non-invasive strategies.

So far, the use of more advanced, automated ML/DL architectures to detect scar-related VTs has not been attempted. Many studies have focused on automating the classification between different types of arrhythmias from ECGs (171–175), using publicly available databases, such as the MIT-BIH(176), or the Physionet's Physiobank(177). However, the extension to continuous localisation of re-entrant VTs is challenged by the lack of labelled datasets for this extremely complex task.

For a more detailed description of different AI-based arrhythmia classification studies, the reader is directed to (173). For the purpose of this Thesis, we will only mention the work of Yao et al.(178) as they proposed an interesting AI architecture that will be of use in **7 Automated Post-Infarct VT Localisation.** The AI architecture was composed of a very deep CNN, followed by LSTM cells and an attention-mechanism, and aimed at classifying different arrhythmias from variable-length ECGs,

increasing robustness of the algorithm compared to previous studies. The combination of a CNN with LSTMs and attention allows to extract and analyse both spatial and temporal features and dependencies, that we believe are crucial for delineation of scar-related VT substrates, and will therefore be pursued in later Chapters.

4.3.3 Limitations

One major limitation of all existing VT localisation approaches is the dependence on ECG traces, which require VT induction. Moreover, a successful ablation procedure, which reduces the chances of VT recurrence in the future, heavily relies on targeting the clinical presenting arrhythmia, which is not assured when inducing and utilising the ECG. Therefore, as for pace-mapping, VT localisation algorithms would greatly benefit from tachycardia information stored in implanted devices as EGM recordings.

Qualitative methods have been useful in regionalising idiopathic, focal VTs over the years, but lack the accuracy and precision of computer-based algorithms, that can extract and establish more complex relationships from QRS morphologies, as well as exploiting and investigating a wider range of cases. The work by Yang et al.(159) is very important in this context as it is one of the first combining computational modelling with DL algorithms to automate focal VT localisation and increase performance accuracy. One major limitation of their study is the dependence of the AI architecture on an idealised heart-torso model, requiring all testing models to be registered to it, and adding complexity and errors to the localisation pipeline. Therefore, it will be interesting to carry-out a deeper analysis of their algorithm, improve the simulation pipeline (which is very simple and perhaps not very realistic), and explore the possibility of automating focal VT localisation from implanted device EGMs.

In the context of scar-related VTs, there is currently a need for a computational modelling, AI-based algorithm that constrains the localisation to the myocardium (which is only assured in (170) during the third phase of algorithm, heavily relying on invasive mapping strategies), that can deal with intramural

episodes, and exploits modelling to investigate a wider range of scenarios, and allow a patient-specific, non-invasive localisation.

4.4 SUMMARY

The literature reviews here presented are particularly useful to understand the aim and context of the subsequent Chapters. Despite the power of the ECG for diagnostic purposes, there is a need for in-silico, computational platforms that could exploit the information stored in implanted devices, and help target the clinical arrhythmia and reduce the need for VT induction. Hence, in the following Chapter, we will show the power of implanted device multi-vector EGMs to aid conventional ECG-based pace-mapping, and identify VT exit sites in presence of structural heart disease. In latter Chapters, we will show how to use such information in the context of computational-AI platforms to automate the localisation of both focal and scar-related VTs. By using fast and physiological computational simulations, we will be able to generate vast libraries of ECGs and EGMs of different VT episodes, and use them in conjunction with more complex DL classification/regression algorithms, that do not require manual inputs or feature extraction, and can achieve desirable and accurate localisation results, applicable in clinical practice and completely non-invasive.

5

IN-SILICO PACE-MAPPING

The previous review on the history, use and novelties of pace-mapping is essential to understand the motivation of this Chapter. Here, we begin to investigate the utility and feasibility of using multi-vector EGMs from implanted devices to target clinical VT episodes, and the power of computational-based studies to improve speed and safety of ablation planning through in-silico pace-mapping. In Section 5.1, we outline the motivation of this Chapter, followed by a thorough description of the methodology developed to create 3D ECG-based and EGM-based pace-maps (Section 5.2). Then, in Section 5.3, we present the results and the comparison between different ECG-based and EGM-based pace-maps, and investigate further the role of so-called 'reference-less' pace-mapping. Finally, in Section 5.4, we conclude by addressing the importance of this in-silico study for clinical purposes, and possible future directions and improvements. The work presented in this Chapter has been published in the Computers in Biology and Medicine Journal(179).

5.1 INTRODUCTION

During the initial clinical description of ventricular arrhythmias (**2.3 Cardiac Arrhythmias**), we saw that the most effective therapeutic option against VT, in the presence of structural heart disease, consists of ablating the substrates (diastolic isthmuses and/or exit sites) that sustain the re-entrant circuits. These substrates are usually located within the BZ of a myocardial infarction, and accurate detection is critical for an effective and successful ablation procedure. In **4.1 Pace-Mapping**, we saw that VT isthmuses and exit sites can be accurately identified and localised with pace-mapping, which has important advantages over the other mapping strategies. Firstly, it requires a shorter period of sustained VT, which overcomes the challenges faced with entrainment and activation mapping when the tachycardia is haemodynamically poorly tolerated. Secondly, pace-mapping may target the VT more specifically than substrate-based approaches. Despite these advantages, pace-mapping is still an invasive and time-consuming procedure, and requires a reference ECG of the clinical VT, which may not be always available or inducible. In the previous Chapter, we reviewed some studies that attempted to overcome these challenges, by proposing a reference-less method that does not require the VT ECG(145) or by utilising implanted device EGM recordings of the clinical VTs as reference signals(14,15). These interesting pieces of work require further investigation, and we believe that a computational, in-silico study could address most of the current limitations and questions. It could be the ideal testbed to provide guidance regarding epicardial or endocardial substrate, and provide highly complementary, and safer information to clinical pace-mapping, especially when combined with stored EGM VT recordings from an implanted device.

In the following section, we present the methodology to develop an in-silico, computational platform to produce individual, virtual pace-maps, and investigate the potential utility of multi-vector EGMs from implanted devices. Our aim is to optimise conventional ECG-based and EGM-based clinical pace-mapping techniques, as well as further exploring and refining reference-less pace-mapping, which shows great promise in targeting critical VT isthmuses without a reference VT signal. Finally, we intend

to explore the possibility of using both ECGs and implanted device EGMs to identify endocardial and epicardial substrates to guide pre-procedural planning.

5.2 METHODS

In this Section, we will illustrate the workflow of this in-silico, computational pace-mapping study, along with a detailed description of each step.

5.2.1 Platform Overview

The overview of this study is illustrated in **Figure 5.1**. A detailed heart-torso model (Step 1) was generated from patient-specific imaging data (Step 0). The model was used to simulate different episodes of sustained, monomorphic VTs (Step 2) in the presence of different myocardial scar patterns, and corresponding 12-lead ECGs (Step 3) and implanted device EGMs (Step 4) were then computed. Detailed pace-maps were reproduced for each VT morphology after pacing the BZ of the infarcts in different locations (Step 5).

5.2.2 Model Generation

A CT trans-catheter aortic valve implantation (TAVI) planning scan (resolution of $0.69 \times 0.69 \times 0.50\ mm^3$) of an anonymised patient was utilised to generate a detailed 3D torso, similar to (107). All major organs (e.g. lungs, bones, skin, fat/muscle, liver, spleen, kidneys, and the pericardium) were segmented in the *Seg3D* software(180) with semi-automatic tools, such as connected components, dilate/erode, Otsu thresholding algorithms, Canny Edge Detection, Distance map and Segmentation level set filters. The patient in question consented for the use of their data in ethically approved research: UK Research Ethics Committee reference number (19/HRA/0502 & 15/LO/1803). The four chambers of the heart, together with the aorta, were segmented from a separate cardiac CT scan of higher resolution ($0.40 \times 0.40 \times 0.50\ mm^3$), using an automatic atlas-based software *Siemens Axseg v4.11*(181), and then incorporated into the torso segmentation(107). An unstructured,

tetrahedral finite element mesh from the combined segmented image stack was generated in the Tarantula meshing software(26), based on the octree method mentioned in **3.3.2 Mesh Generation.** The mesh had a total of 20,747,414 nodes and 121,269,030 elements, and the average ventricular edge length was $376\ \mu m$. The torso organs and tissue were given electrical conductivities as used by *Plancke et al.*(107) (**Table 5.1**), to be able to simulate physiological extracellular potentials.

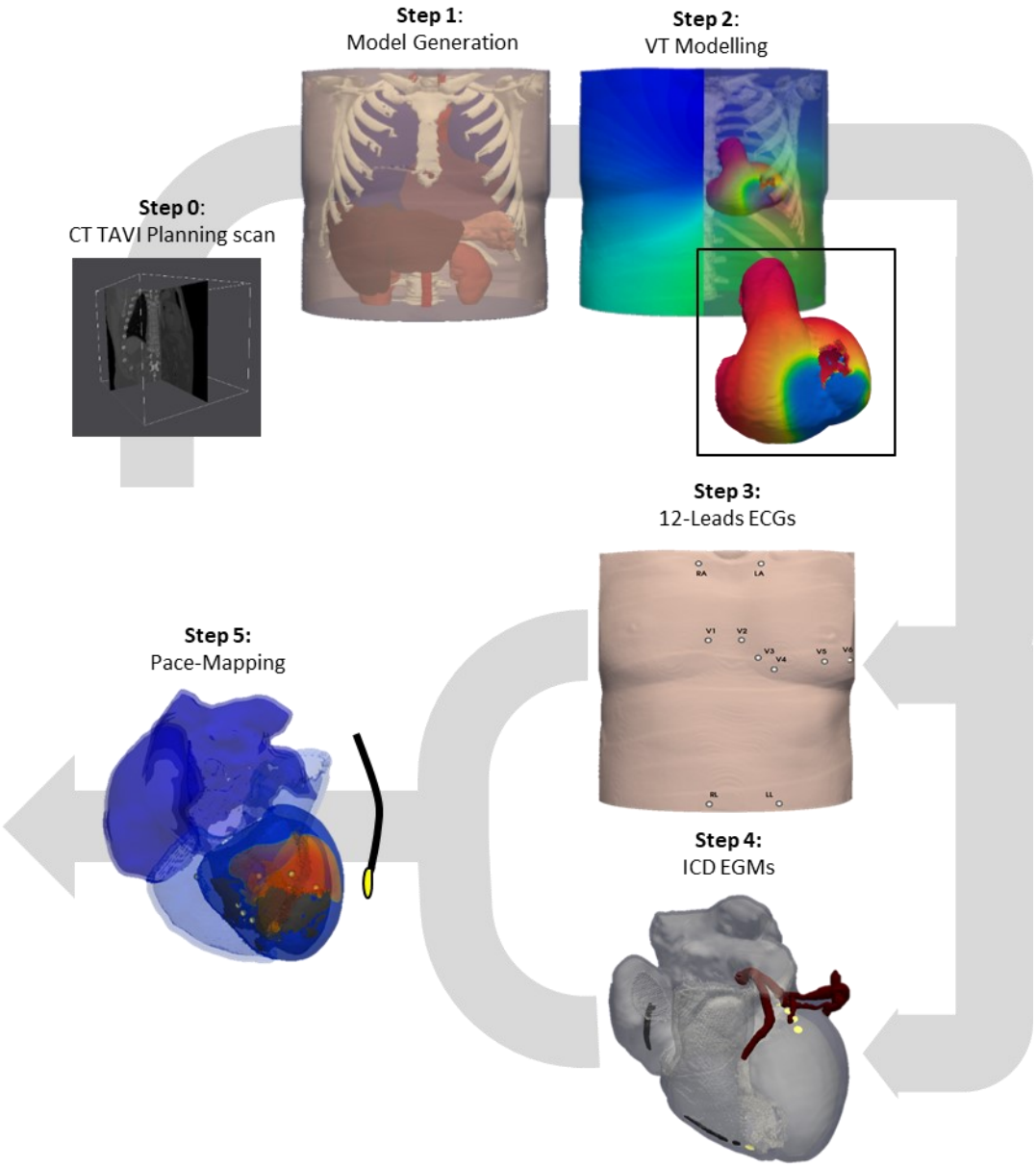

Figure 5.1. *Workflow of our proposed in-silico pace-mapping pipeline. A CT TAVI planning scan of a patient (Step 0) was used to generate a 3D torso model (Step 1) that included all major abdominal and thoracic organs, as well as a highly detailed biventricular mesh. Different VT episodes (Step 2) were simulated on the mesh, and corresponding 12-lead ECGs (Step 3) and*

implanted device EGMs (Step 4) were computed. Finally, virtual pace-mapping was performed to compare the ECGs and EGMs of the several VT morphologies against different pacing locations around the scars to find the substrates (exits and slow conduction isthmuses) responsible for the maintenance of the tachycardia.

Organs	Tissue Conductivities (S/m)
Lungs	0.0714
Bones	0.05
Skin	0.117
Fat/Muscle	0.24725
Liver	0.1667
Spleen	0.1
Kidneys	0.6667
Aorta	0.6667
Ventricular blood pools	0.6667
Atrial blood pools and walls	0.2

***Table 5.1**. Organ conductivities of torso model used to perform in-silico pace-mapping. See also Plancke et al.*(107).

The patient did not have a visible, structural heart disease. In order to virtually induce and simulate sustained, monomorphic post-infarct VTs, which require a region of structural remodelling, three detailed infarct anatomies were mapped onto our human torso model from existing high-resolution 6-week chronic infarcted porcine datasets, resulting in three final torso meshes. The interpolation was performed by computing universal ventricular coordinates (UVC)(182) on our torso mesh, and on the porcine meshes. As illustrated in **Figure 5.2**, UVCs describe a ventricular mesh using three parameters: z—normalized distance between apex (0) and base (1) along the long axis, ρ —normalized distance between endocardial (0) and epicardial (1) surfaces along the short axis, and ϕ —circumferential rotation around the long axes of the LV and RV. The infarcted porcine dataset was acquired in a previous study of our group(183) from LGE-CMR imaging, and consisted of dense fibrotic and BZ regions as shown in **Figure 5.3A-C**. The three infarct anatomies (named Scar 1, 2 and 3) had clear, structured isthmuses, and were known to successfully sustain monomorphic VT in previous porcine experiments(183). An established rule-based approach(182) was use to generate realistic fibres on the biventricular mesh.

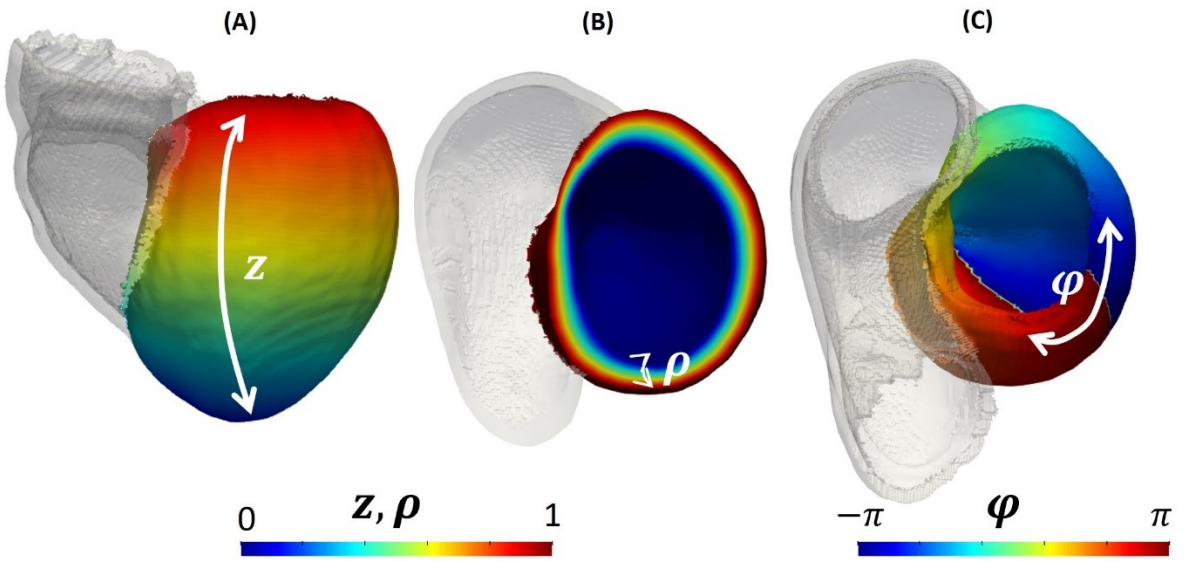

***Figure 5.2**. UVC on left ventricular mesh. (A): z coordinate describes distance between the apex and the base (of the LV in this case. (B): ρ describes the distance between the endocardial and epicardial surfaces. (C): φ describes the angle from the septum.*

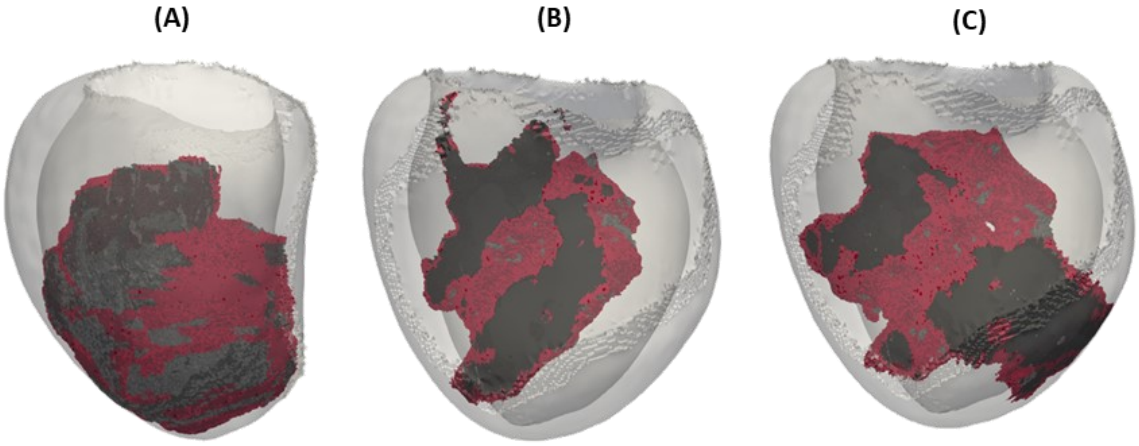

***Figure 5.3**. Infarct anatomies within our human ventricular mesh. Three high-resolution LGE-CMR datasets from porcine were mapped onto our human heart mesh, and were primarily located in the LV in, or in close proximity to, the septum. Scar 1, 2 and 3 are shown in (A), (B) and (C), respectively, all with clear and structured isthmuses in the BZ (in red), framed by dense fibrotic tissue (in dark grey). The healthy myocardium is in white.*

5.2.3 Post-Infarct VT Modelling

To compute extracellular potential maps over the full torso mesh, the pseudo-bidomain formulation within CARP(104), introduced and described in **3.1.2 Mathematical Representation of Cardiac AP**

Propagation, was used. These maps were then used to compute 12-lead ECGs and implanted device EGMs as described later.

Post-infarct VT episodes in the three infarcted ventricular meshes were initiated by using an S1S2 protocol. This consists of pacing the heart with n number of beats (S1) at a certain cycle length. Then, a premature beat (named S2) with a certain coupling interval (CI) is delivered.

By reducing the CI between S1 and S2, a temporary conduction block can form between the tail of the first wave, and the wavefront of the second (due to refractoriness of the tissue), facilitating initiation of a VT circuit. S1S2 protocols are widely used in clinical settings, and in modelling scenarios, to induce the tachycardia. In this study, due to computational constraints, we only utilised one S1 and one S2, separated by a CI of $365ms$, optimised to induce unidirectional block and initiate re-entry. Each infarct geometry was paced with this S1S1 protocol from either an apical or basal location to generate two morphologically-different VT circuits. The TT2(95) described in **3.1.1 Mathematical Representation of Cardiac AP in a Cell** was used to represent ventricular EP. The model had been previously used(184,185) to simulate torso ECGs and intra-cardiac EGMs to closely resemble clinically recorded signals. Cardiac tissue conductivities in the intra- and extracellular spaces were $0.19\ S/m$ and $0.7074\ S/m$, respectively, along the fibre direction, and $0.0371\ S/m$ and $0.1332\ S/m$ transverse to the fibre direction(186). These conductivities resulted in physiological conduction velocities (CVs) of $\sim 0.54\ m/s$ (along fibres) and $\sim 0.15\ m/s$ (transverse to fibres). On the other hand, the conductivities in the BZ of the infarcts were decreased to $0.0098\ S/m$ and $0.00353\ S/m$ in intra- and extracellular spaces, respectively (isotropic), and the corresponding CV was $\sim 0.15\ m/s$ (25). In addition to these modifications, to induce stable monomorphic VT episodes, sodium and potassium ion channel conductances were modified in the BZs as in a previous study(187); GNa, rapid (GKr) and slow delayed (GKs) potassium conductances were decreased to 38%, 30% and 30% of their full capacities, respectively. As seen in **3.1.1 Mathematical Representation of Cardiac AP in a Cell**, tissue depolarisation and repolarisation are primarily driven by sodium and potassium ion currents,

respectively, and by reducing GNa, GKr and GKs, we effectively prolonged the AP duration (APD) in the infarct BZ. As a direct consequence, excitability of the BZ tissue was reduced, facilitating the generation of unidirectional block and leading to re-entry. After induction, to be able to maintain sustained and stable VTs, potassium conductances GKr and GKs were increased back to healthy cardiac values, as performed by Pashakhanloo et al(188).

5.2.4 ECGs and EGMs Recordings

12-lead ECGs of the simulated VTs were computed from extracellular potentials recorded on the skin of the torso models by positioning the electrodes as per common clinical practice, shown in **Figure 5.4A and F**. A generic implanted device was modelled as shown in **Figure 5.4B**. Initially, we considered a standard single-coil ICD with far- and near-field sensing vectors (between the ICD CAN and RV coil, and between RV tip and ring, respectively). Then, we also modelled signals obtained from a quadripolar biventricular CRT-D, following Boston Scientific standard guidelines(80,189).

The device had a RV apical lead, with an SVC coil, as well as RV coil for far-field sensing, and RV tip and ring previously mentioned for near-field. The coils were modelled similarly to (23). An additional lead was modelled through the coronary sinus to sense LV epicardial activity through four $4mm$ in diameter electrodes (LV tips), at $7.5\ mm$ spacing. The CAN of the device was placed close to the left clavicle, and approximated to a single point. With this set-up, 8 different EGM sensing vectors were calculated, as shown in **Figure 5.4F**: far fields CAN-SVC, CAN-RVcoil, SVC-RVcoil and then near-fields RVtip-RVring and each of LVtip-RVtip.

5.2.5 In-Silico Pace-Mapping

To generate in-silico pace-maps for all simulated VTs, the biventricular meshes were paced from 20-30 locations around the infarcts. Utilising the pseudo-domain formulation as above, 12-lead ECG and EGM signals were computed for each pacing site. These time-series data were then compared against

the simulated VT ECGs and EGMs to compute conventional correlation maps and reference-less correlation spatial gradient maps as described in **4.1 Pace-Mapping.**

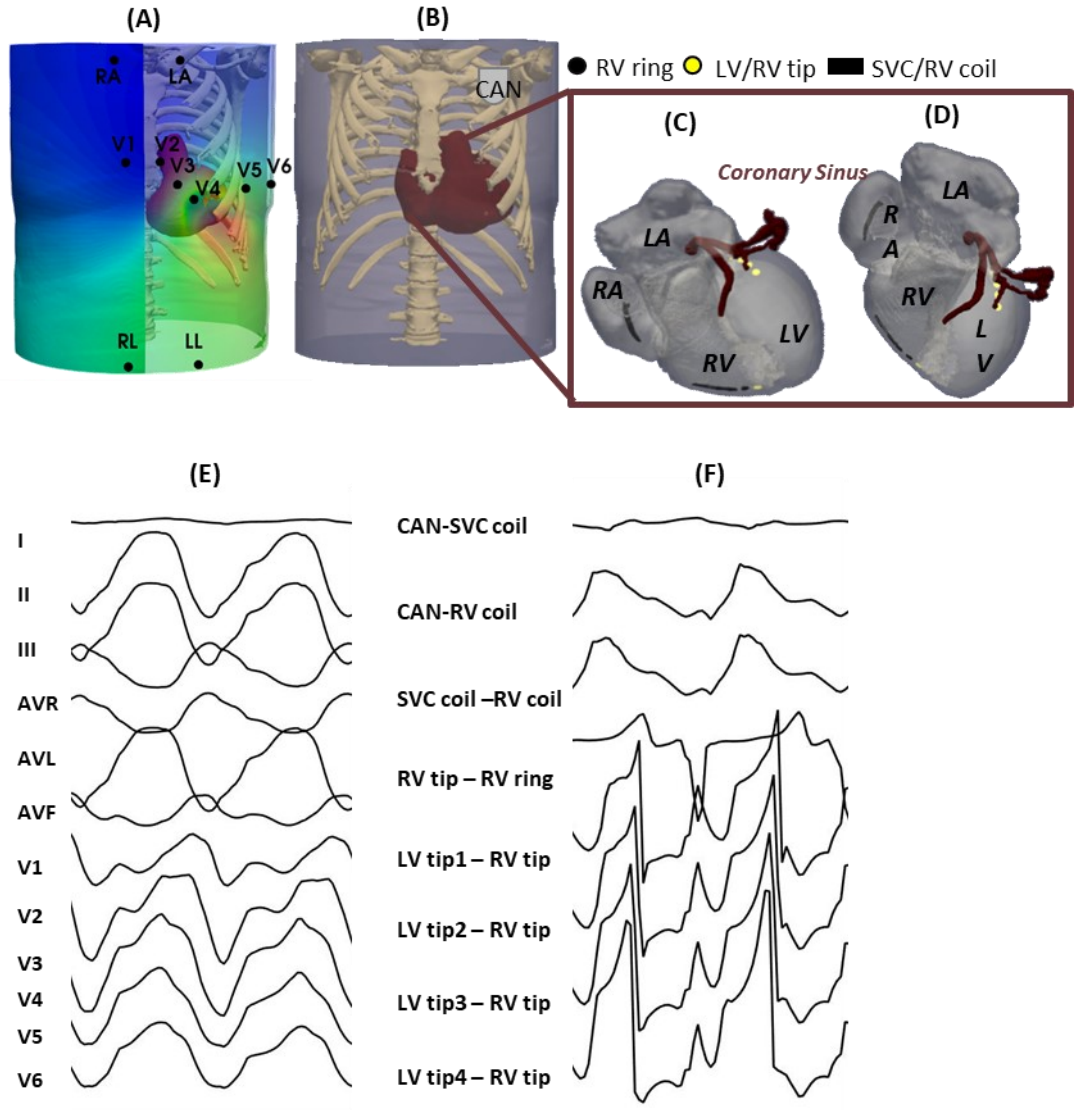

Figure 5.4*. ECG and EGM modelling for in-silico pace-mapping. ECG leads and implanted device configuration can be seen in (A) and (B)-(D) respectively. Example of 12-lead ECGs of a VT episode is shown in (E), and corresponding EGM signals in (F). The VT episode was induced in Scar 3 (apical stimulation).*

Briefly, for the creation of conventional correlation maps, each set of paced ECG and EGM signals were aligned to the target VT according to highest cross correlation in each lead. QRSs of both paced and VT signals were extracted and then standard CCs computed. For each pacing location, the final correlation value was computed differently between ECG and EGM pace-maps (PM). For ECG PMs, as

done clinically, the average of the highest 10/12 leads ECG CCs was computed. For EGM PMs, three values were investigated: the average of all 8 leads, best 6/8 leads and 2 leads EGMs (as previously done). After a correlation value was found for each pacing location, a linear interpolation was performed to create maps across the meshes.

To create reference-less correlation spatial gradient maps (S-PM), we followed a similar pipeline but CCs were computed between each pacing signal and its neighbouring points (within a radius of $20\ mm$). The mean of all leads was then divided by the distance between two points, as in **Equation (4.2)**, and results were interpolated by finding the middle point of each pair of pacing locations, similarly to **4.1 Pace-Mapping**. We also created S-PMs for different search radii ($10\ mm$, $30\ mm$ and $40\ mm$) to investigate how the inclusion of closer or farther neighbouring points influenced the final isthmus localisation. As mentioned in the previous Chapter, conventional pace-mapping allows to identify exit and entrance of a VT re-entrant circuit, whereas reference-less maps highlights abrupt changes in QRS morphologies between neighbouring points that can signify the presence of a slow conducting isthmus.

The principles behind (conventional) pace-mapping approach are illustrated in **Figure 5.5**. The local activation time (LAT) map of a simulated VT episode and corresponding 12-lead ECG traces are shown in **Figure 5.5A** and **B**. The ECG traces in **Figure 5.5C** and **D** of two different pacing locations show the difference in QRS morphologies and CCs between pacing proximal to the exit site (black dot – CC of 94%) and distal to it, near the isthmus entrance (red dot – CC of -31%).

In addition, we sought to investigate the utility and power of in-silico pace-mapping to perform different types of pacing procedures. In clinical practice, pacing procedures can only be epicardial and/or endocardial. Here, we assessed how endocardial-only, epicardial-only and intramural (3D) pacing would influence exit site localisation in simulated conventional PMs. To do this, we paced the

BZ of Scar 2 in the endocardium only, and in the epicardium only, and computed and analysed corresponding PMs with the 3D PM previously generated.

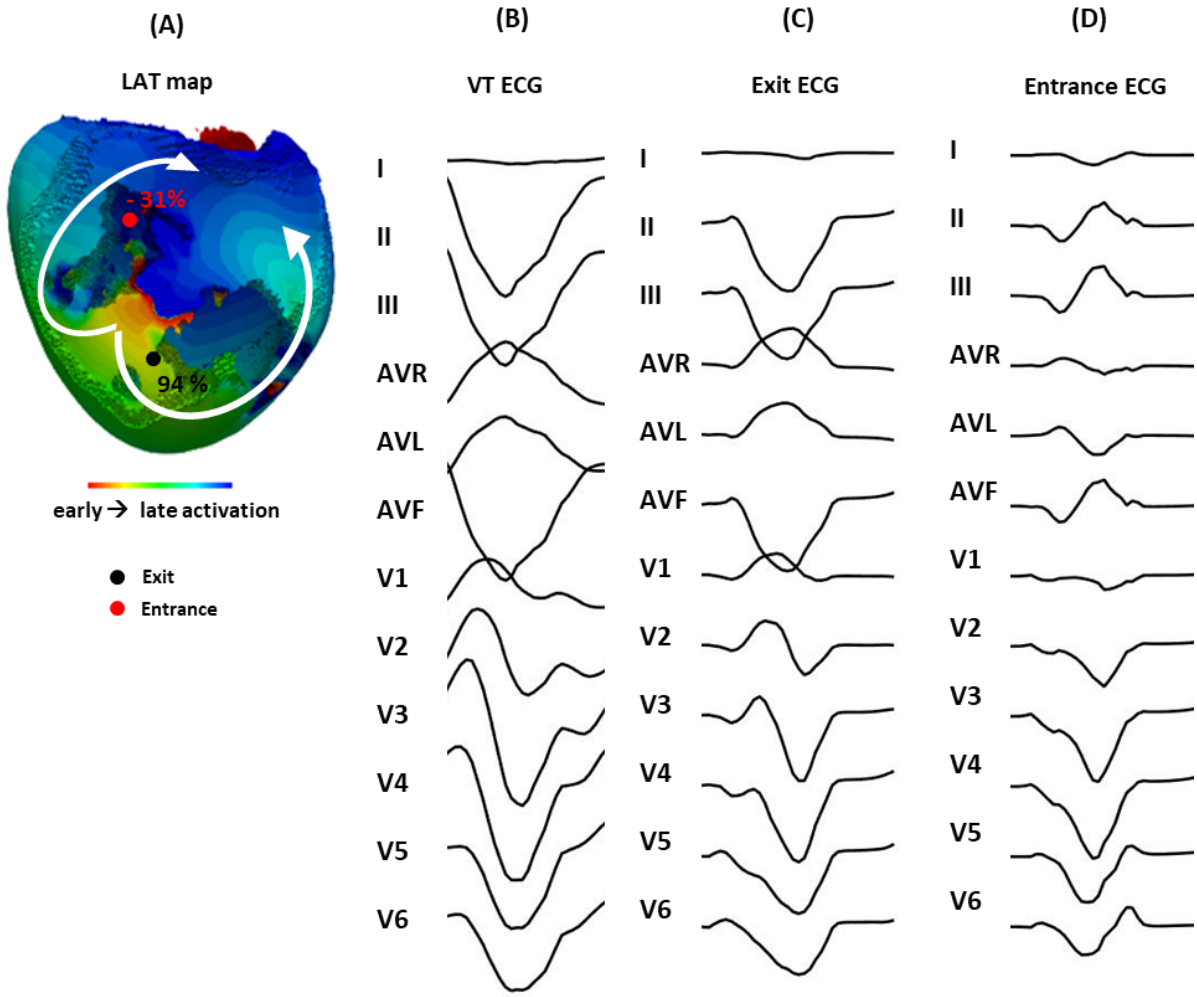

Figure 5.5. *Principles of conventional pace-mapping using our in-silico results. (A) shows a LAT map of a simulated VT episode, with corresponding 12-lead ECG in (B). Early activation is shown in red, signifying the circuit exit site, and late activation in blue. Pacing in proximity to the VT exit site (black dot in the LAT) returns a 12-lead ECG, shown in (C), similar to the reference VT ECG. Conversely, pacing at the entrance of the isthmus (red dot in the LAT) returns a different QRS morphology (12-lead ECG in (D)) in comparison to the VT ECG.*

Furthermore, we inverted Scar 2 using the UVC ρ to obtain a sub-epicardial infarct (as opposed to sub-endocardial, as in the original porcine data). Another VT episode was induced in this modified scar, following apical pacing as before.

5.2.6 Data Analysis

All simulated PMs were visually inspected to derive exit, entrance and slow conducting isthmuses for each VT episode. The identified sites were then compared against the LAT derived for one cycle of each VT episode. Kernel density distributions for each correlation map were also computed to further analyse CCs across different VT morphologies.

5.3 RESULTS

In this Section, we will first analyse the morphologies of the post-infarct VT episodes and corresponding LAT maps to establish a ground truth for the comparison and validation of the in-silico pace-maps. Then, we will look at the conventional and reference-less correlation maps generated from the simulated ECG and EGM signals, and derive exits, entrances and isthmuses. Finally, we will investigate the power of 3D in-silico pace-mapping to distinguish epicardial, endocardial and/or intramural origins of a VT.

5.3.1 VT Morphology

We successfully induced 6 different episodes of monomorphic VT with physiological mean cycle length (CLs) $373.17 \pm 26.51\, ms$ across the different infarcts. Corresponding LAT maps (**Figure 5.6A**) were used to carefully analyse and annotate circuit pathways, exit and entrance sites, and slow conducting isthmuses of each VT. One episode had the characteristic figure-of-eight pattern, with one major isthmus (apical stimulation of Scar 3). The other episodes had more complex morphologies, with multiple possible channels of slow conduction. For each scar morphology, patterns and periods of the VTs were different when performing the S1S2 protocol from different locations.

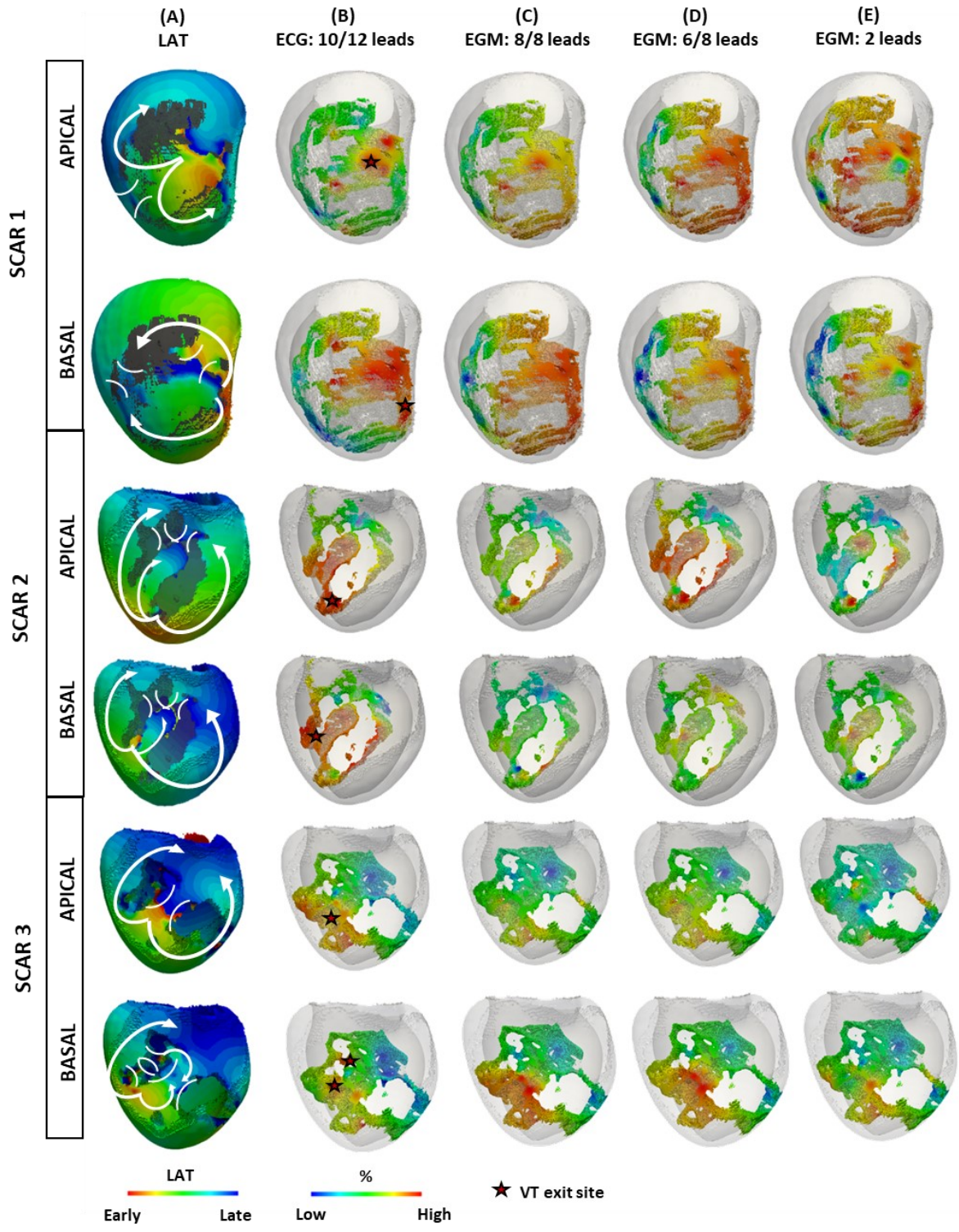

***Figure 5.6**. Summary of VT morphologies and in-silico, conventional correlation maps. (A): shows LAT maps (early activation in red, late in blue) for apical and basal stimulation of Scar 1,2 and 3 – epicardial view. The direction of the circuits (from exit to entrance) is here indicated by white arrows, whereas potential isthmuses are shown with inverse round brackets. For each VT episode, corresponding conventional ECG PMs and EGM PMs are shown in (B), (C), (D) and (E). (B): shows conventional correlation maps generated by first computing correlation coefficients for each lead between QRS complexes of different*

pacing locations and the VT QRS (after aligning the signals). Then, the highest correlations from 10 ECG leads were averaged . (C): shows correlation maps generated in a similar manner, after taking the average of correlations coefficients from all 8 EGM leads. (D): shows the average of the highest correlations from 6 EGM leads and (E) the average of 2-lead EGMs (far field CAN – RV coil and near field RV ring – RV tip).

5.3.2 ECG Conventional Correlation Maps

Figure 5.6B shows 10/12 leads ECG PMs for each VT episode. From these maps, exit sites were identified correctly with correlation values $> 85\ \%$, and were in agreement with the sites localised in the corresponding LAT maps.

Low correlation values in the PMs, which varied for each episode, corresponded to entrance regions, and medium-to-high and/or medium-to-low correlation regions identified isthmuses. As also reported in (141), establishing a specific cut off value for slow conducting regions is challenging due to higher variability in correlation values as compared to exit and/or entrance sites. This variability can also be seen in the kernel density distributions of each ECG PM (and EGM PM), **Figure 5.7.**

5.3.3 EGM Conventional Correlation Maps

Figure 5.6C-E shows EGM PMs**.** The VT exit sites were identified correctly from both 8/8 leads EGM PMs and 6/8 leads EGM PMs, in agreement with corresponding LAT maps and ECG PMs. In only one case, when the VT was induced via basal stimulation in Scar 3 (bottom row), the EGM PMs only identified one of the two exit sites. Entrances and isthmuses between 8/8 leads and 6/8 leads EGM PMs were comparable in all cases except in 6/8 leads EGM PM for the VT episode induced in Scar 2 via basal stimulation. On the other hand, conventional 2 leads EGM PMs seemed to underperform, with generally lower correction values and ambiguities in exit site localisation for Scar 2 and 3.

5.3.4 Reference-less Correlation Gradient Maps

Figure 5.8 shows ECG and EGM S-PMs for each scar morphology. Because S-PMs are generated from CCs between neighbouring points, and do not require a reference VT ECG and/or EGM, these maps are independent to the VT and specific only to an infarct pattern.

The search radius in these maps was $20\ mm$(145) (for the identification of neighbouring pacing points with which to asses correlations). As used in Odille at al. (145), a cut-off value > 3.2 %/mm signified possible slow conduction isthmuses, shown in orange/red in the S-PMs. The EGM S-PMs were constructed by averaging 8/8 leads CCs as these returned a better exit localisation performance in the conventional PMs.

In all ECG S-PMs, isthmuses were localised with mean value $> 3.56 \pm 0.40\ \%/mm$. These channels were also identified In 2/3 EGM S-PMs with mean value $> 3.75 \pm 0.35\ \%/mm$. In one case, there was still an overlap between ECG S-PM **Figure 5.8G** and EGM S-PM **Figure 5.8H** at $> 3.5\ \%/mm$, identifying 2/3 isthmuses. However, the EGM S-PM failed to identify one (highlighted by the black arrow). ECG and EGM S-PMs and corresponding kernel distributions for different search radii ($10\ mm$, $30\ mm$ and $40\ mm$) were also analysed, as shown for Scar 2 in **Figure 5.9**.

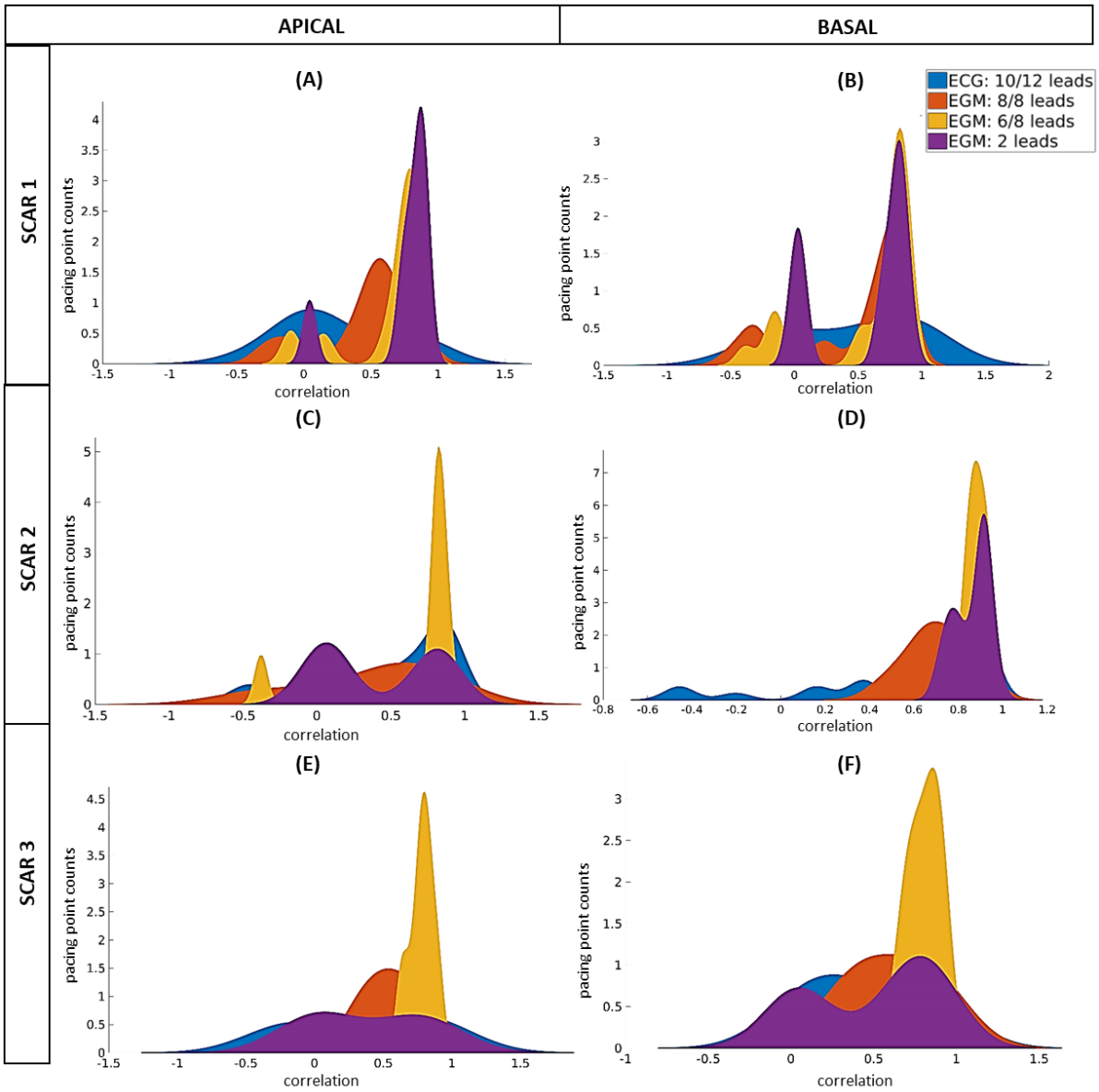

Figure 5.7. *Kernel correlation distributions of each in-silico ECG and EGM pace-map. (A) and (B) show CCs for Scar 1; (C) and (D) for Scar 2; (E) and (F) for Scar 3. In each histogram, CCs of 10/12 leads ECG PM, 8/8 leads EGM PM in orange, 6/8 leads EGM PM in yellow and 2 leads EGM PM are shown in blue, orange, yellow and purple, respectively. On the x-axis, correlation goes from lowest to highest, from left to right.*

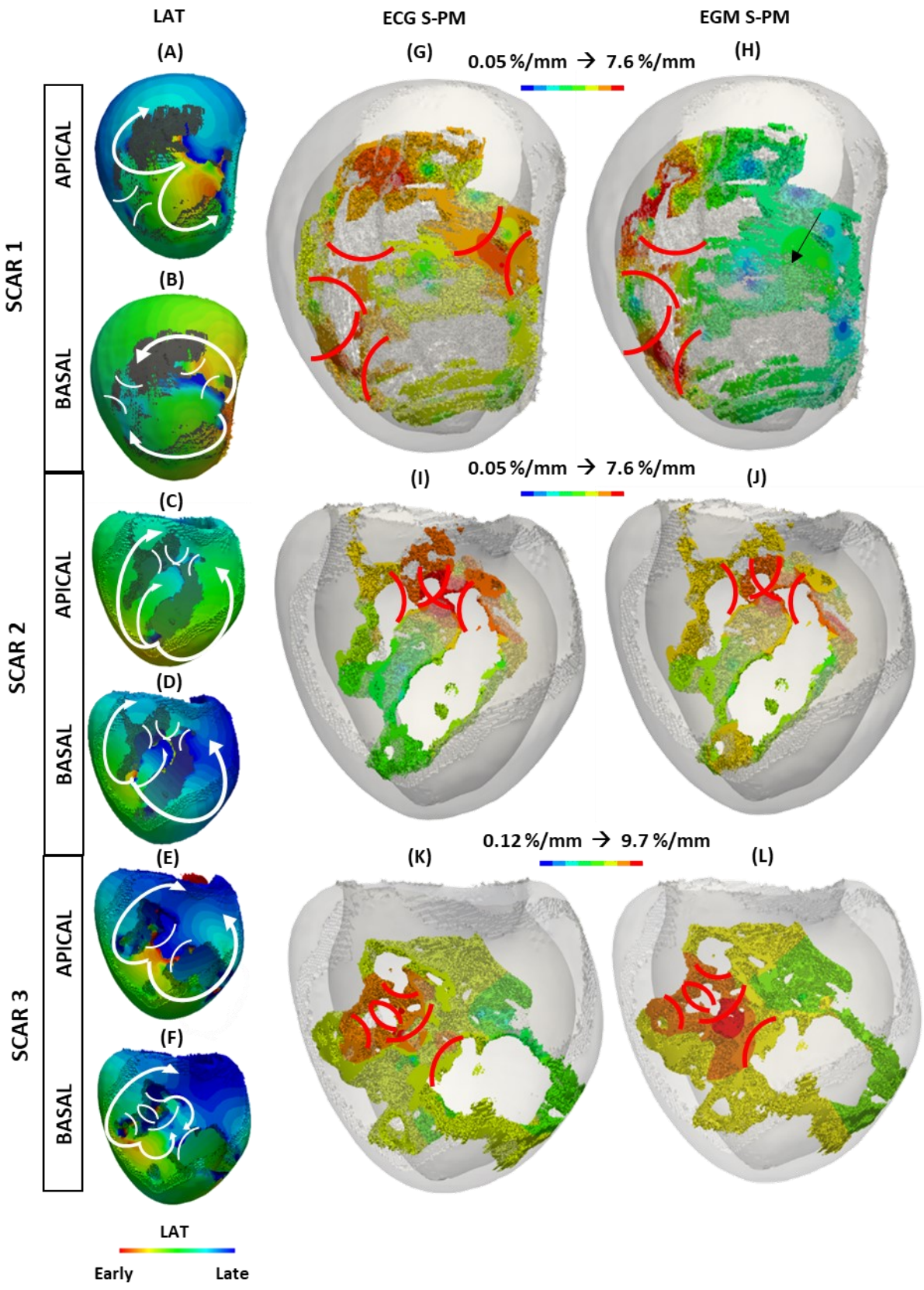

Figure 5.8. *In-silico, spatial, reference-less pace-maps for different scar geometries. (G) and (H) show 10/12 leads ECG S-PM and 8/8 leads EGM S-PM, respectively, for Scar 1, (I) and (J) for Scar 2, and (K) and (L) for Scar 3. In each map, the isthmuses*

can be found in the orange/red regions, above > 3.2 %/mm, and closely compare to the channels shown in the LAT maps (A) – (F) for each VT episode. In these, as above, early activation is in red, making possible exit of the circuit, and late activation in blue. The colour palette for the S-PMs goes from low %/mm in blue to high %/mm in red (in logarithmic scale here for ease of visualisation).

5.3.5 Endocardial vs Epicardial vs 3D Pacing

The utility of in-silico pace-mapping becomes more apparent when investigating the differences between endocardial, epicardial and 3D pacing (pacing from transmural locations). Conventional 10/12 leads ECG PMs and 8/8 leads EGM PMs from transmural, endocardial-only and epicardial-only pacing of Scar 2 are shown in **Figure 5.10**.

Here, both 3D and endocardial pacing identified all exit sites correctly, for both VT episodes, whereas epicardial pacing failed in the EGM maps. It is important to mention that the exit sites for these two VT episodes were located endocardially.

Next, we investigated the efficacy of different pace-mapping techniques (i.e. epicardial, endocardial or transmural) to identify the correct location of a VT exit site across the myocardium. The VT induced in the inverted Scar 2 had an exit site located between the mid-myocardium and the sub-epicardial regions, as shown in **Figure 5.11A**. The 10/12 leads ECG and 8/8 leads EGM PMs for this episodes are shown in **Figure 5.11B-D** and **Figure 5.11E-G**, respectively, for 3D, endocardial and epicardial pacing.

In this case, transmural pacing outperformed endocardial pacing in the 8/8 leads EGM PMs (higher correlation values in the former), whereas small variations were present in the ECG PMs for the different pacing procedures. Interestingly, EGM PMs seemed to perform better than ECG PMs as the latter identified another exit regions towards the apical section of the scar, considered a false positive, which was not seen in the LAT.

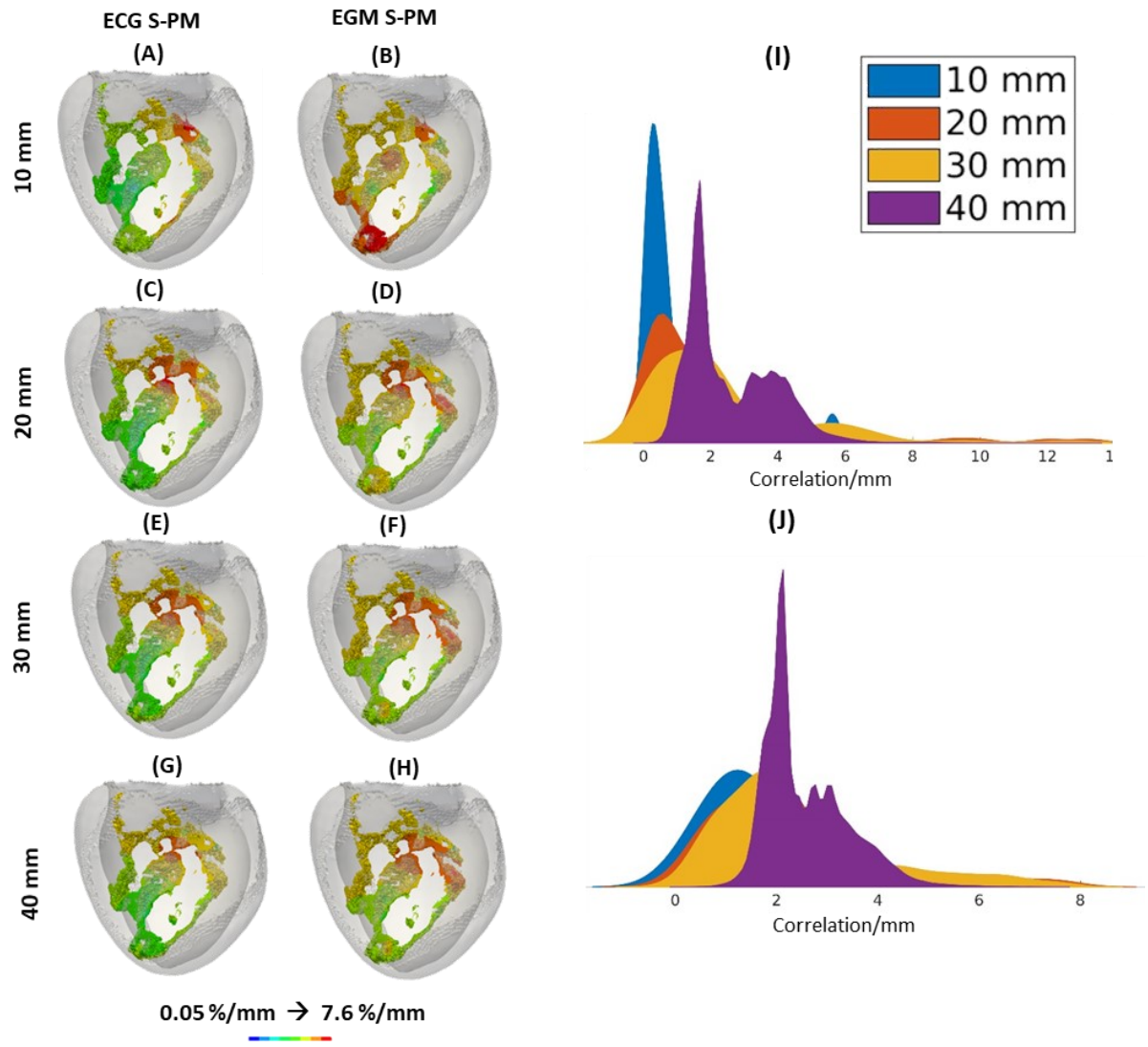

***Figure 5.9**. In-silico, spatial, reference-less pace-maps and kernel distributions for different search radii. (A), (C), (E) and (G) show ECG S-PM for Scar 2 for search radii 10 mm, 20 mm, 30 mm and 40 mm, respectively. The histograms of each of those distributions can also be seen in (I). Similarly, (B), (D), (F) and (H) show EGM S-PM in the same scenarios, with corresponding histograms in (J).*

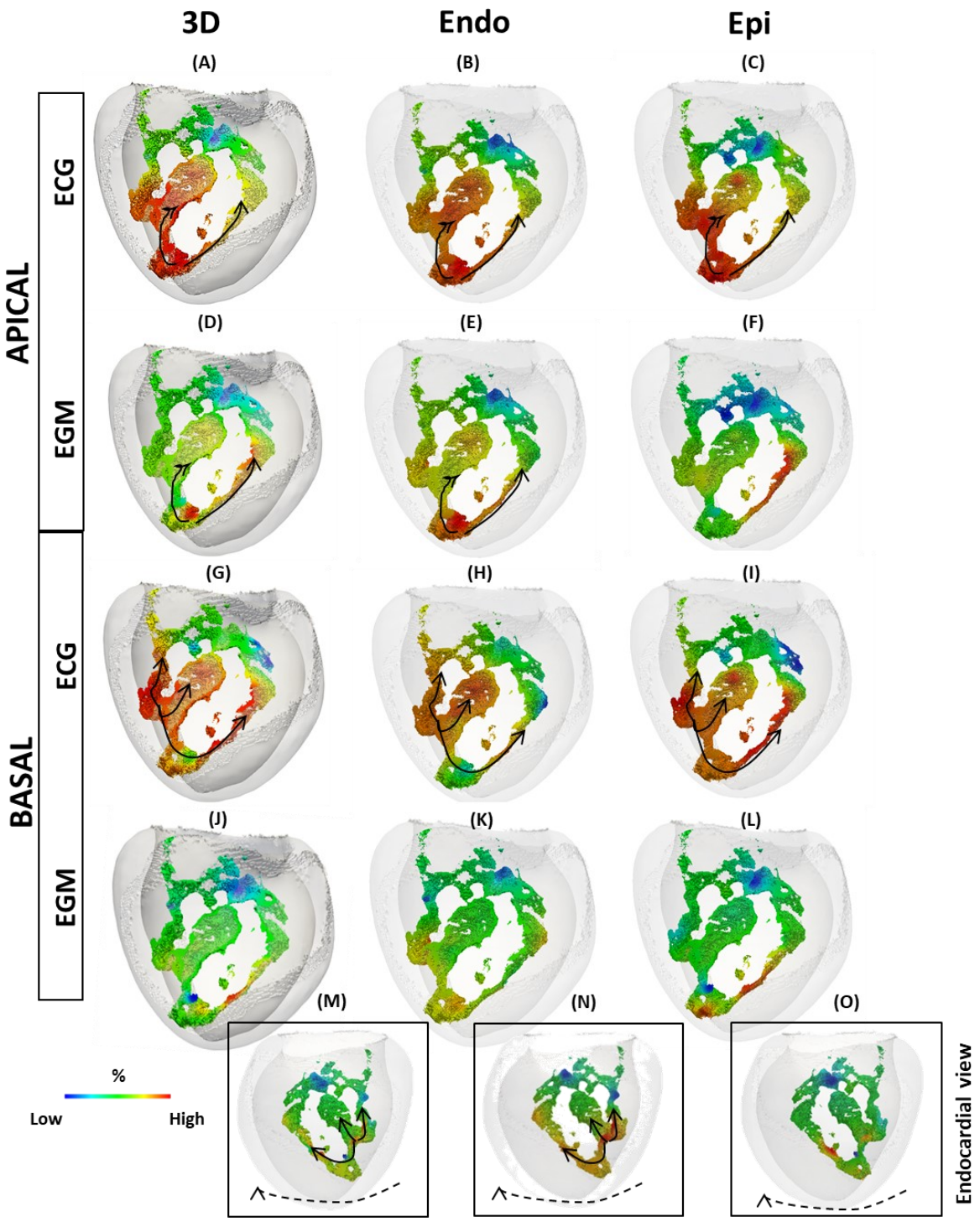

***Figure 5.10**. In-silico ECG and EGM pace-maps for pacing at different surfaces. Left column shows PMs for transmural/3D pacing, central column for endocardial pacing, and right column for epicardial pacing. The PMs shows high correlations in red, and low correlations in blue. Black arrows indicate the direction of the VT from the exit site correctly identified by the correlation map, with only one exception (F). In (J), (K) and (L), arrows are not present because the epicardial view shown here does not allow proper identification of the exit sites. The same maps from endocardial view in (M) and (N) are better at showing the underlying VT circuit trajectory.*

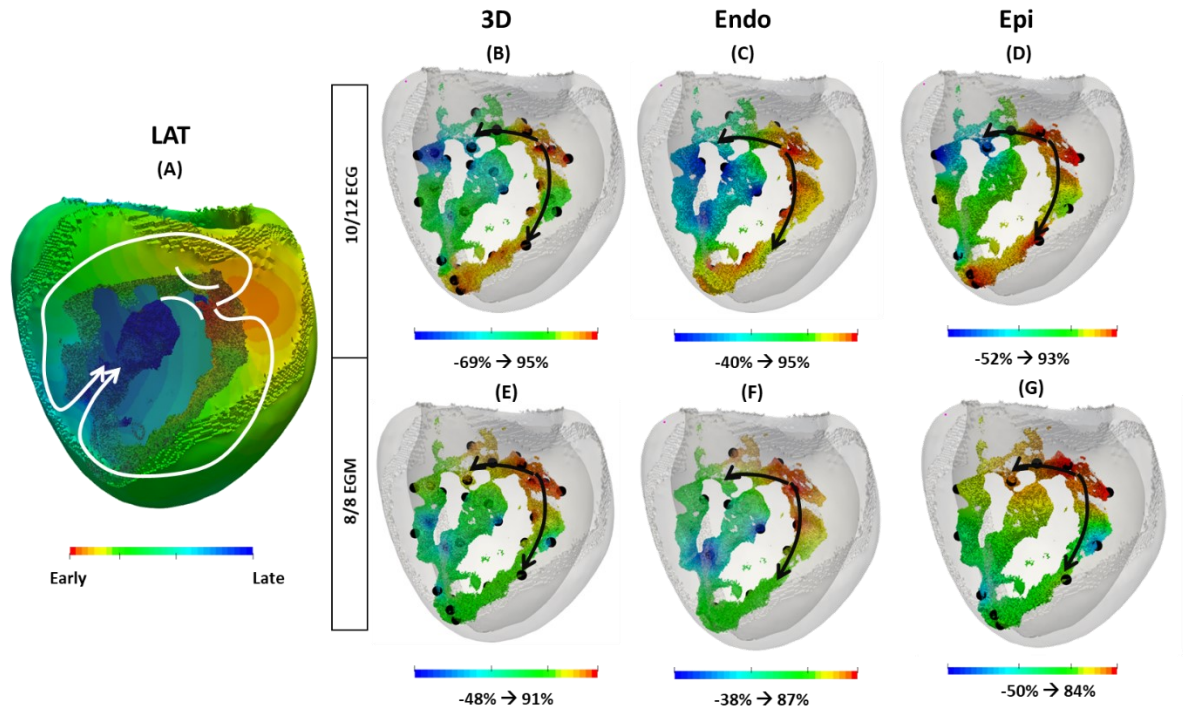

***Figure 5.11**. 3D vs endocardial vs epicardial in-silico pace-mapping in a sub-epicardial scar. (A) shows the LAT of the newly induced VT episode on the inverted Scar 2. (B), (C) and (D) show 10/12 leads ECG PMs after 3D, endocardial and epicardial pacing of the scar, respectively. Similarly, (E), (F) and (G) show the corresponding 8/8 leads EGM PMs. Rainbow palette for these PMs goes from low correlation (blue) to high correlation (red). Black arrows show the direction of the VT from the exit sited correctly identified in the PM, whereas the black dots indicate the pacing locations.*

5.4 Discussion

In this Chapter, a computational platform was created to perform in-silico pace-mapping and localise VT target sites non-invasively, in presence of different infarct anatomies. We demonstrated the possibility of using such a novel in-silico approach to acquire dense, fully transmural pace-maps, which could be of use for pre-procedure ablation planning and initial regionalisation of VT ablation targets. We explored how to potentially avoid VT induction and reduce mismatch between EP-induced and clinical VT episodes by creating pace-maps from multiple sensing vectors stored in implanted devices. Furthermore, we investigated the utility of novel reference-less pace-maps, which do not require a reference VT recording.

In this Section, we will explain the importance of the findings of this study for clinical purposes, and conclude with limitations and future directions.

5.4.1 Utility of Stored EGM Recordings in Conventional Pace-Mapping

VT exit sites identified by conventional ECG pace-maps were all in agreement with the VT patterns and morphologies highlighted on the corresponding activation maps. Moreover, multi-vector EGM pace-maps showed promising results compared to using 2 leads EGMs. As mentioned in the **4 Literature Review**, two studies(14,15) highlighted the potential of using 2-vector EGM recordings of the clinical VT as reference in clinical pace-mapping procedures, but found a lower spatial accuracy compared to conventional ECG maps. With this work, we showed how to increase that accuracy and improve VT exit site localisation by using multiple EGM vectors from a CRT-D. This could also help in reducing pace-mapping procedure times, lessen risk, and reduce the need for VT induction (as the VT episodes are recorded and stored in the device). Lastly, utilising the stored VT from implanted devices has the important advantage of representing a clinical VT, compared to VTs induced during programmed electrical stimulation (PES), whose clinical relevance is often uncertain.

Finally, it is worthwhile mentioning that, to save computation time, our pacing, pseudo-domain simulations utilised prior knowledge of known VT trajectories of all episodes to refine the initial choice of pacing locations. Without this knowledge, more extensive and computationally expensive pace-maps would be required. By simply examining isthmuses, we could theoretically identify the preferable pathways causing re-entry; however, often VT may arise due to less prominent and hidden scar channels that are not visible by eye. Computational simulations are therefore a valuable tool to 'tease-out' these functionally-relevant scar channels that are difficult to see from imaging data alone. Hence, our virtual platform may be used to improve the initial phase of pace-mapping, potentially alongside image-based knowledge(190), reducing standard clinical pace-mapping procedure times.

5.4.2 Complementary Information Provided by Reference-less Pace-Mapping

A previous study by Odille et al.(145) introduced the concept of reference-less pace-mapping, and the possibility of extrapolating information on slow-conducting isthmuses without requiring a reference VT recording. However, the study reported a quite high risk of false positives compared to conventional pace-maps. Previously, we demonstrated how EGM signals could indeed substitute the standard 12-lead ECGs used for conventional pace-mapping because, as they utilise stored VT recordings, they do not require VT induction and allow direct comparison with the actual clinical VT. However, the utility of EGMs for reference-less pace-mapping still remains unclear. Although EGM sensing vectors from implanted devices provide less overall spatial coverage than 12-lead ECGs, they do contain enhanced local information(77) due to their proximity to the heart. Therefore, in this work we explored the benefit of using both ECG and EGM recordings to help augment the localisation of slow conducting isthmuses correctly in the scenario of reference-less pace-mapping. In this Chapter, we showed that both ECG and EGM pace-maps returned similar results, identifying all major VT isthmuses; therefore, clinically, there may not be a great benefit in using EGM pace-maps over ECGs. However, since reference-less maps can be easily constructed in all cases without increasing procedure time (in a clinical setting) or simulation time (for in-silico frameworks, as in this study), they could be easily introduced in conventional pace-mapping to add potentially important information prior to ablation. For instance, once an isthmus is identified from reference-less gradient maps, the original correlation map may be utilised to understand the direction of the VT through the isthmus, propagating from low correlation areas (entrance site) to the high correlation regions (exit site). Finally, due to the fact that reference-less pace-mapping is still in the developmental stages, we also used our modelling framework to elucidate the dependence of the maps upon the radius of neighbouring points considered in the algorithm. The radii which consistently identified the VT substrate were between $20\ mm$ and $30\ mm$, in agreement with (145).

5.4.3 Utility of Transmural Pacing vs Endocardial/Epicardial

One of the greatest benefits of in-silico simulations is the possibility of testing and exploring scenarios that cannot be performed in clinical procedures. To this end, we investigated how pacing transmurally, endocardially-only and epicardially-only affected VT substrate delineation. Although no significant difference in VT localisation was seen between different pacing locations in ECG pace-maps, EGM pace-maps did differ during epicardial pace-mapping of an endocardial VT circuit; on the other hand, transmural and endocardial maps returned comparable results. This could be related to the fact that EGM sensing vectors are very localised to the heart, with a great dependence on endocardial leads. However, in the presence of a transmural VT circuit, transmural EGM PMs outperformed corresponding ECG PMs. These findings thus suggest that combining both endocardial and epicardial pacing in a single procedure would increase the power of corresponding correlation maps, and the ability to locate potential transmural isthmuses and/or exit sites, albeit at the expense of a longer and more involved procedure. It also underscores the utility of computational models in producing detailed in-silico pace-maps, which can automatically perform dense transmural pacing.

5.4.4 Limitations

The work presented in this Chapter has some limitations. We created only a single model from one patient, albeit with 3 separate physiological infarct morphologies represented within it. All scarred regions had clear and structured channels; patchier fibrotic areas may prove more difficult to sustain monomorphic VT and identify exit sites reliably. In addition, we did not capture more complex ionic remodelling effects that manifest clinically after cardiac injury (e.g. in presence of MI and/or heart failure)(191), or as a consequence of pharmacological treatment with anti-arrhythmic drugs. Changes in AP profile and duration, alterations in calcium homeostasis, downregulation of potassium currents and so on have been widely described to occur in the surviving myocytes of the infarcted heart(192,193). In this study, we only remodelled sodium, fast and slow delayed rectifier potassium conductances to facilitate VT induction. The absence of other effects, as well as the lack of modelling

the changes in ion permeation processes and gating mechanisms due to binding of a drug to ion channels and receptors, might affect clinical validation, especially in HF patients, which represent a significant portion of implanted device recipients(194,195). However, we believe that the simplifications and assumptions made in this study were of importance to create a pipeline reproducible in clinical settings, and general VT dynamics at a macroscopic level may still be reproduced accurately. In this regard, previous modelling studies (196,197) suggested the primary role of infarct anatomy over functional changes in the maintenance of scar-related VTs, demonstrating that VT localisation may not be as sensitive to EP variability. Nevertheless, it is important to recognise the limitations of the work presented in this Thesis in terms of EP variability, and the generally low number of scenarios investigated.

In the future, this study may be improved by performing simulations on a larger in-silico cohort. Although a more extensive cohort of torso models would allow greater insight into differences in device EGM recordings and different lead configurations across different heart morphologies, virtual pace-mapping is patient-specific, and the fundamental process should not be torso dependant, given that simulated signals are computed in a similar manner to recorded data. Hence, we do not believe that the final outcomes of this study would be affected when extending our virtual platform to other geometric torso models. Lead orientation of an implanted device might affect the resulting EGM-based pace-maps as five out of eight sensing vectors are bipolar, and thus more sensitive to wavefront direction. However, as previously mentioned, when reproducing this in-silico pace-mapping set-up in clinical settings, we would model the device according to the patient's device, minimising the possible biases between modelled and clinical EGMs. Variability in body compositions and lead configurations will be investigated in the following Chapters, supporting the previous statements.

To achieve clinical translation, as we will see in **8 Clinical Evaluation**, we will need and use real VT ECG (and EGM) data and compare it with the patient-specific simulated pace-maps. Although detailed imaging, with or without infarct information, as well as 12-lead ECG electrodes of a patient are

acquired routinely and would not represent an obstacle for clinical evaluation of this in-silico study, the collection of multi-vector EGM recordings from implanted devices may represent a challenge. However, implanted device technology, along with number of possible electrodes, is constantly evolving, suggesting that this is a promising avenue for incorporation into future multi-electrode device designs. Showing the applicability of our in-silico set-up in clinical settings will also be of importance to demonstrate that the results achieved in this Chapter did not solely stem from the comparison of simulated datasets generated with the same computational model.

At this point, it is worthwhile emphasising the qualitative nature of the definition of success in this in-silico pace-mapping study. The exact identification of exit sites from simulated VT data is not straightforward, and therefore the comparison between a pace-map and the underlying VT was based on visual inspection. It would be useful to develop more objective and accurate metrics to quantify such performance., and as we will see in the following Chapters, DL algorithms could aid in such a task.

The platform here presented relies on computationally demanding simulations for the acquisition of extra potential signals; the process could be simplified and sped up via the lead field method. In the following Chapters, we will see how in-silico pace-mapping could benefit from a more efficient computational environment to achieve clinical applicability. Finally, in this study we exclusively looked at highly detailed infarct imaging data, which might not be always available for ablation patients. In the final Chapter of this Thesis, we will explore the influence of image quality on the performance of in-silico pace-mapping for the identification of clinical VT ablation targets.

5.5 CONCLUSION

In this Chapter, we have demonstrated that in-silico pace-mapping may be used, either directly with standard 12-lead ECG data of the induced VT or in conjunction with pre-recorded EGMs from implanted devices of the clinical VT, for safe and robust localisation of VT ablation targets in pre-procedural planning, in particular in identifying epicardial versus endocardial VT origin to guide access.

Additional utility may be found from integration with the novel 'reference-less' pace-mapping methodology. This study is thus important in the context of this Thesis as it shows how implanted devices can be modelled and utilised to guide VT localisation with comparable results to ECG-based modalities. In the following Chapters, we will improve on the limitations of this study, including additional torso models, investigating different lead configurations and expanding on aiding VT treatment planning by combining computational simulations with AI algorithms for faster localisation, more in-keeping with a clinical workflow.

6

AUTOMATED FOCAL VT LOCALISATION

Previously, we showed the utility of implanted device EGMs to aid conventional ECG-based pace-mapping and improve ablation planning. In this Chapter, we begin to combine computational simulations with DL approaches to automate the localisation of focal VTs from such device EGMs. After presenting the motivation of this Chapter in Section 6.1, building upon the Literature Review presented in Chapter 4, Section 6.2 describes how advanced computational modelling can be utilised to generate a vast library of ECGs and EGMs of focal VTs, and how these can then be used for training and testing of different AI architectures. Then, Section 6.3 investigates the performance of the DL architectures in localising VT episodes under different computational scenarios, and the Chapter concludes by illustrating the importance of this work in the context of this Thesis, presenting limitations and future directions (Section 6.4 and 6.5). The work presented in this Chapter has been published in the Frontiers of Physiology journal(198).

6.1 INTRODUCTION

In the previous Chapter, we investigated the possibility of creating an in-silico platform to perform pace-mapping and localise critical sites of post-infarct VT episodes non-invasively, as well as attempting a further description of the underlying VT dynamics. We showed how implanted device EGMs represent a valid diagnostic tool to aid ablation planning and guide initial localisation of the tachycardia for more invasive mapping strategies, improving safety and speed of the procedure itself. Now, given that the *in-silico* pace-mapping pipeline proposed is still relatively computationally demanding, the initial localisation of a VT episode would highly benefit from automation, and more efficient computational approaches. As seen in **4 Literature Review**, over the last decades, computer algorithms have been developed to identify origins of focal and/or scar-related VTs directly from the ECG. However, all of these methods have their limitations. In this Chapter, we will focus on improving the automation of focal VT localisation, in particular of PVCs.

PVCs are early depolarizations of the myocardium originating in the ventricles and are associated with increased risk of sudden death, especially in presence of structural heart disease(199). However, over the last decade, evidence has shown that also in absence of structural heart disease the occurrence of frequent PVCs can lead to left ventricular dysfunction (PVC-induced cardiomyopathy)(200), and may also trigger polymorphic VT and/or degenerate into VF(201). PVC ablation has been steadily increasing in popularity over recent years(202), however the acquisition of accurate PVC activation maps to guide the procedure is challenging in 30% of patients for which the brief period of an ECG may fail to capture the ectopic beat(s)(203,204). Hence, utilising the recorded episodes stored in implanted devices may increase ablation success rates in those patients, as well as in cases where more invasive mapping strategies cannot be performed.

In **4.2 Targeting Focal VTs**, we introduced studies by Sapp et al.(50), Zhou et al.(160,162) and Yang et al. (159) that attempted localisation of focal VT SoOs using AI. Whereas they all obtained impressive performances, in the range of $\sim 5 - 12mm$ localisation errors, (50,160,162) heavily relied on EAM

data to tailor such localisation to individual patients, not taking advantage of computational modelling. On the other hand, Yang et al. (159) exploited, and combined, EP modelling with DL, and was one of the first to use CNNs to extrapolate information within ECGs, and establish relationships with regions of cardiac activation. However, their method was restricted to ECGs, and as seen previously, the literature lacks further investigation into the power of EGM recordings for AI-based localisation of focal VTs. In addition, the computational pipeline presented by (159) does not utilise rapid EP formulations, such as the RE model, and depends on a Cartesian localisation of the VT episodes, that is not optimal for patient-specific localisation. Moreover, Yang's computational-AI pipeline does not translate easily to clinical settings; a patient-specific torso needs to be registered to a template and the clinical ECGs modified accordingly before clinical testing can be performed.

In this study, we set out to address those limitations to automate focal VT (PVC) localisation by: 1) generating a more efficient and physiological computational environment using RE(100) and LF(102,106) formulations; 2) demonstrating comparable localisation between ECG-based and EGM-based AI localisation; and 3) introducing a novel CNN algorithm that utilises local, ventricular-specific coordinates(182). Finally, we will conduct a thorough computational sensitivity analysis to further understand how noise, changes in ECG electrodes and implanted device configurations, and differences in body composition can influence the AI network. This investigation will be extremely useful to achieve clinical translation in the future.

6.2 METHODS

We begin this study by describing the methodology that enabled the automation of focal (PVC) VT localisation from ECG and EGM traces. Firstly, we will develop a fast and efficient computational pipeline for the generation of such traces. Then, we will use such simulated ECG and EGM datasets to train different AI architectures, and investigate their localisation performance under different

computational scenarios. In the following paragraphs, we will first give an overview of the platform, and then describe each stage in more detail.

6.2.1 Overview

Figure 6.1 illustrates the pipeline of this study. Briefly, a previously generated 3D torso model (Step 1) (see **Chapter 5**) was used to rapidly simulate focal paced beats across the LV. The RE formulation described in **3.1.2 Mathematical Representation of Cardiac AP Propagation** was used to facilitate fast and efficient simulations. These were then combined with the LF matrices computed on the standard 12-lead ECG electrodes and manufacturer-guided implanted device RV and LV leads (Step 3) to reproduce accurate ECG and EGM traces of the paced beats (Step 4). Adapted versions of the CNN architectures proposed by (159) (Step 5) and novel networks (Step 6) utilising UVCs were used to localise the paced beat origins from the processed, simulated ECG and EGM traces (Step 7).

6.2.2 Computational Model Preparation

In this study, we used the healthy 3D torso model previously generated in **Chapter 5** with no infarcted geometries mapped from the porcine dataset. However, the resolution of the biventricular mesh was modified to decrease computational time without a loss of physiological electrical signals, and thus the average ventricular edge length was increased to $738\ \mu m$. As before, a well-established rule-based approach was used to incorporate realistic fibre orientation into the myocardium, and UVCs(182) were computed to facilitate the development of a novel CNN specific to the ventricles, which identifies and constrains the localisation of the paced beats inherently within the myocardium.

To guide the collection of pacing locations, and generate training and testing labels for the CNN architectures, the LV was geometrically divided into 17 segments, according to the AHA guidelines, as illustrated in **Figure 6.2A-F**. Additionally, each segment was subsequently divided into four, for a total of 68 (**Figure 6.2G-H**) to improve localisation performance of the CNN. These 3D-segment models of the LV were also projected into the 2D generic 17-segment diagram by utilising UVCs, as illustrated in

Figure 6.2, to create patient-specific bull's-eye plots and facilitate visualisation of the predicted paced beats.

To replicate focal ectopic VTs across the LV segments, ~ 3767 randomly chosen, single stimuli paced beats (BCL of $400\ ms$) were simulated using the RE formulation(100) in CARP (**Figure 6.5A**). The cell model used was the TT2(95), and intra- and extracellular tissue conductivities were tuned according to the new mesh resolution to achieve physiological QRSs*(205)*; the specific values used were $0.185\ S/m$ and $0.6628\ S/m$ along the fibre direction, respectively, and $0.0493\ S/m$ and $0.1769\ S/m$ transverse to it. The resulting RE CVs were $0.5455\ m/s$ and $0.1802\ m/s$, along and transverse to the fibre direction. This tuning obtained results comparable to equivalent pseudo-domain simulations performed on the higher-resolution mesh in **Chapter 5.**

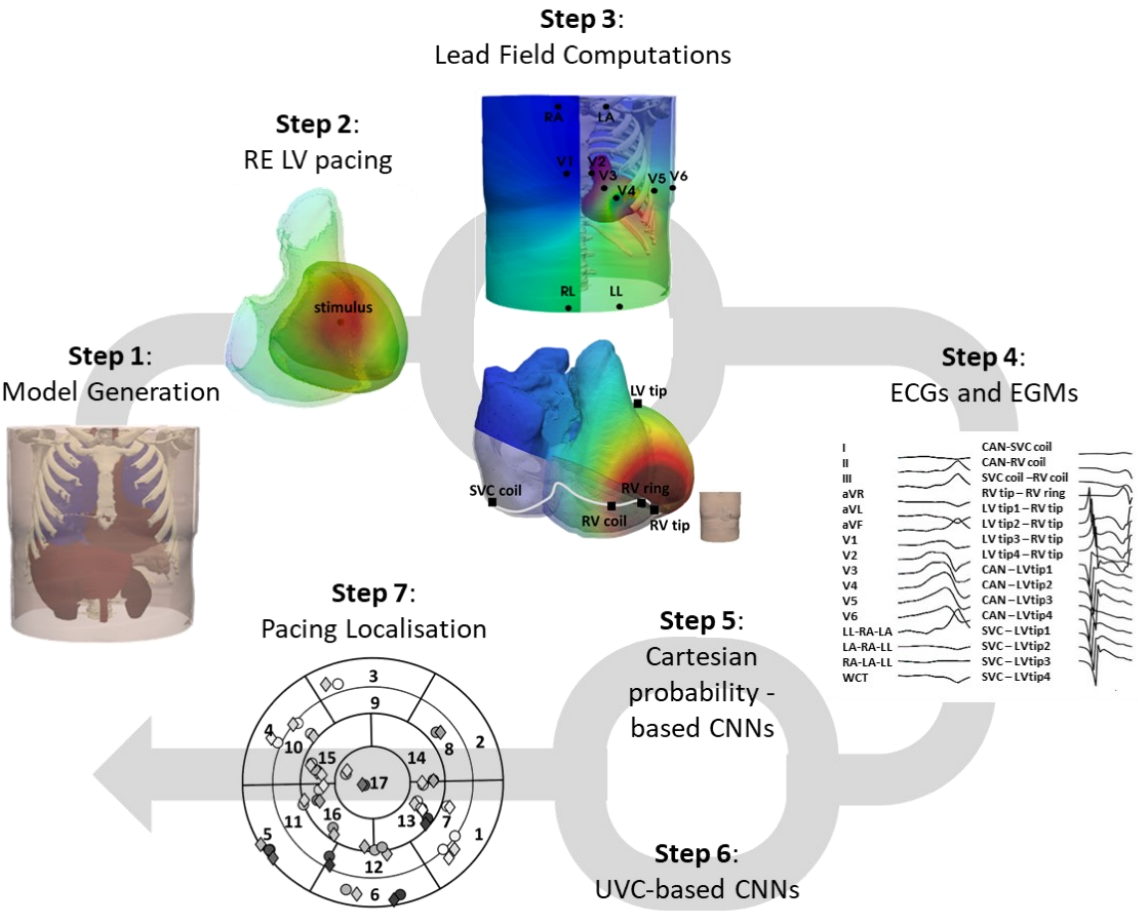

Figure 6.1. *Workflow for the automated localisation of focal VT episodes. A less refined mesh of the torso model generated in the previous Chapter (Step 1) is used to pace the LV from different locations, within a fast RE environment (Step 2). These*

solutions, in combination with the LF matrices (Step 3) computed on the ECG electrodes and implanted device EGM leads, allow to obtain a vast library of ECG and EGM traces (Step 4), which are used as inputs to two different CNNs (Step 5 and 6). Finally, the SoOs of the paced beats are localised and compared to the actual locations of the simulated beats (Step 7).

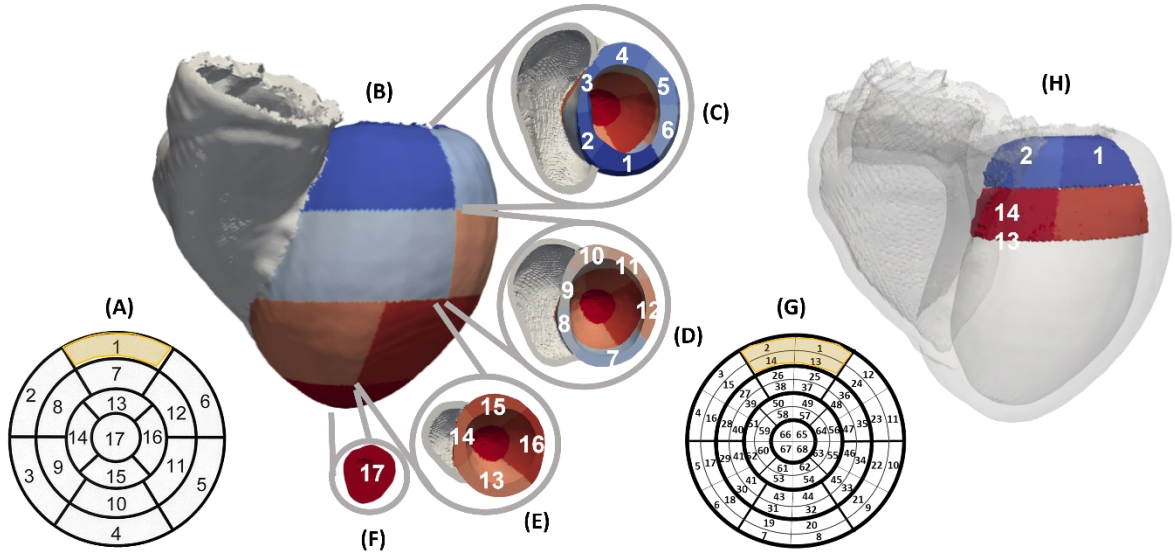

Figure 6.2. *Patient-specific LV segment models. (A) shows generic AHA 17-segment model, and (B) the equivalent patient-specific model. (C – F) illustrate short-axis view of basal, mid, apical segments, respectively. (G) shows an example of the novel 68-segment model in 2D, highlighting the equal division in four parts of each of the 17 segments, also illustrated in 3D in (H).*

Although different torso scenarios were investigated, as we will see shortly, the baseline set-up to compute ECG and EGM traces was similar to our previous study. The 9 ECG electrodes were modelled and positioned on the skin of the torso model as per common clinical practice (shown in **Figure 6.4A**), and the implanted device followed standard Boston scientific guidelines (**Figure 6.4B-D**). However, each sensing tip/coil of the device was approximated to a single point. To decrease computational time and power, the extracellular potential signals on these specific locations (ECG lead locations and implanted device sensing parts) were computed with the LF method(102) in CARP (**Figure 6.5B**). The resulting matrices were then combined with the simulated RE cardiac potentials of each paced beat to retrieve corresponding 12-lead ECG traces and 8-vector EGMs. The latter were chosen as a result of the successful in-silico pace-mapping study. Finally, additional vector combinations for both ECGs and EGMs, as illustrated in **Figure 6.4E-F**, were added to the standard signals to be able to train and test the CNN architectures (see **CNN Training and Testing**).

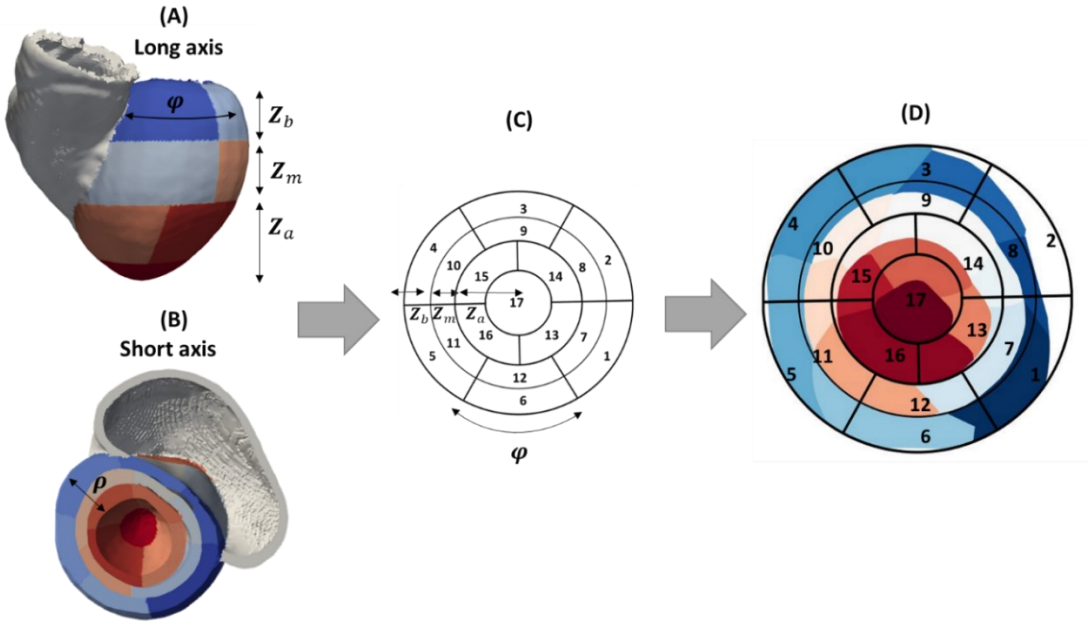

***Figure 6.3**. Construction of patient-specific bull's-eye diagram. (A - B) shows the 3D patient-specific 17-segment model, which can be projected onto the generic 2D representation (C) by considering UVCs φ and z, resulting in (D). Specifically, z, the longitudinal distance between LV apex and base, can be linked to the radius of the 2D diagram, separately for each basal (Z_b), mid (Z_m) and apical section of the model (Z_a). Similarly, along the short, spherical axis, φ can be used to divide the circle into "wedges". The colourbar shows segments 1 – 17 from blue to red.*

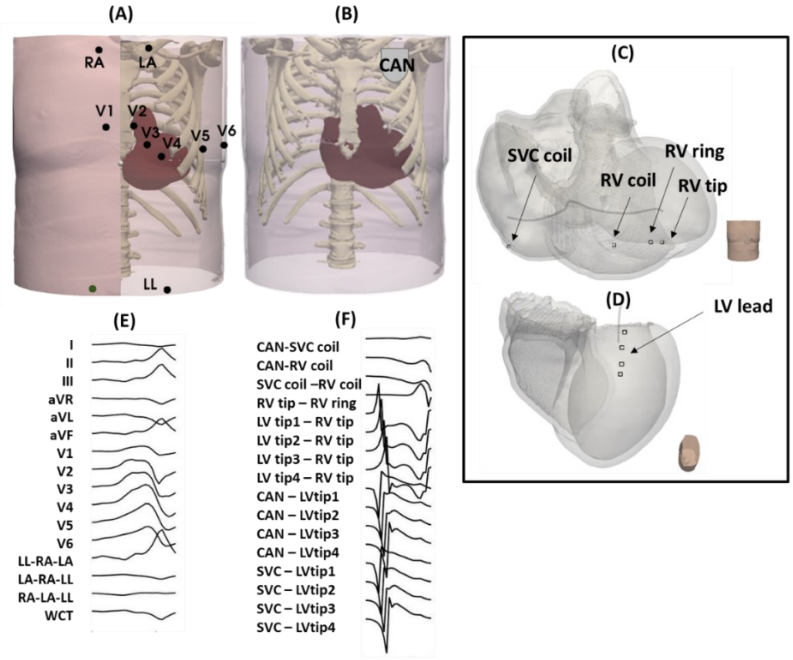

***Figure 6.4.** Torso setup for ECG and EGM modelling for automated focal VT localisation. (A): shows ECG electrodes, (B-D) implanted device configurations. Example of 16 combinations of pacing signals for training and testing are illustrated in (E) for ECGs and (F) for EGMs.*

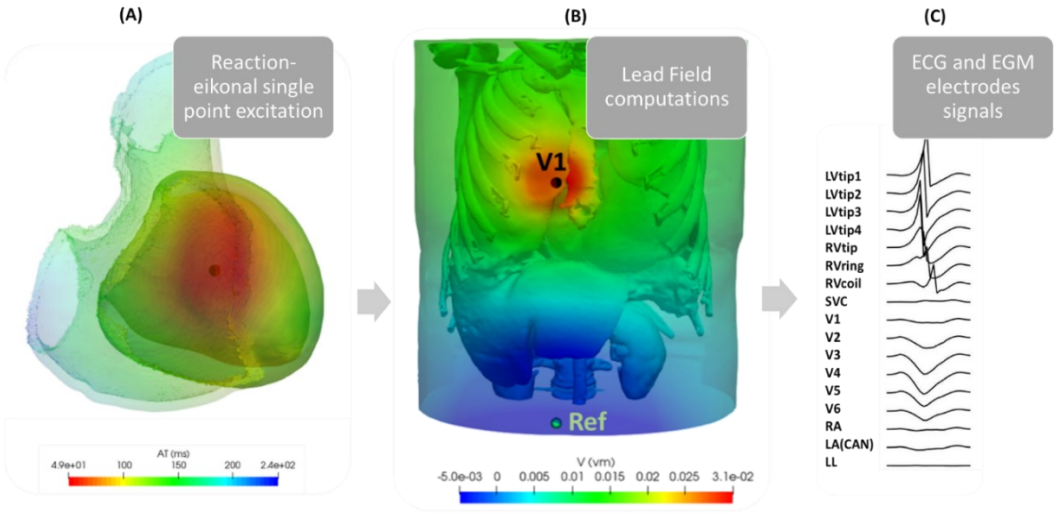

Figure 6.5. *Example of efficient simulation pipeline, combining reaction-eikonal and lead field formulations. Activation sequences of paced beats around the LV were computed with the RE model (example shown in (A)), and used in conjunction with LF matrices computed on the ECG and EGM electrode locations (example for V1 shown in (B)) to compute final extracellular signals (example in (C)).*

6.2.3 CNN Architectures

In this study, we developed two separate 2D CNN architectures, which used the same ECG and EGM traces as inputs to identify the location of a simulated paced beat (representing an ectopic VT), but differ in the way the output is computed and visualised. The first architecture, based on (159), locates the origin of a paced beat in Cartesian coordinates, after converting the outputs of the CNNs. We refer to this architecture as *Cartesian probability-based* in the remainder of the Chapter. The second architecture (*UVC-based*) utilises a regression and a classification CNN to locate the beat in UVC space, naturally constraining the final localisation of the focal source to the myocardium.

The structure of the existing *Cartesian probability-based* architecture was previously described (**Section 4.2.2**). Briefly, it consists of two 5-layer classification CNNs (two hidden layers alternating with two pooling layers, and terminating with a FC layer), one named *Segment* CNN and one *EpiEndo* CNN. *Segment* CNN classifies the segment in which the pacing beat originates, whereas *EpiEndo* determines the surface of origin (whether it is endocardial or epicardia). In our study, we developed

two separate *Segment* CNNs: one classified between 17 LV segments (i.e. CNN with 17 output neurons) and the other between 68 LV segments (68 output neurons). The output of both CNNs is a probability distribution (likelihood of each output neuron being the correct class), which is obtained by using a softmax function on the outputs of the final FC layer. As performed in (159), and seen in **Equation (4.3)** $\left(S = \sum_{i=1}^{N} P_{seg}^{i} \times \left(\sum_{j=1}^{N} P_{epiendo}^{j} \times CoG_{ij}\right)\right)$, the probability distributions **(**P_{seg}^{i} and $P_{epiendo}^{j}$ for *Segment* and *EpiEndo*, respectively) of each output segment (largest probability) and their adjacent segments were then combined with the centres of gravity CoG_{ij} of the corresponding endocardial and epicardial surfaces to localise a paced beat in Cartesian coordinates.

The *UVC-based* architecture is composed of one 68-feature classification CNN, which predicts the rotational coordinate φ, and one regression CNN, that outputs z and ρ. The structure of both CNNs is similar to the *Cartesian probability-based* network (hidden layer – pooling layer - hidden layer – pooling layer – FC layer). The reason why two separate networks were preferred to a single three-output regression CNN was due to the cyclic nature of φ, for which a classification algorithm would return better results than a regression. Hence, we used φ to divide the LV into 68 "wedges" (φ was grouped into intervals of $0.09\ radians$ with each class assigned a label from 1 to 68 from $\varphi = -pi$). For the final localisation of the paced beats, the outputs of the 68-feature classification ("wedges" with the highest probabilities) were converted back to φ, and combined with z and ρ regression predictions.

Both Cartesian probability-based and *UVC-based* architectures were implemented in Python using Scikit-learn(206) and Tensorflow(207).

6.2.4 CNN Localisation Performance

The localisation performance of the architectures was expressed in terms of localisation error (LE) (Euclidean distance) in mm. For the *Cartesian probability-based* architecture, the error was computed directly between the output of **Equation (4.3)** and the known pacing site from simulations. For the

UVC-based architecture, the predicted values were first transformed from UVC space to Cartesian space (by locating the closest node in the mesh, with appropriate scaling of UVC coordinates(182)), and then the distance with the ground truths was evaluated.

For *Segment* CNN of the *Cartesian probability-based* architecture, the testing performance was also evaluated in terms of accuracy, to allow comparison with results from (159). Accuracy is defined as the percentage of paced beats correctly classified within each segment.

6.2.5 CNN Training and Testing

The training and testing inputs to both architectures were the ECG and EGM traces of the simulated paced beats. The 2D CNNs required the inputs to be placed in square matrices, thus we added four additional leads to the standard 12-lead ECGs ($LL - RA - LA$, $LA - RA - LL$, $RA - LA - LL$ and $\frac{LL+ RA+LA}{3}$), as performed in (159), and eight more EGM vectors to the standard 8-vector EGMs (CAN-each LV tip and SVC-each LV tip), achieving a total of 16 combinations. Then, QRSs of all these vectors were extracted, and downsampled to 16 time points, to obtain 16 x 16 matrices. Among ~ 3767 paced beats simulated across the LV, the ECG and EGM matrices of ~ 2767 of them were used for training. This training dataset was uniformly distributed across the myocardium (~ 36% intramural/mid-wall, ~32% epicardial, and ~ 32% endocardial). The distribution of the training data for *EpiEndo* CNN was ~ 50% from the endocardium and ~ 50% from the epicardium (~ 1767 paced beats). Similarly to (159), the training datasets were further augmented by a factor of 10 with the addition of white Gaussian noise (with a signal-to-noise ratio (SNR) of $25\ dB$) 10 consecutive times to all 16 ECG and EGM leads. This was done to increase robustness of the CNN training. A 10-fold cross-validation was performed in the existing *Cartesian probability-based* CNNs as part of the training(159), with a 90% (training)–10% (validation/testing) split. After training, the localization performance of both *Cartesian probability-based* and *UVC-based* networks was tested by performing inference on the retained 1000 sets of ECG and EGM QRSs, which had an initial SNR of $25\ dB$.

The *Cartesian probability-based* CNNs were parametrised according to (159); batch size was set to 23, number of epochs was set to 10, learning rate was set to 0.001, and cross-entropy was used as loss function. A ReLU function was used as the activation function for feed-forward propagation, and a gradient-descent-projection method was used as the back propagation algorithm. In our *UVC-based* networks, we used similar parameters, except for the regression where the number of epochs was set to 15, and mean absolute error used as the loss function.

6.2.6 Investigation of Model Uncertainties

After training and testing both CNN architectures as described above, we investigated further the localisation performance of the networks by introducing different noise levels to the retrained 1000 sets ($SNR = 5, 10, 15, 20, 30\ db$). In addition, we investigate the network performances under different computational settings: we varied body compositions of the torso model, as seen in **Table 6.1**, as well as ECG electrode locations (**Figure 6.6**) and implanted device configurations (**Figure 6.7**). For each of these variations, LF matrices were recomputed (according to the new organ conductivities and/or electrode/lead position), and combined with the retained 100 intramural excitations to obtain new testing ECG and EGM matrices. These datasets were used to test both previously trained CNN architectures.

Variations in body compositions. Some of the major organ conductivities were varied according to physiological variations(208,209). For instance, blood within cardiac cavities can have different conductivities according to which moment of the cardiac cycle we are considering, and the electric behaviour of the lungs can change according to how much air they are holding (they have different values when they are deflated or inflated). Similarly, the liver can have different conductivities according to fat deposition, and what we referred to as “bath” can have a higher percentage of fat or muscle. We chose to match specific changes (for instance, liver and lungs, fat/muscle, named “bath” and liver, and different blood pools, etc. as seen in **Table 6.1**) to challenge CNN localization performance.

Standard Conductivities	Variations
Liver: 0.1667 (S/m)	(1) Liver: 0.023 (S/m), Lungs: 0.039 (S/m)
Lungs: 0.0714 (S/m)	(2) Bath: 0.45 (S/m) (pure muscle), Lungs: 0.039 (S/m)
Bath: 0.24725 (S/m)	(3) Bath: 0.05 (S/m) (pure fat), Lungs: 0.203 (S/m)
Skin: 0.05 (S/m)	(4) Liver: 0.2 (S/m), Lungs: 0.039 (S/m)
Atria, Ventricles, Aorta: 0.6667 (S/m)	(5) Bath: 0.05 (S/m), Lungs: 0.039 (S/m)
	(6) Bath: 0.45 (S/m), Lungs: 0.203 (S/m)
	(7) Bath (all organs except lungs): 0.24 (S/m), Lungs: 0.07 (S/m)
	(8) Skin: 0.117 (S/m)
	(9) Atria, Ventricles, Aorta: 0.84 (S/m)

Table 6.1. *Variations in body compositions. On the left, we can see the standard conductivities of the major organs we varied values of. On the right, we can see the different scenarios tested.*

Variations in ECG lead placement. ECG electrodes were displaced by $5\ cm$ in all major orthogonal directions, and across all leads. Specifically, we shifted all ECGs leads upward (**Figure 6.6A**) and downward (**Figure 6.6B**)—RA and LA were always shifted downward, and LL upward—toward the left (**Figure 6.6C**) and the right (**Figure 6.6D**). Moreover, in one configuration (**Figure 6.6E**), the distance between ECG leads was increased by $\sim 10\ cm$.

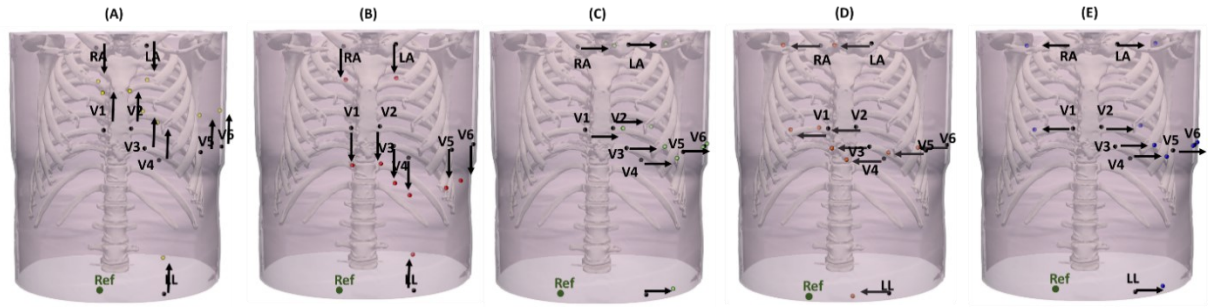

Figure 6.6*. Variations in ECG electrode placements. (A): shows original ECG leads (black) displaced by ~ 5cm upward, (B) downward, (C) toward the left, (D) toward the right, and (E) by ~ 10 cm (mixed displacements toward the right and left).*

Variations in implanted device configurations. Finally, we simulated variations in electrode location and diameter of the virtual implanted device, as reported in (80) for different CRT-D devices available in the market (**Figure 6.7**). Specifically, we changed the spacing between the sensing electrodes of the

straight LV lead, to account for shorter or longer inter-electrode distance; in addition, we increased the diameter of RV and LV tips to $\sim 2\ mm$, instead of considering single point electrodes. The EGM vectors from this configuration were then obtained by averaging the signals within the $2\ mm$ radius (simulating more realistic conduction), and we investigated whether our single point approximation of the device leads could affect the final localisation. Finally, we considered the case of a septal RV coil configuration, which has been tested in CRT-D(210) and ICD(211) before.

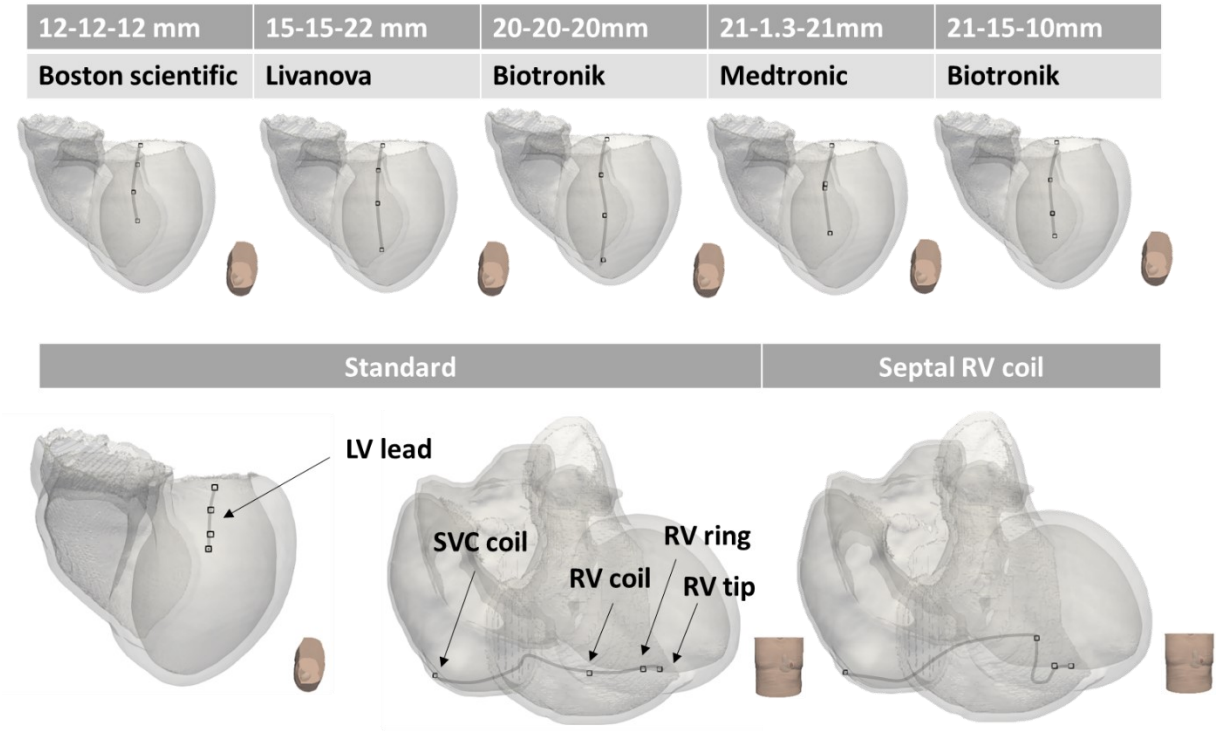

Figure 6.7. *Variations in implanted device configurations. On the top panel, different configurations of the LV lead across manufacturers (Boston Scientific, Livanova, Biotronik, Medtronic) are shown. The inter-electrode distance is the primary difference among the different scenarios. The standard configuration of the RV and LV leads is illustrated in the bottom left panel, and the septal RV coil configuration in the bottom right.*

6.3 RESULTS

In this Section, we will first investigate the performance of the existing *Cartesian probability-based* networks (*Segment* and *EpiEndo* CNNs) in localising focal paced beats from ECGs and implanted device EGMs in comparison to previous work utilising the ECG only(159). We will see how localisation

precision was affected by increasing the number of segments classified by the *Segment* CNN from 17 to 68. Then, we will investigate the performance of our novel *UVC-based* localisation algorithm, and how it compares to segment-based, Cartesian approaches, and conclude the section by investigating the influence of noise, body composition and electrode configuration on both *Cartesian probability-based* and *UVC-based* networks.

6.3.1 Comparison in CNN Performances with Existing Work

Yang et al. (159) proposed two CNNs (*Segment* and *EpiEndo*) that could be used to identify the origin of a focal beat from the standard ECGs. In this study, we successfully reproduced such an architecture, and showed the possibility of utilising not only ECG traces but also 16 different combinations of EGM vectors from a generic implanted device. Testing performance of *Segment* CNN, evaluated in terms of testing accuracy, was similar when using both ECGs and EGMs as inputs. Specifically, an accuracy of 86.76% was achieved for ECG-based testing, and 79.70% for EGM-based testing (**Figure 6.8A**), when SNR on ECG and/or EGM traces was $25\ db$.

The ECG-based and EGM-based performances of *Segment* CNN were also evaluated in terms of precision per segment, quantifying how exact the network is at classifying a focal paced beat in each segment of the 17-segment LV model (**Figure 6.8B**). The network is influenced in a similar manner by both ECGs and EGMs in almost every segment, with only few exceptions. The three highest precisions are in segments 1,10 and 4 for ECG-based testing, and 1,10 and 16 for EGM-based testing. The three lowest are in 2,3 and 15 when using ECGs, and 2,7 and 9 when using EGMs.

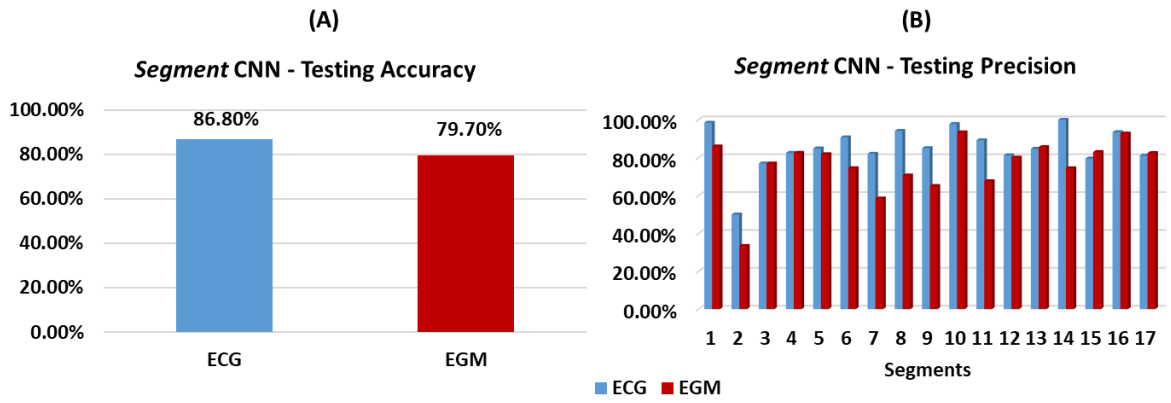

***Figure 6.8**. Performance of Cartesian probability-based Segment CNN. (A) shows testing performance of 17-feature Segment CNN, in terms of accuracy %, when utilising ECGs (blue) and EGMs (red) as inputs. (B) reports the precision of the network for each of the 17 segments of the LV mesh (how well the network classifies focal paced beats in each segment), for both ECG-based (blue) and EGM-based (red) performances.*

6.3.2 Utility of EGMs in Cartesian Probability-based Localisation

The localisation in Cartesian space of each paced beat of the 1000 testing dataset, from either ECG or EGM signals, was achieved by combining probability distributions of *Segment* and *EpiEndo* CNNs, as shown in **Equation (4.3).**The distance between such estimated source and the real location of the simulated paced beat is then quantified in terms of LE in mm, which then enables to assess and compare the localisation performance of the architecture between ECGs and EGMs. The mean errors are reported in **Figure 6.9A** for ECG-based ($11.76 \pm 5.32\,mm$) and EGM-based testing ($13.25 \pm 6.79\,mm$).

Increasing the number of segments classified by *Segment* CNN to 68 was able to reduce mean localisation errors to $6.69 \pm 3.19\,mm$ for ECG-based testing, and $8.74 \pm 6.41\,mm$ for EGM-based testing, as shown in **Figure 6.9B.**

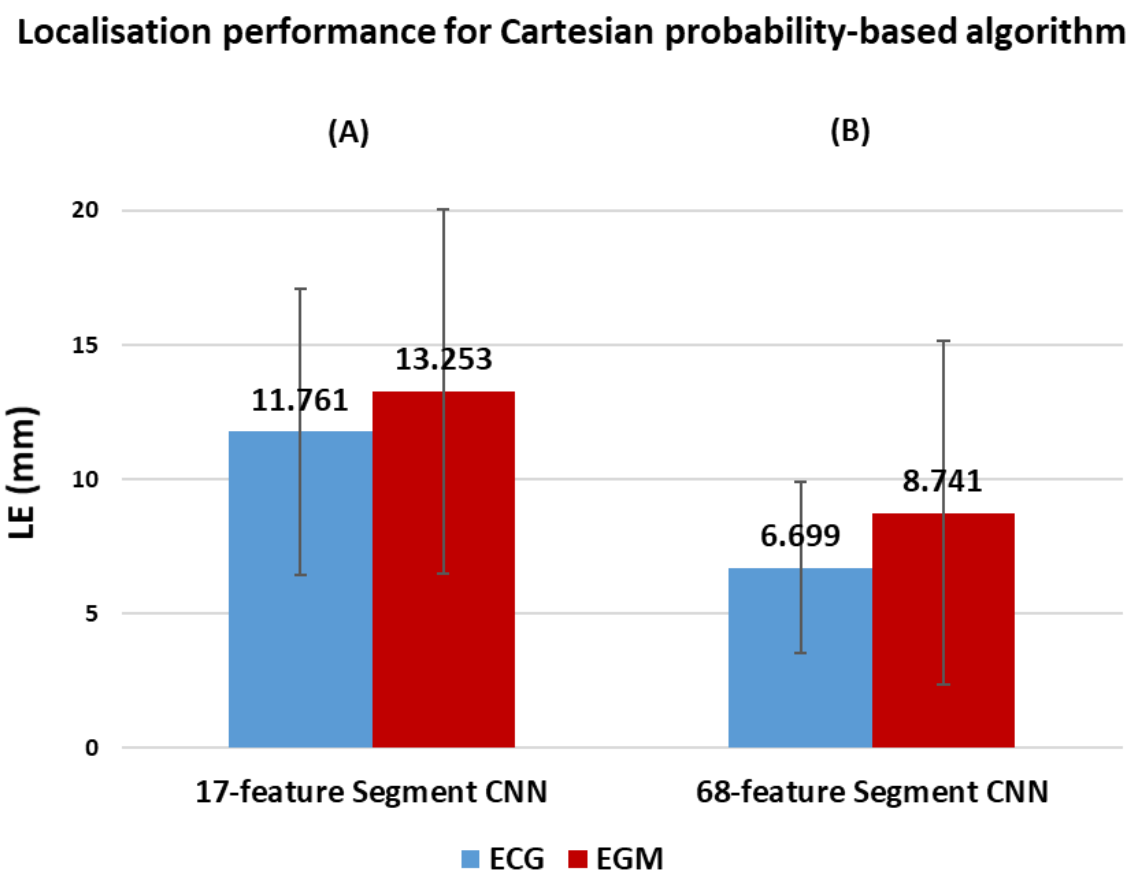

Figure 6.9. *Performance of Cartesian probability-based localisation performance. (A) shows mean localisation errors (LE) in mm for ECG-based (blue) and EGM-based (red) testing when Segment CNN has 17 output neurons. (B) reports the errors as a result of using a 68-feature Segment CNN.*

6.3.3 UVC-based Localisation

Localisation performance was further improved by developing two CNNs that returned the location of a paced beat in a reference frame specific to the ventricles (UVCs). With this *UVC-based* localisation, mean LEs were reduced to $4.06 \pm 2.47\ mm$ and $8.07 \pm 8.26\ mm$ for ECG-based and EGM-based testing, respectively, as reported in **Figure 6.10A**.

Predictions from the *UVC-based* networks can be easily visualised in the 3D patient-specific ventricular mesh, or in the 2D patient-specific bull's-eye diagram, previously shown in **Figure 6.2**. In **Figure 6.10B**, we can see an example of how 3D *UVC-based* localised sources compare with the ground truths, revealing a close match between all pairs. UVC z of the paced beats is used to describe their distances

from the LV apex (centre of the diagram), and φ visualises the position of a beat along the circumferential direction, within a specific segment. The intramural location of the beat, described by UVC ρ, can be visualised in a grey scale; black indicates endocardial origin, white epicardial.

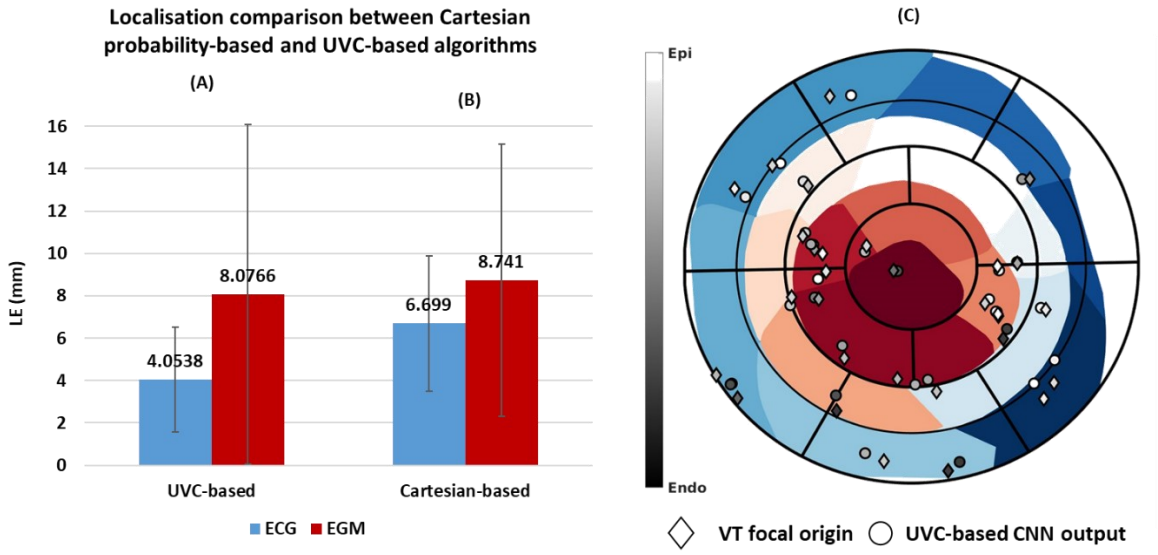

Figure 6.10. *Localisation comparison between UVC-based and Cartesian probability-based algorithms. (A) reports mean localisation errors (LE) in mm for ECG-based (blue) and EGM-based (red) testing in UVC space, and (B) in Cartesian space, when using the 68-feature Segment CNN. (B) shows example of simulated focal origins (diamonds) compare to UVC-based localised source (circles) in the 2D patient-specific bull's-eye diagram.*

6.3.4 Sensitivity to Noise

Overall, localisation of a paced beat in both Cartesian and UVC spaces was only slightly affected by noise, as **Figure 6.11A-B** illustrates for ECG-based and EGM-based testing, respectively. As the level of noise is increased by decreasing SNR, mean errors only marginally increased, except at $SNR = 5\ db$, where both *UVC-based* and *Cartesian probability-based* localisation were more strongly affected. Errors were $< 12.5mm$ for ECG-based localisation, and $< 13.55\ mm$ for EGM-based localisation (except at $SNR = 5db$). Noise on EGM traces likely affected networks' localisation more than on ECGs.

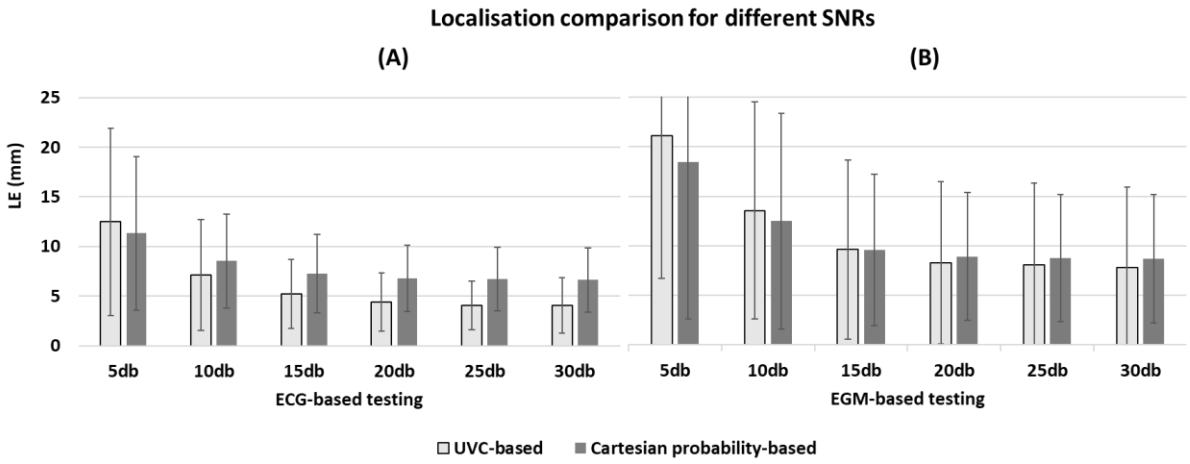

Figure 6.11. *Localisation performance at different noise levels. (A) shows mean localisation errors (LE) in mm for ECG-based testing, for UVC-based (light grey) and Cartesian probability-based (dark grey) localisation, and (B) for EGM-based testing.*

6.3.5 Sensitivity to Electrode Locations

Localisation performance of both algorithms was affected by changes in ECG leads and in device configurations. As **Figure 6.12** shows, mean errors for both ECG-based and EGM-based testing were $> 15\,mm$. ECG-based localisation was more affected by displacements away from the heart, right and downward shifts, with mean LEs $\sim 20\,mm$. EGM-based localisation reported higher errors ($> 20\,mm$) when increasing inter-electrode distance (Biotronik $20-20-20mm$ configuration), lead surface diameter, and when considering a septal configuration of the RV coil.

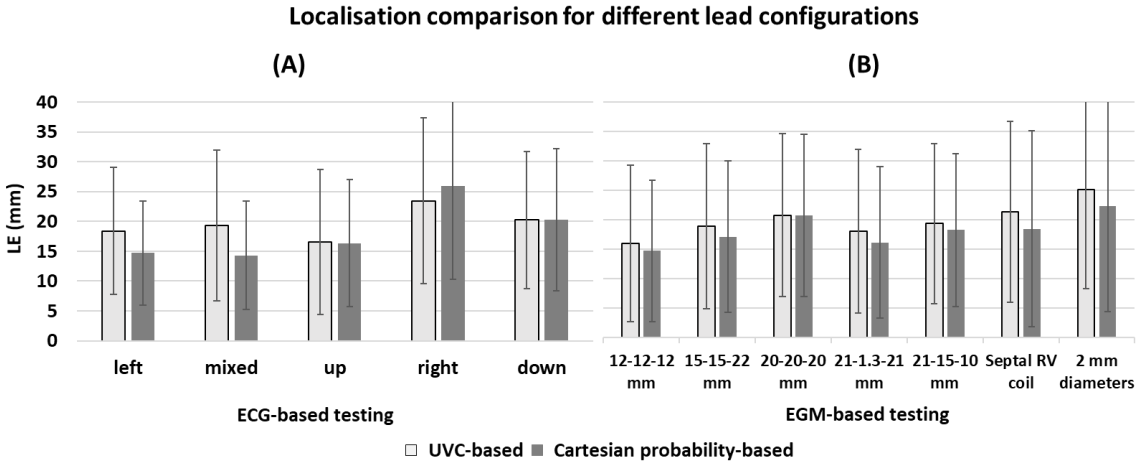

Figure 6.12. *Localisation performance for different displacements of ECG and device electrodes. (A) shows mean localisation errors (LE) in mm for ECG-based testing, for UVC-based (light grey) and Cartesian probability-based (dark grey) localisation*

as ECG electrodes were displaced from the standard locations in various directions. (B) reports mean LEs for EGM-based testing, for different device configurations.

6.3.6 Sensitivity to Tissue Conductivities in Torso model

Figure 6.13A-B show comparisons between ECG-based and EGM-based localisation, respectively, for *Cartesian probability-based* and *UVC-based* algorithms, as different organ and tissue conductivities were applied to the torso model. Only a high increase of conductivity in the fat tissue (scenario 3 and 5), as well as a simplification of the whole torso to bath and lungs (scenario 7), affected ECG-based localisation. In those three scenarios, mean LEs increased to $17.75 \pm 9.88\,mm$, $20.72 \pm 10.99\,mm$, and $14.08 \pm 7.38\,mm$ for *UVC-based* testing, respectively, and to $13.01 \pm 8.89\,mm$, $15.07 \pm 11.20\,mm$, and $13.88 \pm 8.40\,mm$ for 68-segment *Cartesian probability-based* testing. Other variations of tissue conductivity did not affect the performance of either algorithm (LEs $< \sim 8\,mm$).

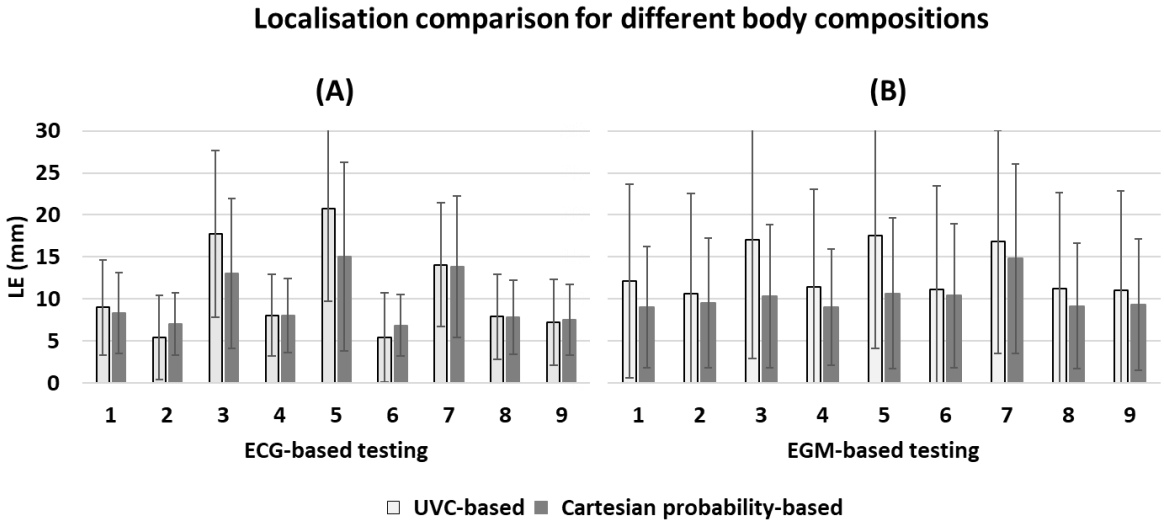

Figure 6.13. *Localisation sensitivity to tissue conductivities. (A) shows mean localisation errors (LE) in mm for ECG-based testing, during UVC-based (light grey) and Cartesian probability-based (dark grey) localisation as different organ conductivities were changed in the torso model, see* ***Table 6.1.*** *Similarly, (B) reports mean LEs for EGM-based testing.*

Finally, EGM-based testing was less affected by changes in body compositions during *Cartesian probability-based* localisation. Similarly to above, a simplification of the torso model to bath and lungs (Scenario 7 in **Table 6.1**) caused the highest mean error ($14.83 \pm 11.24\,mm$) during *Cartesian probability-based* localisation, but in all other scenarios, LEs ranged between $9.04\,mm$ and $10.66\,mm$. On the other hand, during *UVC-based* localisation, similar trends to ECG-based localisation were seen in Scenario 3, 5 and 7, with errors $> 15\,mm$.

6.4 DISCUSSION

In this Chapter, we successfully developed a computational-AI pipeline to localise virtual focal VT origins from simulated implanted device EGMs, achieving accuracies that could be of benefit in clinical settings. A similar algorithm was previously created by (159), which however utilised 12-lead ECGs to localise VT origins; here, we managed to replicate a similar structure of the CNN architecture for EGM traces, improving the overall performance by introducing a higher number of segments in the AHA LV model. Furthermore, we introduced a novel architecture composed of regression and classification algorithms, which identified the source in a framework specific to the ventricles, which is easily interpretable by clinicians, more patient-specific and constrains localisation to the myocardium. Finally, the robustness of both CNN architectures was investigated under the introduction of different sources of error, such as different noise levels in the data, and possible inter-patient variabilities (different body composition, ECG lead positions, and implanted device configuration).

6.4.1 Successful Application of EGMs in Existing Cartesian Probability-based Algorithm

In this study, we successfully showed the feasibility of utilising 16 combinations of implanted device EGM vectors to automate the localisation of focal VT sources. In the previous study that utilised standard ECG traces as inputs to the networks, localisation precision was in the range of $10 - 11\,mm$;

we were able to decrease such errors to $6.69\ mm$ (for ECG traces), and achieve a comparable localisation for EGMs ($8.74\ mm$), by incrementing the number of segments in the LV to 68. These results would be desirable in clinical settings, for guiding initial ablation planning, given that the average ablation lesion size is $> 8.5\ mm$ (212). Especially in haemodynamically unstable patients, ablation pre-planning could be expedited and aided by utilising information stored in implanted devices, as we have also shown in the previous Chapter. However, in this study, we propose a quicker, first level of investigation, that could direct clinicians to the region of interest with high precision, and require less manual interaction.

For both ECG-based and EGM-based localisation performances, we achieved testing accuracies in ranges comparable to (159) ($> 77\%$). Moreover, similar patterns to the previous study were seen when investigating the sensitivity of our networks to signal noise; only a loss in accuracy and localization precision was seen with $SNR = 5\ dB$. Interestingly, noise seems to exert a greater impact on EGM-based localisation than on ECG-based. This could be explained by the fact that implanted device sensing vectors are closer to one another and to the cardiac electrical activity, amplifying variations caused by noise, and thus affecting EGM-based localisation to a greater degree. In clinical settings, high levels of noise appearing on EGM traces have been shown to be cause of inappropriate shocks from the implanted device and/or inhibition of pacing(213), and thus our analysis is in line with what seen clinically.

6.4.2 Novel UVC-based Algorithm Improves Localisation

A more desirable localisation performance was achieved when introducing a novel *UVC-based* algorithm for the localisation of focal VT origins, which decreases localisation errors to $4.06\ mm$ and $8.07\ mm$ for ECGs and EGMs, respectively. Whereas the *Cartesian probability-based* algorithm proposed by (159) relies on combining probabilities of two networks with the geometrical centres of gravity of each LV segment to locate a VT origin, our *UVC-based* predictions are intrinsically bound to the myocardium, and more accurately describe the location of a source in terms of its (normalised)

distance from the apex, the LV septum and, most importantly, the endocardium. The choice of power, tip diameter and lesion size to apply to achieve a successful ablation of a focal VT episode could really benefit from knowing the exact intramural (mid-wall) location of the originating source. Finally, it is worth mentioning the utility of our *UVC-based* approach to facilitate visualisation of focal sources within a patient-specific bulls-eye diagram, if 3D visualisation on the patient-specific mesh is not desired or feasible (e.g. lack of imaging data).

6.4.3 Extreme Changes in Lead Positions May Affect Localisation

Interestingly, focal VT localisation is only marginally affected by differences in body composition, showing the feasibility of applying this platform in clinical settings, and for different patients. However, hypothetically, to increase the accuracy of results, when constructing a torso model from patient imaging data to train the algorithm, all major thoracic and abdominal organs with realistic conductivity values should be included. Our findings suggest that representing bath and lungs only (as used in (159)) produces signals that could have a negative impact on the final localisation accuracy. The requirement of a more detailed torso model could be marginally avoided by utilising EGM traces, as the EGM-based algorithms seemed less affected by tissue variations. The closer positioning of the device leads to the electrical cardiac source might explain why the extracellular potentials at the electrodes are less affected by surrounding tissue/organ conductivities. However, it is important to stress the dependence of the localisation algorithms on the locations of ECG electrodes and implanted device configuration used during training; this suggest the necessity of integrating a higher variability in the training data, and/or extrapolating ECG or implanted device patient-specific information from imaging data to strengthen future automated algorithms for clinical applicability.

6.4.4 Limitations

A notable limitation of this study is the absence of clinical validation, which we will address in the final Chapters of this Thesis. In the next Chapter, we will show how to tune a computational-AI platform to

achieve clinical translation by providing certain information of the patient-specific model (e.g. ECG electrode locations and/or implanted device leads) during the training of the network. Another important limitation of this study is the simplicity and depth of the CNN architecture, which might not be ideal for more complex tasks. As we will see in the next Chapter, deeper networks, the use of different input data shapes (e.g. 1D instead of 2D), and the introduction of algorithms that are more specific to temporal series will be useful to extend the automation of VT localisation to re-entrant episodes. Finally, we only considered beats originating in the LV. A common region of PVCs is around the RVOT, however a third of idiopathic PVCs originate from different locations in the LV(214), for which further investigation was of importance. In addition, training the algorithm on a high-density, random distribution of paced beats, rather than more localised foci based on true incidence of ventricular ectopic locations, limits over-fitting and increases the accuracy and precision of detection. In future studies, we could add an additional deep-learning architecture that distinguishes ectopic beats originating from the right and left ventricular chambers based on the fourth coordinate of the UVC. This will increase complexity of our pipeline, and might not have a significant impact in the final localisation performance, but may be of importance for future clinical evaluation if both RV and LV PVCs are of interest.

6.5 CONCLUSION

In the previous Chapter, we began to investigate the possibility of extracting and utilising a wider range of information from generic implanted devices to improve VT management. Here, we showed the utility of those multi-vector EGMs to automate focal VT localisation, and improve ablation planning further. In addition, we proposed a more efficient computational environment, which will be of use in the following Chapters to address more complex simulation problems. In those scenarios, the generation of fast and physiological simulations on patient-specific torso meshes could really help tailor the training of AI algorithms to achieve accurate, patient-specific localisation in clinical settings. In conclusion, the work presented in this Chapter represents an important stepping stone for the

remainder of this Thesis, where we will improve on the major limitations of this study, and show the applicability of our platforms when dealing with clinical VT episodes.

7

AUTOMATED POST-INFARCT VT LOCALISATION

The previous two Chapters have focused on showing the utility of simulated EGMs in in-silico pace-mapping and CNN algorithms to ease the identification of VT ablation targets. We showed how the simulation of focal paced beats could be eased by combining RE and LF methods, and the importance of combining computational simulations with DL algorithms to create large training and testing libraries for a robust performance. In this Chapter, we aim to bridge the two studies. We will develop a pipeline that enables fast simulation of scar-related VTs and corresponding ECGs and EGMs, and uses CNNs, LSTMs and attention mechanisms (shown to be more suitable for time series analysis) to predict the corresponding exit sites. The motivation and methodology of this study will be presented in Section 7.1 and 7.2. In Section 7.3 and 7.4, we will investigate and discuss different scenarios to understand the importance of incorporating simple, patient-specific, paced beat simulations in the training stage of the algorithm, improving the final localisation performance. Moreover, we will show how to replicate the pipeline in the presence of clinical data. Finally, the Chapter will conclude with a summary section (Section 7.5), linking to the final Chapters of this Thesis. The work presented here has been published in EP Europace(215).

7.1 INTRODUCTION

In previous Chapters, we illustrated the importance of accurate and precise detection of VT exit sites in presence of structural heart disease to successfully reduce recurrence of future arrhythmic episodes. We saw that invasive mapping strategies may allow accurate characterisation of the VT, but are limited by non-inducibility or non-sustained and/or hemodynamically poorly tolerated VTs. This led to the proposal of an in-silico pace-mapping platform that could identify VT circuits non-invasively from implanted device EGMs (**Chapter 5**). This platform was still dependant on good imaging data of the infarcts, and relied on time-consuming computational simulations. A more efficient computational environment was developed in **Chapter 6** to be able to train and test CNN architectures for automating the localisation of focal VTs from implanted device EGMs. This study was of importance to demonstrate how to improve the chance of ablation success by proposing a non-invasive, fast and accurate approach that could guide planning. In this Chapter, we intend to build on those previous studies, and develop another computational-AI platform that can accurately localise critical post-infarct VT exit sites from surface ECGs and implanted device EGMs, outperforming the limitations of current post-infarct VT localisation algorithms presented in the **4 Literature Review**.

The most relevant studies that have proposed algorithms for the localisation of post-infarct VTs from ECGs are by the group of Zhou et al.(51,160,169,170). Although they achieved a mean localisation error of ~ *6 mm* in clinical settings, their algorithm was still heavily dependent on EP and structural properties acquired during EAM procedures, as well as requiring VT induction and/or VT ECGs. In this study, we therefore aim to propose an architecture that could greatly speed up the initial regionalisation of VT re-entrant circuits, with only little dependence on a patient's imaging data, and that utilises implanted device EGMs.

In summary, we aim to 1) automate post-infarct VT localisation from the standard ECGs to improve on existing ECG-based algorithms, and 2) carry-out the first proof-of-concept study to assess the feasibility of using implanted device EGMs within automate AI architectures in the preliminary

investigation of post-infarct VTs, which may be of value to target the clinical episodes, as well as potentially reducing the need for arrhythmia induction. In addition, we also seek to show the direct clinical application of our platform to localise VTs from clinically-recorded ECGs.

7.2 METHODS

In this Section, we will describe the computational environment built to rapidly simulate not only focal VT episodes and corresponding ECG and implanted device EGM traces, but also more complex, re-entrant VTs. For this, we will generate simple, virtual infarcts within the ventricular meshes, and use them in combination with RE and LF EP formulations to obtain corresponding extracellular signals. Then, we will describe the AI model for automating detection of the tachycardia from those traces, and finally illustrate the computational and clinical scenarios investigated to test the algorithm in predicting the VT exit sites.

7.2.1 Overview of Computational-AI framework

Figure 7.1 outlines the framework for the automation of post-infarct VT localisation. Briefly, computational models from patient-specific anatomies, constructed by (216), were used to simulate multiple focal paced beats and post-infarct VT episodes, along with corresponding ECGs and implanted device EGM recordings. An AI architecture and pipeline was then developed to predict the exit sites of post-infarct VTs from this comprehensive library of simulated time traces. The architecture was first evaluated on simulated post-infarct VTs, and then tested on a clinically-induced VT episode as shown in **Figure 7.1B**. The components of our pipeline are described in more detail in the following paragraphs.

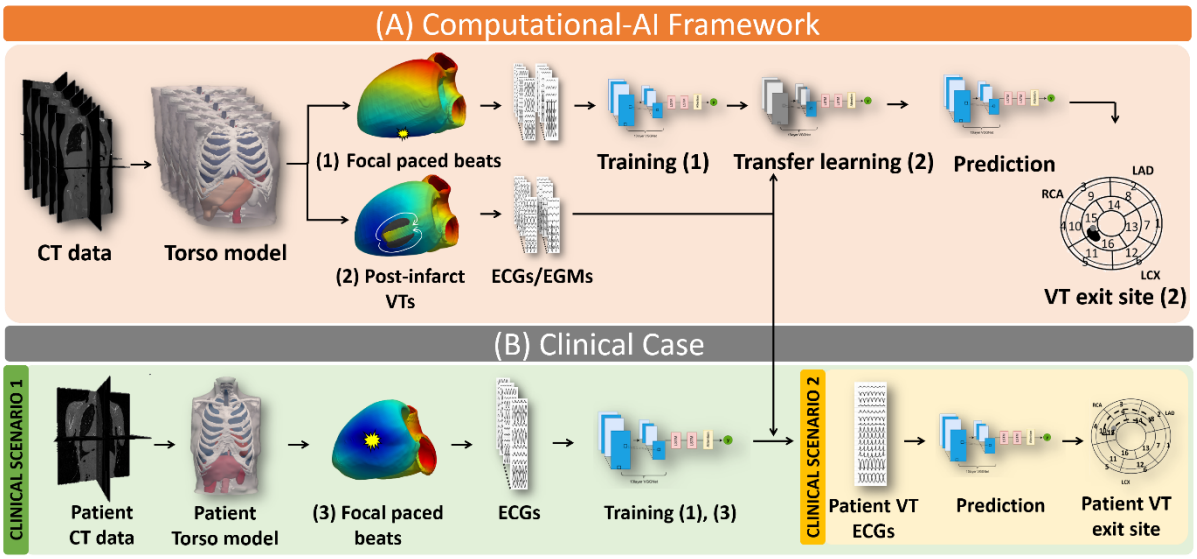

Figure 7.1. *Workflow of the computational AI framework for automating scar-related VT localisation. (A) shows the computational-AI platform trained and tested on simulated ECGs and EGMs to predict exit sites from post-infarct VTs. (B) shows how the platform can be used in clinical settings by investigating two different scenarios.*

Patient-Specific Torso Models

As in previous Chapters, torso models were generated from CT TAVI planning scans, and additional higher resolution contrast cardiac scans. In this study, the imaging data of an additional five patients was available, and processed by (216). The five patients did not present any visible structural heart disease and consented for the use of their data in ethically approved research: UK Research Ethics Committee reference number 19/HRA/0502 & 104 15/LO/1803. Briefly, major organs and tissues were segmented in Simpleware™ (Synopsys, Inc., Mountain View, USA), including lungs, bones, skin, liver, spleen, kidneys, stomach, aorta, fat and muscle, using similar tools as in **Chapter 5**. Each cardiac scan was segmented into separate chambers and blood pools using Siemens Axseg v4.11(181). All segmentations were then combined together in Simpleware™, and corresponding 3D tetrahedral finite element meshes were generated. The mean edge length of each myocardial mesh is reported in **Table 7.1**, together with the imaging resolutions of the CT TAVI planning and cardiac scans.

As done in **5.2.2 Model Generation** and **6.2.2 Computational Model Preparation**, we incorporated realistic myofibre architectures into the myocardial meshes(217), as well as computing UVCs(182) and 17-AHA segments.

Patient	Resolution CT TAVI planning scan	Resolution CT cardiac scan	Ventricular Mesh Resolution
(A)	$0.6875\ x\ 0.6875\ x\ 0.5\ mm$	$0.4082\ x\ 0.4082\ x\ 0.5\ mm$	$835\ \mu m$
(B)	$0.6914\ x\ 0.6914\ x\ 0.5\ mm$	$0.3164\ x\ 0.3164\ x\ 0.5\ mm$	$765\ \mu m$
(C)	$0.6914\ x\ 0.6914\ x\ 0.5\ mm$	$0.3027\ x\ 0.3027\ x\ 0.5\ mm$	$778\ \mu m$
(D)	$0.7421\ x\ 0.7421\ x\ 0.5\ mm$	$0.4004\ x\ 0.4004\ x\ 0.5\ mm$	$826\ \mu m$
(E)	$0.6542\ x\ 0.6542\ x\ 0.5\ mm$	$0.3613\ x\ 0.3613\ x\ 0.5\ mm$	$826\ \mu m$

Table 7.1. *Resolutions of CT TAVI planning and cardiac scans, and corresponding ventricular meshes (from left to right) for five anonymised patients - (A), (B), (C), (D) and (E).*

In each torso mesh (A-E), the standard 9 ECG electrodes and generic implanted devices were modelled as illustrated in **Figure 7.2**, as previously described in **6.2.2 Computational Model Preparation.**

EP properties

Before illustrating the protocol to simulate focal and post-infarct VT episodes, it is worth mentioning that each patient-specific model was assigned EP properties according to literature, given that no personalised EP data was available. Thoracic and abdominal organs and tissues were given extracellular tissue conductivities as in **Table 5.1** with minor modifications (skin was given a value of $0.05\ S/m$, and stomach of $0.1\ S/m$). Intra- and extra-cellular conductivities of the myocardial meshes were tuned according to the mesh resolution to achieve physiological QRSs(205), as shown in **Table 7.2**. Corresponding CVs along and transverse to the fibre direction were $0.67\ m/s$ and $0.30\ m/s$, respectively, in all five models. The TT2 cell model(95) was utilised in all simulations.

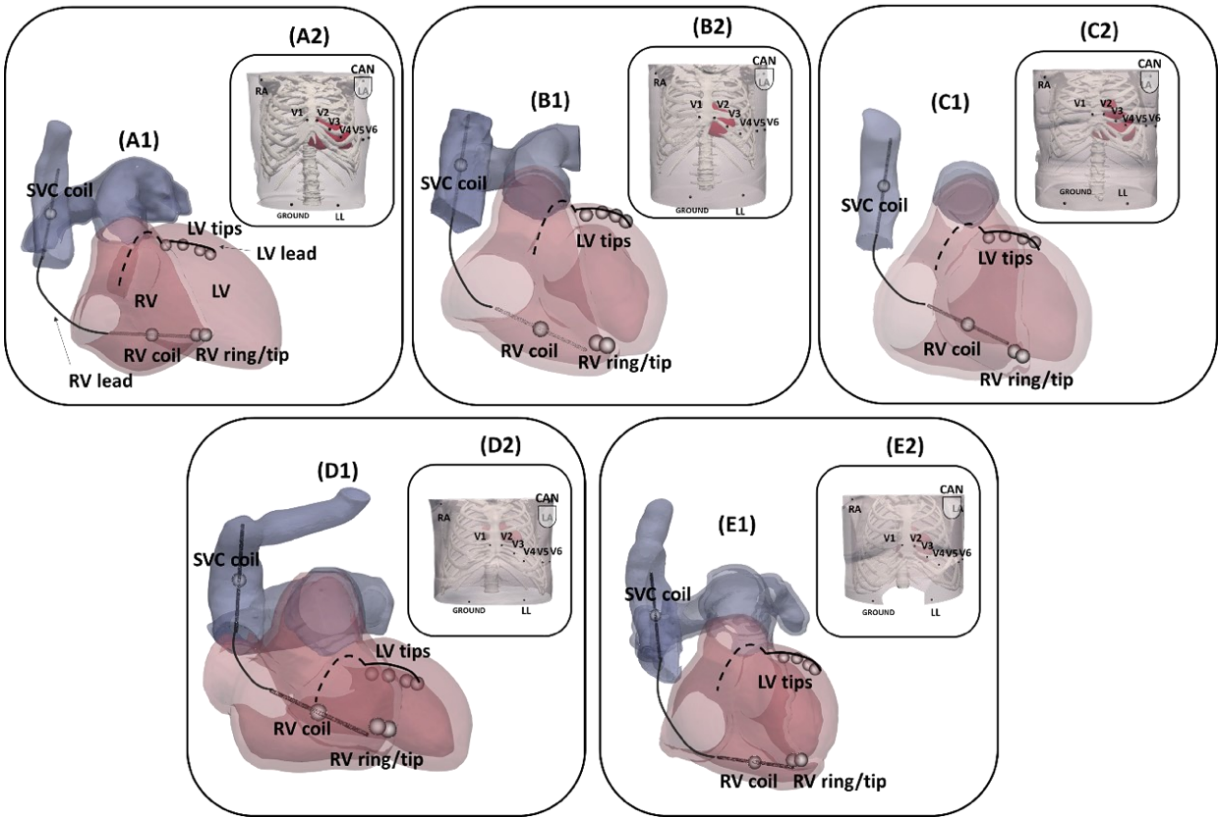

***Figure 7.2**. Modelling of implanted device leads (1) and ECG electrodes (2) in patient-specific torso models for patients (A) – (E).*

Patient	Intracellular conductivities (S/m)		Extracellular conductivities (S/m)	
	Longitudinal	Transverse	Longitudinal	Transverse
(A)	0.2674	0.0921	0.9605	0.3307
(B)	0.2548	0.0861	0.9152	0.3093
(C)	0.2571	0.0872	0.9236	0.3133
(D)	0.2657	0.09125	0.9542	0.3279
(E)	0.2657	0.09125	0.9542	0.3279

***Table 7.2.** Intra- and extra-cellular conductivities along and transverse to the fibre direction across the five models. Values were tuned according to the mean ventricular edge length of the meshes*(205).

Simulation Protocol

Firstly, we simulated ~3000 focal paced beats per model, equally distributed across the whole LV myocardium (endocardially, epicardially, and intramurally). LAT maps of each beat were obtained with

the eikonal solve in CARP(104) (**Figure 7.3A**), and then used in our fast and efficient RE+ (with diffusion) - LF environment to obtain corresponding 12-lead ECGs and 8-vector EGMs (**Figure 7.3B**) of two beats for each location ($bcl = 400\ ms$).

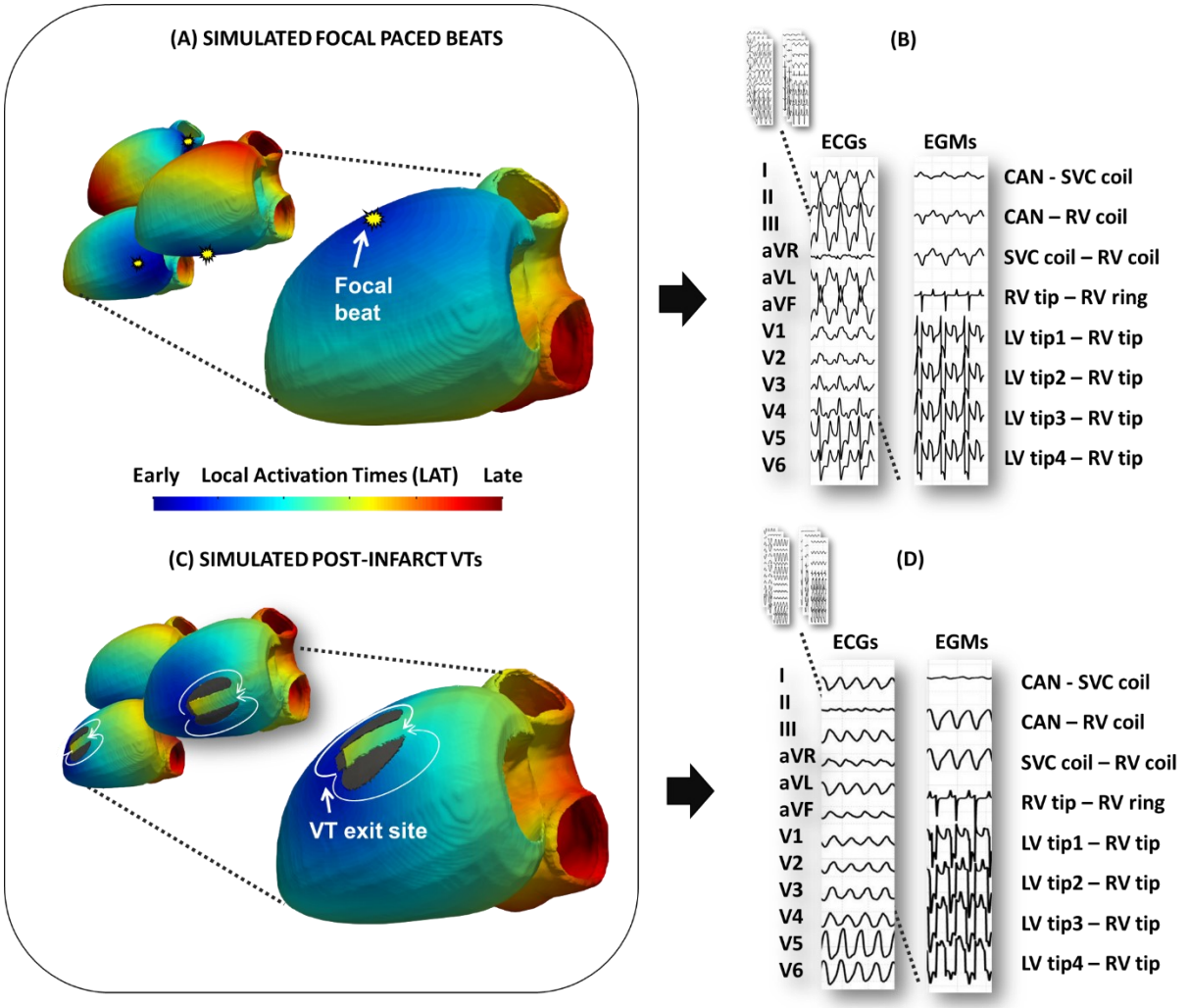

***Figure 7.3**. Example of simulation protocols for the generation of ECGs and EGMs for focal paced beats and scar-related VTs. (A) shows LAT maps of simulated focal paced beats in different LV locations, which were used in our RE+-LF environment to generate corresponding (B) ECGs and EGMs. Similarly, figure-of-eight LAT maps (C) were used for corresponding (D) ECGs and EGMs. Colour maps describe early activation of the tissue in blue, and late activation in red. The yellow stars in (A) identify the location of initial focal stimuli, whereas white arrows in (C) describe VT trajectories.*

To rapidly simulate post-infarct VTs across the models, idealised transmural infarcts were generated across the LV segments, in 50 different locations in each LV mesh, for a total of 250 scars. The scars were designed to produce the characteristic figure-of-eight re-entrant pattern, commonly associated

with scar-related VT post-infarction(62), whereby two regions of inexcitable tissue frame a narrow region of reduced conduction (isthmus). The direction of the latter changed according to fibre orientation(218), given the known dependence of post-infarct VTs on poorly-coupled surviving fibres, and the length ($\sim 24-30\ mm$) and width ($\sim 8-11\ mm$) of the channels were chosen according to a clinical study(219). The isthmuses of these infarcts were prescribed a CV of $0.30\ m/s$ to be able to simulate stable VT episodes with physiological cycles (ranging between $200-450\ ms$ across the five torsos). With the eikonal model, two re-entrant circuits were simulated per scar (with opposing chiralities), as follows: one mouth of the virtual isthmus was temporarily blocked, creating an artificial conduction block orthogonal to the isthmus (**Figure 7.4A)**, and then the region of healthy tissue after the block, outside the isthmus, was paced (**Figure 7.4B**). By doing so, the electrical wave was forced to propagate around the non-conducting scar regions (**Figure 7.4C)**, returning the characteristic figure-of-eight activation pattern (**Figure 7.3C**). The same procedure was repeated for the other mouth of the isthmus. After a single re-entrant circuit, the tissue set temporarily to be non-conducting at the isthmus mouth was restored to conducting tissue, and diffusion was utilised to maintain the re-entrant circuit for multiple periods ($\sim 4.6s$). Diffusion coefficients were adjusted so that overall CVs and VT periods were not altered. Finally, ECG and EGM signals were computed as described above (**Figure 7.3D**). The exit site of each episode – utilised as testing ground truth in our AI architecture - was defined as a 5mm-in-radius region around the exit site of the figure-of-eight circuit, based on the size of the tip of conventional ablation catheters(220), and hence the minimum ablation lesion size feasible in clinical practice.

AI model

The proposed AI model was designed with reference to (15), which was described in the **4 Literature Review** (**Figure 7.5**). Some modifications to the structure and parameters of the algorithm were made to fit the present task.

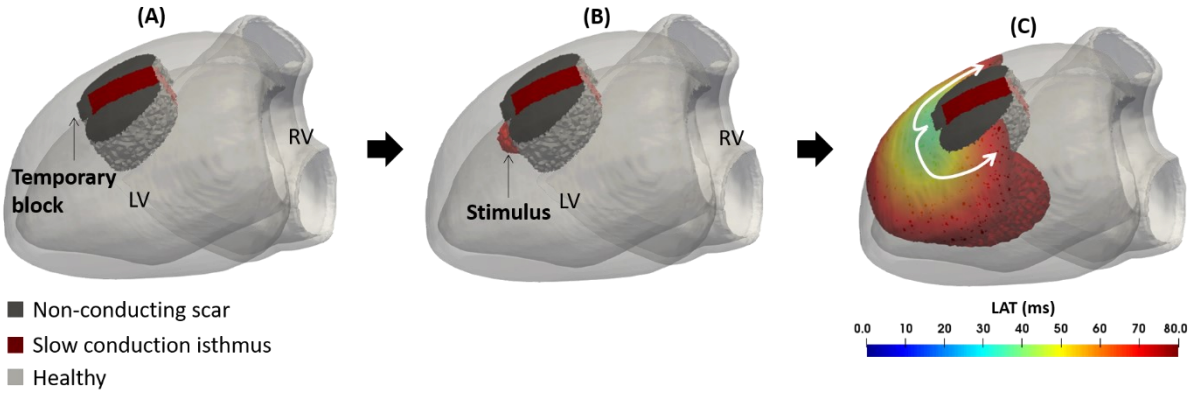

Figure 7.4. *Example of fast VT induction from idealised infarcts. (A) an artificial, temporary conduction block is appled to either end of the slow conduction isthmus (red). Then, (B) a point after such block is stimulated, and (C) the presence of two non-conducting regions (grey) forces the impulse to bifurcate, returning LATs with the eikonal solve that can be used within our RE+-LF environemnt to obtain multiple cycles of sustained, monomoprhic re-entrant episodes, and corresponding extracelular signals.*

Firstly, the model, similar to the UVC-based algorithm in **Chapter 6**, was comprised of two identical 1D 8-layer CNNs (as opposed to 13-layer(15)), following the well-established 11-layer VGGNET structure(221), in order to derive the localisation of a VT episode in UVC space. One of the two architectures classified the UVC φ by discretising it into 17 classes, and the other returned UVC z and ρ after a linear regression layer. These CNNs were followed by two LSTMs and an attention mechanism, similarly to (15). Differences with (15) are also present in the kernel size and stride of pooling layers (2x2 instead of 3x3), in the absence of batch normalisation, in the number of input cells in LSTMs (128 and 64, instead of 512 and 512), and in the kernel size of the first two convolutional layers (5x5 instead of 3x3). These modifications were made after investigating the training and validation performances of the networks for different parameter sets, and choosing the best model. Activation functions in each layer (ReLU for CNNs, sigmoid for LSTMs) were not modified, and the networks were trained utilising the Adam optimiser, and a 0.2 dropout rate in the LSTM cells. Learning rates of 0.0001 and 0.0002, and batch sizes of 75 and 100 were utilised for φ and (z, ρ) architectures, respectively. Number of epochs were 70 and 50 for φ and (z, ρ) networks respectively, but early

stopping was prescribed in both. The AI algorithm was implemented in Python using TensorFlow(207), and the attention layer was exported from (222).

The AI model takes as inputs either 16-lead ECGs (standard 12-lead ECGs with the addition of 4 vector combinations as in **6.2.5 CNN Training and Testing**), or 8-vector EGMs, and predicts VT exit sites. The simulated traces of focal paced beats and post-infarct VTs were augmented to increase training datasets, and the robustness of the AI networks, as it will be described in **Data augmentation for training** below**.**

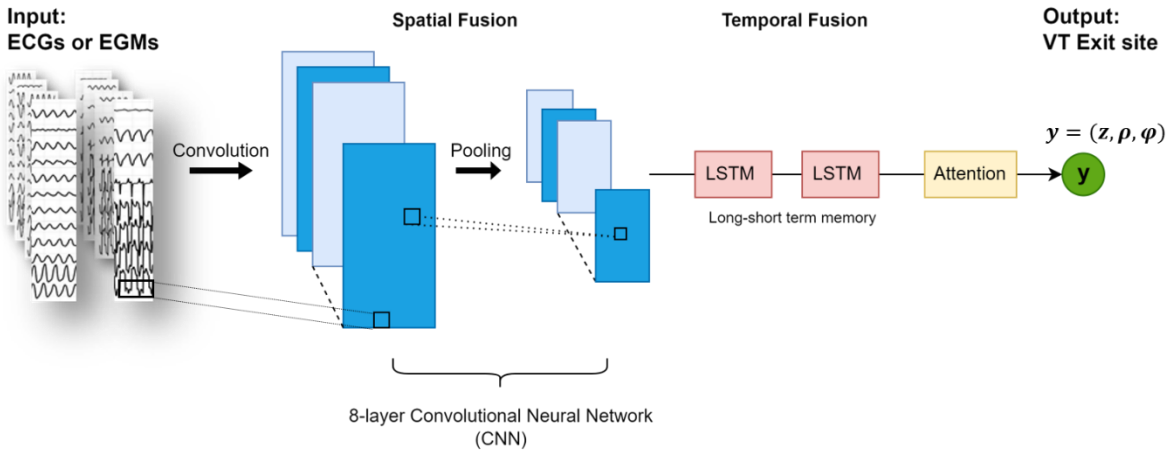

Figure 7.5. *Structure of the AI architecture for the automation of scar-related VTs from ECGs and/or EGMs. The AI model consists of an 8-layer CNN, that allows spatial fusion of the features present in the 16-lead ECGs and/or 8-vector EGMs, followed by two LSTM cells, allowing temporal analysis of the time traces. The model ends with an attention mechanism, followed by either a classification or regression layer. The model takes either ECGs or EGMs as inputs, and it predicts the VT exit site in universal ventricular coordinates.*

VT prediction

The exit site of a post-infarct VT is predicted by the AI model in the UVC space, similarly to our previous study. The performance of the model is also expressed in terms of LE: Euclidean distance in mm between the model predictions and the known VT exit sites from simulations, as described **Simulation Protocol**, after converting the predicted UVC-based site to a point in the mesh of interest.

Transfer Learning

To be able to develop a robust localisation algorithm, the AI model was initially trained on the paced beat ECGs and EGMs, and then parts of the networks (the last 4 CNN layers, LSTMs and attention) were re-trained on the traces of the post-infarct VTs. This transfer of knowledge between two similar tasks is known as *Transfer Learning*. This was done so that we could limit the number of post-infarct VT simulations to 500 (which are not as computationally efficient to simulate as focal paced beats), while still achieving an acceptable performance. Transfer learning also allowed us to provide important information to the networks using the initial pacing training (e.g. patient-specific anatomy, ECG/implanted device lead locations, relationship between extracellular potentials and locations in the heart), which could have a number of benefits for clinical application, as we will see later on.

Data augmentation for training

Before describing the training and testing scenarios investigated, we will briefly mention the post-processing applied to the paced beats and post-infarct VT ECGs and EGMs to increase training datasets. QRS complexes of the second paced beats were extracted, and replicated six times to create a total signal of length $2.4s$ including 6 separate QRS complexes. Then, three different $1.5s$ long windows of the signals were taken into consideration (at $t = 0, 240, 690\, ms$), to reduce the sensitivity of the algorithm to the starting point of the input signals. In addition, we considered five different levels of white Gaussian noise - SNR of $10, 15, 20, 25, 30\, db$. A total of 266,724 16-lead ECGs and 8-vector EGMs of simulated focal paced beats were therefore available for initial training of the AI architecture.

For the post-infarct VTs, $4.6s$ long signals (VT periods mentioned **Simulation Protocol**) were stretched/compressed by factors of $0.9, 1.5\ and\ 1.7$ to increase VT cycles per scar, and seven different levels of white Gaussian noise were added (SNRs $5, 10, 15, 20, 25, 30, 35\, db$). Seven different $1.5s$ long windows were extracted at $t = 0, 500, 700, 900, 1100, 1300, 1500\, ms$, for the

same reason as above. A total of 96,000 16-lead ECGs and 8-vector EGMs were available for transfer learning.

Training and Testing

Once the signals were post-processed, they were used as inputs to the AI model, and we investigated two computational scenarios, named *Scenario 1* and *2*. In *Scenario 1*, the AI model was trained on focal paced beats of all five torsos, and then it was re-trained five separate times on post-infarct VTs of four torsos (excluding a different torso every time). These five re-trained models were each tested to localise simulated post-infarct VTs from ECGs/EGMs of the torso excluded during transfer learning. In *Scenario 2*, the AI model was trained five separate times on focal paced beats of four torsos (excluding a different torso every time), and each trained model was re-trained on the post-infarct VTs of the same four torsos, and then tested on *unseen* post-infarct VTs of the *unseen* torso model. In each testing case, $1.5s$ long 16-lead ECGs and 8-vector EGMs (no noise) of 100 simulated post-infarct VTs were utilised (un-processed signals). The AI model was tested at different starting points of the signals, and the predictions of each window were averaged across the different windows for each torso, and scenario, returning 10 LEs.

The analysis of these two computational scenarios is of importance to understand how clinical applicability of our platform can be carried-out. As it will be more evident in the remainder of this Chapter, it is of interest to understand whether the direct AI prediction of a VT episode from an ECG or EGM trace (which would correspond to *Scenario 2*) could return equally desirable results to providing the AI with some information of a patient's set-up via modelling (*Scenario 1*). From a ML prospective, it could be argued that *Scenario 1* contains some *data leakage* (i.e. knowledge of the hold-out test set is leaked into the training dataset). However, this is not the case as the traces of the testing torso seen by the network during initial training constitute a different problem. In addition, some difference is present in the testing torso model itself (the torso seen during initial training has no infarct modelled).

7.2.2 Clinical Case

Our proposed computational-AI framework was tested in clinical settings, by utilising CT and ECGi(28) data from a patient with refractory (incessant) VT. The patient underwent successful cSBRT, which was indicated due to previous extensive cardiac surgical interventions, including mechanical aortic and mitral valve replacement, which precluded direct LV access for conventional VT ablation. The VT substrate of the patient was likely ischemic, due to an emergency bypass performed after the valve procedures, suggesting occlusion of a coronary vessel and possible ischemia (and therefore, possible infarct). The clinical VT (cycle length $\sim 340\, ms$) was induced with non-invasive programmed simulation via a CRT-D device. After careful clinical interpretation of the epicardial VT map (**Figure 7.6A-B**) reconstructed from ECGi during the programmed stimulation, two target volumes were suggested for ablation: segment 9 and 10. This decision was also in agreement with the ECV values measured from CT, suggesting the location of an infarct in the LV/RV septum (**Figure 7.6C-E**). The ECG traces of this clinically-induced VT were used to test our AI algorithm (blinded to the clinical targets), following two scenarios similar to the computational investigation described in **Training and Testing**, and then the predicted VT exit sites were compared with the ablation targets and reconstructed VT maps.

Clinical Scenario 1: VT Prediction following Computational Simulations

A 3D torso model of the patient was constructed from patient CT data, in a similar way to **Patient-Specific Torso Models.** On this newly generated myocardial mesh, only paced beats were simulated (in ~3000 randomly chosen locations as previously described), and corresponding ECGs were computed. These traces were used in combination with the paced beats of the previous five torso models, as additional training data, for the initial training of the AI algorithm.

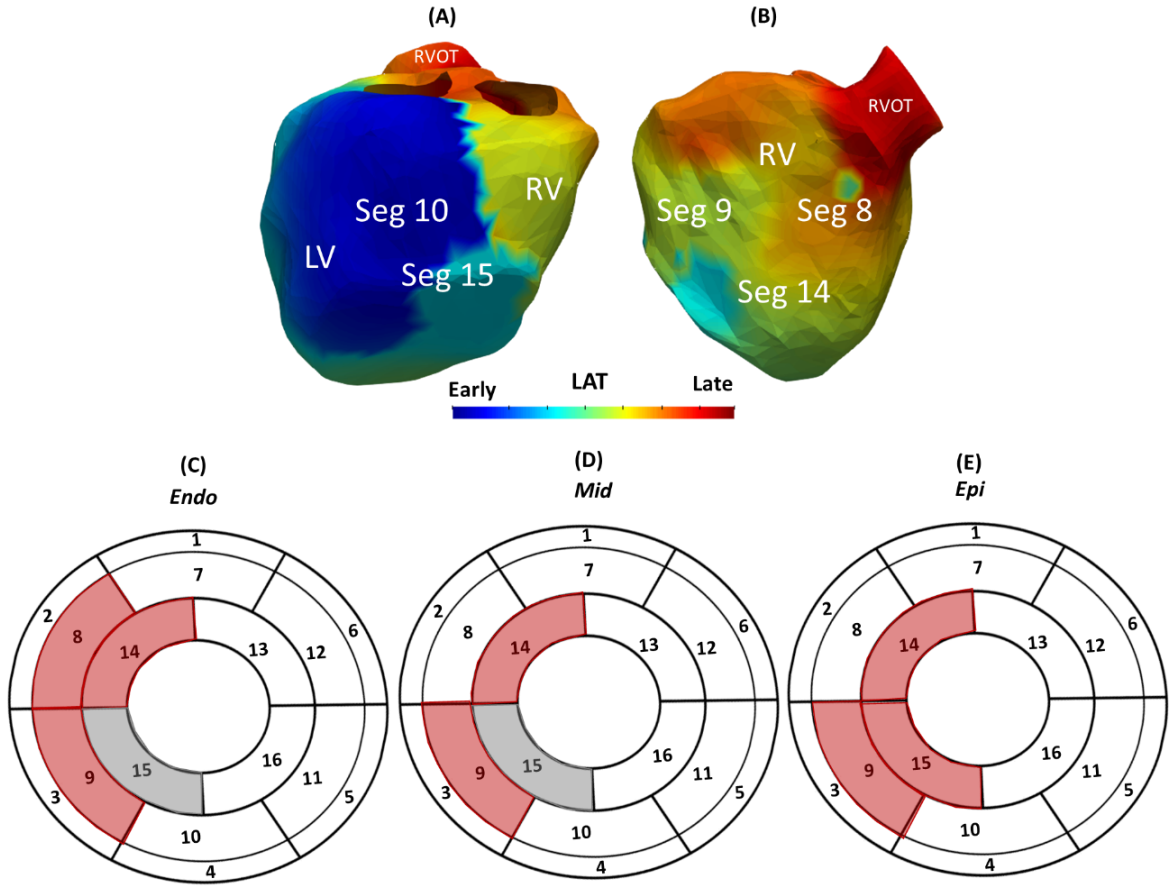

Figure 7.6. *Clinical investigation of cSBRT patient with refractory VT. (A) and (B) show the epicardial activation map reconstructed from ECGi (different views). Early activation (blue) may signify location of exit site (in segment 10), with possible isthmus in segment 8/9. (C) – (E) show possible slow conduction regions (red) and no conduction (grey) for endocardial, epicardial and mid-cardiac segments, respectively, extracted from ECVs,*

No post-infarct VTs were simulated on this patient's mesh, given that we previously showed the possibility of testing the AI on a torso model that was only seen during initial pacing training (*Scenario 1*). Therefore, transfer learning was performed by using the post-infarct VT datasets from the five previous torsos. By performing only simple paced beat simulations, without modelling any infarct, we were able to reduce computational load, while tailoring the AI training to the patient-specific anatomy and clinical setting. The AI model trained in this way was tested on the clinical 16-lead ECG traces derived from ECGi (as described below in **Clinical Scenario 2: Direct VT Prediction**) of the clinically-

induced VT, and the predicted exit site was compared to the ablation targets in the 2D 17-segment AHA model and 3D patient-specific geometry.

Clinical Scenario 2: Direct VT Prediction

Body surface potentials were collected with Medtronic CardioInsight Noninvasive 3D Mapping system(28), and utilised to compute standard 12-lead ECGs (with the additional 4 vectors as above) of the clinically-induced VT. These were used as sole direct inputs to the previously trained AI architecture, returning the VT exit site with no prior knowledge on patient's anatomy and EP modelling simulations.

7.3 RESULTS

After describing the computational-AI platform developed to automate localisation of post-infarct VTs from ECGs and implanted device EGMs, and illustrating the different computational and clinical scenarios investigated, we will now present and analyse the results and performance of our platform. We will first report errors from the localisation of simulated data, and then illustrate how the clinical ablation targets and clinical VT investigation compare with the AI predictions.

7.3.1 Evaluation of the Computational-AI Platform on Simulated Data

Firstly, we evaluated the localisation performance of the proposed computational-AI platform on simulated post-infarct VTs under two scenarios. In *Scenario 1*, we localised *unseen* VT episodes from ECGs and EGMs of models *seen* during initial pacing training. In *Scenario 2*, we localised *unseen* VT episodes from ECGs and EGMs of models completely *unseen* during any training stage.

Scenario 1: VT Prediction of Models Seen during Pacing Training

In this Scenario, the AI was tested on localising *unseen* simulated post-infarct VTs from ECGs and implanted device EGMs of models *seen* during the initial pacing training. In doing so, the AI had only limited knowledge on the torso model in question. Across the torso models, the algorithm successfully

localised post-infarct VTs from ECGs with mean LE $9.61 \pm 2.61\,mm$, ranging from $5.92 - 12.76\,mm$ (**Figure 7.7A**). Encouragingly, the localisation performance from device EGMs was similar to ECGs, with slightly higher mean LE across torsos, $13.10 \pm 2.36\,mm$, ranging from $10.04 - 16.36\,mm$ (**Figure 7.7A**). The predicted VT exit sites can be visualised in the standard 2D 17-AHA LV model, or in the patient-specific 3D myocardial mesh. An example of an ECG-based VT prediction for torso (B) is shown in (**Figure 7.7B-C**), and is compared to the known VT exit site.

Scenario 2: VT Prediction of Models Unseen during Any Training

In this Scenario, we investigated how the absence of a patient-specific computational model during initial pacing training affected the localisation performance of our AI algorithm in localising entirely *unseen* simulated post-infarct VTs. In this scenario, data simulated on a torso model was excluded from both training stages, and the AI model was tested on post-infarct VT signals of the excluded torso (thus with no prior knowledge of the model in question). Across models, ECG-based localisation returned mean LE $16.59 \pm 2.79\,mm$, ranging from $12.41 - 19.68\,mm$ (**Figure 7.8A**). Successful localisation of post-infarct VTs was also achieved utilising EGMs, with a mean LE $15.80 \pm 4.65\,mm$, ranging from $12.42 - 22.79\,mm$ (**Figure 7.8A**). Errors for ECG-based predictions increased in all five torsos compared to *Scenario 1* ($\Delta LE = 6.98\,mm$), whereas EGM-based predictions seemed to be less affected by initial pacing training ($\Delta LE = 2.70\,mm$). **Figure 7.8B-C** shows the ECG-based prediction of the same VT episode as in *Scenario 1.*

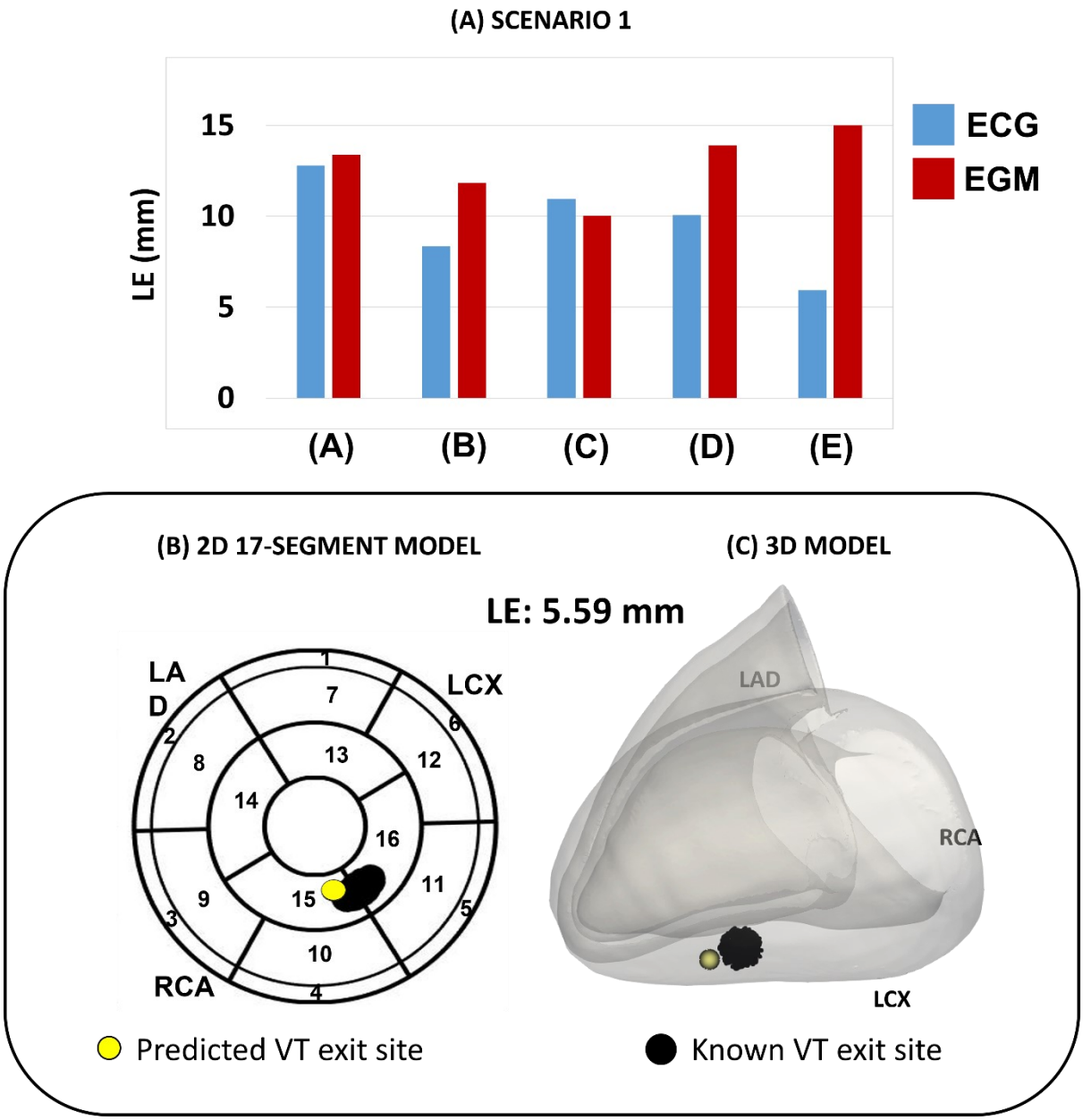

Figure 7.7.*Computational Scenario 1: VT prediction of models seen during pacing training. (A) shows LEs across torso models for patients (A) – (B). ECG-based LEs are shown in blue, and EGM-based LEs in red. (B) and (C) report an example of how a predicted VT exit site (yellow) compares to the known VT exit site from simulations (black) in 2D and 3D, respectively.*

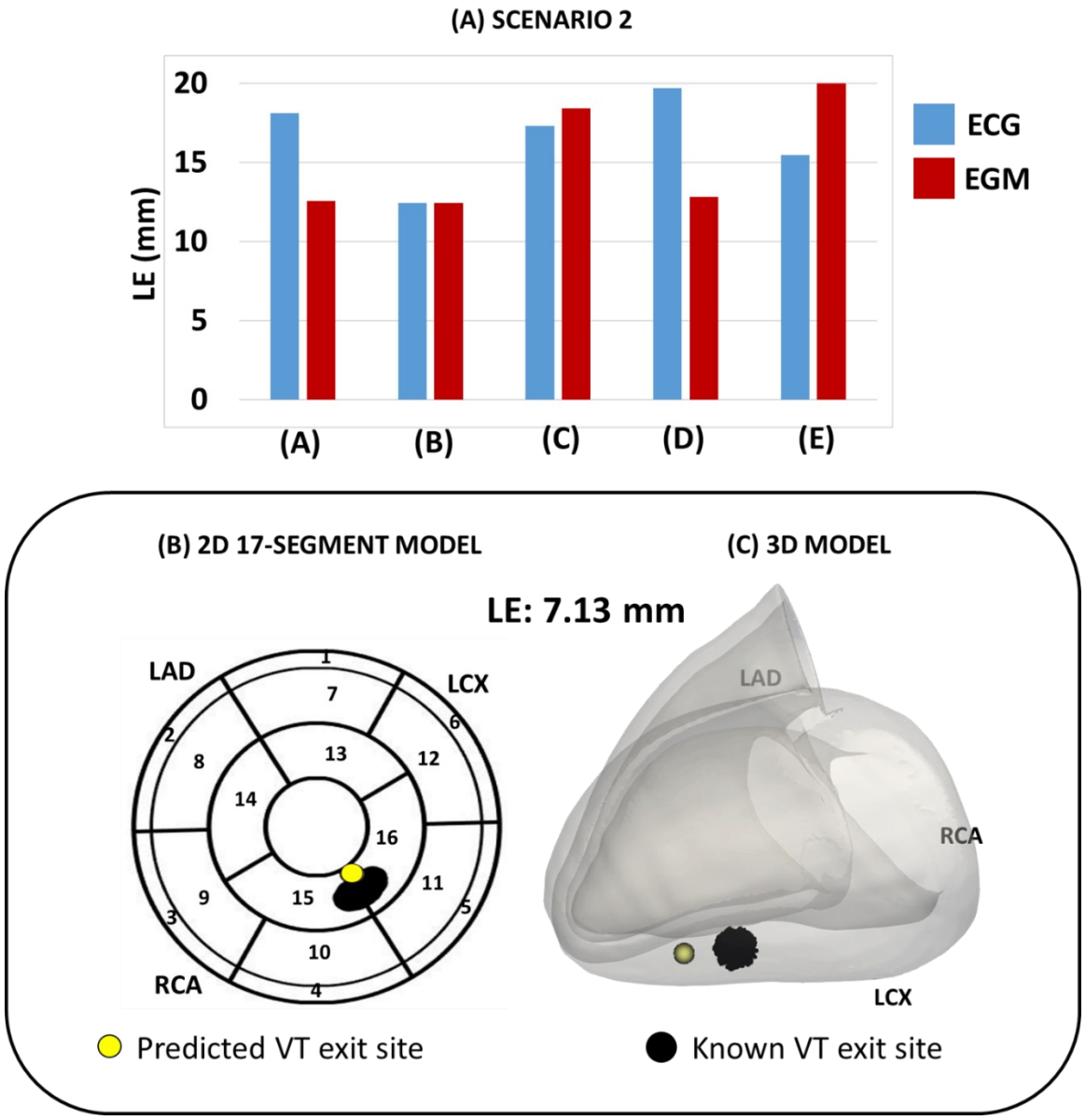

Figure 7.8. *Computational Scenario 2: VT prediction of models unseen during any training. (A) shows LEs across torso models for patients (A) – (B). ECG-based LEs are shown in blue, and EGM-based LEs in red. (B) and (C) report the same example as above, but when the torso model was not seen during initial pacing training. Here, we can see how the predicted VT exit site (in yellow) compares to the known VT exit site from simulations (in black) in 2D and 3D, respectively.*

7.3.2 Evaluation of the Computational-AI Platform on Clinical Data

Finally, the localisation performance of the proposed platform was evaluated on clinical data, following similar scenarios to the computational investigation presented above. The AI architecture was tested on the patient's VT ECGs after integrating imaging and simulation data into the pipeline (*Clinical Scenario 1*), and directly tested on the patient's VT ECGs (*Clinical Scenario 2*).

Clinical Scenario 1: VT Prediction following Computational Simulations

We investigated the localisation of the clinically-induced VT episode after generating a patient-specific model from the patient imaging data, and utilising the newly simulated data to train part of the AI model. With this increased patient-specific training data, the algorithm localised the VT episode from the clinical ECGs in the upper part of segment 15, closer to both segment 9 and 10 (**Figure 7.9A-B**). Detailed (blinded) clinical analysis of epicardial activation patterns from the ECGi jacket data during the induced VT suggested VT exit site to be in segments 9 and 10.

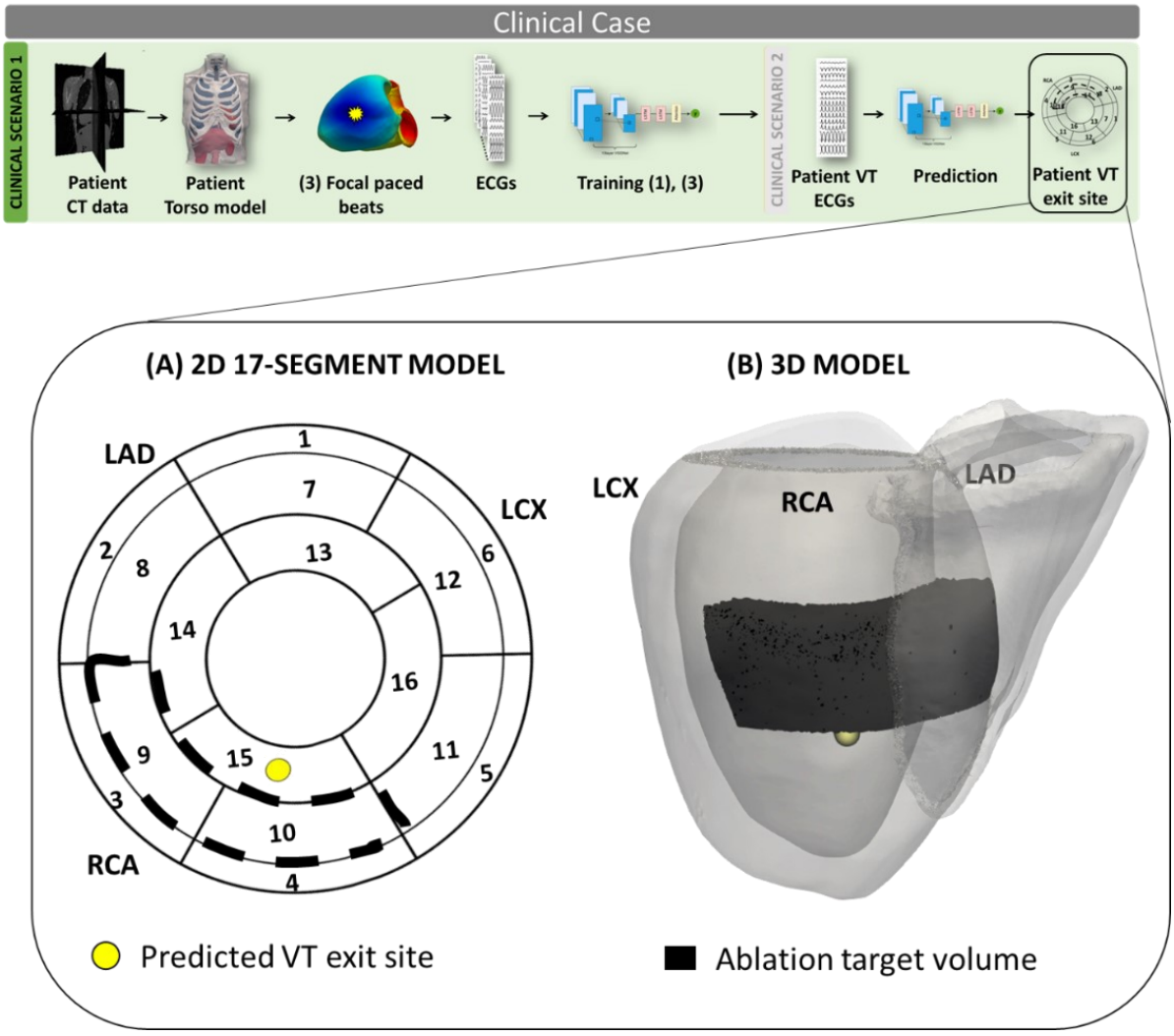

Figure 7.9. *Clinical Scenario 1: VT prediction following simulations. (A) and (B) show how the predicted VT exit site (yellow) compares to the clinical ablation target volumes (black) in 2D and 3D, respectively. This result should also be compared to clinical investigation of epicardial VT map and ECV patterns (**Figure 7.6**).*

Clinical Scenario 2: Direct VT Prediction

The AI model trained on simulated data of all five torsos was directly tested on the ECG traces (**Figure 7.10A**) recorded during the clinically-induced VT. The model prediction was now located in the inferior-apical part of segment 11, in close proximity to segment 10 (**Figure 7.10B-C**)

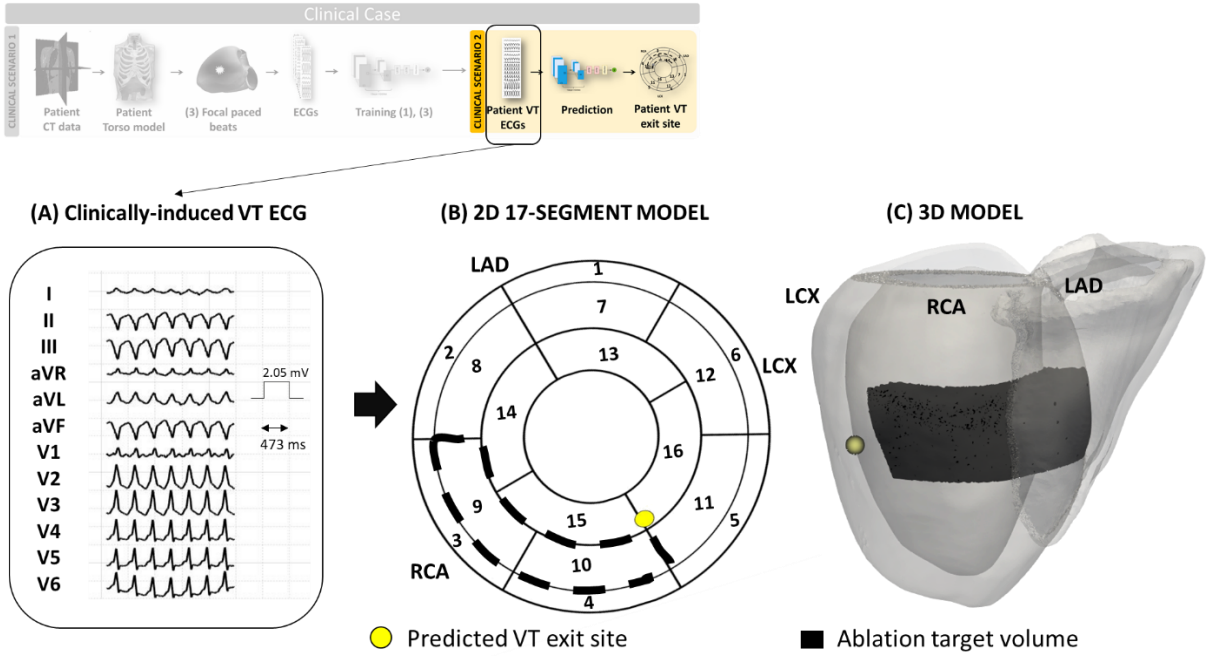

Figure 7.10. *Clinical Scenario 2: VT prediction following simulations. (A) and (B) show how the predicted VT exit site (yellow) compares to the clinical ablation target volumes (black) in 2D and 3D, respectively. This result should also be compared to clinical investigation of epicardial VT map and ECV patterns (**Figure 7.6**).*

7.4 DISCUSSION

In this study, we proposed a novel, non-invasive platform for automating the localisation of post-infarct VTs from ECGs and device EGMs, aiming at guiding pre-procedural ablation planning. Building upon the work of the previous Chapters, we were able to develop an algorithm that 1) accurately and reliably localises VT exit sites from ECGs, with precision comparable to existing algorithms, while simplifying the overall pipeline, 2) achieves a comparable localisation performance from intracardiac EGM recordings stored in implantable devices, and 3) can be feasible in clinical settings.

7.4.1 Successful Localisation of Post-Infarct VTs from ECGs

When predicting post-infarct VTs simulated on torso models that were only *seen* during the initial pacing training (*Scenario 1*), our platform successfully localised the corresponding exit sites from ECGs with mean error $9.61 \pm 2.61\ mm$ across models. In *Scenario 2*, when the AI model had no prior knowledge on the testing torso, mean error was slightly higher, $16.59 \pm 2.79\ mm$. However, both performances of our platform, with LE $<= 17\ mm$, may be deemed clinically useful in identifying initial VT ablation targets and guiding pre-planning procedures non-invasively and efficiently, given that the majority of VT ablation lesions are often extensive, and greater than our errors. Moreover, we improved on previous methods which localised only to the nearest AHA segment(48,49), or utilised more complex pipelines and required the acquisition of EAM data (51,160,169,170).

Our AI platform was seen to be robust to differences in patient anatomies, with little variation in LEs across torso models (standard deviation $< 3\ mm$ in both *Scenario 1* and *2*). However, it is important to mention that lower errors in *Scenario 1* compared to *2* suggested the necessity of integrating patient-specific simulations in the initial training stage of the platform to provide some information to the network that would increase accuracy later in the localisation of post-infarct VTs. Nevertheless, the localisation performance in *Scenario 2* may be of benefit for immediate identification of VT critical sites (requiring only patient ECG traces as input), thus showing the utility of our platform in the absence of imaging data.

As extensively reviewed in **4.3 Targeting Scar-related VTs**, the majority of current methods that utilise the ECG to predict VT substrates either rely on clinical expertise, can only localise an episode within large LV anatomical regions (for instance, with areas $> 10\ cm^2$ (49)), or propose a continuous localisation that is dependent on the acquisition of EAM data and/or more complex, and indirect pipelines. To the best of our knowledge, this is the first study that has utilised a computational-DL approach to automate localisation of post-infarct re-entrant VTs, achieving a 3D localisation precision that may be of benefit in clinical practice.

7.4.2 Successful Localisation of Post-Infarct VTs from EGMs

Not only did our platform successfully localise VTs from ECGs, but it also achieved a good performance from generic implanted device EGMs, with overall LEs $< 16\,mm$, which is comparable to using ECGs. As above, anatomical differences between the in-silico patients did not have a great impact on the localisation. However, interestingly, there was a smaller increase in LEs between *Scenario 1* and *2* ($\Delta LE = 2.70\,mm$) compared to ECG-based localisation ($\Delta LE = 6.98\,mm$). This finding would suggest the reliability of stored EGM recordings for direct localisation of the clinical VT, when the tachycardia is non-inducible or unmappable, and may show great potential to guide non-invasive ablation therapies, such as cSBRT.

In previous Chapters, we saw that there is a need for more extensive investigations into the utility of stored EGMs to guide ablation planning to target the clinical episodes, and potentially reduce the need for VT induction. Previously, we showed how EGM-based paced-maps and EGM-based automated focal localisation algorithms can achieve comparable results to using ECGs, especially when increasing the number of sensing vectors used. In this Chapter, we went a step further, and showed how the enhanced information contained in sensed EGMs from multi-polar devices can achieve robust performance in the localisation of more complex arrhythmic episodes, such as re-entrant VT post-infarction.

7.4.3 Applicability of our Platform in Clinical Settings

Finally, in contrast to previous Chapters, in this study we were able to show the applicability of our computational-AI platform in clinical settings. In both clinical scenarios investigated, the exit site of the clinically-induced VT was localised in proximity to segment 10 from the clinical VT ECGs, which was consistent with the clinical ablation targets (segment 9 and 10), and with the clinical investigation of the reconstructed VT EAM maps, identifying the exit site in segment 10. Moreover, by analysing the ECVs from the patient's CT data, the scarred tissue was mostly located near/in the septum. It is

important to mention that while *Clinical Scenario 2* – direct VT prediction from ECGs without the creation of a patient-specific computational model – can return immediate results, with acceptable accuracy, the creation of a patient-specific model and integration of simple pacing simulations into the pipeline (*Clinical Scenario 1*) can increase localisation accuracy further, at a relatively low computational expense. Thus, in patients for which invasive mapping cannot be performed, our computational-AI platform may provide rapid ECG-based localisation of post-infarct VTs, accompanied by a more thorough, patient-specific analysis, if CT imaging data is available. In future studies, this work might be of importance to investigate alternative, non-invasive tools to aid ablation procedures (e.g. cSBRT) where invasive mapping cannot be performed. Although implanted device EGMs of this patient were not available to evaluate EGM-based localisation performance, from our computational analysis carried-out in the previous sections, we believe that EGM-based localisation of the clinical VT would be similar to ECG-based.

7.4.4 Study Limitations

Simulating and inducing post-infarct VTs via common computational methods (as seen in **5 In-Silico Pace-Mapping**) can be very challenging, as well as computationally expensive. Because of this, we simplified the problem by simulating figure-of-eight VT circuits from virtual and simplistic scars, which may limit the application of our platform in the presence of diffuse fibrosis, and/or more complex VT morphologies. In the future, it would be useful to develop pipelines to generate more complex infarct geometries while minimising the computational load of the simulations, to investigate their impact in the final localisation of the VTs. Other types of re-entrant VTs are fascicular/bundle branch. Although the inclusion and engagement of the conduction system would increase significantly the complexity of our models, it would be useful to model a simplification of the bundle of his and branches, and reproduce re-entrant episodes with and/or without involvement of myocardial tissue. Given that fascicular/ bundle branch VTs behave electrophysiologically very similarly to the VTs we addressed in this study(223), where the circuit trajectory can be simplified to a figure-of-eight with a region of slow

conduction and an exit(224,225), our current DL algorithm may still identify the critical region maintaining fascicular VT/bundle branch reentry.

Our focus on localising VT exit sites to improve ablation outcomes was primarily dictated by the difficulties in localising isthmuses during pace-mapping due to changes in ECG morphology seen between entrance(s) and exit(s). Moreover, the majority of research and clinical interest, as reviewed in **Chapter 4**, seemed to be directed toward the identification of exit sites. However, it would be useful to compare localisation performances of our DL architecture when targeting isthmuses, which may improve localisation performance when dealing with more complex VT morphologies, where multiple exit site(s) and dead ends might be present.

Another limitation of this study is the inclusion of only one patient for clinical evaluation. In the following Chapter, we will test our platform on more clinical ECG data. Furthermore, we were not able to retrieve the EGM data. In clinical practice, retrieving 8-lead EGMs may be challenging from the current generation of implanted cardiac devices, as many implanted patients do not have an SVC coil, or multipolar LV lead, or are not able to record and/or store multiple vectors at a time. Nonetheless, device technology and design are constantly evolving, which may open up possibilities of additional EGM sensing vectors, driving VT management beyond using the standard ECG. Finally, future studies may extend validation of our platform to a wider variety of CA patients in order to quantify localisation performance against more specific ablation targets.

7.5 CONCLUSION

In this Chapter, we have developed a computational-AI framework that may be utilised for direct localisation of post-infarct VT exit sites from ECGs and/or implanted device EGMs, in the absence of patient imaging data, or in combination with computationally efficient, patient-specific modelling, ultimately enhancing safety and speed of pre-procedure ablation planning. In comparison to **Chapter 5**, where we proposed an in-silico pace-mapping approach to localise post-infarct VTs, the platform

presented here may be more efficient and less dependent on imaging data, and does not require accurate modelling of the infarct substrate. In addition, we expanded on the limitations and findings of **Chapter 6**, by including more torso models and ECG/EGM lead variability in the AI training stages, as well as attempting evaluation of the platform with clinical data. In the following Chapter, we will explore different clinical scenarios, and show how the work so far presented can guide initial ablation planning, with promising results.

8

CLINICAL EVALUATION

In the previous three Chapters, we used simulated implanted device EGMs, as well as ECGs, to construct pace-maps, and automate the localisation of both focal and scar-related VTs, with the aim to guide ablation planning non-invasively. Furthermore, in the concluding paragraphs of Chapter 7, we demonstrated how we could apply our computational-AI platform in clinical settings, showing the feasibility of automating VT detection from clinical VT ECGs. In this Chapter, we will focus on extending in-silico pace-mapping and scar-related VT localisation to other clinical episodes and analyse the benefits and challenges of our work for future applications. In Section 8.1, we will provide a brief introduction to the problems we will aim to tackle. In Section 8.2, we will present the workflows of our previously described platforms to aid cSBRT ablation planning of three VT patients. In Section 8.3 and 8.4, we will illustrate how both ECG-based pace-maps and AI VT predictions can be used jointly to aid clinical pre-procedure ablation planning, and how to improve the work of this Thesis to enable further clinical translation.

8.1 INTRODUCTION

In previous Chapters, we thoroughly reviewed and described the importance and power of computational simulations, as well as automated DL approaches, to aid VT ablation planning from recorded extracellular signals (ECGs and/or implanted device EGMs). The clinical applicability of all our platforms faces many non-trivial challenges, such as the high variability in data collection, the difficulty in establishing whether a computational-based (or AI-based) result can be accurate and useful, and the time required to create such models/algorithms.

In the previous Chapter, we were able to illustrate how our scar-related VT localisation platform could be used in clinical settings to aid cSBRT planning. Despite not being able to extract and use the EGM recordings stored in the patient's CRT-D, we obtained fairly promising results from the standard surface ECGs. In this Chapter, we seek to extend automated VT localisation to two additional cSBRT patients, as well as evaluating our in-silico pace-mapping study against clinical ECGs and improving on some of the limitations of **Chapter 5**. Finally, we will show the value of combining all our studies to provide a more robust visualisation and description of a VT episode for clinical use. Ultimately, we aim to investigate and discuss the benefits and potential pitfalls of this Thesis in real-life problems, and tackle some of the clinical challenges mentioned above.

8.2 METHODS

In this Section, we will attempt to reproduce the workflows presented in **Chapter 5, 6** and **7** across three cSBRT patients. For each patient, we will first illustrate the clinical picture and VT history, which will be of interest to understand and interpret the results of our platforms. Then, we will move on to describe how we parametrised the models to generate accurate in-silico ECG-based pace-maps, and how to automate VT localisation from clinical ECGs.

8.2.1 Patient 1

We will begin our clinical investigation by generating in-silico pace-maps for *Patient 1*, which was introduced in **Chapter 7.** Briefly, they were referred for cSBRT due to history of refractory VT, unsuccessful CA procedures, and presence of mechanical valves which precluded invasive catheter access. The VT episode (cycle length $\sim 343\ ms$) was identified in $Segment\ 9$ and 10, after careful interpretation of the patient's imaging and ECGi datasets. In the previous Chapter, we utilised these datasets to create a detailed 3D torso model of the patient, position the ECG leads according to the CardioInsight Medtronic(28) vest, and localise the VT episode from the clinical ECG traces via our computational-AI platform. Here, we will perform in-silico pace-mapping, following the steps outlined in **Figure 8.1B-C**.

Tissue Parametrisation from ECVs

After the torso model was generated from CT data (**Chapter 7**), ECVs were computed on the epicardial, endocardial and mid-wall surfaces of the 17-AHA segments of the patient's LV. The corresponding scar pattern was identified after assigning ECVs to three categories (healthy, BZ and infarct)(67), as illustrated in **Figure 8.2**. The infarct was located in *Segment 15* (sub-endocardially), with extensive BZ in *Segment 9, 10* and *14*. These ECV distributions were then used to parametrise CVs and conductivities along and transverse to the fibre orientation of the biventricular mesh, similarly to (226).

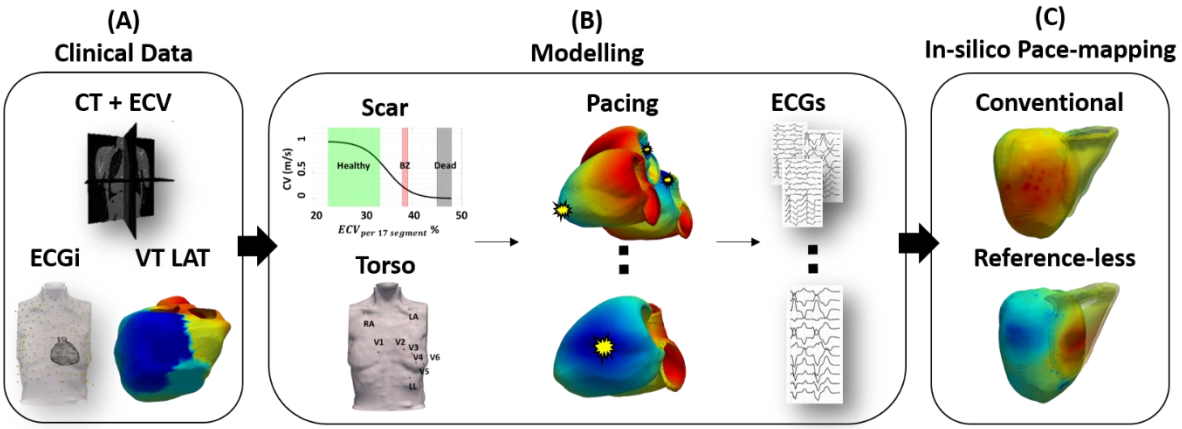

Figure 8.1. *In-silico pace-mapping workflow for Patient 1. (A): Clinical data involved acquiring whole torso CT scans and ECV measurements, as well as ECGi measurements during CRT-D pacing and VT induction. (B): Scar was modelled by parametrising CVs and cardiac tissue conductivities according to ECVs on the 17-AHA segments. Then, rapid pacing around the LV was performed within our RE-LF environment to obtain different ECGs that could be compared against the clinically-induced VT ECG and construct in-silico conventional and reference-less pace-maps (C).*

Briefly, a sigmoid function was used to describe the changes in EP properties as ECV increases. The upper bound of the sigmoid function was found by first parametrising the healthy tissue CVs so that the total activation of the ventricles (computed with the eikonal method, see **Reaction-Eikonal Formulation**) matched the clinical measurements. Then, the CVs and conductivities were further tuned so that the simulated QRS duration (computed with RE-LF) matched the measured, clinical QRS duration (from one of the pacing sites of the CRT-D) (205). The lower bound of the sigmoid function was $CV = 0.01\ m/s$, corresponding to non-conducting tissue. The inflection point, at $ECV \sim 35\ \%$ (between healthy and BZ), was assigned a $CV \sim 0.5455\ m/s$. To assign the resulting CVs and conductivities to each endocardial, epicardial and mid LV segments, the 3D 17-AHA segment model of the patient's mesh was further divided into 51 segments, splitting each segment along the transmural UVC direction (ρ).

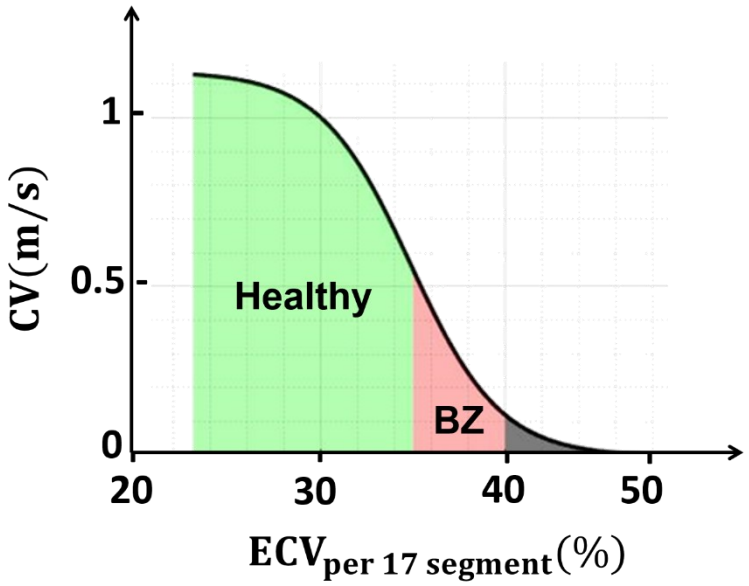

Figure 8.2. *CV parametrisation according to ECVs: Patient 1. A sigmoid function was used to relate ECVs to corresponding CVs in healthy, BZ and dead tissue.*

In-silico Pace-mapping

To perform in-silico pace-mapping, we placed the 9 ECG leads according to the ECGi vest, after registering our torso model to the CardioInsight(28) reconstructed meshes. The corresponding ECG traces of the clinically-induced VT (obtained via non-invasive programmed stimulation from the CRT-D) can be seen in **Figure 7.10A**. The RE-LF formulation in CARP(104), previously described, was used to simulate ~ 343 paced beats across the LV, and corresponding ECGs. Each location was stimulated twice ($bcl = 600\,ms$), and the second beat of each pace was extracted and used to generate ECG-based conventional and reference-less pace-maps, as in **Chapter 5**. Briefly, conventional ECG-based pace-maps are generated by aligning the QRS complex of each simulated paced beat to the reference VT QRS, computing correlation coefficients between each pair, and averaging the results across the highest 10/12 leads. The final 3D correlation map is then generated by linearly interpolating the correlation coefficients on each paced location to the myocardial mesh. On the other hand, reference-less pace-maps are obtained by comparing QRS complexes (in a similar manner as before) of neighbouring paced beats (within a $radius = 20\,mm$). Conventional pace-mapping can provide information on the exit and entrance sites of a re-entrant circuits, whereas reference-less pace-mapping can return the location of a high gradient, signifying the presence of potential channels driving the VT.

8.2.2 Patient 2

Another patient with refractory VT (*Patient 2*), was referred for cSBRT, after two failed CA procedures, and ablation complications (stroke). The patient had ischemic cardiomyopathy, with LV impairment and a history of cardiac arrest. The VT (cycle length $\sim 270\,ms$) was induced via non-invasive programmed stimulation from the CRT-D, and the final ablation targets were identified in *Segment 4*, *10* and *11*, after careful clinical evaluation of the reconstructed LAT maps and ECVs**.** As **Figure 8.3** illustrates, similar imaging and ECGi datasets to Patient 1 were available. A 3D torso model, including lungs, bones, skin, fat + muscle, aorta, cardiac blood pools and walls, was generated, as in **Chapter 5.**

8.2 Methods

Briefly, a thorax CT scan (chest and upper abdomen) was segmented in *Seg3D*(180), and a higher resolution heart scan in *Siemens Axseg v4.11*(181). The mesh of the combined segmentations was then generated using *Tarantula*(26). In contrast to previous models, this torso mesh was much shorter along the sagittal plane, and less detailed (lacked some major abdominal organs, such as liver, kidneys, spleen, stomach). Ventricular fibre architecture(217), UVCs(182), 17-AHA and 51 LV segments were computed, as previously done.

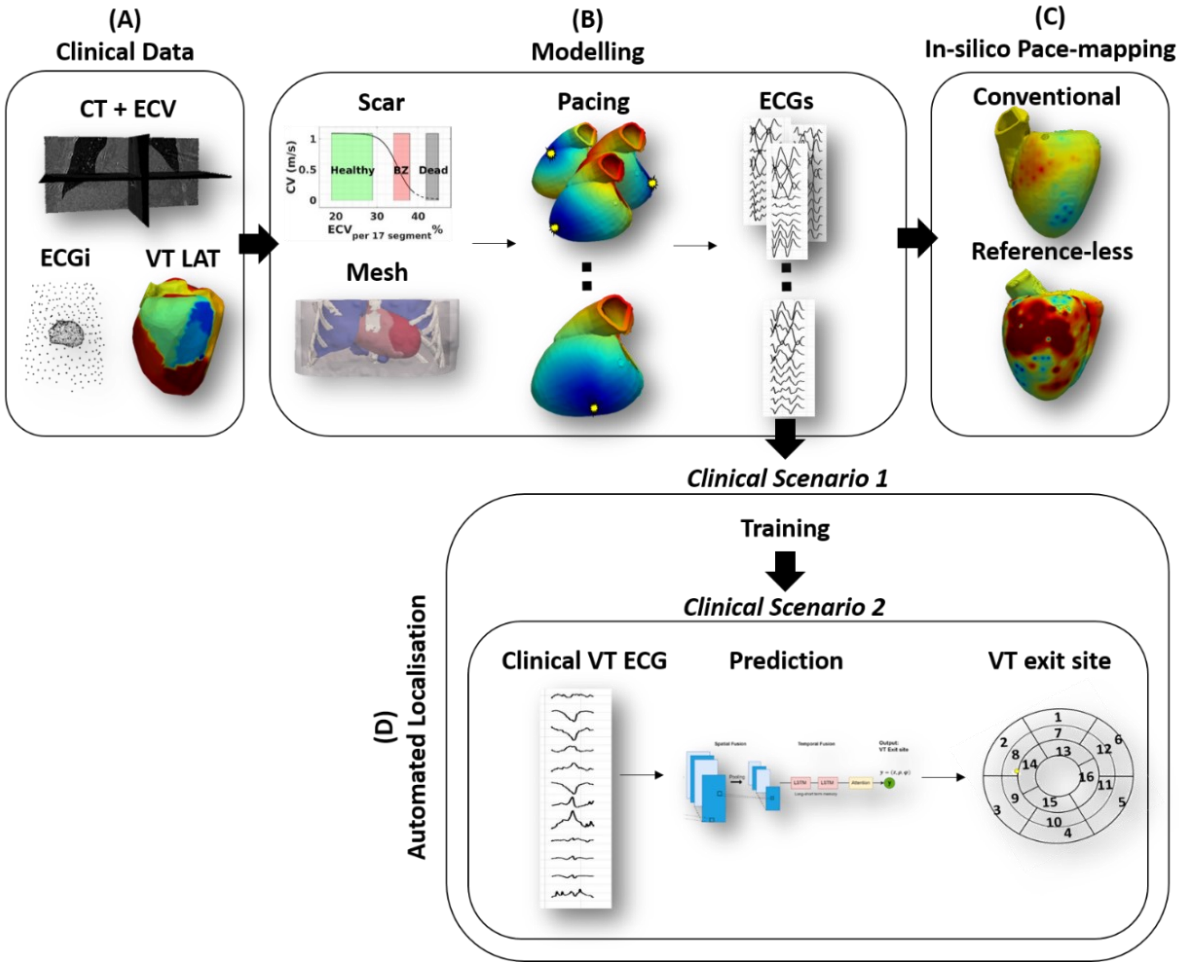

Figure 8.3. *Workflow for Patient 2: clinical evaluation of in-silico pace-mapping and automated scar-related VT localisation. (A): As for Patient 1, CT scans, together with ECV and ECGi measurements, were available for Patient 2. (B): ECVs on the 17-AHA segments were used to model the scar, and parametrise the tissue EP accordingly. Our RE-LF environment was used to simulate rapid pacing around the LV, and corresponding ECGs, to construct (C) in-silico pace-maps, and (D) test our computational-AI platform under two scenarios.*

Tissue Parametrisation from ECVs

As before, the scar was modelled from ECVs. However, as **Figure 8.4** shows, ECVs were generally lower ($< 38.8\ \%$), and we only identified two segments with reduced conduction: Segment 9 and 14 (**Figure 8.5D-E**). CVs and conductivities were parametrised following a similar procedure to above. Firstly, EP properties in the healthy myocardium were found by matching the measured activation times and QRS duration to the simulations. Then, a sigmoid function was fitted to find CVs at each different ECV. The inflection point (at $ECV = 35\%$) was assigned a $CV = 0.5\ m/s$.

In-silico Pace-mapping

Similarly to *Patient 1*, the ECG lead locations were modelled according to the ECGi vest, and ~ 369 paced beats across the LV were simulated within our efficient RE-LF environment. The corresponding traces were used to generate both conventional and reference-less pace-maps as before. The ECG traces of the clinically-induced VT can be seen in **Figure 8.5A**, and the VT activation map reconstructed from ECGi in **Figure 8.5B-C**.

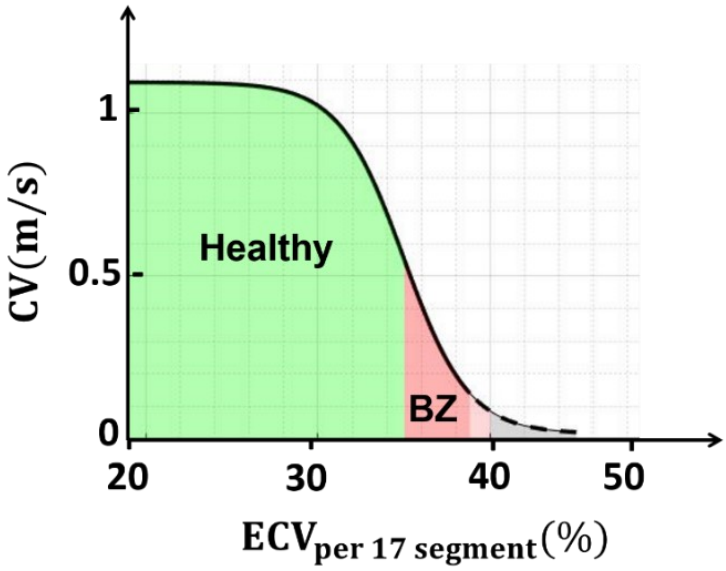

Figure 8.4. *CV parametrisation according to ECVs: Patient 2. A sigmoid function was used to relate ECVs to corresponding CVs in healthy, BZ and dead tissue. For this patient, ECVs were < 38%, and therefore the cardiac tissue was predominantly modelled as healthy,*

Automated scar-related VT localisation

As in **7.2.2 Clinical Case**, we tested the performance of our computational-AI platform under two different scenarios, that will be illustrated below. To recap, the AI architecture takes an ECG as input, and predicts the exit site of the VT in UVC space, that can be visualised in the 2D 17-AHA model and in the 3D patient-specific mesh.

***Clinical Scenario 1*: VT prediction following computational simulations**. In this scenario, we performed simulations on a *healthy* version of the patient-specific torso mesh, removing the scar and EP parametrisation described as above. The mesh was then stimulated twice in ~3000 randomly chosen locations across the LV ($bcl = 400\ ms$), following **EP properties** and **Simulation Protocol** in **Chapter 7** described in the previous Chapter. Briefly, the biventricular mesh was assigned healthy CVs of $0.67\ m/s$ and $0.30\ m/s$ along and transverse to the fibre orientation, with tissue conductivities tuned accordingly(205), as was done for all previous torso models in **Chapter 7**. The corresponding 12-lead ECGs, with the additional 4 vector combinations, were augmented as in **Data augmentation for training** in **Chapter 7**, and used in combination with the paced beats simulations of the five torso models previously generated for the initial training of the AI algorithm. Then, transfer learning was performed on the previously simulated post-infarct VT datasets, and the so trained AI was tested on the patient's VT ECG traces to predict the corresponding exit site.

***Clinical Scenario 2*: Direct VT Prediction**. In addition to above, the AI model, trained on the simulated focal paced beats and post-infarct VT datasets of **Chapter 7** torso models, was tested directly on this patient's VT ECG traces, returning a prediction based on no prior knowledge of the patient's anatomy and ECG lead settings.

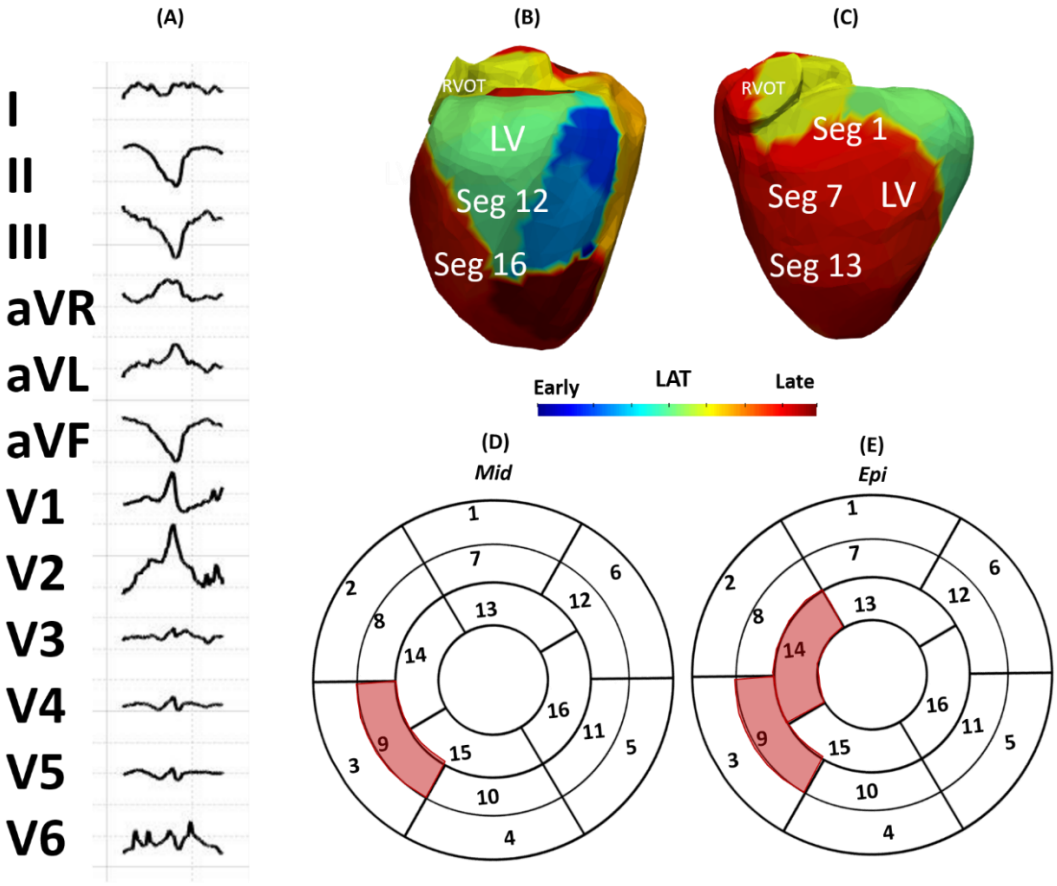

Figure 8.5. *Clinical VT substrate: Patient 2. (A) shows the VT ECG, extracted from the ECGI working channels. (B) and (C) show the LAT (early activation in blue, late activation in red) of the clinically-induced VT. (D) and (E) show the potential BZ pattern (red) extracted from the ECVs.*

8.2.3 Patient 3

Patient 3 had ischemic heart disease and severe LV dysfunction, and before being referred for cSBRT, underwent 5 unsuccessful endocardial VT ablations. The clinical data collected for this patient was marginally different to the previous cases, thus requiring some modifications to the overall pipeline, as illustrated in **Figure 8.6**. No imaging data and body surface potentials were available for this patient, which prevented the generation of a 3D torso model. The heart mesh was therefore generated from EAM surfaces extracted from the inHEART software(227) using *fTetWild*(228). The scar pattern, derived from thickness measurements of the myocardial wall, was fairly extensive (**Figure 8.7B-C**), and was divided into BZ and dense fibrotic regions. The corresponding infarct mesh was therefore more

detailed than the ECV-derived patterns of the previous cases. The clinically-induced VT had a cycle length $\sim 370\,ms$, and the corresponding ECG can be seen in **Figure 8.7A**. The final cSBRT ablation volume was quite extensive, given the patient's VT history, including $Segment\ 3, 5, 9, 10, 11\ and\ 15$. Fibre orientation(217) and UVCs(182) were incorporated and computed as above, and the ECG leads were modelled by registering the biventricular mesh to one of our previous torso models, and extracting the corresponding ECG leads.

Tissue Parametrisation

In contrast to the previous models where each one of the 17-AHA segments had different CVs and conductivities according to the corresponding ECV, the biventricular mesh of this patient was parametrised in two regions only (the healthy myocardium and the BZ), and the dense fibrotic regions were modelled as non-conducting. In the healthy myocardium, CVs and conductivities along and transverse to the fibre direction were parametrised by matching the measured, clinical QRS to a simulated trace with a similar two-step approach to before (considering the whole mesh healthy). The final conductivities in the intra- and extracellular spaces were $0.2506\,S/m$ and $0.9001\,S/m$ along the fibre direction, respectively, and $0.0798\,S/m$ and $0.2868\,S/m$ transverse to it, returning $CV = 0.70\,m/s$ and $0.31\,m/s$ along and transverse to the fibres. The EP properties of the BZ were instead tuned so that CV was $0.155\,m/s$ (half the value of the transverse healthy CV), as was done **Chapter 5**. Corresponding conductivities were $0.0798\,S/m$ and $0.2868\,S/m$ in the intra- and extracellular spaces, respectively.

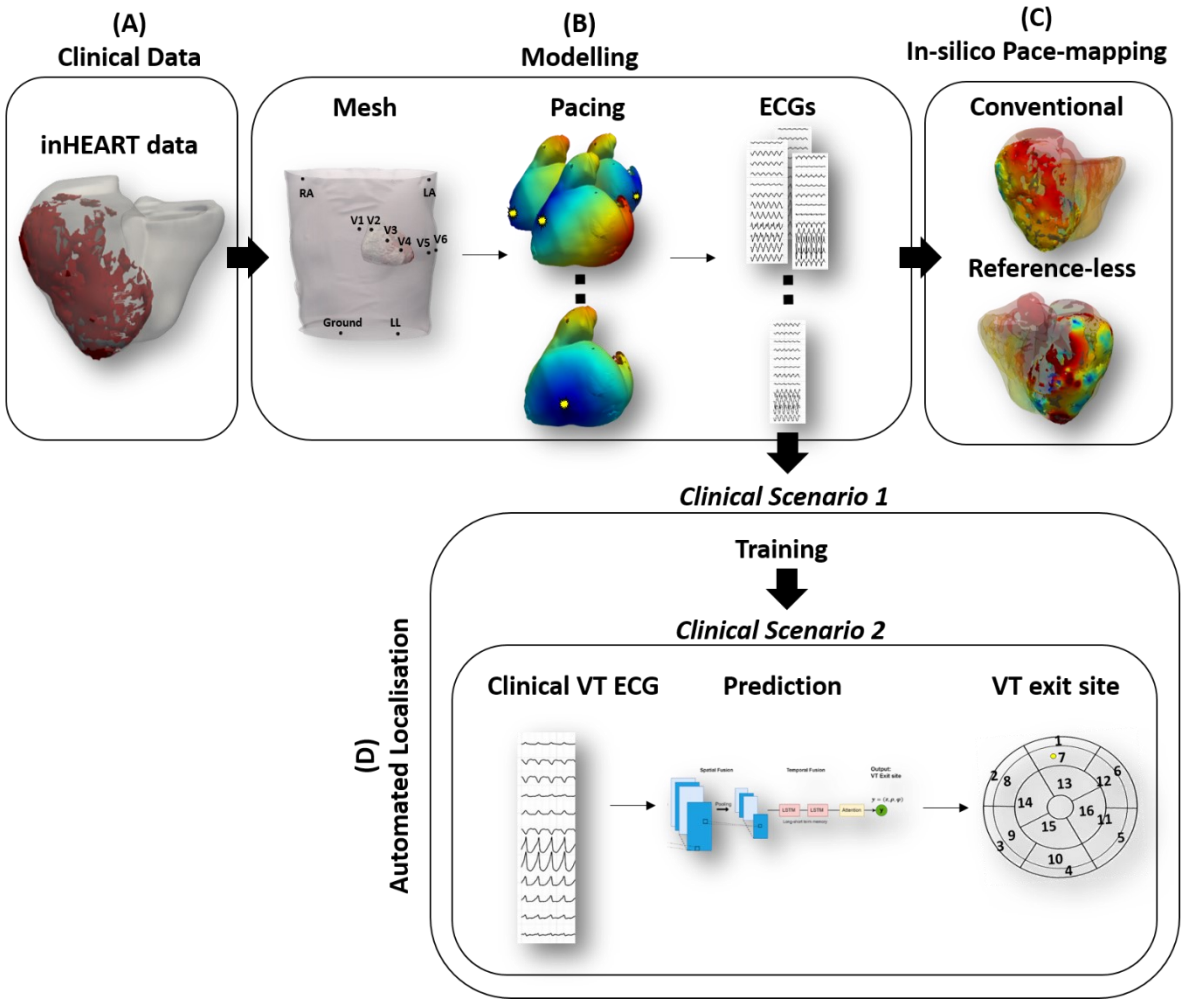

Figure 8.6. *Workflow for Patient 3: clinical evaluation of in-silico pace-mapping and automated scar-related VT localisation. (A): For this patient, the only data available was from the InHeart software, returning more detailed information on the infarct pattern. (B): Due to the absence of CT imaging and lack of body surface potentials, the biventricular mesh was generated from the endocardial and epicardial surfaces extracted from the InHeart EAM maps, and it was registered to the generic ECG leads of one of our previous torso models. The scar was parametrised as in Chapter 5, and paced beats around the LV, and corresponding ECGs, were simulated in a different RE-PR environment, which did not require a torso model. (C): In-silico pace-mapping was performed as before, and (D) our automated scar-related VT localisation platform was tested to predict the exit site of the patient's VT from the clinical ECGs, either directly or after combining the newly simulated paced beat ECGs with the simulations of Chapter 7 and re-training the AI architectures.*

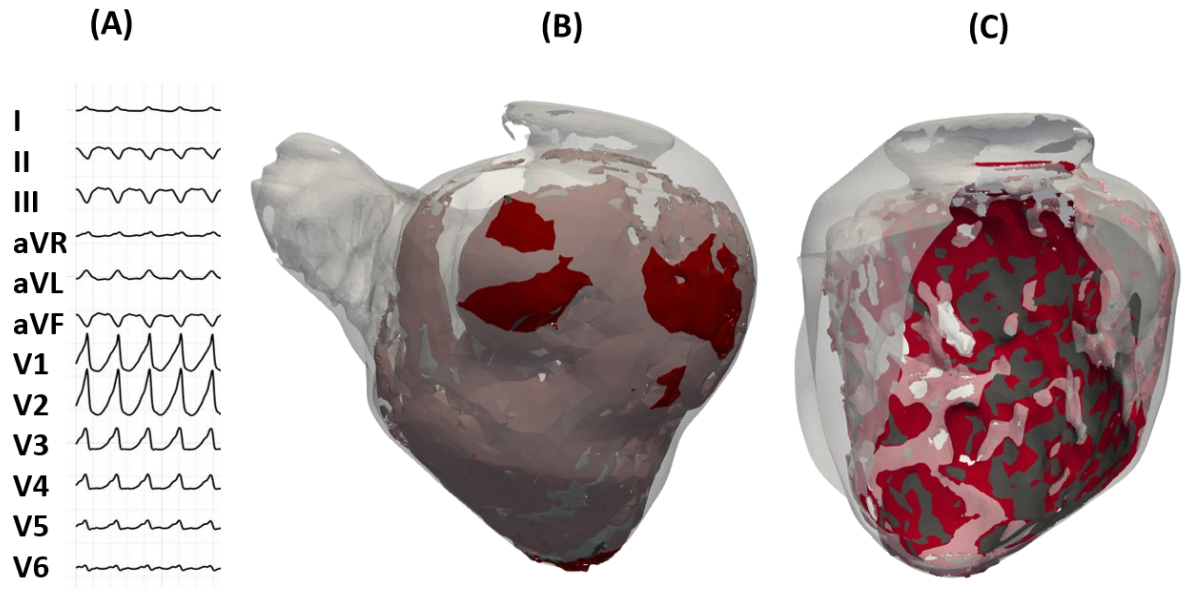

Figure 8.7. *Scar pattern and VT ECGs for Patient 3. (A) shows the 12-lead ECGs of the patient's VT. (B) and (C) show the BZ (red) and infarcted (grey) regions in the LV, epicardially and endocardially, respectively.*

In-silico Pace-mapping

Because of the lack of a torso model, a different mathematical formulation was used to compute extracellular potentials φ_e on the ECG locations, referred to as *phie recovery* (PR) in CARP(104). Differently from the LF, the extracellular space is assumed to be a conductor of infinite extent, and homogenous conductivity $\sigma_{bath} = 1.0\ S/m$(229). The unipolar electrograms on a specific field point $\boldsymbol{r}$ (at a distance d from the cardiac tissue) can be estimated according to

$$\varphi_e = \frac{1}{4\pi\sigma_{bath}} \int \frac{\beta I_m}{\|\boldsymbol{r}\| + d}\, d\Omega \qquad (8.1)$$

where $\beta I_m$is derived from the monodomain formulation.

This formulation was combined with the RE method to simulate ~ 222 paced beats around the LV, and retrieve corresponding ECGs, to generate in-silico conventional and reference-less pace-maps.

Automated scar-related VT localisation

As before, the computational-AI platform was tested under two scenarios (**Clinical Scenario 1: VT Prediction following Computational Simulations** and **Clinical Scenario 2: Direct VT Prediction**) to

identify the patient's VT exit site. The workflow for the two scenarios was similar to above. However, given the lack of a torso model, the RE-PR formulation was used in place of the RE-LF to simulate the paced beats on the healthy version of the patient's biventricular mesh, and the AI was trained and tested on the standard 12-lead ECGs.

8.3 RESULTS

In this Section, we will first analyse how ECG-based in-silico pace-maps can be utilised to extrapolate information on VT substrate and dynamics from both conventional and reference-less approaches across the three patients. Then, we will see how the AI platform can be used to provide complementary information on the location of VT exit sites, either directly from surface ECGs or in conjunction with simple, pacing simulations.

8.3.1 Localisation of VT Exit Sites and Isthmuses via In-Silico Pace-Mapping

For each patient, we will first analyse the in-silico pace-maps constructed from the comparison of simulated ECG traces with the clinical VT ECGs. We will compare the exit sites and isthmuses extracted from the conventional and reference-less pace-maps respectively against the ablation targets and the LAT maps of the clinically-induced VTs.

Patient 1

In *Patient 1*, the segment with the highest correlation was *Segment 15* (89.58%), followed by Segment 9 (87.95%) and 10 (85.71%), as shown in **Figure 8.8C**. The conventional, in-silico 3D pace-map in **Figure 8.8A** locates the VT exit site more precisely, in the top-right corner of Segment 15, in close proximity to Segment 10 (one of the final ablation targets). In addition, the VT pattern extracted from the pace-map seemed in agreement with the LAT map of the clinically-induced VT (**Figure 7.6A-B**), and with the final ablation targets ($Segment\ 9$ and 10).

In addition to the conventional pace-map, our reference-less in-silico approach was useful at identifying the main VT channel in $Segment\ 9$ (**Figure 8.8B-D**), by computing correlations between traces of neighbouring paced beats ($radius\ =\ 20\ mm$). This result supports the results extracted from the conventional pace-map, providing further understanding of the VT dynamics, as shown in .**Figure 8.9A-B**.

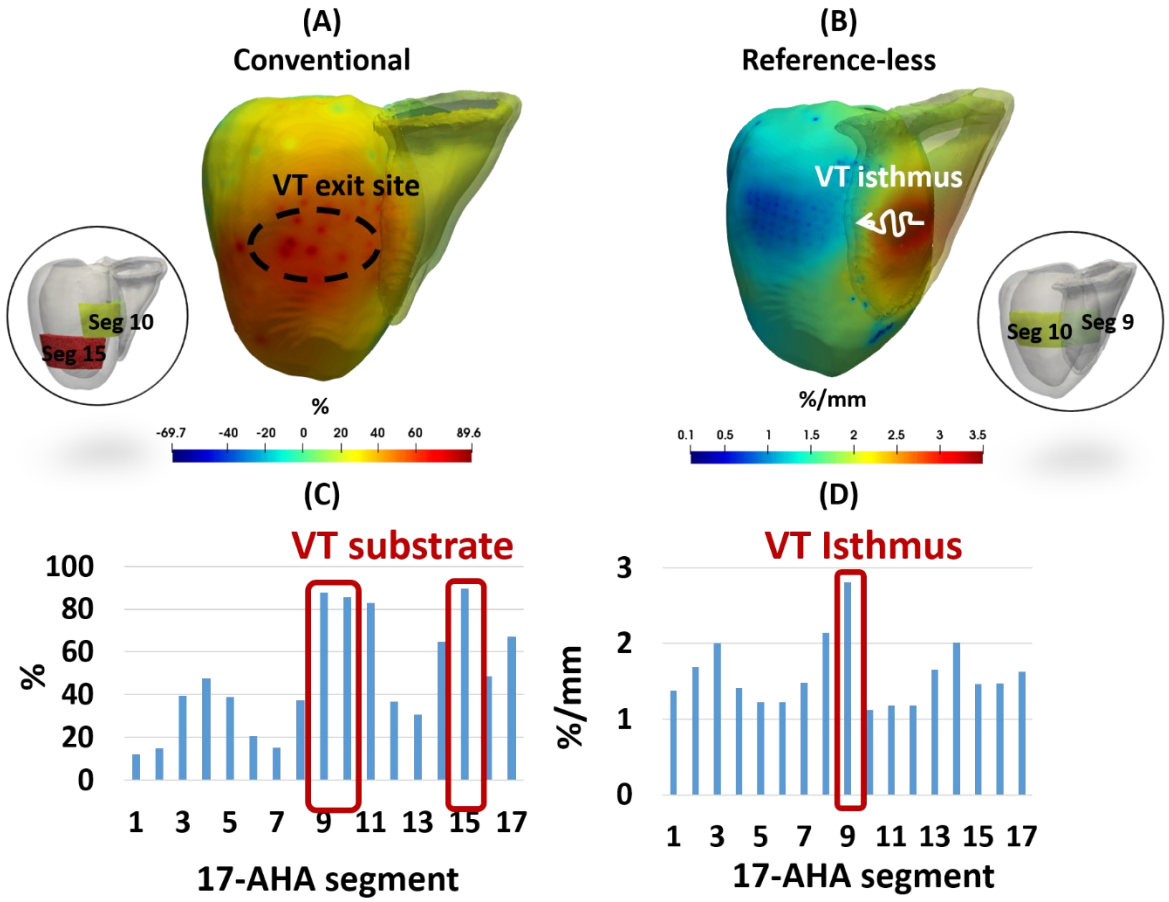

Figure 8.8. *Clinical applicability of In-silico pace-mapping: Patient 1. (A) shows the 3D conventional pace-map identifying the VT exit site in Segment 15 (black circle). (B) illustrates how the reference-less 3D pace-map can provide information on the presence of a VT isthmus in Segment 9 (white arrow). (C) reports the highest correlations per segment from the in-silico, conventional pace-map, and (D) reports the mean correlation/mm per segment from the in-silico, reference-less pace-map.*

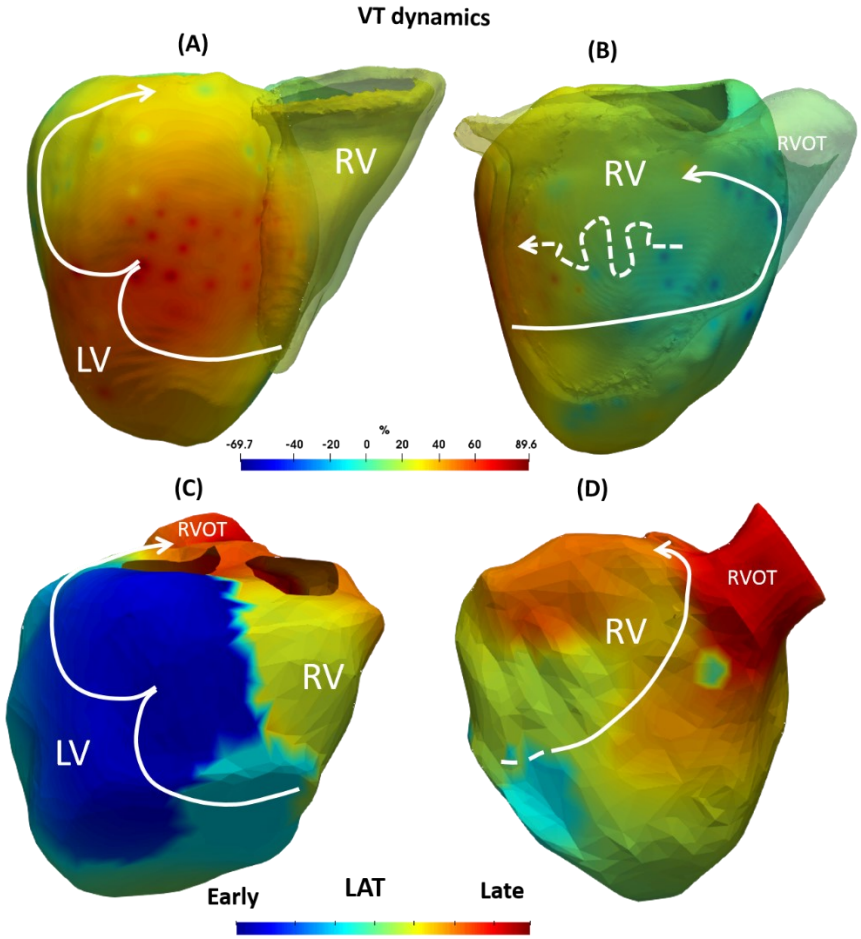

Figure 8.9. *VT pattern: Patient 1. (A) and (B) illustrate the possible VT pathway by considering regions of high correlations (exit sites) and low correlations (entrance sites). The possible isthmus (dotted arrow), connecting high and low correlations, is located in Segment 9, in agreement with the reference-less pace-maps. (C) and (D) show the activation map (LAT) of the clinically-induced VT, reconstructed from body surface potential maps, and the possible VT dynamics.*

Patient 2

In *Patient 2*, the regions of highest correlations were identified in *Segment 7* (83.15%) and *14* (82.60%), with the lowest correlations in *Segment 16* (-56.2%), as highlighted in **Figure 8.10A-C**. This, together with the results from the reference-less pace-mapping approach in **Figure 8.10A-C**, which identified regions of slow conduction ($> 3.5\ \%/mm$), in *Segment 4*, *6* and *14*, may suggest a VT pattern as seen in **Figure 8.11A-B**, in close agreement to pattern extracted from the LAT map of the clinical VT reconstructed from ECGi (**Figure 8.11C-D**).

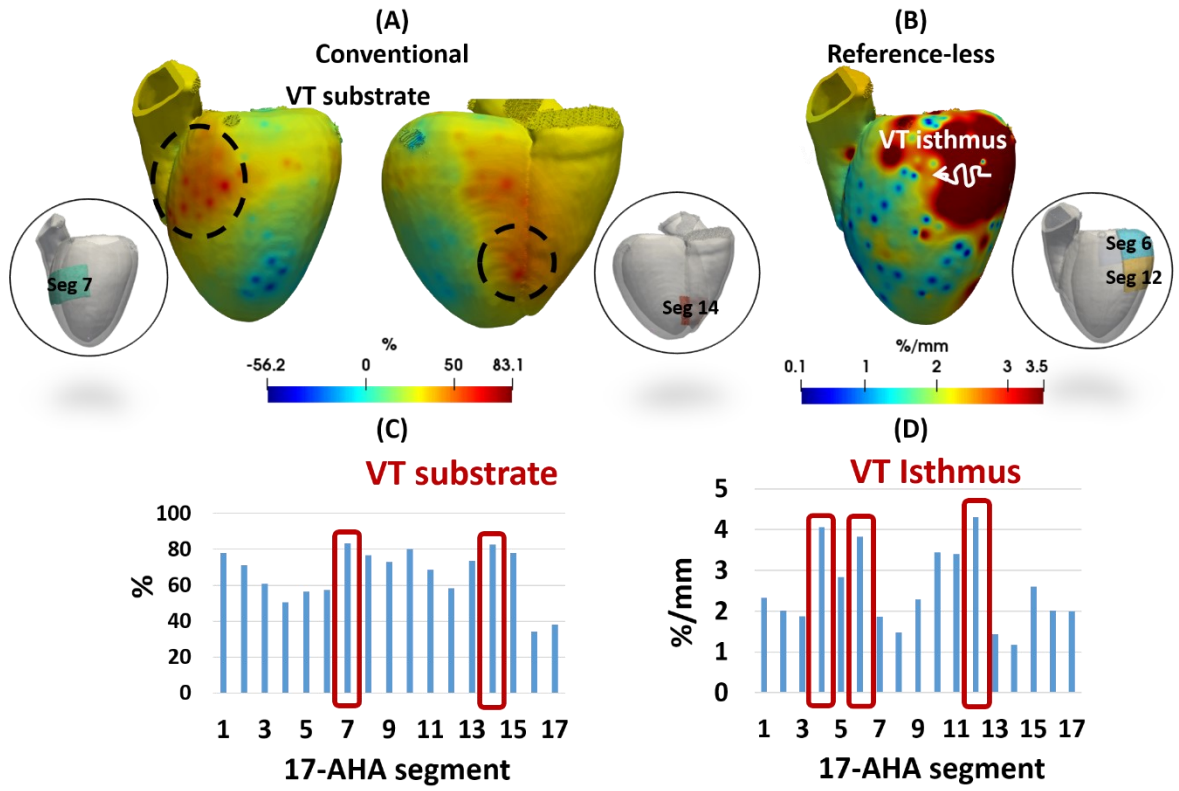

Figure 8.10. *Clinical evaluation of In-silico pace-mapping: Patient 2. (A) shows the 3D conventional pace-map identifying the VT exit site in Segment 7 on the left, and another region of high correlation in Segment 14 on the right. (B) illustrates how the reference-less 3D pace-map can provide information on the presence of a VT isthmus in Segment 4,6 and 14 (white arrow). (C) reports the highest correlations per segment from the in-silico, conventional pace-map, and (D) reports the mean correlations/mm per segment from the in-silico, reference-less pace-map.*

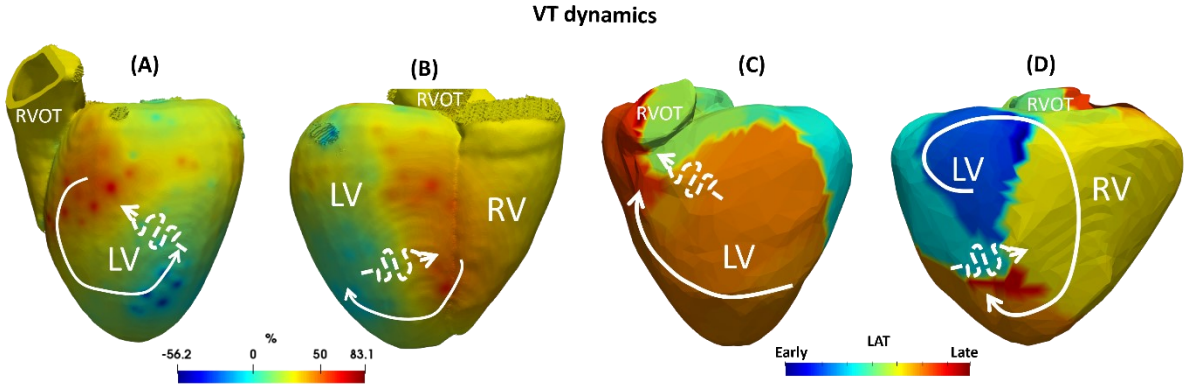

Figure 8.11. *VT pattern: Patient 2. (A) and (B) illustrate the possible VT pathway by considering regions of high correlations (exit sites) and low correlations (entrance sites). The possible isthmuses, connecting high and low correlations, are shown by the dotted arrows. (C) and (D) show the activation map (LAT) of the clinically-induced VT, reconstructed from body surface potential maps, and the possible VT dynamics.*

Patient 3

Our in-silico evaluation of *Patient 3* was aided by a more detailed scar pattern, with two major structural channels in *Segment 4 - 10*, and *2 - 8*. By visualising the correlation pattern on the BZ of the infarct (**Figure 8.12A-C**), the highest correlations were located in *Segment 10* and *5* (78.86% and 78.51%). The highest changes in the reference-less pace-map (**Figure 8.12B-D**) were in $Segment\ 8$ ($3.35\ \%/mm$) (and in the apex). The ablation was quite extensive, targeting the majority of the inferolateral wall ($Segments\ 3, 5, 9, 10, 11, 15$), which agreed with the majority of our results.

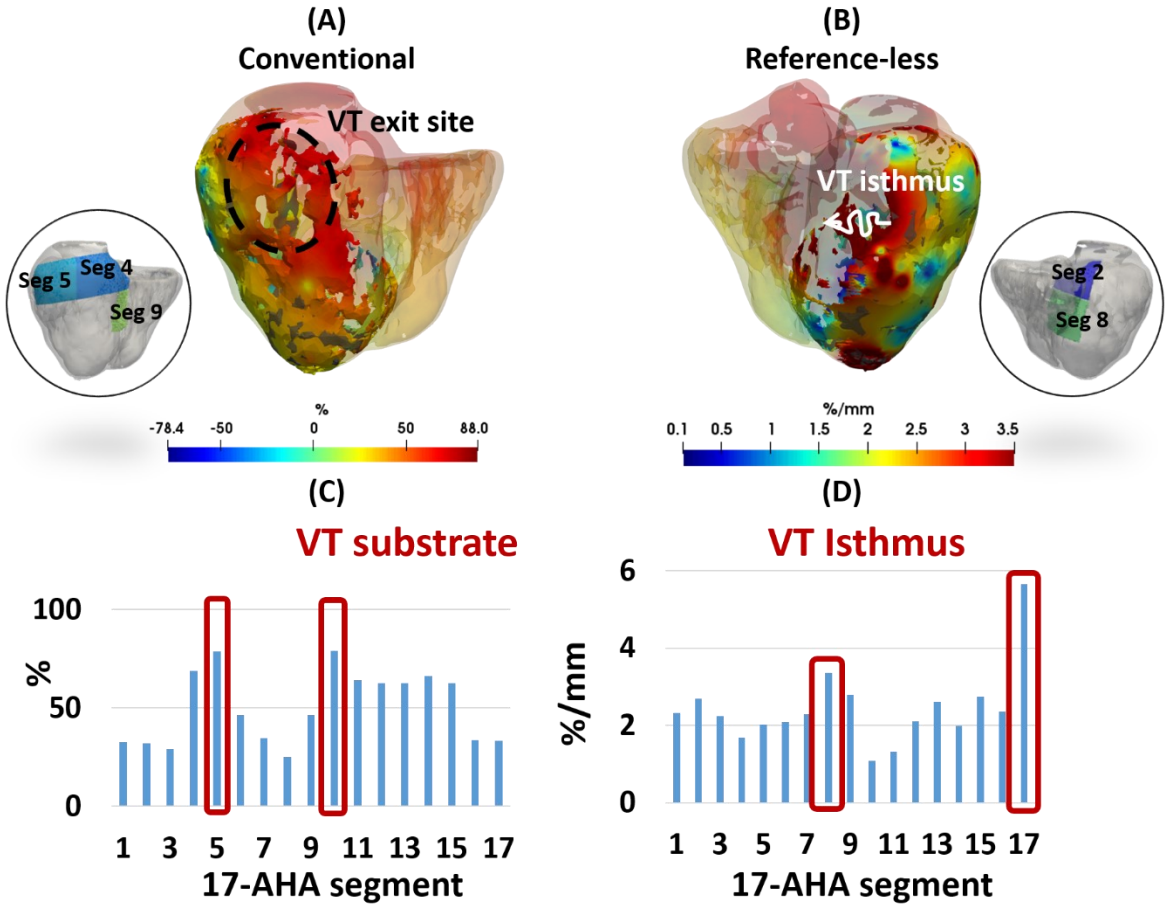

Figure 8.12. *Clinical evaluation of In-silico pace-mapping: Patient 3. (A) shows the 3D conventional pace-map on the BZ of the infarct, identifying the VT exit site in Segment 5/10. (B) illustrates how the reference-less 3D pace-map can provide information on the presence of a VT isthmus in Segment 8 (white arrow). (C) reports the highest correlations per segment on the BZ, and (D) the mean correlations within a 20-mm radius per segment.*

8.3.2 AI Localisation of VT exit sites

The exit sites of each clinically-induced VT were also localised within our computational-AI platform, and compared with the previous in-silico pace-maps. For each patient, we tested the automated algorithm under two scenarios: in *Clinical Scenario 1*, we used paced beat simulations on each patient-specific mesh to aid the initial training of the AI, whereas in *Clinical Scenario 2* we tested the AI solely on the patient's VT ECGs.

Patient 1

The results from the automated localisation of this patient's VT were previously presented in **Chapter 7.** Briefly, in both scenarios (with and without the aid of computational simulations), the VT exit site was localised in close proximity to $Segment\ 10$. In **Figure 8.13A-B**, we can see that these results are in agreement with the region of highest correlation identified via in-silico, conventional pace-mapping.

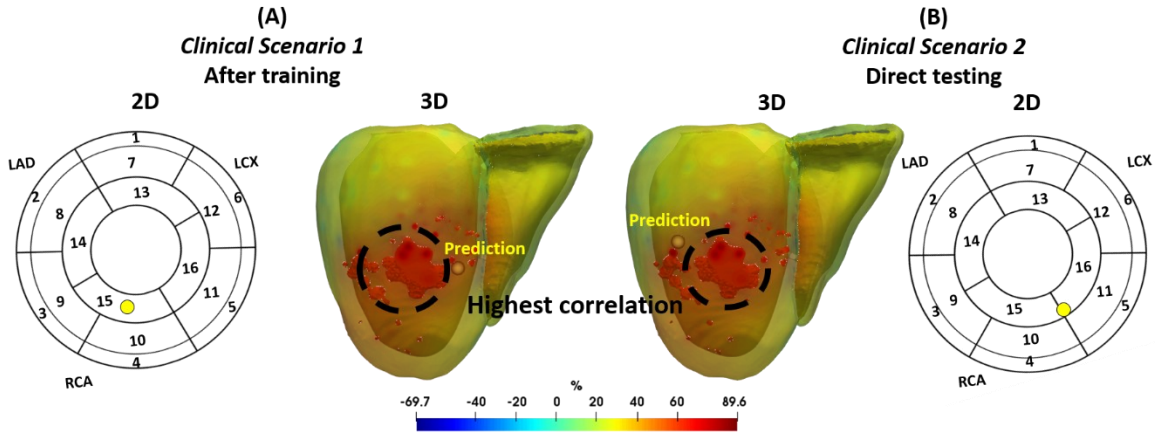

Figure 8.13. *Comparison of AI VT localisation with in-silico pace-mapping: Patient 1. (A) shows how the AI predicted VT exit site (yellow dot) compares to the region of highest correlation extracted from the in-silico conventional correlation pace-map (black circle) in Clinical Scenario 1. Similarly, (B) shows the comparison for Clinical Scenario 2 (direct testing). In both scenarios, the AI prediction can be visualised in 2D or 3D.*

Patient 2

In *Patient 2*, the automated localisation of the clinically-induced VT from ECGs differed slightly in the two scenarios analysed. After additional training of the AI (*Clinical Scenario 1*), the exit site was localised in $Segment\ 8$, in close proximity to the region of high correlation of the in-silico pace-map (**Figure 8.14A**). Direct localisation from the VT ECG (*Clinical Scenario 2*) resulted in a prediction between *Segment 11* and *12*, which was surprisingly close to the other region of highest correlation (**Figure 8.14B**), but opposite to the prediction of *Clinical Scenario 1*.

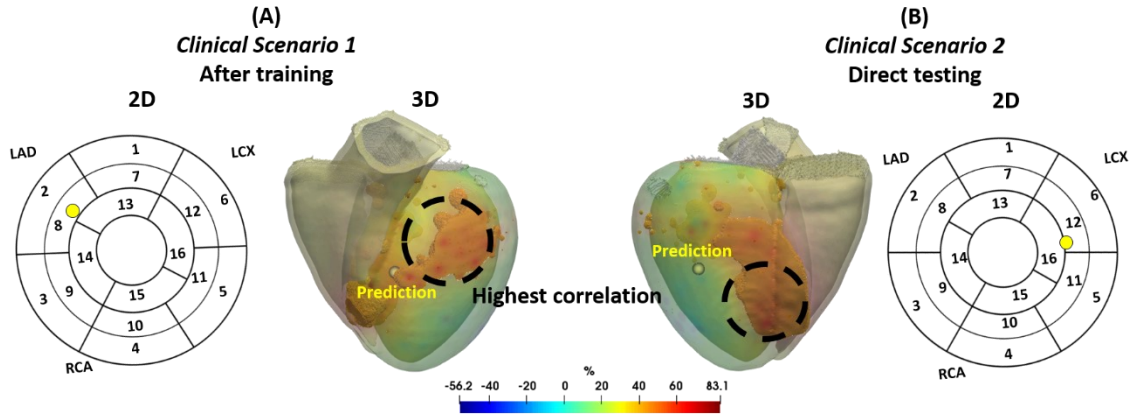

Figure 8.14. *Comparison of AI VT localisation with in-silico pace-mapping: Patient 2. (A) shows how the AI predicted VT exit site (yellow dot) compares to the regions of highest correlation (Segment 7 and 14) extracted from the in-silico conventional correlation pace-map (black circle) in Clinical Scenario 1. For this Patient, as seen in* ***Figure 8.10****, the segments with the highest correlations (Segment 7 and 14) were located in opposite regions of the heart. Surprisingly, the AI prediction in Clinical Scenario 1 was close to Segment 7, and the prediction in Clinical Scenario 2 (B) to Segment 14.*

Patient 3

In *Patient 3*, our automated algorithm localised the VT in the upper region of $Segment\ 15$ during *Clinical Scenario 1* (**Figure 8.1A**), which was located close to the region of high correlation extracted from the in-silico pace-map. In *Clinical Scenario 2* (direct testing), the episode was located in the opposite wall, in the upper part of $Segment\ 7$ (**Figure 8.15B**).

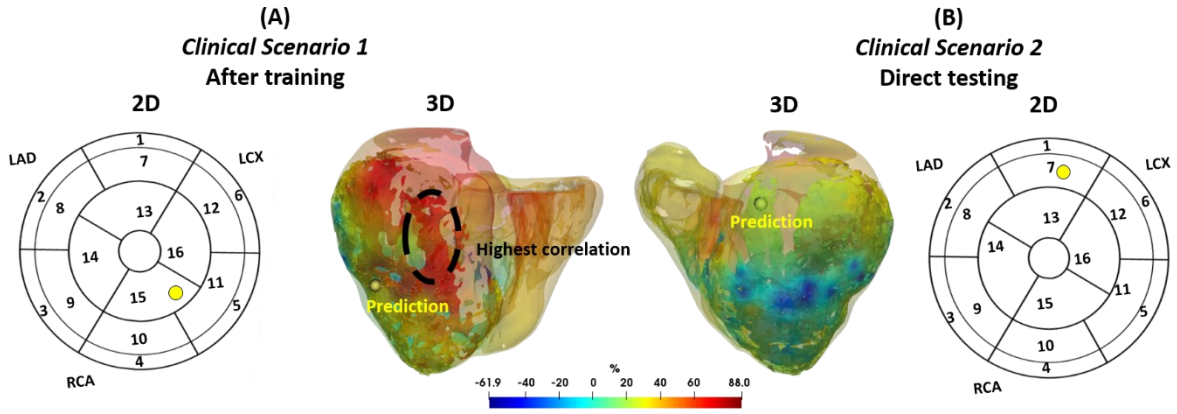

Figure 8.15. *Comparison of AI VT localisation with in-silico pace-mapping: Patient 3. (A) shows how the AI predicted VT exit site (yellow dot) compares to the region of highest correlation extracted from the in-silico conventional correlation pace-map (black circle) in Clinical Scenario 1. Similarly, (B) shows the comparison from Clinical Scenario 2 (direct testing). In both scenarios, the AI prediction can be visualised in 2D or 3D.*

8.4 Discussion

In this Chapter, we evaluated the performance of our previously described methods in the context of three cSBRT patients with refractory VTs and infarcted hearts. We first generated in-silico conventional and reference-less pace-maps to find exit sites (with correlations $> 83\%$) and isthmuses ($> 3\,\%/mm$), respectively, and describe the VT dynamics. Then, we tested our computational-AI platform under two different scenarios to localise the main exit sites.

In this Section, we will address and discuss the robustness of our platforms, and how our computational and AI results can be used jointly to provide better insight into the patients' VT dynamics, non-invasively and efficiently. We will conclude this Chapter by addressing the limitations of our computer-based tools when attempting clinical translation.

8.4.1 The power of In-Silico Pace-mapping

Across the three patients, both our in-silico conventional and reference-less pace-maps returned promising results in uncovering the VT dynamics, exit sites and isthmuses non-invasively. Our efficient RE-LF and RE-PR environment enabled the creation of high density, 3D pace-maps that cannot be

performed in clinical practice due to time and physiological constraints. They may also be of great benefit to plan non-invasive ablation procedures, such as cSBRT. In *Patient 1*, we achieved a high correlation match ($\sim 90\%$) between the simulated ECGs and the clinical traces. This could represent a promising validation of our RE-LF environment in clinical settings, as well as showing the feasibility of modelling and parametrising a scar pattern from CT ECV measurements. Despite LGE-MRI being the golden standard for the characterisation of myocardial scar and fibrosis, in recent years MRI-derived ECV values have also been used to achieve a robust scar assessment especially in presence of diffuse and patchy distributions (230,231). Similarly, recently CT-derived ECV has also been shown to be a suitable and valuable approach to assess the same problem, returning results comparable to MRI-derived ECV (232) and histologic findings (233).

Despite following a similar pipeline to *Patient 1*, slightly lower correlation coefficients ($\sim 84\%$) were registered for *Patient 2*. This could be related to the lower ECV distribution not reflecting the true scar pattern, that might have affected the overall EP parametrisation, and/or to the noisier reference VT ECG trace. Despite the different set-up, high correlations (~88%) were achieved in *Patient 3*, showing the possibility of utilising a simpler formulation (phie recovery) to derive extracellular potentials that does not require a detailed torso model. This suggests that imaging and segmenting a patient's full torso might be not necessary, as long as the comparison between simulated and measured ECGs (and/or implanted device EGMs) is carried-out after placing the sensing leads as closely as possible to the clinical set-up.

Furthermore, we showed the possibility of performing in-silico pace-mapping when detailed infarct imaging is not available. We achieved promising results when modelling the scar from both ECV and wall thickness (inHEART(227)) measurements. The former might allow a better EP parametrisation of the tissue. On the other hand, the inHEART software(227) returns a more detailed pattern of the infarct, that might be useful to accurately identifying the structural channels responsible for the maintenance of the tachycardia. All in all, in this study we were able to show how to generate in-silico

pace-mapping pipelines for clinical purposes, within a fast computational environment, and how to model scar patterns from ECVs. In addition, we managed to validate our simulated ECGs against clinical values.

8.4.2 Patient-Specific Training Improves Automated VT Localisation from Clinical ECGs

Because of the high variability in clinical datasets and scenarios, it is extremely difficult to propose an AI architecture that can predict the exit site of a VT solely from an ECG trace. For *Patient 1* (as seen in the previous Chapter as well), we had an ideal test-bed, as the clinical ECG electrodes matched closely to the set-up of the other torsos, and the clinically-induced VT had a fairly simplistic, figure-of-eight trajectory. This led to promising results in both scenarios investigated, where the AI VT predictions were located closely to one another, and to the results extracted from the pace-mapping investigation. For *Patient 2* and *3*, direct localisation of the VT episodes (*Clinical Scenario 2*) differed significantly from *Clinical Scenario 1*, challenging the interpretation and robustness of our platform. The predictions from *Clinical Scenario 1* were in stronger agreement to the in-silico pace-mapping results, showing the necessity of training the AI on simulations performed on the patient-specific mesh. Compared to in-silico pace-mapping, our computational-AI platform provides some benefits (no infarct modelling, no EP parametrisation, less user dependence and interaction) that might be of interest for a quicker, initial investigation of a clinical VT episode. However, it is of importance to use it in combination of in-silico pace-maps to provide a wider picture on the VT morphology and pattern.

8.4.3 Limitations & Conclusion

One of the major challenges of this clinical evaluation of computer-based approaches is the difficulty in establishing a ground truth to compare our results to. For *Patient 1* and *2*, LAT maps of the clinically-induced VT reconstructed from ECGi could be partially used to describe the general VT dynamics, but may not be reliable for a more detailed 3D (intramural and septal) analysis of the episode, as they only

contain epicardial information. They might not be accurate and precise enough to localise the VT exit site(s) and isthmus(es) if not located epicardially. In addition, the localisation accuracy achieved with ECGi may depend heavily on the mathematical formulation used to find the inverse solution, on the reconstruction techniques used to adjust for cardiac and respiratory motions, and on the registration with cardiac imaging(234). It is important to take into consideration that the ablation targets of these patients, due to their VT history, were fairly extensive. Despite localising origins and isthmuses of the VT episodes within segments that were indeed targeted during cSBRT, we were unable to quantify our in-silico pace-mapping results more precisely. Future validation should include CA patients, for which more detailed VT maps, and more precise ablation targets could be available for comparison, and cases with a less complicated and intense VT history. Finally, given the complexity of the scar-related re-entrant VT circuits analysed here, there is the need for a more interpretable AI algorithm, that goes beyond returning a single point output.

For two of the three patients, we used CT-derived ECVs to quantify scar distribution. Despite being validated against histologic findings and MRI-derived ECVs as previously mentioned, the thresholds used to differentiate healthy from BZ and scarred tissue may be operator dependant, and in this study were chosen according to (67), and adjusted according to the overall distributions of our patients.

In conclusion, despite the limitations and assumptions of our computational approaches, we were able to propose fast and efficient frameworks to tackle three clinical cases, and combine in-silico pace-mapping with AI predictions for a more robust preliminary analysis of VT dynamics and critical sites.

9

CONCLUSION

“There is no real ending. It is just the place where you stop the story”

Frank Herbert

9.1 SUMMARY

This Thesis concludes with a brief review of all that has been attempted and achieved in the preceding Chapters, and the interesting studies that may lead on from this work.

Cardiac arrhythmias represent a huge burden for society, posing a significant threat to life. Carefully managing VT from its onset may help reduce SCDs and increase quality of life. The first line of treatment against VT consists of implanting cardiac electronic devices, which however only provide a short-term solution against the tachycardia, and might be not ideal in the presence of recurrent episodes. A more effective, long-term solution is considered cardiac tissue ablation. Successful VT termination with ablation relies on the accurate localisation of anatomical and/or functional sites responsible for the initiation and maintenance of the episodes. As a result, significant academic and clinical interest has been invested in improving, facilitating and speeding up the identification of such optimal ablation targets. Current strategies that map cardiac electrical activity to describe the VT are either invasive and time-consuming, such as entrainment, activation and pace-mapping, or non-invasive, such as ECGi, but they all rely on acquiring an ECG during the clinical and/or EP-induced episode. The difficulty in inducing VT in patients with severe structural heart diseases, mechanical valves, and/or poorly tolerated VTs, and the possible mismatch between the presenting and the induced arrhythmia may limit ablation success, and cause VT recurrence. This led us to explore further the possibility of utilising the information that is already present in the form of EGM recordings in implanted devices, that the majority of VT patients are given as initial treatment for the prevention of VF and SCD. Given the limited amount of research on the matter, we proposed to achieve this goal by utilising computational modelling to investigate a variety of different scenarios, and generate non-invasive platforms that can help clinicians guide ablation planning and mapping from EGMs. In addition, we demonstrated how VT management could further benefit from automation, and the use of AI/DL algorithms.

9.1 Summary

To show the potential and utility of implanted device EGMs to guide VT ablation planning, we first proposed, in **Chapter 5**, an in-silico pace-mapping platform that, by generating a torso model from imaging data, and modelling standard ECG electrodes and a generic CRT-D device, would allow the identification of VT exit sites and isthmuses (critical to the maintenance of re-entrant circuits in the presence of infarcted hearts) from the comparison of simulated ECGs and EGMs of paced beats with a reference simulated VT trace. Moreover, we investigated a novel pace-mapping technique that does not require a reference VT, and could be used in conjunction with conventional methods to provide further insights on VT isthmuses. These analyses were carried-out entirely on simulated data, and relied on heavier, less computationally efficient simulations. However, it allowed a first investigation of how EGM-based pace-maps can provide additional information on VT dynamics, and help target the VT without VT induction. In addition, we showed how to improve the spatial resolution of EGM-based pace-maps, and the power and importance of in-silico pace-mapping in comparison to the clinical equivalent.

We continued our investigation by improving and speeding up the computational pipeline of simulated ECGs and EGMs in **Chapter 6**. Here, we proposed an environment that uses novel mathematical formulations to decrease computational load while allowing computation of extracellular potentials with high physiological fidelity. This fast environment was used to generate the training and testing datasets for DL architectures to detect the origins of VT episodes from focal sources from both surface ECGs and implanted device EGMs. A sensitivity analysis was also carried-out to investigate how signal noise, body composition of the torso models, ECG leads positioning and implanted device configurations could affect the AI/DL performance. Important conclusions were drawn from this investigation, used in the remainder of the Thesis to allow clinical evaluation.

In the following **Chapter 7**, we proposed a similar, efficient computational environment to simulate more complex VT episodes, in the presence of simplistic scars. We aimed to demonstrate how to automate the identification of not only focal VTs, but also scar-related episodes. To do so, we built a

pipeline that would integrate simulations of both focal and scar-related VTs to train DL architectures in two stages, improving the final localisation performance but also reducing the size of the training dataset required to perform such a complex task. We investigated two computational scenarios to show the feasibility of predicting the exit site of a VT directly from a surface ECG or intracardiac EGMs, or by adding simple pacing simulations on the torso of interest in the initial training stage to provide a more robust localisation.

Finally, at the end of **Chapter 7**, and in **Chapter 8**, we tackled the problem of "trustworthiness and validity" of our proposed computer-based tools. We attempted to perform in-silico pace-mapping on actual clinical data, by developing fast pipelines that could be used to generate heart and/or torso meshes from patient-specific imaging data, include infarct patterns, and quickly parametrise the model EP to return simulated extracellular potentials similar to measured traces. We also showed how we could use our AI architecture to predict the exit site from the clinically-induced VT ECGs, and/or in conjunction with simulations on the patients' meshes, and the utility of combining both in-silico pace-mapping results and AI predictions to ease visualisation and interpretation of the results. Despite not being able to use the actual EGM recordings of the CRT-Ds of the patients, **Chapter 8** represents a crucial piece of work to understand the difficulties in dealing with real clinical data. We showed how computational and/AI pipelines need to be adjusted to take into account the high variability of clinical datasets. In addition, we discussed what types of simplifications and assumptions can be made to the models without a decrease in performance and/or loss of correlation between measured and simulated signals.

9.2 Important Findings and Key Contributions

The in-silico pace-mapping platform presented in **Chapter 5**, and evaluated in **Chapter 8** on clinical data, enabled the acquisition of dense, fully transmural pace-maps that would not be feasible in clinical practice, not only due to time constraints but also to pacing electrode technology. In clinical

practice, the visualisation of a complex, post-infarct VT episode on a 2D (endocardial or epicardial) surface limits the accurate identification of exits, entrances and channels across the myocardium, thus underscoring the utility of our computational models. We showed that accurate and precise non-invasive pace-maps can be generated from both surface ECGs and implanted device EGMs, especially when increasing the number of "recordings" extracted from implanted devices. Instead of modelling a simple ICD, from which only two EGM fields can be extrapolated, we modelled a CRT-D with multiple sensing coils and tips on both ventricular chambers. Despite the recent advances in device technology and design, there is a pressing need to make the raw information recorded on those devices available for clinical and academic use. The difficulty in getting that data, and the lack of some devices of the SVC coil and/or sensing capabilities in the LV lead, limited the extension and validation of our in-silico platform to clinical EGMs. However, our work showed the importance of integrating such information, urging medical companies to improve data accessibility, manipulation and storage from the devices.

Furthermore, we suggested the integration of conventional pace-mapping with novel reference-less techniques for a more complete picture on VT dynamics and critical sites without an increase in clinical procedure or simulation time. Given the ambiguity in isthmus(es) identification from conventional pace-maps, the reference-less method could be used to highlight all possible channels responsible for a reduction in electrical conduction. The conventional pace-map would then help understand the direction of the known VT through those channels.

The fast computational environment presented in **Chapter 6** played an important role for this Thesis, and for future applications. The use of LF methods in combination with RE formulation allowed to compute extracellular potentials on the modelled ECG electrodes and implanted device leads at a fraction of the computational cost of conventional methods (pseudo-domain and/or bidomain) with little changes in the final traces. The great novelty of this Chapter was, however, the integration of these fast simulations with DL architectures to automate localisation of focal VTs. An existing study(159) attempted to combine computational simulations of focal paced beats with CNNs to

automate the localisation of focal sources. However, they used very simplistic computational simulations, and the proposed pipeline to achieve clinical validation was extremely time-consuming. We improved on those limitations, and outperformed the final localisation performance, achieving errors desirable to guide ablation planning. This was achieved by proposing an algorithm that does not rely on Cartesian coordinates, which did not seem appropriate given the geometry of the heart, but on a coordinate frame specific to the ventricles. The latter could also ease visualisation of the predicted origins, as well as returning a more accurate placement of the origin across the myocardium that could help the choice between endocardial and epicardial ablation, and energy and size of the lesion. In addition to these key contributions, our fast computational environment enabled the exploration of different scenarios, which led to the conclusion that significant variations in body composition, ECG lead positioning and device configuration from the training dataset may decrease the localisation performance of the AI/DL. This finding suggested the necessity of incorporating more variability in the training, and the importance of introducing some information on a patient's clinical settings in the AI/DL training.

The above points were taken into account when developing the workflow of **Chapter 7** and **Chapter 8**, and enabled us to show how we can evaluate automated architectures trained on simulated data on real ECGs. **Chapter 7** was extremely important to show how scar-related VTs can also be simulated in an efficient way combining LFs with RE+ formulations. To the best of our knowledge, we provided the largest library of simplistic, figure-of-eight VT ECGs and EGMs within reasonable simulation times. We showed how to automate the localisation of scar-related VTs from both ECGs and EGMs by combining deep convolutional and recurrent networks, and using transfer learning. By developing a one-dimensional CNN that is not restricted on having square inputs (as the 2D CNN architectures proposed in **Chapter 6** were), we had more flexibility on the number of leads (for both ECG and EGM recordings) that can be used for training and testing, and on the length of signals. Moreover, the integration of recurrent networks (LSTMs) and attention mechanisms can ease the recognition of pattern repetition along the trace. Most importantly, the work of **Chapter 7** was of importance to

examine the applicability of our platform in clinical settings. The investigation of two different scenarios gave insights on how to use the platform in future studies, the steps and directions needed to obtain a good localisation performance, and analyse the impact and benefit of minimal computational model construction and simulation for a particular patient. We showed that our pre-trained AI architecture (trained on a large library of simulated data) may be used to directly localise a VT exit site from a clinical trace. This was achieved in Patient 1, and we believe it was thanks to the fairly simple morphology of the clinical VT, and on the good quality of the clinical VT ECG (and ECGi channel locations). However, the variability in clinical data, the presence of more diffuse and severe infarcts (e.g. Patient 3), and poor quality VT ECGs (e.g. Patient 2) may challenge this direct localisation, thus suggesting the necessity of integrating patient's specific computational simulations into the training stage of the AI/DL.

In conclusion, all the work of this Thesis comes together in **Chapter 8**. Here, we demonstrated how our models and simulated ECGs compared to real clinical data. In addition, we showed how to utilise all the above-described tools (fast simulation environments, AI, modelling pipelines) to aid real ablation planning, and how to tackle discrepancies and variability in clinical datasets. Despite the limitations and assumptions of all our platforms, we were able to demonstrate the reliability of our in-silico pace-maps, and how EP properties can be quickly parametrised when infarct patterns are derived from different imaging approaches, returning simulated traces that closely compare to measured data. Although LGE-MRI is the preferred modality to generate highly detailed meshes of infarct patterns, we demonstrated that ECVs measured from CT represent a valid alternative to introduce BZs and slow conduction regions in a model, and help tune the EP in a specific patient. Lastly but not least, we presented how a more robust and trustworthy picture of a VT can be built by combining in-silico pace-maps with the predictions from the AI/DL algorithms.

9.3 FUTURE WORK & CONCLUDING REMARKS

In this last, concluding Section of the Thesis we will focus on interesting directions that could arise from our findings and contributions.

Firstly, being able to use the information stored in an implanted device would not only help ablation planning, but also device pacing. The integration of algorithms within implantable devices that can identify the location of a VT episode from the recorded multi-polar EGM vectors in real-time could really help reduce the recurrence of inappropriate shocks, and unsuccessful VT termination. Moreover, a deeper understanding of EGM signals with respect to the underlying arrhythmia could help improve and tailor device programming, and help choose between shocking or pacing. Finally, the immediate localisation of a VT episode from the device recordings could improve clinical decision making during remote monitoring. At the moment, these interesting directions are limited by device design and technology, but future advances in the field might change that.

From a modelling point of view, the use of clinical VT EGMs to validate simulated EGMs (given that the in-silico device is modelled as closely as possible to the clinical settings, as we have done for ECG/ECGi) would help understand how to simplify and/or increase complexity of the patient-specific EP parametrisation, and increase robustness of clinical translation. Extracting and analysing clinical EGM recordings would allow the validation of VT simulations and protocols, helping overcome the limitations of current modelling studies. Moreover, the comparison between simulated and clinical VT EGMs could help elucidate important properties of the underlying scar substrate, guide ablation strategies accordingly, and ablation technology. Moreover, it will help validate other algorithms that aim to increase ablation success and lessen risk and time of ablation mapping by using patient-specific modelling to assess the risk of VT after infarction(21), or to automate induction (near-real time) of all unique VT morphologies(196) for a given infarct pattern.

The integration of computational and AI tools represents another important path for the growth of personalised modelling. Whereas in our work we have focused on localising single "origins" of focal and/or scar-related VTs, future work might focus on returning probability maps of VT dynamics for a given ECG or EGM, and increase interpretability of the AI. The use of AI in cardiac computational modelling might be used to increase the speed of the overall personalisation pipeline, or to extract the likelihood of VT recurrence given a certain scar geometry and ablation target(s).

In conclusion, we strongly believe that the work presented in this Thesis has contributed to explore different ways of achieving and improving non-invasive, personalised ablation planning of VT patients with the use of modelling and artificial intelligence. It is hoped that these tools and insights will be of good use to the academic and medical community in future studies.

BIBLIOGRAPHY

1. Srinivasan NT, Schilling R. Sudden Cardiac Death and Arrhythmias. Arrhythmia Electrophysiol Rev. 2018;7(2):111–7.

2. Sapp JL, Wells GA, Parkash R, Stevenson WG, Blier L, Sarrazin J-F, et al. Ventricular Tachycardia Ablation versus Escalation of Antiarrhythmic Drugs. N Engl J Med. 2016;375(2):111–21.

3. Tung R, Ellenbogen KA. Emergence of Multielectrode Mapping: On the Road to Higher Resolution. Circ Arrhythmia Electrophysiol. 2016 Jun 1;9(6).

4. Zellerhoff S, Eckardt L, Breithardt G. History of Cardiac Mapping. Card Mapp. 2019 Apr 5;1–6.

5. Mahida S, Sacher F, Dubois R, Sermesant M, Bogun F, Haïssaguerre M, et al. Cardiac Imaging in Patients with Ventricular Tachycardia. Circulation. 2017 Dec 19;136(25):2491–507.

6. Sattar Y, Chhabra L. Electrocardiogram. StatPearls Publishing; 2021.

7. Fye WB. A history of the origin, evolution, and impact of electrocardiography. Am J Cardiol. 1994 May 15;73(13):937–49.

8. Haqqani HM, Marchlinski FE. The Surface Electrocardiograph in Ventricular Arrhythmias: Lessons in Localisation. Hear Lung Circ. 2019 Jan;28(1):39–48.

9. Liao Z, Zhan X, Wu S, Xue Y, Fang X, Liao H, et al. Idiopathic Ventricular Arrhythmias Originating From the Pulmonary Sinus Cusp: Prevalence, Electrocardiographic/Electrophysiological Characteristics, and Catheter Ablation. J Am Coll Cardiol. 2015 Dec 15;66(23):2633–44.

10. Betensky BP, Park RE, Marchlinski FE, Hutchinson MD, Garcia FC, Dixit S, et al. The V2 Transition Ratio: A New Electrocardiographic Criterion for Distinguishing Left From Right Ventricular Outflow Tract Tachycardia Origin. J Am Coll Cardiol. 2011 May 31;57(22):2255–62.

11. Dixit S, Gerstenfeld EP, Callans DJ, Marchlinski FE. Electrocardiographic patterns of superior

right ventricular outflow tract tachycardias: Distinguishing septal and free-wall sites of origin. J Cardiovasc Electrophysiol. 2003 Jan 1;14(1):1–7.

12. de Bliek EC. ST elevation: Differential diagnosis and caveats. A comprehensive review to help distinguish ST elevation myocardial infarction from nonischemic etiologies of ST elevation. Turkish J Emerg Med. 2018 Mar 1;18(1):1.

13. Candiotti KA, Vivek M. Proposed diagnostic criteria for the Brugada syndrome: Consensus report. Circulation. 2002 Nov 5;106(19):2514–9.

14. Yoshida K, Liu T-Y, Scott C, Hero A, Yokokawa M, Gupta S, et al. The Value of Defibrillator Electrograms for Recognition of Clinical Ventricular Tachycardias and for Pace Mapping of Post-Infarction Ventricular Tachycardia. J Am Coll Cardiol. 2010 Sep;56(12):969–79.

15. Yokokawa M, Kim HM, Sharaf Dabbagh G, Siontis KC, Lathkar-Pradhan S, Jongnarangsin K, et al. Targeting Noninducible Clinical Ventricular Tachycardias in Patients With Prior Myocardial Infarctions Based on Stored Electrograms. Circ Arrhythmia Electrophysiol. 2019 Jul;12(7).

16. Trayanova NA. Whole-heart modeling : Applications to cardiac electrophysiology and electromechanics. Circ Res. 2011;108:113–28.

17. Clayton R. H, Bishop M. J. Computational models of ventricular arrhythmia mechanisms: recent developments and future prospects. Drug Discov Today Dis Model. 2014;4.

18. Henriquez CS. A brief history of tissue models for cardiac electrophysiology. IEEE Trans Biomed Eng. 2014;61(5):1457–65.

19. Niederer SA, Lumens J, Trayanova NA. Computational models in cardiology. Nat Rev Cardiol. 2019 Feb 25;16(2):100–11.

20. Yu JK, Franceschi W, Huang Q, Pashakhanloo F, Boyle PM, Trayanova NA. A comprehensive, multiscale framework for evaluation of arrhythmias arising from cell therapy in the whole post-

myocardial infarcted heart. Sci Rep. 2019 Dec 1;9(1):1–16.

21. Arevalo HJ, Vadakkumpadan F, Guallar E, Jebb A, Malamas P, Wu KC, et al. Arrhythmia risk stratification of patients after myocardial infarction using personalized heart models. Nat Commun. 2016;7.

22. Gray RA, Pathmanathan P. Patient-Specific Cardiovascular Computational Modeling: Diversity of Personalization and Challenges. J Cardiovasc Trans Res. 2018;11(2):80–8.

23. Rantner LJ, Vadakkumpadan F, Spevak PJ, Crosson JE, Trayanova NA. Placement of implantable cardioverter-defibrillators in paediatric and congenital heart defect patients: a pipeline for model generation and simulation prediction of optimal configurations. J Physiol. 2013 Sep 1;591(17):4321–34.

24. Trayanova NA, Pashakhanloo F, Wu KC, Halperin HR. Imaging-Based Simulations for Predicting Sudden Death and Guiding Ventricular Tachycardia Ablation. Circ Arrhythmia Electrophysiol. 2017 Jul;10(7).

25. Mendonca Costa C, Neic A, Kerfoot E, Porter B, Sieniewicz B, Gould J, et al. Pacing in proximity to scar during cardiac resynchronization therapy increases local dispersion of repolarization and susceptibility to ventricular arrhythmogenesis. Hear Rhythm. 2019 Oct 1;16(10):1475–83.

26. Prassl AJ, Kickinger F, Ahammer H, Grau V, Schneider JE, Hofer E, et al. Automatically Generated, Anatomically Accurate Meshes for Cardiac Electrophysiology Problems. IEEE Trans Biomed Eng. 2009 May;56(5):1318–30.

27. Relan J, Chinchapatnam P, Sermesant M, Rhode K, Ginks M, Delingette H, et al. Coupled personalization of cardiac electrophysiology models for prediction of ischaemic ventricular tachycardia. Interface Focus. 2011;1(3):396–407.

28. Medtronic. Cardioinsight Mapping Vest [Internet]. 2016. Available from: https://www.medtronic.com/us-en/healthcare-professionals/products/cardiac-

rhythm/cardiac-mapping/cardioinsight-mapping-vest.html

29. Cedilnik N, Duchateau J, Dubois R, Sacher F, Jaïs P, Cochet H, et al. Fast personalized electrophysiological models from computed tomography images for ventricular tachycardia ablation planning. EP Eur. 2018;20:94–101.

30. Le Bras A. 3D virtual heart to guide VT ablation. Nat Rev Cardiol. 2018 Nov 1;15(11):654.

31. Potse M, Krause D, Kroon W, Murzilli R, Muzzarelli S, Regoli F, et al. Patient-specific modelling of cardiac electrophysiology in heart-failure patients. EP Eur. 2014 Nov 1;16(suppl_4):iv56–61.

32. Camps J, Lawson B, Drovandi C, Minchole A, Wang ZJ, Grau V, et al. Inference of ventricular activation properties from non-invasive electrocardiography. Med Image Anal. 2021 Oct 1;73:102143.

33. Corral-Acero J, Margara F, Marciniak M, Rodero C, Loncaric F, Feng Y, et al. The 'Digital Twin' to enable the vision of precision cardiology. Eur Heart J. 2020 Dec 21;41(48):4556–64.

34. Pathmanathan P, Gray RA. Validation and trustworthiness of multiscale models of cardiac electrophysiology. Front Physiol. 2018 Feb 15;9(FEB):106.

35. Roache PJ. Perspective: Validation - What does it mean? J Fluids Eng Trans ASME. 2009 Mar 1;131(3):0345031–4.

36. Topol EJ. High-performance medicine: the convergence of human and artificial intelligence. Nat Med. 2019;25:44–56.

37. Hung AJ, Chen J, Gill IS. Automated Performance Metrics and Machine Learning Algorithms to Measure Surgeon Performance and Anticipate Clinical Outcomes in Robotic Surgery. JAMA Surg. 2018 Aug 1;153(8):770–1.

38. Gehlbach PL. Robotic surgery for the eye. Nat Biomed Eng 2018 29. 2018 Sep 11;2(9):627–8.

39. Wang X, Peng Y, Lu L, Lu Z, Bagheri M, Summers RM. ChestX-ray8: Hospital-scale Chest X-ray

Database and Benchmarks on Weakly-Supervised Classification and Localization of Common Thorax Diseases. Proc - 30th IEEE Conf Comput Vis Pattern Recognition, CVPR 2017. 2017 May 5;2017-January:3462–71.

40. Seetharam K, Brito D, Farjo PD, Sengupta PP. The Role of Artificial Intelligence in Cardiovascular Imaging: State of the Art Review. Front Cardiovasc Med. 2020 Dec 23;7:374.

41. Strodthoff N, Strodthoff C. Detecting and interpreting myocardial infarction using fully convolutional neural networks. Physiol Meas. 2018 Jun 18;40(1).

42. Rajpurkar P, Hannun AY, Haghpanahi M, Bourn C, Ng AY. Cardiologist-Level Arrhythmia Detection with Convolutional Neural Networks. 2017 Jul 6;

43. Mathotaarachchi S, Pascoal TA, Shin M, Benedet AL, Kang MS, Beaudry T, et al. Identifying incipient dementia individuals using machine learning and amyloid imaging. Neurobiol Aging. 2017 Nov 1;59:80–90.

44. Trayanova NA, Popescu DM, Shade JK. Machine Learning in Arrhythmia and Electrophysiology. Circ Res. 2021 Feb 19;128(4):544–66.

45. Perez M V., et al. Large-Scale Assessment of a Smartwatch to Identify Atrial Fibrillation. N Engl J Med. 2019;

46. Muthalaly RG, Evans RM. Applications of Machine Learning in Cardiac Electrophysiology. Arrhythmia Electrophysiol Rev. 2020 Jun 1;9(2):71–7.

47. Feeny AK, Chung MK, Madabhushi A, Attia ZI, Cikes M, Firouznia M, et al. Artificial Intelligence and Machine Learning in Arrhythmias and Cardiac Electrophysiology. Circ Arrhythm Electrophysiol. 2020;13(8):873–90.

48. Andreu D, Fernández-Armenta J, Acosta J, Penela D, Jáuregui B, Soto-Iglesias D, et al. A QRS axis–based algorithm to identify the origin of scar-related ventricular tachycardia in the 17-

segment American Heart Association model. Hear Rhythm. 2018;15(10):1491–7.

49. Yokokawa M, Liu TY, Yoshida K, Scott C, Hero A, Good E, et al. Automated analysis of the 12-lead electrocardiogram to identify the exit site of postinfarction ventricular tachycardia. Hear Rhythm. 2012;9(3):330–4.

50. Sapp JL, Bar-Tal M, Howes AJ, Toma JE, El-Damaty A, Warren JW, et al. Real-Time Localization of Ventricular Tachycardia Origin From the 12-Lead Electrocardiogram. JACC Clin Electrophysiol. 2017 Jul 1;3(7):687–99.

51. Zhou S, AbdelWahab A, Sapp JL, Sung E, Aronis KN, Warren JW, et al. Prospective Multicenter Assessment of a New Intraprocedural Automated System for Localizing Idiopathic Ventricular Arrhythmia Origins. JACC Clin Electrophysiol. 2021 Mar 1;7(3):395–407.

52. Yang KC, Kyle JW, Makielski JC, Dudley SC. Mechanisms of Sudden Cardiac Death. Circ Res. 2015 Jun 5;116(12):1937–55.

53. Jackson N, Gizurarson S, Massé S, Nanthakumar K. Mechanisms of Human Ventricular Tachycardia and Human Ventricular Fibrillation. In: Cardiac Electrophysiology: From Cell to Bedside: Seventh Edition. Elsevier; 2018. p. 453–64.

54. Goyal A, Senst B, Bhyan P, Zeltser R. Reentry Arrhythmia. StatPearls Publishing; 2022.

55. Samie FH, Jalife J. Mechanisms underlying ventricular tachycardia and its transition to ventricular fibrillation in the structurally normal heart. Cardiovasc Res. 2001 May 1;50(2):242–50.

56. Stevenson WG, Friedman PL, Sager PT, Saxon LA, Kocovic D, Harada T, et al. Exploring Postinfarction Reentrant Ventricular Tachycardia With Entrainment Mapping. J Am Coll Cardiol. 1997 May 1;29(6):1180–9.

57. Aliot EM, Stevenson WG, Almendral-Garrote JM, Bogun F, Calkins CH, Delacretaz E, et al.

EHRA/HRS Expert Consensus on Catheter Ablation of Ventricular Arrhythmias: Developed in a partnership with the European Heart Rhythm Association (EHRA), a Registered Branch of the European Society of Cardiology (ESC), and the Heart Rhythm Society (HRS); i. Europace. 2009 Jun 1;11(6):771–817.

58. Mines GR. On dynamic equilibrium in the heart. J Physiol. 1913;46(4–5):349–83.

59. Smeets JLRM, Allessie MA, Lammers WJEP, Bonke FI, Hollen J. The wavelength of the cardiac impulse and reentrant arrhythmias in isolated rabbit atrium. Circ Res. 1986;58(1):96–108.

60. Frankel DS, Marchlinski FE. Ischemic Heart Disease. In: Cardiac Electrophysiology: From Cell to Bedside: Seventh Edition. Elsevier; 2018. p. 814–9.

61. Enriquez A, Riley M, Marchlinski F. Noninvasive clues for diagnosing ventricular tachycardia mechanism. J Electrocardiol. 2018 Mar 1;51(2):163–9.

62. Ciaccio EJ, Anter E, Coromilas J, Wan EY, Yarmohammadi H, Wit AL, et al. Structure and function of the ventricular tachycardia isthmus. Hear Rhythm. 2022 Jan;19(1):137–53.

63. Kezdi P, Rosenbaum MB. Classification of ventricular extrasystoles according to form. J Electrocardiol. 1969;2(3):289–97.

64. Josephson ME, Horowitz LN, Waxman HL, Cain ME, Spielman SR, Greenspan AM, et al. Sustained Ventricular Tachycardia: Role of the 12-lead Electrocardiogram in Localizing Site of Origin. Circulation. 1981;64(2):257–72.

65. Waxman HL, Josephson ME. Ventricular activation during ventricular endocardial pacing: I. Electrocardiographic patterns related to the site of pacing. Am J Cardiol. 1982;50(1):1–10.

66. Park KM, Kim YH, Marchlinski FE. Using the Surface Electrocardiogram to Localize the Origin of Idiopathic Ventricular Tachycardia. Pacing Clin Electrophysiol. 2012 Dec 1;35(12):1516–27.

67. Haaf P, Garg P, Messroghli DR, Broadbent DA, Greenwood JP, Plein S. Cardiac T1 Mapping and

Extracellular Volume (ECV) in clinical practice: A comprehensive review. J Cardiovasc Magn Reson. 2016 Nov 30;18(1):1–12.

68. Dixit S, Callans DJ. Mapping for Ventricular Tachycardia. Card Electrophysiol Rev. 2002;6:436–41.

69. Almendral JM, Stamato NJ, Rosenthal ME, Marchlinski FE, Miller JM, Josephson ME. Resetting response patterns during sustained ventricular tachycardia: relationship to the excitable gap. Circulation. 1986;74(4):722–30.

70. Josephson ME, Anter E. Substrate Mapping for Ventricular Tachycardia Assumptions and Misconceptions. Vol. 1, JACC: Clinical Electrophysiology. Elsevier Inc.; 2015. p. 341–52.

71. Maury P, Monteil B, Marty L, Duparc A, Mondoly P, Rollin A. Three-dimensional mapping in the electrophysiological laboratory. Arch Cardiovasc Dis. 2018 Jun 1;111(6–7):456–64.

72. Spartalis M, Spartalis E, Tzatzaki E, Tsilimigras DI, Moris D, Kontogiannis C, et al. Novel approaches for the treatment of ventricular tachycardia. World J Cardiol. 2018 Jul 26;10(7):52.

73. Wei C, Qian PC, Boeck M, Bredfeldt JS, Blankstein R, Tedrow UB, et al. Cardiac stereotactic body radiation therapy for ventricular tachycardia: Current experience and technical gaps. J Cardiovasc Electrophysiol. 2021 Nov 1;32(11):2901–14.

74. Anselmino M, Dusi V, M-c V, Jumeau R, Ozsahin M, Schwitter J, et al. Stereotactic Radiotherapy for the Management of Refractory Ventricular Tachycardia: Promise and Future Directions. Front Cardiovasc Med. 2020;1:108.

75. Tang PT, Do DH, Li A, Boyle NG. Team Management of the Ventricular Tachycardia Patient. Arrhythmia Electrophysiol Rev. 2018;7(4):1.

76. Martinek M, Manninger M, Schönbauer R, Scherr D, Schukro C, Pürerfellner H, et al. Expert consensus on acute management of ventricular arrhythmias – VT network Austria. IJC Hear

Vasc. 2021 Jun 1;34.

77. Swerdlow CD, Asirvatham SJ, Ellenbogen KA, Friedman PA. Troubleshooting Implanted Cardioverter Defibrillator Sensing Problems I. Circ Arrhythmia Electrophysiol. 2014 Dec;7(6):1237–61.

78. Padeletti L, Arnar DO, Boncinelli L, Brachman J, Camm JA, Daubert JC, et al. EHRA Expert Consensus Statement on the management of cardiovascular implantable electronic devices in patients nearing end of life or requesting withdrawal of therapy. Europace. 2010;12(10):1480–9.

79. Gierula J, Paton MF, Witte KK. Advances in cardiac resynchronization and implantable cardioverter/defibrillator therapy: Medtronic Cobalt and Crome. Future Cardiol. 2021 Jul 1;17(4):609–18.

80. Antoniadis AP, Behar JM, Sieniewicz B, Gould J, Niederer S, Rinaldi CA. A comparison of the different features of quadripolar left ventricular pacing leads to deliver cardiac resynchronization therapy. Expert Rev Med Devices. 2017 Sep 2;14(9):697–706.

81. O'Donnell D, Nadurata V. Radiofrequency Ablation for Post Infarction Ventricular Tachycardia. Indian Pacing Electrophysiol J. 2004 Apr 1;4(2):63.

82. Anderson RD, Ariyarathna N, Lee G, Virk S, Trivic I, Campbell T, et al. Catheter ablation versus medical therapy for treatment of ventricular tachycardia associated with structural heart disease: Systematic review and meta-analysis of randomized controlled trials and comparison with observational studies. Hear Rhythm. 2019;16(10):1484–91.

83. Stevenson WG, Soejima K. Catheter ablation for ventricular tachycardia. Circulation. 2007 May 29;115(21):2750–60.

84. Nazer B, Gerstenfeld EP. Catheter Ablation of Ventricular Tachycardia in Patients with Post-Infarction Cardiomyopathy. Korean Circ J. 2014;44(4):210.

85. Buch E, Boyle NG, Shivkumar K. Catheter Ablation: Technical Aspects. Card Electrophysiol From Cell to Bedside Seventh Ed. 2018 Jan 1;1185–93.

86. Samuel M, Elsokkari I, Sapp JL. Ventricular Tachycardia Burden and Mortality: Association or Causality? Can J Cardiol. 2022 Jan;1–11.

87. Clayton RH, Bernus O, Cherry EM, Dierckx H, Fenton FH, Mirabella L, et al. Models of cardiac tissue electrophysiology: Progress, challenges and open questions. Prog Biophys Mol Biol. 2011;104(1–3):22–48.

88. Bishop MJ, Plank G, Burton RAB, Schneider JE, Gavaghan DJ, Grau V, et al. Development of an anatomically detailed MRI-derived rabbit ventricular model and assessment of its impact on simulations of electrophysiological function. AJP Hear Circ Physiol. 2010;

89. Trayanova NA, Boyle PM. Advances in modeling ventricular arrhythmias: From mechanisms to the clinic. Wiley Interdiscip Rev Syst Biol Med. 2014;

90. Trayanova NA, O'Hara T, Bayer JD, Boyle PM, McDowell KS, Constantino J, et al. Computational cardiology: How computer simulations could be used to develop new therapies and advance existing ones. Europace. 2012.

91. Peirlinck M, Costabal FS, Yao J, Guccione JM, Tripathy S, Wang Y, et al. Precision medicine in human heart modeling: Perspectives, challenges, and opportunities. Vol. 20, Biomechanics and Modeling in Mechanobiology. Springer Science and Business Media Deutschland GmbH; 2021. p. 803–31.

92. Hodgkin AL, Huxley AF. A quantitative description of membrane current and its application to conduction and excitation in nerve. J Physiol. 1952;117:500–44.

93. NOBLE D. Cardiac Action and Pacemaker Potentials based on the Hodgkin-Huxley Equations. Nature. 1960 Nov;188(4749):495–7.

94. ten Tusscher KHWJ, Noble D, Noble PJ, Panfilov A V. A model for human ventricular tissue. Am J Physiol Circ Physiol. 2004;286(4):H1573–89.

95. ten Tusscher KHWJ, Panfilov A V. Alternans and spiral breakup in a human ventricular tissue model. Am J Physiol Circ Physiol. 2006 Sep;291(3):H1088–100.

96. Einthoven W, Flohil A, Battaerd PJT. On Vagus Currents Examined with the String Galvanometer. Exp Physiol. 1908;

97. Einthoven W. The different forms of the human electrocardiogram and their signification. Lancet. 1912;179(4622):853–61.

98. Alghatrif M, Lindsay J. Journal of Community Hospital Internal Medicine Perspectives ISSN: (Print) 2000-9666 (Online) Journal homepage: https://www.tandfonline.com/loi/zjch20 A brief review: history to understand fundamentals of electrocardiography. J Community Hosp Intern Med Perspect. 1438;2(1).

99. Pernod E, Sermesant M, Konukoglu E, Relan J, Delingette H, Ayache N, et al. A Multi-Front Eikonal Model of Cardiac Electrophysiology for Interactive Simulation of Radio-Frequency Ablation . Comput Graph. 2011;35:431–40.

100. Neic A, Campos FO, Prassl AJ, Niederer SA, Bishop MJ, Vigmond EJ, et al. Efficient computation of electrograms and ECGs in human whole heart simulations using a reaction-eikonal model. J Comput Phys. 2017;346:191–211.

101. Bishop MJ, Plank G. Bidomain ECG simulations using an augmented monodomain model for the cardiac source. IEEE Trans Biomed Eng. 2011;58(8):2297–307.

102. Potse M. Scalable and Accurate ECG Simulation for Reaction-Diffusion Models of the Human Heart. Front Physiol. 2018 Apr 20;9(APR):370.

103. Bishop MJ, Plank G. Representing cardiac bidomain bath-loading effects by an augmented

monodomain approach: Application to complex ventricular models. IEEE Trans Biomed Eng. 2011;58(4):1066–75.

104. Vigmond EJ, Hughes M, Plank G, Leon LJ. Computational tools for modeling electrical activity in cardiac tissue. J Electrocardiol. 2003;36:69–74.

105. Strocchi M, Augustin CM, Gsell MAF, Karabelas E, Neic A, Gillette K, et al. A publicly available virtual cohort of four-chamber heart meshes for cardiac electro-mechanics simulations. PLoS One. 2020 Jun 1;15(6):e0235145.

106. Gillette K, Gsell MAF, Prassl AJ, Karabelas E, Reiter U, Reiter G, et al. A Framework for the generation of digital twins of cardiac electrophysiology from clinical 12-leads ECGs. Med Image Anal. 2021;71:102080.

107. Plancke AM, Connolly A, Gemmell PM, Neic A, McSpadden LC, Whitaker J, et al. Generation of a cohort of whole-torso cardiac models for assessing the utility of a novel computed shock vector efficiency metric for ICD optimisation. Comput Biol Med. 2019 Sep 1;112.

108. Habijan M, Babin D, Galić I, Leventić H, Romić K, Velicki L, et al. Overview of the Whole Heart and Heart Chamber Segmentation Methods. Cardiovasc Eng Technol. 2020;11(6):725–47.

109. Lawson CL, Curtis R, Fletche R, Powell MJB, Reid JK. Transforming triangulations. Discrete Math. 1972;3(4):365–72.

110. Lo SH. A new mesh generation scheme for arbitrary planar domains. Int J Numer Methods Eng. 1985;21(8):1403–26.

111. Shephard MS, Georges MK. Automatic three-dimensional mesh generation by the finite octree technique. Int J Numer Methods Eng. 1991 Sep 1;32(4):709–49.

112. Tu J, Yeoh G-H, Liu C. CFD Mesh Generation: A Practical Guideline. In: Computational Fluid Dynamics. Elsevier; 2018. p. 125–54.

113. Mitchell TM. Machine Learning. 1997.

114. Hastie T, Tibshirani R, Friedman J. he Elements of Statistical Learning Data Mining, Inference, and Prediction. Second. 2001.

115. Understanding LSTM Networks -- colah's blog [Internet]. [cited 2022 Apr 14]. Available from: https://colah.github.io/posts/2015-08-Understanding-LSTMs/

116. Hochreiter S, Schmidhuber J. Long Short-Term Memory. Neural Comput. 1997 Nov 15;9(8):1735–80.

117. Cho K, Van Merriënboer B, Gulcehre C, Bahdanau D, Bougares F, Schwenk H, et al. Learning Phrase Representations using RNN Encoder-Decoder for Statistical Machine Translation.

118. Gers FA, Schmidhuber J. Recurrent nets that time and count. Proc Int Jt Conf Neural Networks. 2000;3:189–94.

119. Yao K, Cohn T, Vylomova K, Duh K, Dyer C. Depth-Gated Recurrent Neural Networks.

120. Bahdanau D, Cho K, Bengio Y. NEURAL MACHINE TRANSLATION BY JOINTLY LEARNING TO ALIGN AND TRANSLATE.

121. Niu Z, Zhong G, Yu H. A review on the attention mechanism of deep learning. Neurocomputing. 2021 Sep 10;452:48–62.

122. Jin G, Zhu T, Akram MW, Jin Y, Zhu C. An Adaptive Anti-Noise Neural Network for Bearing Fault Diagnosis under Noise and Varying Load Conditions. IEEE Access. 2020;8:74793–807.

123. Pan SJ, Yang Q. A Survey on Transfer Learning. IEEE Trans Knowl Data Eng. 2010;22(10):1345–59.

124. Feurer M, Hutter F. Hyperparameter Optimization. In: Automated Machine learning. Springer, Cham; 2019. p. 3–33.

125. Smith LN. Cyclical Learning Rates for Training Neural Networks. Proc - 2017 IEEE Winter Conf Appl Comput Vision, WACV 2017. 2015 Jun 3;464–72.

126. Hinton GE, Srivastava N, Krizhevsky A, Sutskever I, Salakhutdinov RR. Improving neural networks by preventing co-adaptation of feature detectors. 2012 Jul 3;

127. Gal Y, Uk ZA. Dropout as a Bayesian Approximation: Representing Model Uncertainty in Deep Learning Zoubin Ghahramani. 2016;

128. Tung R, Mathuria N, Michowitz Y, Yu R, Buch E, Bradfield J, et al. Functional pace-mapping responses for identification of targets for catheter ablation of scar-mediated ventricular tachycardia. Circ Arrhythmia Electrophysiol. 2012;5(2):264–72.

129. Josephson ME. NASPE HISTORY SERIES Electrophysiology of Ventricular Tachycardia: A Historical Perspective.

130. Josephson ME, Waxman HL, Cain ME, Gardner MJ, Buxton AE. Ventricular activation during ventricular endocardial pacing. II. Role of pace-mapping to localize origin of ventricular tachycardia. Am J Cardiol. 1982 Jul 1;50(1):11–22.

131. Guandalini GS, Liang JJ, Marchlinski FE. Ventricular Tachycardia Ablation. JACC Clin Electrophysiol. 2019 Dec 1;5(12):1363–83.

132. Curry P, O'Keefe D, Pitcher D, Sowton E, Deverall P, Yates A. Localization of ventricular tachycardia by a new technique—pace-mapping (abstr) . Circulation. 1979;80(2):II–25.

133. O'Keeffe D, Curry P, Prior A, Yates A, Deverall P, Sowton E. Surgery for ventricular tachycardia using operative pace mapping. Br Heart J. 1980;83.

134. Josephson ME, Waxman HL, Cain ME, Gardner MJ, Buxton AE. Ventricular activation during ventricular endocardial pacing. II. Role of pace-mapping to localize origin of ventricular tachycardia. Am J Cardiol. 1982 Jul;50(1):11–22.

135. Kastor JA, Spear JF, Moore EN. Localization of ventricular irritability by epicardial mapping. Origin of digitalis-induced unifocal tachycardia from left ventricular Purkinje tissue. Circulation. 1972;45(5):952–64.

136. Horowitz LN, Spear JF, Moore EN. Subendocardial Origin of Ventricular Arrhythmias in 24-Hour-Old Experimental Myocardial Infarction.

137. Li A, Davis JS, Wierwille J, Herold K, Morgan D, Behr E, et al. Relationship between Distance and Change in Surface ECG Morphology during Pacemapping as a Guide to Ablation of Ventricular Arrhythmias: Implications for the Spatial Resolution of Pacemapping. Circ Arrhythmia Electrophysiol. 2017 Jan 1;10(1).

138. Wrobleski D, Houghtaling C, Josephson ME, Ruskin JN, Reddy VY. Use of Electrogram Characteristics During Sinus Rhythm to Delineate the Endocardial Scar in a Porcine Model of Healed Myocardial Infarction. Vol. 14, J Cardiovasc Electrophysiol. 2003.

139. Callans DJ, Ren J-F, Michele J, Marchlinski FE, Dillon SM. Electroanatomic Left Ventricular Mapping in the Porcine Model of Healed Anterior Myocardial Infarction Correlation With Intracardiac Echocardiography and Pathological Analysis. 1999.

140. Gerstenfeld EP, Dixit S, Callans DJ, Rajawat Y, Rho R, Marchlinski FE. Quantitative comparison of spontaneous and paced 12-lead electrocardiogram during right ventricular outflow tract ventricular tachycardia. J Am Coll Cardiol. 2003 Jun 4;41(11):2046–53.

141. de Chillou C, Groben L, Magnin-Poull I, Andronache M, Abbas MM, Zhang N, et al. Localizing the critical isthmus of postinfarct ventricular tachycardia: The value of pace-mapping during sinus rhythm. Hear Rhythm. 2014 Feb;11(2):175–81.

142. Marchlinski FE, Callans DJ, Gottlieb CD, Zado E. Linear Ablation Lesions for Control of Unmappable Ventricular Tachycardia in Patients With Ischemic and Nonischemic Cardiomyopathy. Circulation. 2000 Mar 21;101(11):1288–96.

143. Berruezo A, Fernández-Armenta J, Andreu D, Penela D, Herczku C, Evertz R, et al. Scar dechanneling: new method for scar-related left ventricular tachycardia substrate ablation. Circ Arrhythm Electrophysiol. 2015 Apr 20;8(2):326–36.

144. Azegami K, Wilber DJ, Arruda M, Lin AC, Denman RA. Spatial resolution of pacemapping and activation mapping in patients with idiopathic right ventricular outflow tract tachycardia. J Cardiovasc Electrophysiol. 2005;16(8):823–9.

145. Odille F, Battaglia A, Hoyland P, Sellal J-M, Voilliot D, De Chillou C, et al. Catheter Treatment of Ventricular Tachycardia: A Reference-Less Pace-Mapping Method to Identify Ablation Targets. IEEE Trans Biomed Eng. 2019;66(11):3278–87.

146. Guandalini GS, Liang JJ, Marchlinski FE. Ventricular Tachycardia Ablation: Past, Present, and Future Perspectives. JACC Clin Electrophysiol. 2019 Dec;5(12):1363–83.

147. Sosa E, Scanavacca M, D'Avila A, Piccioni J, Sanchez O, Velarde JL, et al. Endocardial and epicardial ablation guided by nonsurgical transthoracic epicardial mapping to treat recurrent ventricular tachycardia. J Cardiovasc Electrophysiol. 1998;9(3):229–39.

148. Hanaki Y, Komatsu Y, Nogami A, Kowase S, Kurosaki K, Sekiguchi Y, et al. Combined endo- and epicardial pace-mapping to localize ventricular tachycardia isthmus in ischaemic and non-ischaemic cardiomyopathy. EP Eur. 2022 Apr 5;24(4):587–97.

149. Kamakura S, Shimizu W, Matsuo K, Taguchi A, Suyama K, Kurita T, et al. Localization of Optimal Ablation Site of Idiopathic Ventricular Tachycardia from Right and Left Ventricular Outflow Tract by Body Surface ECG. 1998.

150. S U, Iwa T, Magara T. Diagnosis of the site of origin of ventricular tachycardia by body surface mapping. Adv Electrocardiol. 1985;89–91.

151. S K, Aihara N, Matsuhisa M, Ohe T, Sato I, Shimomura K. The role of initial minimum potentials on body surface maps in localizing the earliest endocardial site of ectopic ventricular excitation.

Circulation. 1988;78(II):II–138.

152. Hayashi H, Watabe S, Takami K, Yabe S, Uematsu H, Mizutani M, et al. Sites of origin of ventricular premature beats in patients with and without cardiovascular disease evaluated by body surface mapping. J Electrocardiol. 1988;21:137–46.

153. SippensGroenewegen A, Spekhorst H, Van Hemel NM, Kingma JH, Hauer RN, de Zwart M, et al. Body surface mapping during endocardial pacing at multiple left ventricular sites: Impact of apical aneurysm on ventricular activation patters. PACE. 1989;12(6777).

154. SippensGroenewegen A, Spekhorst H, Van Hemel NM, Kingma JH, Hauer RNW, Janse MJ, et al. Body surface mapping of ectopic left and right ventricular activation. QRS spectrum in patients without structural heart disease. Circulation. 1990;82(3):879–96.

155. Potse M, Linnenbank AC, Peeters HAP, SippensGroenewegen A, Crimbergen CA. Continuous localization of cardiac activation sites using a database of multichannel ECG recordings. IEEE Trans Biomed Eng. 2000 May;47(5):682–9.

156. Messinger-Rapport BJ, Rudy Y. Computational issues of importance to the inverse recovery of epicardial potentials in a realistic heart-torso geometry. Math Biosci. 1989 Nov 1;97(1):85–120.

157. Oster HS, Rudy Y. The Use of Temporal Information in the Regularization of the Inverse Problem of Electrocardiography. IEEE Trans Biomed Eng. 1992;39(1):65–75.

158. Oster HS, Taccardi B, Lux RL, Ershler PR, Rudy Y. Noninvasive electrocardiographic imaging: Reconstruction of epicardial potentials, electrograms, and isochrones and localization of single and multiple electrocardiac events. Circulation. 1997 Aug 5;96(3):1012–24.

159. Yang T, Yu L, Jin Q, Wu L, He B. Localization of Origins of Premature Ventricular Contraction by Means of Convolutional Neural Network From 12-Lead ECG. IEEE Trans Biomed Eng. 2018;65(7):1662–71.

160. Zhou S, AbdelWahab A, Sapp JL, Warren JW, Horáček BM. Localization of Ventricular Activation Origin from the 12-Lead ECG: A Comparison of Linear Regression with Non-Linear Methods of Machine Learning. Ann Biomed Eng. 2019;47(2):403–12.

161. He K, Nie Z, Zhong G, Yang C, Yang C, Sun J. Localization of origins of premature ventricular contraction in the whole ventricle based on machine learning and automatic beat recognition from 12-lead ECG. Physiol Meas. 2020 May 1;41(5):055007.

162. Zhou S, Sapp JL, Horáček BM, Warren JW, MacInnis PJ, Davis J, et al. Automated intraprocedural localization of origin of ventricular activation using patient-specific computed tomographic imaging. Hear Rhythm. 2020 Apr 1;17(4):567–75.

163. Miller JM, Marchlinski FE, Buxton AE, Josephson ME. Relationship between the 12-lead electrocardiogram during ventricular tachycardia and endocardial site of origin in patients with coronary artery disease. Circulation. 1988;77(4):759–66.

164. Kuchar DL, Ruskin JN, Garan H. Electrocardiographic localization of the site of origin of ventricular tachycardia in patients with prior myocardial infarction. J Am Coll Cardiol. 1989 Mar 15;13(4):893–900.

165. Segal OR, Chow AWC, Wong T, Trevisi N, Lowe MD, Davies DW, et al. A Novel Algorithm for Determining Endocardial VT Exit Site from 12-Lead Surface ECG Characteristics in Human, Infarct-Related Ventricular Tachycardia. J Cardiovasc Electrophysiol. 2007 Feb 1;18(2):161–8.

166. Wijnmaalen AP, Stevenson WG, Schalij MJ, Field ME, Stephenson K, Tedrow UB, et al. ECG Identification of Scar-Related Ventricular Tachycardia With a Left Bundle-Branch Block Configuration. Circ Arrhythmia Electrophysiol. 2011;4:486–93.

167. Selvadurai BSN, Puntmann VO, Bluemke DA, Ferrari VA, Friedrich MG, Kramer CM, et al. Definition of Left Ventricular Segments for Cardiac Magnetic Resonance Imaging. JACC Cardiovasc Imaging. 2018;11(6):926–8.

168. Cerqueira MD, Weissman NJ, Dilsizian V, Jacobs AK, Kaul S, Laskey WK, et al. Standardized myocardial sementation and nomenclature for tomographic imaging of the heart: A Statement for Healthcare Professionals from the Cardiac Imaging Committee of the Council on Clinical Cardiology of the American Heart Association. Circulation. 2002 Jan 29;105(4):539–42.

169. Zhou S, Abdelwahab A, Horáček BM, Macinnis PJ, Warren JW, Davis JS, et al. Prospective Assessment of an Automated Intraprocedural 12-Lead ECG-Based System for Localization of Early Left Ventricular Activation. Circ Arrhythmia Electrophysiol. 2020 Jul 1;13(7):665–75.

170. Zhou S, AbdelWahab A, Sapp JL, Sung E, Aronis KN, Warren JW, et al. Assessment of an ECG-Based System for Localizing Ventricular Arrhythmias in Patients With Structural Heart Disease. J Am Heart Assoc. 2021 Oct 19;10(20):e022217.

171. Acharya UR, Fujita H, Lih OS, Hagiwara Y, Tan JH, Adam M. Automated detection of arrhythmias using different intervals of tachycardia ECG segments with convolutional neural network. Inf Sci (Ny). 2017 Sep 1;405:81–90.

172. Kachuee M, Fazeli S, Sarrafzadeh M. ECG Heartbeat Classification: A Deep Transferable Representation.

173. Lyon A, Mincholé A, Martínez JP, Laguna P, Rodriguez B. Computational techniques for ECG analysis and interpretation in light of their contribution to medical advances. JRSoc Interface. 2018;15.

174. Hazra D, Byun YC. Synsiggan: Generative adversarial networks for synthetic biomedical signal generation. Biology (Basel). 2020 Dec 1;9(12):1–20.

175. Alfaras M, Soriano MC, Ortín S. A Fast Machine Learning Model for ECG-Based Heartbeat Classification and Arrhythmia Detection. Front Phys. 2019 Jul 18;0:103.

176. Moody GB, Mark RG. The impact of the MIT-BIH arrhythmia database. IEEE Eng Med Biol Mag. 2001;20(3):45–50.

177. Goldberger AL, Amaral LA, Glass L, Hausdorff JM, Ivanov PC, Mark RG, et al. PhysioBank, PhysioToolkit, and PhysioNet. Circulation. 2000 Jun 13;101(23).

178. Yao Q, Wang R, Fan X, Liu J, Li Y. Multi-class Arrhythmia detection from 12-lead varied-length ECG using Attention-based Time-Incremental Convolutional Neural Network. Inf Fusion. 2020;53(June 2019):174–82.

179. Monaci S, Strocchi M, Rodero C, Gillette K, Whitaker J, Rajani R, et al. In-silico pace-mapping using a detailed whole torso model and implanted electronic device electrograms for more efficient ablation planning. Comput Biol Med. 2020;125:104005.

180. CIBC. Seg3D: Volumetric Image Segmentation and Visualization. Scientific Computing and Imaging Institute (SCI) [Internet]. 2016. Available from: http://www.seg3d.org

181. Zheng Y, Barbu A, Georgescu B, Scheuering M, Comaniciu D. Four-chamber heart modeling and automatic segmentation for 3-D cardiac CT volumes using marginal space learning and steerable features. IEEE Trans Med Imaging. 2008;27(11):1668–81.

182. Bayer J, Prassl AJ, Pashaei A, Gomez JF, Frontera A, Neic A, et al. Universal ventricular coordinates: A generic framework for describing position within the heart and transferring data. Med Image Anal. 2018;45:83–93.

183. Whitaker J, Neji R, Byrne N, Puyol-Antón E, Mukherjee RK, Williams SE, et al. Improved co-registration of ex-vivo and in-vivo cardiovascular magnetic resonance images using heart-specific flexible 3D printed acrylic scaffold combined with non-rigid registration. J Cardiovasc Magn Reson. 2019;21(1).

184. Campos FO, Orini M, Taggart P, Hanson B, Lambiase PD, Porter B, et al. Characterizing the clinical implementation of a novel activation-repolarization metric to identify targets for catheter ablation of ventricular tachycardias using computational models. 2019 May 1;108:263–75.

185. Gemmell PM, Gillette K, Balaban G, Rajani R, Vigmond EJ, Plank G, et al. A computational investigation into rate-dependant vectorcardiogram changes due to specific fibrosis patterns in non-ischæmic dilated cardiomyopathy. Comput Biol Med. 2020 Aug 1;123:103895.

186. Caldwell BJ, Trew ML, Sands GB, Hooks DA, Legrice IJ, Smaill BH. Three Distinct Directions of Intramural Activation Reveal Nonuniform Side-to-Side Electrical Coupling of Ventricular Myocytes. Circ Arrhythmia Electrophysiol. 2009;2:433–40.

187. Arevalo HJ, Plank G, Helm P, Halperin H, Trayanova NA, McDowell KS, et al. Tachycardia in Post-Infarction Hearts: Insights from 3D Image-Based Ventricular Models. PLoS One. 2013;8(7):1–10.

188. Pashakhanloo F, Herzka DA, Halperin H, McVeigh ER, Trayanova NA. Role of 3-Dimensional Architecture of Scar and Surviving Tissue in Ventricular Tachycardia. Circ Arrhythmia Electrophysiol. 2018;11(6).

189. ACUITY™ X4 Quadripolar LV Leads - Boston Scientific [Internet]. Available from: https://www.bostonscientific.com/en-US/products/leads/acuity-x4-quadripolar-lv-lead.html

190. Mukherjee RK, Whitaker J, Williams SE, Razavi R, O'Neill MD. Magnetic resonance imaging guidance for the optimization of ventricular tachycardia ablation. Europace. 2018;20(11):1721–32.

191. Azevedo PS, Polegato BF, Minicucci MF, Paiva SAR, Zornoff LAM. Cardiac Remodeling: Concepts, Clinical Impact, Pathophysiological Mechanisms and Pharmacologic Treatment.

192. Gordon ´, Tomaselli F, Marban E. Electrophysiological remodeling in hypertrophy and heart failure. Cardiovasc Res. 1999;42:270–83.

193. Pinto JMB, Boyden PA. Electrical remodeling in ischemia and infarction. Cardiovasc Res. 1999 May;42(2):284–97.

194. Ghosh N, Mangat I, O' SS, Msc D, Pinter A, Korley V, et al. Outcomes in heart failure patients referred for consideration of implantable cardioverter defibrillator for primary prophylaxis of sudden cardiac death: What are the risks of waiting? Can J Cardiol. 2009;25:342.

195. Zipes DP, Camm JA. ACC/AHA/ESC 2006 Guidelines for Management of Patients With Ventricular Arrhythmias and the Prevention of Sudden Cardiac Death: A Report of the American College of Cardiology/American Heart Association Task Force and the European Society of Cardiology Com. J Am Coll Cardiol. 2006 Sep 5;48(5):e247–346.

196. Campos FO, Neic A, Costa CM, Whitaker J, O'Neill M, Razavi R, et al. An automated near-real time computational method for induction and treatment of scar-related ventricular tachycardias. Med Image Anal. 2021;80:102483.

197. Deng D, Prakosa A, Shade J, Nikolov P, Trayanova NA. Characterizing Conduction Channels in Postinfarction Patients Using a Personalized Virtual Heart. Biophys J. 2019;117(12):2287–94.

198. Monaci S, Gillette K, Puyol-Antón E, Rajani R, Plank G, King A, et al. Automated Localization of Focal Ventricular Tachycardia From Simulated Implanted Device Electrograms: A Combined Physics–AI Approach. Front Physiol. 2021;12:943.

199. Messineo FC. Ventricular ectopic activity: Prevalence and risk. Am J Cardiol. 1989 Dec 5;64(20):J53–6.

200. Ahn M-S. Current Concepts of Premature Ventricular Contractions. J Lifestyle Med. 2013;3(1):26–33.

201. Marcus GM. Evaluation and Management of Premature Ventricular Complexes. Circulation. Lippincott Williams and Wilkins; 2020. p. 1404–18.

202. Hayashi T, Liang JJ, Shirai Y, Kuo L, Muser D, Kubala M, et al. Trends in Successful Ablation Sites and Outcomes of Ablation for Idiopathic Outflow Tract Ventricular Arrhythmias. JACC Clin Electrophysiol. 2020 Feb 1;6(2):221–30.

203. Jáuregui B, Penela D, Fernández-Armenta J, Acosta J, Terés C, Soto-Iglesias D, et al. Impact of a predefined pacemapping protocol use for ablation of infrequent premature ventricular complexes: A prospective, multicenter study. Hear Rhythm. 2021 Oct 1;18(10):1709–16.

204. Farzam K, Richards J. Premature Ventricular Contraction. Treasure Island (FL): StatePearls Publishing; 2022.

205. Costa CM, Hoetzl E, Rocha BM, Prassl AJ, Plank G. Automatic Parameterization Strategy for Cardiac Electrophysiology Simulations. Comput Cardiol (2010). 2013;40:373–6.

206. Pedregosa F, Michel V, Grisel O, Blondel M, Prettenhofer P, Weiss R, et al. Scikit-learn: Machine Learning in Python Gaël Varoquaux Bertrand Thirion Vincent Dubourg Alexandre Passos PEDREGOSA, VAROQUAUX, GRAMFORT ET AL. Matthieu Perrot. Vol. 12, Journal of Machine Learning Research. 2011.

207. Abadi M, Agarwal A, Barham P, Brevdo E, Chen Z, Citro C, et al. TensorFlow: Large-scale machine learning on heterogeneous systems [Internet]. 2015. Available from: tensorflow.org

208. Trakic A, Akhand M, Wang H, Mason D, Liu F, Wilson S, et al. Computational modelling of blood-flow-induced changes in blood electrical conductivity and its contribution to the impedance cardiogram. Physiol Meas. 2010;31(1):13–33.

209. Sovilj S, Magjarević R, Abed A Al, Lovell NH, Dokos S. Simplified 2D Bidomain Model of Whole Heart Electrical Activity and ECG Generation. Meas Sci Rev. 2014 Jun 1;14(3):136–43.

210. Leclercq C, Sadoul N, Mont L, Defaye P, Osca J, Mouton E, et al. Comparison of right ventricular septal pacing and right ventricular apical pacing in patients receiving cardiac resynchronization therapy defibrillators: the SEPTAL CRT Study. Eur Heart J. 2016;37:473–83.

211. Winter J, Heil JE, Schumann C, Lin Y, Schannwell CM, Michel U, et al. Effect of implantable cardioverter/defibrillator lead placement in the right ventricle on defibrillation energy requirements. A combined experimental and clinical study1. Eur J Cardio-Thoracic Surg. 1998

Oct 1;14(4):419–25.

212. Wittkampf FH, Hauer RN, Robles de Medina EO. Control of radiofrequency lesion size by power regulation. Circulation. 1989 Oct;80(4):962–8.

213. Kowalski M, Ellenbogen KA, Wood MA, Friedman PL. Implantable cardiac defibrillator lead failure or myopotential oversensing? An approach to the diagnosis of noise on lead electrograms.

214. Agarwal S, Panizo JG, Barra S, Mellor G, Heck P. Premature Ventricular Complex-induced Cardiomyopathy. Arrhythmia Electrophysiol Rev. 2018;7(2):128–34.

215. Monaci S, Qian S, Gillette K, Puyol-Antón E, Mukherjee R, Elliott MK, et al. Non-invasive localization of post-infarct ventricular tachycardia exit sites to guide ablation planning: a computational deep learning platform utilizing the 12-lead electrocardiogram and intracardiac electrograms from implanted devices. EP Eur. 2022 Nov 12;

216. Qian S, Monaci S, Mendonca Costa C, Campos F, Gemmell P, Zaidi S, et al. Optimization of defibrillation thresholds in right-sided ICD generator placement using a cohort of whole-torso models. Submitt to JACC. 2022;

217. Bayer JD, Blake RC, Plank G, Trayanova NA. A Novel Rule-Based Algorithm for Assigning Myocardial Fiber Orientation to Computational Heart Models. Ann Biomed Eng. 2012;40(10):2243–54.

218. Martin R, Hocini M, Haïsaguerre M, Jaïs P, Sacher F. Ventricular Tachycardia Isthmus Characteristics: Insights from High-density Mapping. Arrhythmia Electrophysiol Rev. 2019 Mar 12;8(1):54–9.

219. De Chillou C, Lacroix D, Klug D, Magnin-Poull I, Marquié C, Messier M, et al. Isthmus Characteristics of Reentrant Ventricular Tachycardia After Myocardial Infarction. Circulation. 2002;105(6):726–31.

220. Ilg K, Baman TS, Gupta SK, Swanson S, Good E, Chugh A, et al. Assessment of Radiofrequency Ablation Lesions by CMR Imaging After Ablation of Idiopathic Ventricular Arrhythmias. JACC Cardiovasc Imaging. 2010 Mar;3(3):278–85.

221. Simonyan K, Zisserman A. Very Deep Convolutional Networks for Large-Scale Image Recognition. 3rd Int Conf Learn Represent ICLR 2015 - Conf Track Proc. 2014;

222. Winata GI, Kampman OP, Fung P. Attention-Based LSTM for Psychological Stress Detection from Spoken Language Using Distant Supervision. ICASSP, IEEE Int Conf Acoust Speech Signal Process - Proc. 2018;2018-April:6204–8.

223. Eynon CA, Howe L, Firoozan S. Fascicular tachycardia: uncommon or just unrecognised? Emerg Med J. 2002 Sep 1;19(5):477 LP – 478.

224. Chen H, Chan K, Po SS, Chen M. Idiopathic left ventricular tachycardia originating in the left posterior fascicle. Arrhythmia Electrophysiol Rev. 2019 Mar 1;8(4):249–54.

225. Phanthawimol W, Nogami A, Haruna T, Morishima I, Hasebe H, Mizutani Y, et al. Reverse-Type Left Posterior Fascicular Ventricular Tachycardia: A New Electrocardiographic Entity. JACC Clin Electrophysiol. 2021 Jul 1;7(7):843–54.

226. Cedilnik N, Duchateau J, Dubois R, Sacher F, Jaïs P, Cochet H, et al. Fast personalized electrophysiological models from computed tomography images for ventricular tachycardia ablation planning. Europace. 2018 Nov 1;20(suppl_3):III94–101.

227. inHEART Medical [Internet]. [cited 2022 Jun 15]. Available from: https://www.inheartmedical.com/

228. Hu Y, Schneider T, Wang B, Zorin D, Panozzo D. Fast tetrahedral meshing in the wild. ACM Trans Graph. 2020 Jul 8;39(4).

229. Keller DUJ, Weber FM, Seemann G, Dössel O. Ranking the influence of tissue conductivities on

forward-calculated ecgs. IEEE Trans Biomed Eng. 2010;57(7):1568–76.

230. Kato Y, Kizer JR, Ostovaneh MR, Lazar J, Peng Q, Van Der Geest RJ, et al. Comparison of three dimensional reconstruction and conventional computer tomography angiography in patients undergoing zero-ischemia laparoscopic partial nephrectomy. 2020;

231. Miller CA, Naish JH, Bishop P, Coutts G, Clark D, Zhao S, et al. Comprehensive validation of cardiovascular magnetic resonance techniques for the assessment of myocardial extracellular volume. Circ Cardiovasc Imaging. 2013 May;6(3):373–83.

232. Nacif MS, Kawel N, Lee JJ, Chen X, Yao J, Zavodni A, et al. Interstitial Myocardial Fibrosis Assessed as Extracellular Volume Fraction with Low-Radiation-Dose Cardiac CT. Radiology. 2012 Sep;264(3):876.

233. Bandula S, White SK, Flett AS, Lawrence D, Pugliese F, Ashworth MT, et al. Measurement of Myocardial Extracellular Volume Fraction by Using Equilibrium Contrast-enhanced CT: Validation against Histologic Findings. Radiology. 2013 Nov;269(2):396–403.

234. Sapp JL, Zhou S, Wang L. Mapping ventricular tachycardia with electrocardiographic imaging. Vol. 13, Circulation: Arrhythmia and Electrophysiology. Lippincott Williams and Wilkins; 2020. p. E008255.